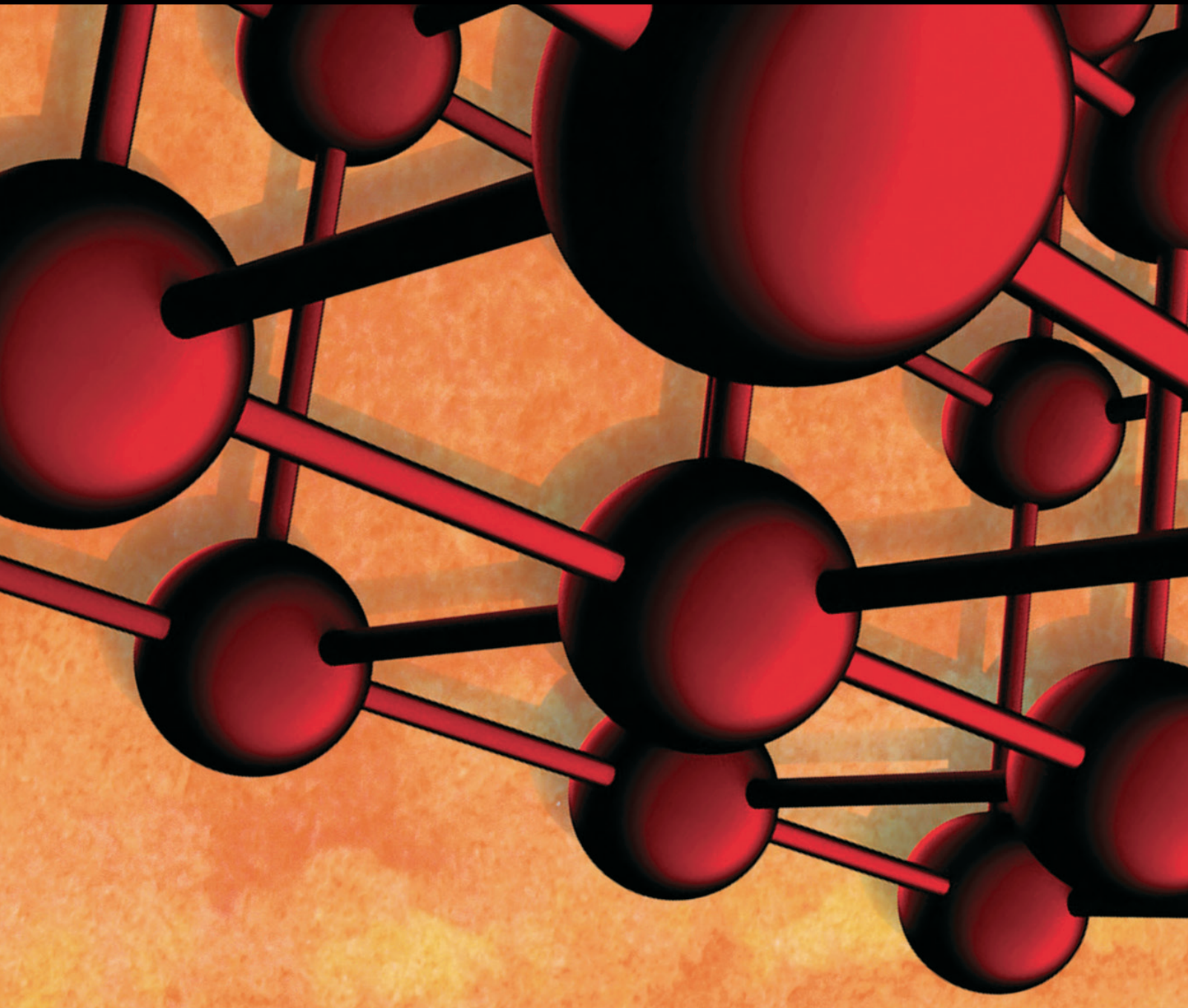


Advances in Materials Science and Engineering

Failure Mechanisms and Damage Modelling for Advanced Materials

Lead Guest Editor: Francesco Caputo

Guest Editors: Carlos N. Pintado and Paulo M. S. T. de Castro





Failure Mechanisms and Damage Modelling for Advanced Materials

Advances in Materials Science and Engineering

Failure Mechanisms and Damage Modelling for Advanced Materials

Lead Guest Editor: Francesco Caputo

Guest Editors: Carlos N. Pintado and Paulo M. S. T. de Castro



Copyright © 2017 Hindawi. All rights reserved.

This is a special issue published in “Advances in Materials Science and Engineering.” All articles are open access articles distributed under the Creative Commons Attribution License, which permits unrestricted use, distribution, and reproduction in any medium, provided the original work is properly cited.

Editorial Board

- Michael Aizenshtein, Israel
Jarir Aktaa, Germany
K. G. Anthymidis, Greece
Santiago Aparicio, Spain
Renal Backov, France
Markus Bambach, Germany
Amit Bandyopadhyay, USA
Massimiliano Barletta, Italy
Mikhael Bechelany, France
Bernd-Arno Behrens, Germany
Avi Bendavid, Australia
Jamal Berakdar, Germany
Jean-Michel Bergheau, France
G. Bernard-Granger, France
Giovanni Berselli, Italy
Patrice Berthod, France
Federica Bondioli, Italy
Susmita Bose, USA
Heinz-Günter Brokmeier, Germany
Steve Bull, UK
Gianlorenzo Bussetti, Italy
Marco Cannas, Italy
Peter Chang, Canada
Daolun Chen, Canada
Gianluca Cicala, Italy
Francesco Colangelo, Italy
Marco Consales, Italy
Maria Criado, UK
Gabriel Cuello, France
Narendra B. Dahotre, USA
João P. Davim, Portugal
Angela De Bonis, Italy
Luca De Stefano, Italy
Francesco Delogu, Italy
Maria Laura Di Lorenzo, Italy
Marisa Di Sabatino, Norway
Ana María Díez-Pascual, Spain
Guru P. Dinda, USA
Nadka Tzankova Dintcheva, Italy
Frederic Dumur, France
Kaveh Edalati, Japan
Philip Eisenlohr, USA
Claude Estournès, France
Michele Fedel, Italy
Paolo Ferro, Italy
- Massimo Fresta, Italy
Germà Garcia-Belmonte, Spain
Santiago Garcia-Granda, Spain
Carlos Garcia-Mateo, Spain
Vincenzo Guarino, Italy
Daniel Guay, Canada
Gianluca Gubbiotti, Italy
Xuchun Gui, China
Benoit Guiffard, France
Ivan Gutierrez-Urrutia, Japan
Hiroki Habazaki, Japan
Simo-Pekka Hannula, Finland
David Holec, Austria
Satoshi Horikoshi, Japan
David Houivet, France
Rui Huang, USA
Michele Iafisco, Italy
Saliha Ilican, Turkey
Iliia Ivanov, USA
Katsuyuki Kida, Japan
Akihiko Kimura, Japan
Soshu Kirihara, Japan
Fantao Kong, China
Hongchao Kou, China
Andrea Lamberti, Italy
Luciano Lamberti, Italy
Marino Lavorgna, Italy
Laurent Lebrun, France
Joon-Hyung Lee, Republic of Korea
Pavel Lejcek, Czech Republic
Cristina Leonelli, Italy
Ying Li, USA
Yuanshi Li, Canada
Jun Liu, China
Meilin Liu, Georgia
Shaomin Liu, Australia
Yunqi Liu, China
Fernando Lusquiños, Spain
Peter Majewski, Australia
Enzo Martinelli, Italy
Bobby Kannan Mathan, Australia
Philippe Miele, France
Andrey E. Miroshnichenko, Australia
Hossein Moayedi, Iran
Jose M. Monzo, Spain
- Michele Muccini, Italy
Alfonso Muñoz, Spain
Rufino M. Navarro, Spain
Miguel Navarro-Cia, UK
Luigi Nicolais, Italy
Hiroshi Noguchi, Japan
Chérif Nouar, France
Tsutomu Ohzuku, Japan
Olanrewaju Ojo, Canada
Laurent Orgéas, France
Gianfranco Palumbo, Italy
Anna Maria Paradowska, Australia
Matthew Peel, UK
Gianluca Percoco, Italy
Claudio Pettinari, Italy
Giorgio Pia, Italy
Fabrizio Pirri, Italy
Alain Portavoce, France
Simon C. Potter, Canada
Manijeh Razeghi, USA
Yuri Ribakov, Israel
Aniello Riccio, Italy
Anna Richelli, Italy
Antonio Riveiro, Spain
Marco Rossi, Italy
Pascal Roussel, France
Francesco Ruffino, Italy
Antti Salminen, Finland
F.H. Samuel, Canada
Hélder A. Santos, Finland
Carlo Santulli, Italy
Fabrizio Sarasini, Italy
Michael J. Schuck, Germany
Fridon Shubitidze, USA
Donato Sorgente, Italy
Charles C. Sorrell, Australia
Andres Sotelo, Spain
Costas M. Soukoulis, USA
Damien Soulat, France
Adolfo Speghini, Italy
Antonino Squillace, Italy
Manfred Stamm, Germany
Baozhong Sun, China
Sam-Shajing Sun, USA
Kohji Tashiro, Japan



Miguel Angel Torres, Spain
Laszlo Toth, France
Achim Trampert, Germany
Luca Valentini, Italy
Ashkan Vaziri, USA
Rui Wang, China
Lu Wei, China

Jörg M. K. Wiezorek, USA
Guoqiang Xie, Japan
Dongmin Yang, UK
Hemmige S. Yathirajan, India
Yee-wen Yen, Taiwan
Wenbin Yi, China
Ling Yin, Australia

Belal F. Yousif, Australia
Michele Zappalorto, Italy
Jinghuai Zhang, China
Li Zhang, China
Ming-Xing Zhang, Australia
Wei Zhou, China
You Zhou, Japan

Contents

Failure Mechanisms and Damage Modelling for Advanced Materials

Francesco Caputo, Carlos Navarro, and Paulo M. S. T. de Castro
Volume 2017, Article ID 6910685, 2 pages

Numerical and Experimental Investigation on the Structural Behaviour of a Horizontal Stabilizer under Critical Aerodynamic Loading Conditions

R. Sepe, R. Citarella, A. De Luca, and E. Armentani
Volume 2017, Article ID 1092701, 12 pages

Shear Strength Reduction Factor of Prestressed Hollow-Core Slab Units Based on the Reliability Approach

Hae-Chang Cho, Min-Kook Park, Hyunjin Ju, Jae-Yuel Oh, Young-Hun Oh, and Kang Su Kim
Volume 2017, Article ID 8280317, 11 pages

Experimental Investigation of Delamination Growth in Composite Laminates under a Compressive Load

A. Riccio, R. Cristiano, G. Mezzacapo, M. Zarrelli, and C. Toscano
Volume 2017, Article ID 3431093, 17 pages

Stochastic Effect of Grain Elongation on Nanocrystalline Materials Strain and Strain Rate Produced by Accumulative Roll-Bonding and Equal Channel Angular Pressing

P. Baonhe Sob, A. Alfayo Alugongo, and T. Ba Bob Tengen
Volume 2017, Article ID 5418769, 9 pages

Experimental and Numerical Evaluation of Rock Dynamic Test with Split-Hopkinson Pressure Bar

Kang Peng, Ke Gao, Jian Liu, Yujiao Liu, Zhenyu Zhang, Xiang Fan, Xuyan Yin, Yongliang Zhang, and Gun Huang
Volume 2017, Article ID 2048591, 12 pages

Chloride Diffusivity and Life Prediction of Cracked RC Beams Exposed to Different Wet-Dry Ratios and Exposure Duration

Jieqiong Wu, Bo Diao, Yinghua Ye, and Xiaoning Zheng
Volume 2017, Article ID 5762048, 13 pages

Micromechanics of Cracked Laminates under Uniaxial Load: A Comparison between Approaches

J. A. Rivera-Santana, A. Guevara-Morales, and U. Figueroa-López
Volume 2017, Article ID 3707329, 12 pages

Study on the High Temperature Friction and Wear Behaviors of Cu-Based Friction Pairs in Wet Clutches by Pin-on-Disc Tests

Er-Hui Zhao, Biao Ma, and He-Yan Li
Volume 2017, Article ID 6373190, 8 pages

Effects of Voids on Concrete Tensile Fracturing: A Mesoscale Study

Lei Xu and Yefei Huang
Volume 2017, Article ID 7989346, 14 pages

Experimental Analysis and Discussion on the Damage Variable of Frozen Loess

Cong Cai, Wei Ma, Shuping Zhao, and Yanhu Mu

Volume 2017, Article ID 1689251, 13 pages

Flexural Strengthening of Damaged T-Joists with Severe Corrosion Using CFRP Sheets

Jose Vercher, Enrique Gil, Ángeles Mas, Carlos Lerma, and M. Eugenia Torner

Volume 2017, Article ID 6030357, 9 pages

Analytical Model for Deflections of Bonded Posttensioned Concrete Slabs

Min Sook Kim, Joowon Kang, and Young Hak Lee

Volume 2017, Article ID 3037946, 7 pages

Mechanical and Failure Criteria of Air-Entrained Concrete under Triaxial Compression Load after Rapid Freeze-Thaw Cycles

Feng-kun Cui, Huai-shuai Shang, Tie-jun Zhao, Guo-xi Fan, and Guo-sheng Ren

Volume 2017, Article ID 6786270, 8 pages

Mechanical and Durability Evaluation of Concrete with Sulfate Solution Corrosion

Feng Ming, You-sheng Deng, and Dong-qing Li

Volume 2016, Article ID 6523878, 7 pages

Editorial

Failure Mechanisms and Damage Modelling for Advanced Materials

Francesco Caputo,¹ Carlos Navarro,² and Paulo M. S. T. de Castro³

¹*Department of Industrial and Information Engineering, University of Campania "Luigi Vanvitelli", Via Roma 29, 81031 Aversa, Italy*

²*University of Seville, Camino de los Descubrimientos s/n, Sevilla, Spain*

³*FEUP, University of Porto, Rua Dr. Roberto Frias s/n, Porto, Portugal*

Correspondence should be addressed to Francesco Caputo; francesco.caputo@unina2.it

Received 25 September 2017; Accepted 26 September 2017; Published 16 November 2017

Copyright © 2017 Francesco Caputo et al. This is an open access article distributed under the Creative Commons Attribution License, which permits unrestricted use, distribution, and reproduction in any medium, provided the original work is properly cited.

Advanced materials are widely used in several engineering applications, involving primary and secondary structures, especially where high specific strength plays a critical factor for designers. Advanced materials applications can be found in both military and civilian fields, such as aerospace, automotive, and building, and there is no shortage of applications in medical and sport equipment. However, despite their great advantages, their application is limited by many critical aspects, such as the fact that they are prone to different typologies of defects and damage respect to conventional materials. Many of such defects and damage can be very critical for structures, because they may be invisible and cause a significant decrease of the residual strength. Developing further knowhow about understanding failure mechanisms in advanced materials, due to phenomena such as impacts, fatigue, creep, and stress corrosion, is mandatory to build up a safe and efficient structure. For such reasons, before employing new materials in structures, several tests are usually carried out. Static, corrosion, impact, fatigue, high strain rate, and several other tests are usually carried out at both coupon and full scale component in order to understand the behaviour and to increase the structural performance. As a matter of the fact, the knowledge about the onset and evolution failure mechanisms in advanced materials is still not enough to face properly the design phase. Hence, during the design current practice, in order to fill the knowledge gap about the ability in predicting the failures, structural components are usually oversized. Such design strategy allows the structure to tolerate damage so its structural health is not compromised under the real loading conditions, according

to a damage tolerance design philosophy. As a result, the scientific community is aimed to develop analytical, empirical, and semiempirical models able to predict the failure mechanisms under different loading conditions and nondestructive examinations, inspections, and evaluations which are widely performed to achieve all possible information about the failure mechanisms in order to develop predicting models. Achieving detailed information about such mechanisms is a necessary condition to design a safe and an efficient structure.

In more detail, the state of the art is full of atomistic models related to several types of failures, efficient for specific test cases. However, failure prediction knowledge at macro-scale lever is still poor. Empirical analyses and analytical models are often developed and used to describe failure mechanism at micro-scale level. The challenge is to transfer such detailed information to higher scales in order to reproduce the structural behaviour of a real component. Different tools are, in fact, used to achieve constitutive damage law at micro-scale level to implement inside macro-scale models able to predict the structural behaviour of a specific structure. In fact, thanks to the current computational power, multiscale numerical models are developed in order to simulate the behaviour of components, assemblies, and whole structures under both real and critical loading conditions, before proceeding to the manufacturing.

The present special issue contains original research and review articles that seek to address modelling and optimizing structural behaviour and damage of advanced materials. Among the areas emphasized in the special issue are case histories; sample calculations of practical

design problems; material characterization procedures; failure mechanisms assessment of critical components; stochastic modelling; propagation mechanisms; effect of microstructure and defects on fatigue behaviour; life prediction and remaining useful life estimation. The papers submitted by the authors have been subjected to the normal journal peer-review process. Special topics include but are not limited to continuum mechanics, crack propagation, criteria for fatigue and fracture, multiphysics damage modelling and analysis, effect of process and design parameters on fatigue resistance, life prediction and remaining useful life estimation, scale effect and structural failure, and ageing.

Francesco Caputo

Carlos Navarro

Paulo M. S. T. de Castro

Research Article

Numerical and Experimental Investigation on the Structural Behaviour of a Horizontal Stabilizer under Critical Aerodynamic Loading Conditions

R. Sepe,¹ R. Citarella,² A. De Luca,³ and E. Armentani¹

¹Department of Chemical, Materials and Production Engineering, University of Naples Federico II, P.le V. Tecchio 80, 80125 Naples, Italy

²Department of Industrial Engineering, University of Salerno, Via Giovanni Paolo II 132, 84084 Fisciano, Italy

³Department of Industrial and Information Engineering, Università della Campania "Luigi Vanvitelli", Via Roma 29, 81031 Aversa, Italy

Correspondence should be addressed to R. Sepe; raffsepe@unina.it

Received 4 March 2017; Revised 3 June 2017; Accepted 18 June 2017; Published 27 July 2017

Academic Editor: Paulo M. S. T. De Castro

Copyright © 2017 R. Sepe et al. This is an open access article distributed under the Creative Commons Attribution License, which permits unrestricted use, distribution, and reproduction in any medium, provided the original work is properly cited.

The aim of the proposed research activity is to investigate the mechanical behaviour of a part of aerospace horizontal stabilizer, made of composite materials and undergoing static loads. The prototype design and manufacturing phases have been carried out in the framework of this research activity. The structural components of such stabilizer are made of composite sandwich panels (HTA 5131/RTM 6) with honeycomb core (HRH-10-1/8-4.0); the sandwich skins have been made by means of Resin Transfer Moulding (RTM) process. In order to assess the mechanical strength of this stabilizer, experimental tests have been performed. In particular, the most critical inflight recorded aerodynamic load has been experimentally reproduced and applied on the stabilizer. A numerical model, based on the Finite Element Method (FEM) and aimed at reducing the experimental effort, has been preliminarily developed to calibrate amplitude, direction, and distribution of an equivalent and simpler load vector to be used in the experimental test. The FEM analysis, performed by using NASTRAN code, has allowed modelling the skins of the composite sandwich plates by definition of material properties and stack orientation of each lamina, while the honeycomb core has been modelled by using an equivalent orthotropic plate. Numerical and experimental results have been compared and a good agreement has been achieved.

1. Introduction

In order to improve the performance of transport systems, many companies are spending resources to find a way for achieving structural lightweight and strength. As a result, several studies are made for substituting traditional materials with more efficient ones. So, new structural solutions, based on innovative materials, are often applied in such fields. As a matter of fact, advanced materials, such as composites, represent an efficient solution to these problems. However, their application is affected by critical aspects, due to their sensitivity to notch effect, environmental conditions, damaging under low velocity impacts, and so on. There are many works in literature showing the application and investigation on aerospace structural components entirely made of

composite materials. In order to investigate the structural behaviour of aircraft composite components, also several experimental tests can be found in literature. A common approach to investigate and study the phenomena involved during in-service/critical loading conditions is based on the joint usage of both Finite Element Method (FEM) and laboratory experimental tests.

Bossak and Kaczkowski [1] investigated the crashworthiness of a lightweight composite aircraft. A full scale finite element model was provided in such work, in an attempt to investigate the phenomena involving a crash landing event, with a focus on the passenger's safety.

Wittenberg et al. [2] investigated, by FEM modeling and experimental tests, the postbuckling phenomenon, involving

stiffened shear panels of ultra-high capacity aircraft under compression loading conditions.

Linde et al. [3] investigated different modelling techniques and solution methods for the study of the postbuckling behaviour of stiffened aircraft fuselage panels. The virtual testing proposed in such paper is based on the main goal of reducing experimental test efforts, leveraging on virtual parametric models.

Frulla and Cestino [4] carried out their research activities on the design of an autonomous high altitude long-endurance unmanned air vehicle (HALE-UAV) platform. A scaled-prototype was designed in order to perform structural static and dynamic tests and the results were compared with numerical and analytical computations. The main structure was made of CFRP materials.

Romano et al. [5] carried out research activities on the design of a new CFRP aileron, considering as a baseline reference an aluminium aileron installed on the PI80 AVANTI aircraft. Composite laminates used for such structure were manufactured by using the Resin Transfer Moulding (RTM) process. An iterative design methodology, developed by using both simplified and detailed design approaches, was used in such study, leading to an optimized aileron concept characterized by a strong reduction of the number of the structural subparts and by a considerable increase of the weight/costs ratio. Finally, the effectiveness of the developed full scale demonstrator was successfully assessed at the ultimate static load, satisfying the same test performed for the certification of the aluminium aileron.

Armentani et al. [6] and Citarella et al. [7, 8] carried out studies on a full scale aeronautic panel made of fibre metal laminate, tested under both static and fatigue biaxial loads, applied by means of an innovative multiaxial fatigue machine. The methodology proposed in these papers aims at providing a general purpose evaluation tool for a better understanding of the fatigue resistance of aeronautic panels, providing a deeper insight into the role of fibre stiffness and of delamination extension on the stress intensity factors of a crack in the middle bay. The fatigue test was simulated in [6] by the Dual Boundary Element Method (DBEM) in a bidimensional approach, whereas in [7] a three-dimensional FEM-BEM coupled approach was introduced to better detail the analysis in the cracked area.

Further studies, performed at coupon level and aimed at the characterization of composite materials under both critical and in-service loading conditions, are provided; for example, Schön et al. [9] dealt with end notch composite specimens under bending loading conditions and provided numerical-experimental outcomes concerning the fracture behaviour under both static and cyclic loads.

Jones and Alesi [10] investigated another critical phenomenon involving composite materials when affected by compressive loading conditions. The authors analysed one of the most critical events which can affect a stiffened composite panel, the separation/debonding of the skin from the stiffeners, as a consequence of excessive “through the thickness” stresses. In particular, this paper shows the results of a series of experimental, analytical, and numerical studies,

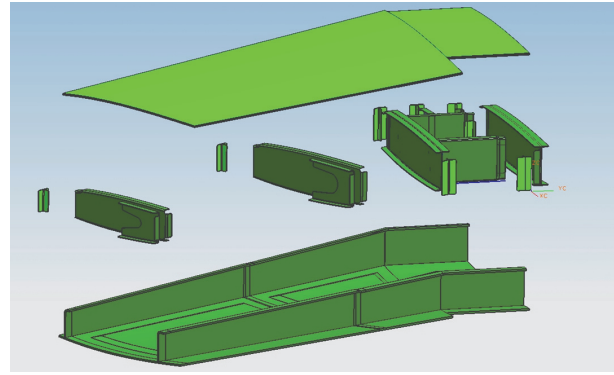


FIGURE 1: Exploded view of the stabilizer.

aimed at analysing the matrix-dominated failures involving a rib stiffened panel under compression load.

Other authors, such as Caputo et al. [11] and Sepe et al. [12], provided several numerical and experimental investigations on the structural behaviour of aircraft composite components under LVI (low velocity impact) phenomena. The dangerousness of such phenomena is related to the fact that after a LVI a composite panel may return to its original shape without any detectable damage (Barely Visible Impact Damage (BVID)), while it has suffered massive internal damage. The main goal of such research activity consists in the prediction of interlaminar and intralaminar failure mechanisms by means of finite element procedures involving composite components under such loading conditions. According to the numerical-experimental comparison, fibre, matrix, and delamination damage were well predicted by the developed FE model.

The main focus of the work illustrated in this paper is to analyse the mechanical behaviour of a part of aircraft horizontal stabilizer made of composite materials. A prototype of the stabilizer in hand has been designed for such purpose and then manufactured. It was made by composite sandwich panels (HTA 5131/RTM 6) with honeycomb core (HRH-10-1/8-4.0). The sandwich facing skins were made by means of RTM process [13, 14], which is one of the most efficient available technologies for the production of such materials.

Some experimental tests were carried out on the prototype. In particular, the most critical aerodynamic load, recorded during the flights of a small aircraft [15], was experimentally reproduced and applied to the stabilizer.

2. Materials and Manufacturing of Stabilizer

An exploded view of the analysed stabilizer is shown in Figure 1. The stabilizer is made out of two skin panels: a lower skin, in which the two main spars (front spar and rear spar) are integrated, and an upper skin. Moreover, there are two ribs between the spars and two root ribs, whose aim is to make the stabilizer end stiffer, providing the needed constraints during the static test. Each rib is bonded by T clips to the lower skin and to the spars. All parts were manufactured using 5131 6K HexForce G1157 (Hexcel) carbon fibres and LY 5052 (Huntsman) epoxy resin by RTM process. Finally,

TABLE 1: Staking sequence of each part.

| Part | Number of plies | Thickness [mm] | Staking sequence |
|----------------------|-----------------|----------------|--|
| Lower and upper skin | 28 | 7.84 | [+45/-45/90/-45/0/45/90/-45/0/45/90/-45/45/0] _S |
| Ribs | 9 | 2.52 | [+45/90/-45/0/0/0/-45/90/+45] |
| Root ribs | 10 | 2.8 | [+45/-45/0/90/0] _S |
| T-clips | 10 | 2.8 | [+45/-45/0/90/0] _S |

a honeycomb insert core HRH-10-1/8-4.0 (Hexcel) is placed in the central zone, between the lower and upper skin.

In the RTM process the resin is injected into a closed mould filled with dry fibres. Fibre reinforcement is preliminary preformed in order to make its positioning easier in the mould. Such technique allows some benefits, as the possibility of producing net shape and reduced tolerance parts, which provide benefits also during the assembly phase.

The staking sequence of each part is reported in Table 1. All parts were bonded with epoxy bicomponent adhesive HYSOL EA934 N/A (Henkel Aerospace), the weight ratio between mixing resin and hardener being 100 : 33. The grit blasting, using alumina folder strip (220 grit), and the surfaces cleaning and drying (using propanol) were performed to prepare the laminate surfaces for the subsequent bonding. The cure cycle used for the adhesively bonding process was determined based on the associated technical datasheet and the entire process took approximately 108 h [16].

3. FE Analyses

In order to reproduce by experimental tests the critical aerodynamic load condition acting on the stabilizer, FE analyses were performed, by means of NASTRAN code, in order to define an equivalent load system that turns out to be easily reproducible experimentally and, at the same time, allows simulating the structural behaviour of the stabilizer under in-service loads.

3.1. FE Model. All the stabilizer parts were modelled with SHELL elements CQUAD4 (an isoparametric membrane-bending element with four nodes with six degrees of freedom per node). A global view of the finite element model is shown in Figure 2; it is based on 7783 elements and 7694 nodes. The thickness of each lamina and the fibre orientation were defined using the composite laminates tool. The mechanical properties of the lamina material are reported in Table 2. MSC PATRAN® preprocessor environment was used for modelling the stabilizer and linear static analyses were performed by means of NASTRAN® code.

3.2. Loads and Constraints. A complex loading condition (MB MAX-800xVD-xFL2-2UCU-FUEL: START CRUISE 2544.7 kg) [15], corresponding to the most critical aerodynamic loads recorded during the flight (Table 3), will be applied to the stabilizer.

The directions of each load vector are defined in the local system 10 (Figure 3), while the coordinates X , Y , and Z

TABLE 2: Mechanical material properties of lamina HTA 5131/RTM6.

| | |
|---|-----------|
| Longitudinal Young Modulus, E_{11} | 92.10 GPa |
| Transverse Young Modulus, $E_{22} = E_{33}$ | 7.61 GPa |
| In Plane Shear Modulus, $G_{12} = G_{13}$ | 3.26 GPa |
| In Plane Shear Modulus, G_{23} | 3.26 GPa |
| Poisson ratio, $\nu_{12} = \nu_{13}$ | 0.36 |
| Poisson ratio, ν_{23} | 0.48 |
| Longitudinal tensile strength X_t | 1222 MPa |
| Longitudinal compressive strength X_c | 654 MPa |
| Transverse tensile strength $Y_t = Z_t$ | 42.8 MPa |
| Transverse compressive strength $Y_c = Z_c$ | 104 MPa |
| Shear strength $S_{12} = S_{13}$ | 62.5 MPa |
| Ply thickness | 0.28 mm |

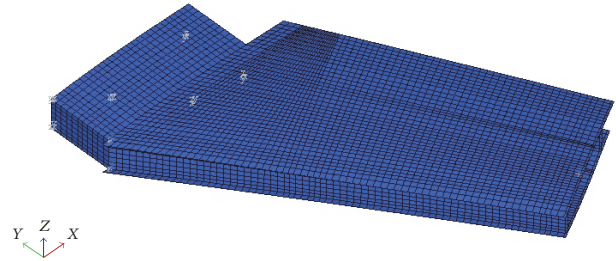


FIGURE 2: FE model.

reported in Table 3 are referred to the global reference system 0 (Figure 3).

The points of load introduction are put in connection with the stabilizer main structure by means of RBE3 rigid elements, whereas the nodes in the stabilizer rear zone, close to root ribs, are constrained for all six DOFs (Figure 4).

3.3. Equivalent Load System. In order to experimentally reproduce the aforementioned most critical aerodynamic load, FE analyses have been carried out considering different loading conditions. As previously said, the aim of this procedure is to find an equivalent load system, easily reproducible by experimental test but still able to simulate the real structural behaviour of the stabilizer under the true loads.

This equivalent load configuration has been calculated by means of eight linear numerical analyses: each one was performed by applying in turn a unit load on the points shown in Figure 5. Such loads have been applied through the modelled test pads (Figure 5).

TABLE 3: Load point position and load components.

| ID | position | load | X [mm] | Y [mm] | Z [m] | F_x [N] | F_y [N] | F_z [N] | M_x [N·m] | M_y [N·m] | M_z [N·m] |
|-------|----------|------|--------|--------|-------|-----------|-----------|-----------|-------------|-------------|-------------|
| P_1 | | | 477 | -330 | 0 | -83.2 | 182.2 | -6081.2 | -27 | -30 | -136 |
| P_2 | | | 660 | -630 | 0 | -169.6 | 231.3 | -7556.9 | -39 | -272 | -167 |
| P_3 | | | 992 | -1170 | 0 | -200.2 | 254.5 | -9042.1 | -38 | 53 | -141 |
| P_4 | | | 1286 | -1650 | 0 | -180.9 | 221.0 | -19659.3 | 47 | 70 | -117 |

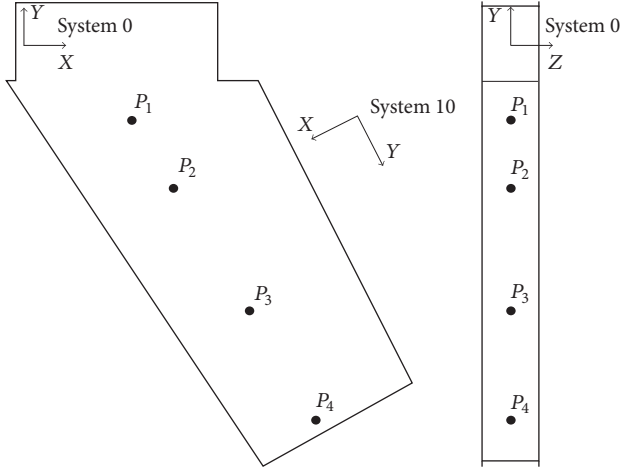


FIGURE 3: Reference system and loading point.

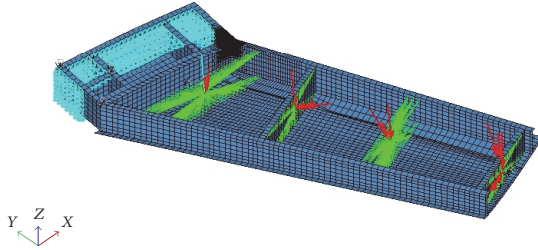


FIGURE 4: Loads and boundary conditions.

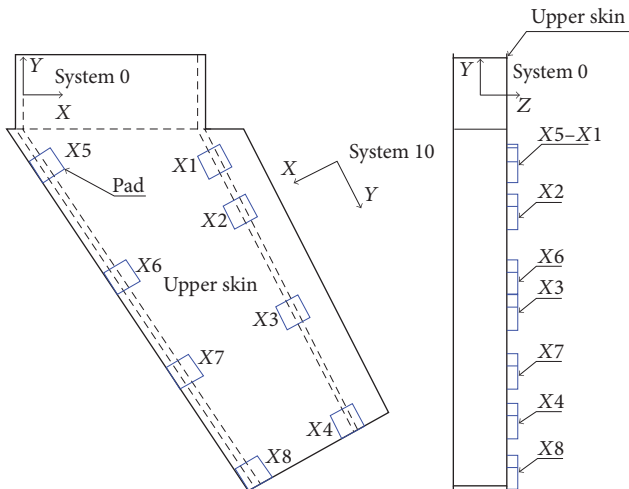


FIGURE 5: Modelled test pads.

Finding an equivalent loads system means to set up a linear combination of elementary loads able to reproduce the stabilizer deflection recorded in the FE analysis considering the real load system. The new load configuration can be calculated by using

$$E(X_1, X_2, \dots, X_8) = \sum_{h=1}^{N_{\text{dof}}} \left[\sum_{k=1}^8 (u_{h,k} \cdot X_k) - \bar{u}_h \right]^2, \quad (1)$$

where

$E(X_1, X_2, \dots, X_8)$ is the error function to minimize;

X_1, X_2, \dots, X_8 are the weights of such linear combination (they correspond to the load amplitudes of the new equivalent load system);

$u_{h,k}$ is the translational displacement of h th degree of freedom due to the k th unit force;

\bar{u}_h is the translational displacement of h th degree of freedom due to the loads shown in Table 3;

N_{dof} is the number of translational degrees of freedom of the whole model (equal to 23082).

In order to apply only downwards vertical forces, the unknown linear combination coefficients X_1, X_2, \dots, X_8 cannot be negative. So in order to find the minimum of the error function, the following constraints must be added:

$$\begin{aligned} X_1 &\geq 0 \\ X_2 &\geq 0 \\ X_3 &\geq 0 \\ X_4 &\geq 0 \\ X_5 &\geq 0 \\ X_6 &\geq 0 \\ X_7 &\geq 0 \\ X_8 &\geq 0. \end{aligned} \quad (2)$$

In more detail, the new loads configuration come out from the combination of the 8 coefficients X_1, X_2, \dots, X_8 that minimizes the sum of squared differences between the displacements caused by the new loads system and those caused by the loads system shown in Table 3. The minimum square differences were calculated by MATLAB® code with *lsqnonneg* function, which can retrieve the solution by means of the algorithm reported in [17]. Therefore, it is possible

TABLE 4: Equivalent loads system.

| ID position (Figure 5) | Load | X [mm] | Y [mm] | Z [mm] | F_z [N] |
|------------------------|-----------|--------|---------|--------|-----------|
| X_4 | P_{EQ1} | 1520 | -1515.7 | 63.3 | -16204.4 |
| X_8 | P_{EQ2} | 1069.9 | -1761.6 | 63.3 | -13790.8 |

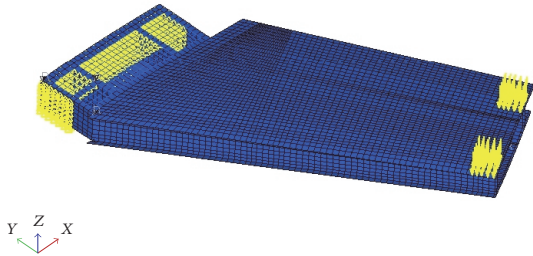


FIGURE 6: Equivalent load system and boundary conditions.

to simulate experimentally the load condition reported in Table 3 by means of the application of only two forces, as reported in Table 4.

The coordinates X , Y , and Z and the load component F_z reported in Table 4 are referred to the global reference system 0 (Figure 3). The equivalent load system and boundary conditions are reported in Figure 6.

3.4. Results and Discussion. In order to check the accuracy of the new equivalent model, some considerations have been made. The equivalent load system (Table 4) causes a maximum deflection equal to 25.69 mm (Figure 7), with a difference from the deflection caused by the real load system (Table 3) equal to 1.64%.

The respective strain fields contour plots are also consistent: the maximum strains among all the plies, in tension and in compression, along the local x direction, are shown in Figures 8 and 9, respectively. Difference between the maximum strains due to the real load system (Table 3) and equivalent load system (Table 4) is equal to -0.000028 (1.09%) while in compression it is equal to -0.000075 (2.64%).

Likewise, the maximum strain, among all the plies, in tension and in compression, along the local y direction is shown in Figures 10 and 11, respectively. The difference between maximum strains due to the real load system (Table 3) and equivalent load system (Table 4) is equal to -0.000028 (1.09%) while in compression it is equal to -0.000075 (2.64%).

The maximum in-plane shear strain among all the plies is shown in Figure 12: the difference between strains due to two different loading conditions is equal to 0.000084 (2.64%).

Displacements along the spars for the real and equivalent load systems are shown in Figure 13(a). The curves relative to displacements measured, for example, along the paths (red lines) shown in Figure 13(b) are well matching. There is a small difference (lower than 6.3%) only at the spar ends: this is due to the presence of pads, responsible for an increase of the structure stiffness in the area of load application.

In conclusion, the illustrated results confirm that the load system reported in Table 4 can be considered as equivalent to the real load system reported in Table 3.

4. Experimental Test

The equivalent load configuration has been experimentally reproduced in laboratory (Figure 14), applying the load system by means of two pads (in-plane sizes 30×30 mm \times mm).

Two hydraulic cylinders (Eland HD 20) with load cell of 20 kN have been used to apply the loads. In order to check the stabilizer displacements, 6 transducers (range 0–500 mm) have been applied on it. The stabilizer has been constrained by means of two “C” beams joined to the support fixture by means of 10 bolts M16 (Figure 15). Two compliant plates (same curvature of the skin) are bonded to the skin with PLEXUS MA420 adhesive in order to enforce a continuity constraint.

Before starting with the test, the constraints efficiency has been checked by partial application (40%) of the equivalent loads. The stabilizer has been instrumented by strain gages, located on the upper and lower skin. Fifteen strain gages, type CEA-13-250UW-350 of MM Vishay, were bonded on the specimen. The strain gages S_1 – S_8 (Figure 16(a)) provide the strains on the upper skin, while S_9 – S_{15} (Figure 16(b)) provide those on the lower skin. All strain gages provide the strains along spanwise direction. The strain gages were bonded by a two-component epoxy adhesive in order to ensure good performance in case of large strains and each strain gage was attached to an acquisition system through a quarter bridge connection. The strain gages position coordinates (X , Y , Z) are reported in Table 5 and are referred to the global reference system 0 (Figure 16).

The values of strain and loads measured during experimental test are reported in Table 6 while the strain versus load P_{EQ1} (chosen parameter) is shown in Figure 17.

Numerical strains, provided along the strain gage directions, are compared with the corresponding experimental data in Table 7 in order to validate the overall numerical-experimental procedure. The numerical strains obtained with the equivalent load system (Table 4) may be considered in good agreement with the strain gages outcomes (e.g., lower than 8.5% relative difference). In fact, the results of strain gages S_2 and S_8 , which are on the upper skin, are affected by the presence of ribs nearby S_2 and of a pad nearby S_8 (load introduction area). Again, the relative difference between numerical and strain gage values on the inferior skin is lower than 8.5% but for strain gages S_{12} , S_{13} , and S_{15} . In particular, S_{12} and S_{13} results are affected by secondary bending effects, whereas the S_{15} strain gages are bonded in a low stress zone.

TABLE 5: Strain gages positions on stabilizer (see reference system in Figure 16).

| Strain gage | X [mm] | Y [mm] | Skin | Direction |
|-----------------|--------|---------|-------|----------------|
| S ₁ | 387.9 | -152.9 | Upper | Along spanwise |
| S ₂ | 893.5 | -591.2 | Upper | Along spanwise |
| S ₃ | 1265.9 | -1023.5 | Upper | Along spanwise |
| S ₄ | 1459.8 | -1567.6 | Upper | Along spanwise |
| S ₅ | 205.5 | -493.9 | Upper | Along spanwise |
| S ₆ | 522.1 | -799.7 | Upper | Along spanwise |
| S ₇ | 766.4 | -1328.0 | Upper | Along spanwise |
| S ₈ | 1144.2 | -1743.1 | Upper | Along spanwise |
| S ₉ | 393.5 | -151.1 | Lower | Along spanwise |
| S ₁₀ | 878.6 | -363.8 | Lower | Along spanwise |
| S ₁₁ | 1238.4 | -1048.0 | Lower | Along spanwise |
| S ₁₂ | 218.0 | -486.5 | Lower | Along spanwise |
| S ₁₃ | 792.5 | -1392.3 | Lower | Along spanwise |
| S ₁₄ | 692.7 | -700.5 | Lower | Along spanwise |
| S ₁₅ | 1295.1 | -1647.5 | Lower | Along spanwise |

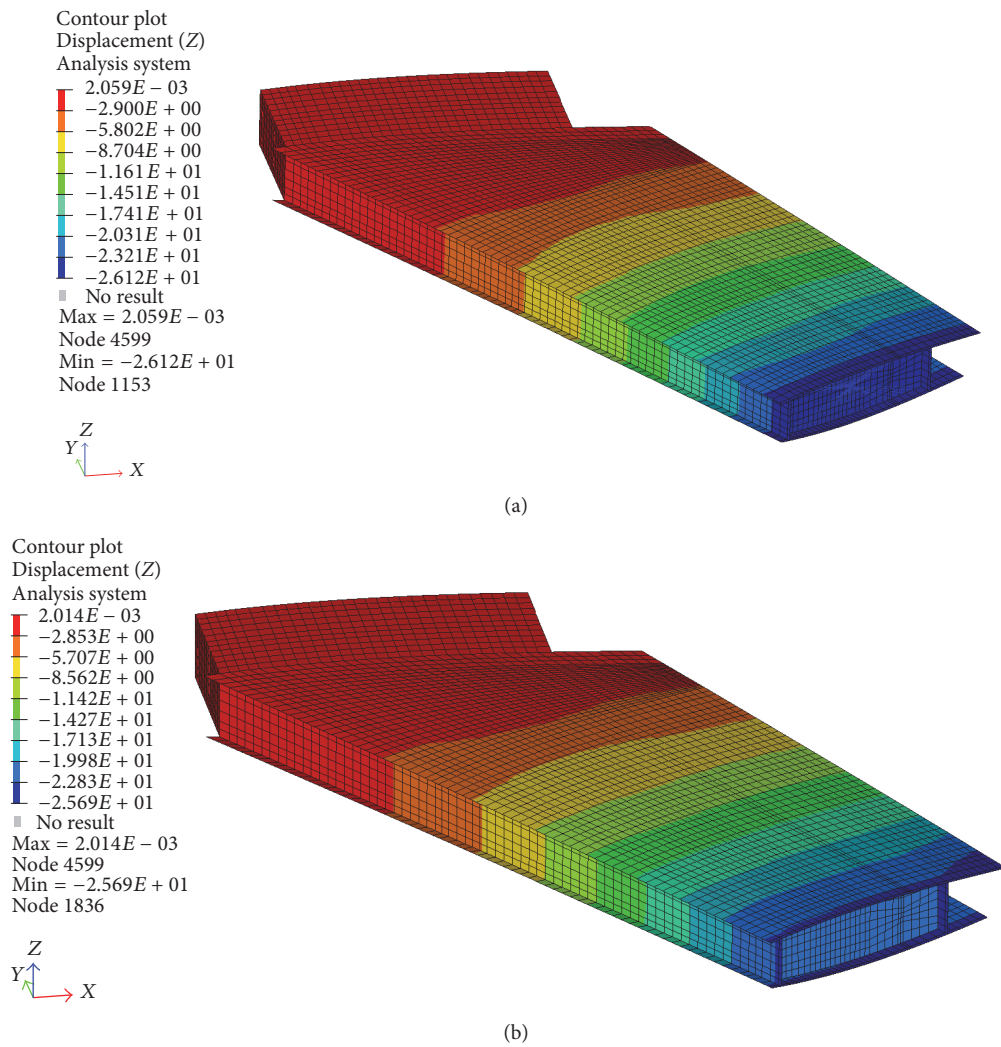
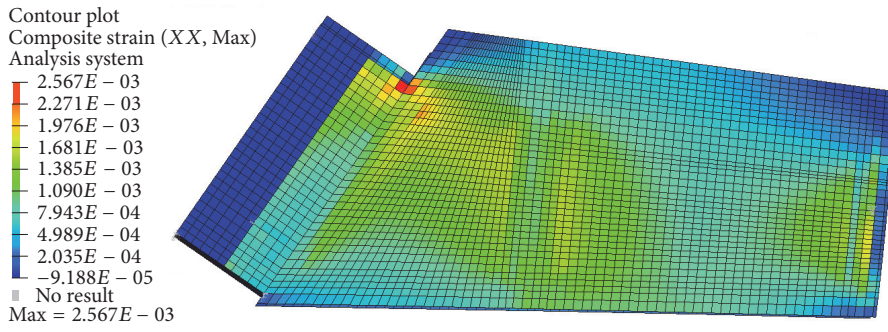
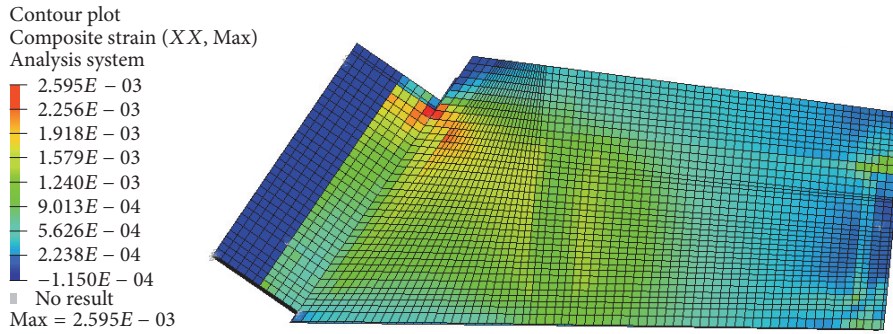


FIGURE 7: Deflection [mm] along z-direction due to real system load (a) and equivalent system load (b).

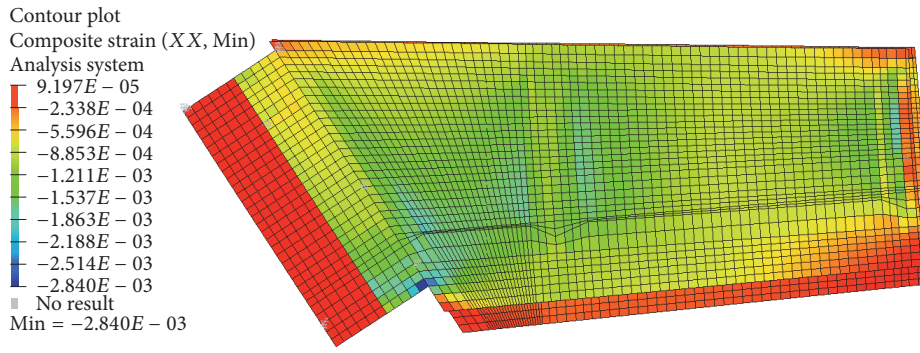


(a)

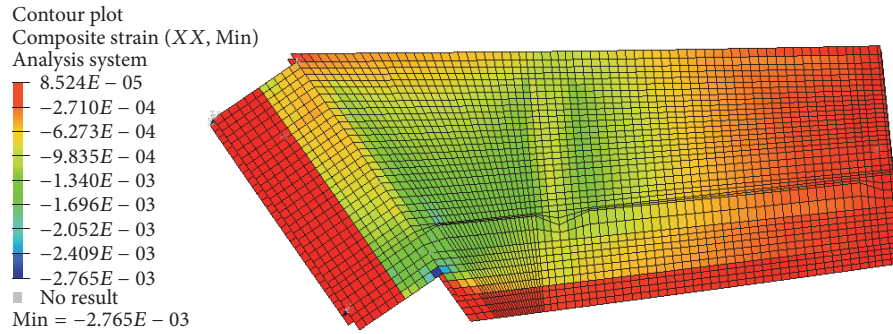


(b)

FIGURE 8: Maximum strain, among all the plies, in tension along the local x -axes, due to real load system (a) and equivalent load system (b).

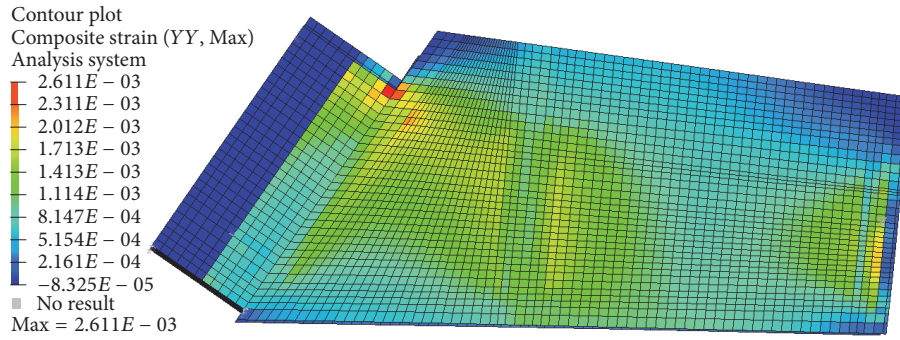


(a)

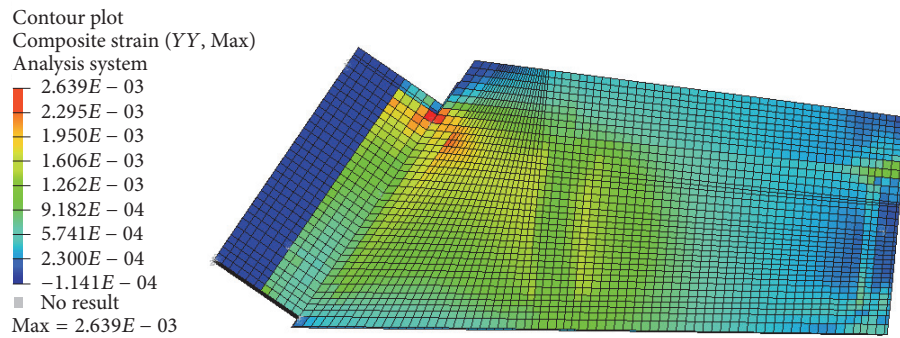


(b)

FIGURE 9: Maximum strain, among all the plies, in compression along the local x -axes, due to real load system (a) and equivalent load system (b).

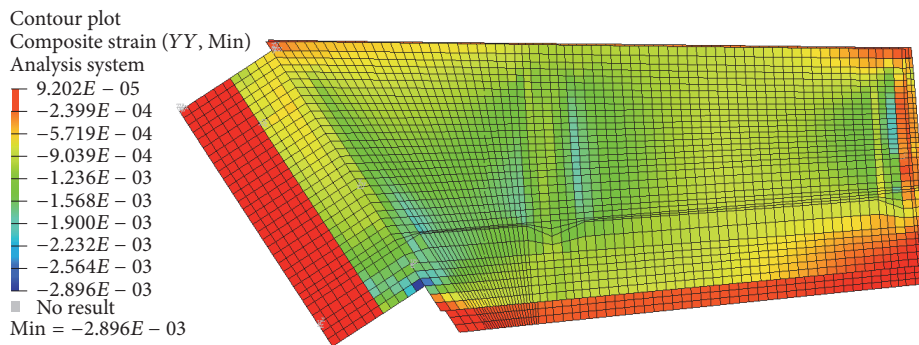


(a)

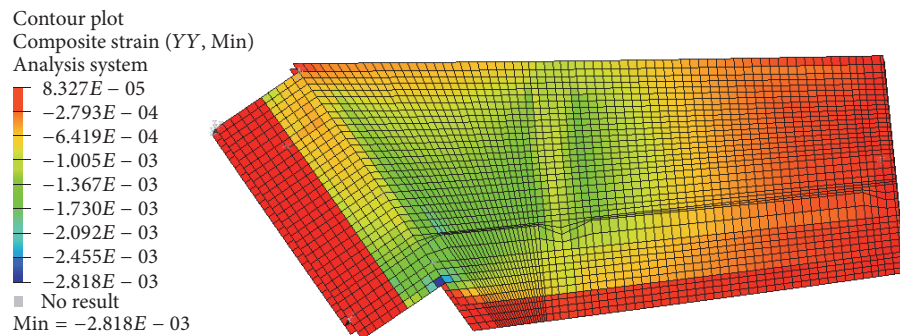


(b)

FIGURE 10: Maximum strain, among all the plies, in tension along the local y -axes, due to real system load (a) and equivalent system load (b).



(a)



(b)

FIGURE 11: Maximum strain, among all the plies, in compression along the local y -axes, due to real system load (a) and equivalent load system (b).

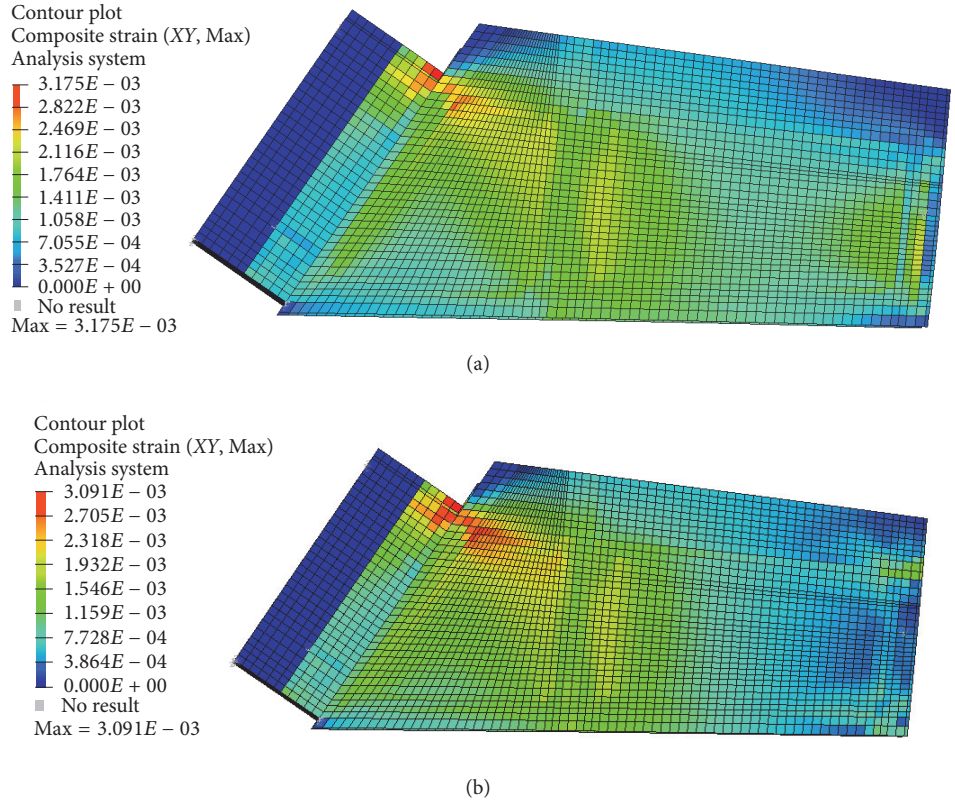


FIGURE 12: Maximum in-plane shear strain, among all the plies, along local x - and y -axis, due to real system load (a) and equivalent load system (b).

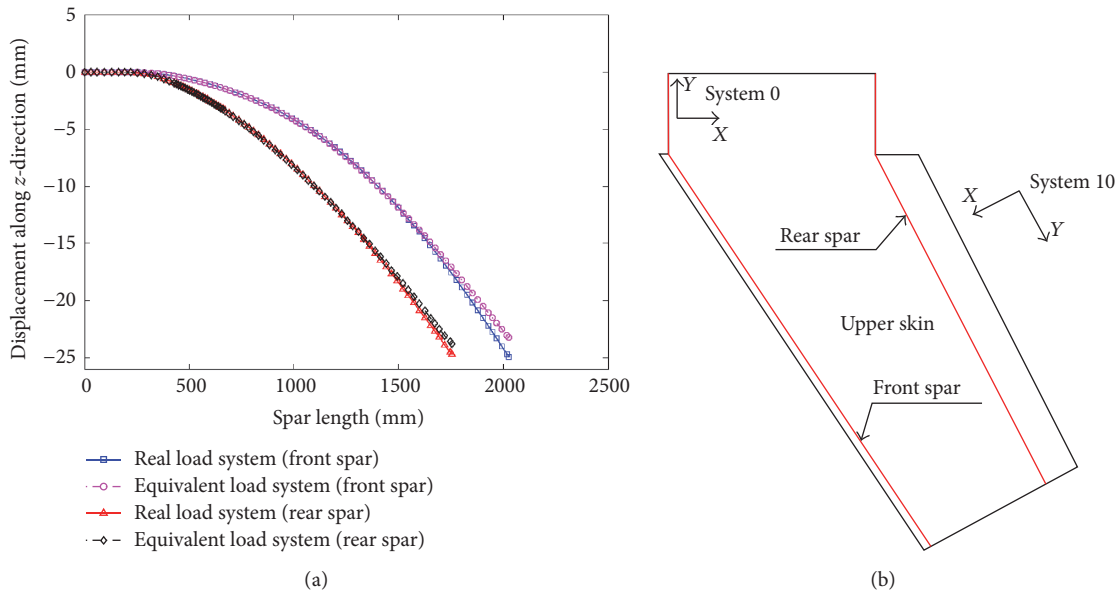


FIGURE 13: Displacement variation along the spars (a); paths along which the displacements are measured (b).

5. Conclusions

A FE numerical model has been developed for studying the best way to experimentally simulate an aerodynamic load in

terms of amplitude, direction, and distribution of equivalent forces. Related experimental tests have been illustrated, with a good agreement achieved between numerical and experimental results.

TABLE 6: Values of strain and loads measured during experimental tests.

| Load [N] | | Strain [$\mu\text{m}/\text{m}$] | | | | | | | | | | | | | | |
|-----------|-----------|-----------------------------------|-------|-------|-------|-------|-------|-------|-------|-------|----------|----------|----------|----------|----------|----------|
| P_{EQ1} | P_{EQ2} | S_1 | S_2 | S_3 | S_4 | S_5 | S_6 | S_7 | S_8 | S_9 | S_{10} | S_{11} | S_{12} | S_{13} | S_{14} | S_{15} |
| 5 | 3 | 0 | -1 | 0 | 1 | 0 | 1 | 0 | 0 | -1 | 0 | 1 | 0 | 1 | -1 | -1 |
| -3114 | -2769 | 208 | 290 | 174 | 46 | 149 | 231 | 105 | 8 | -126 | -182 | -87 | -96 | -63 | -122 | -5 |
| -6329 | -5518 | 416 | 567 | 340 | 87 | 295 | 451 | 205 | 14 | -252 | -373 | -176 | -197 | -136 | -250 | -14 |
| -9522 | -8284 | 617 | 848 | 513 | 136 | 441 | 677 | 309 | 23 | -372 | -554 | -261 | -290 | -197 | -368 | -18 |
| -12761 | -11027 | 816 | 1126 | 683 | 182 | 582 | 897 | 413 | 32 | -493 | -744 | -349 | -386 | -266 | -491 | -24 |
| -16200 | -13786 | 1006 | 1398 | 850 | 229 | 723 | 1110 | 517 | 43 | -607 | -929 | -435 | -478 | -333 | -609 | -29 |

TABLE 7: Numerical and experimental correlation for equivalent loading condition.

| Strain gage | FEM strain (a) [$\mu\text{m}/\text{m}$] | Experimental strain (b) [$\mu\text{m}/\text{m}$] | Deviation = $(a - b) * 100/b$ [%] |
|-------------|--|---|--------------------------------------|
| S_1 | 920.78 | 1006 | -8.5 |
| S_2 | 1126.63 | 1398 | -19.4 |
| S_3 | 783.19 | 850 | -7.88 |
| S_4 | 242.10 | 229 | 5.67 |
| S_5 | 664.13 | 723 | -8.14 |
| S_6 | 1157.87 | 1110 | 4.31 |
| S_7 | 558.58 | 517 | 8.04 |
| S_8 | 23.52 | 43 | -45.3 |
| S_9 | -654.01 | -607 | 7.74 |
| S_{10} | -1005.10 | -929 | 8.19 |
| S_{11} | -460.56 | -435 | 5.87 |
| S_{12} | -650.11 | -478 | 36.00 |
| S_{13} | -389.21 | -333 | 16.81 |
| S_{14} | -585.83 | -609 | -3.80 |
| S_{15} | -24.23 | -29 | -16.43 |



FIGURE 14: Experimental testing setup.

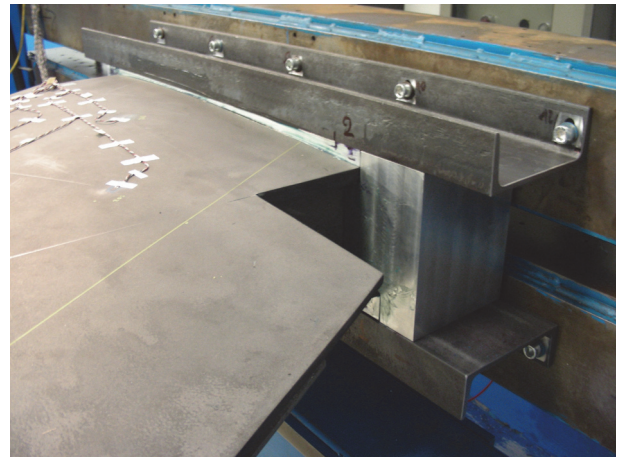


FIGURE 15: Support fixture.

According to the performed static test, in fact, the experimental-numerical differences in most cases are comparable to the intrinsic error level inherent in the strain gage usage.

Hence the proposed numerical model appears to be an efficient method to design quasi-static experimental tests for the investigation of the mechanical behaviour of an aerospace horizontal stabilizer made of composite materials and undergoing aerodynamic loading conditions.

Conflicts of Interest

The authors declare that there are no conflicts of interest regarding the publication of this paper.

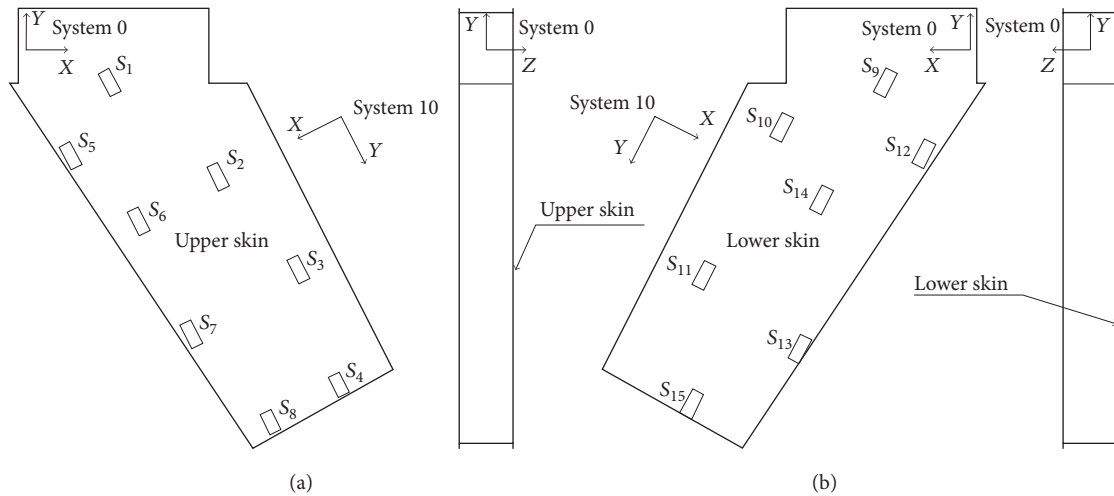


FIGURE 16: Strain gages' layout.

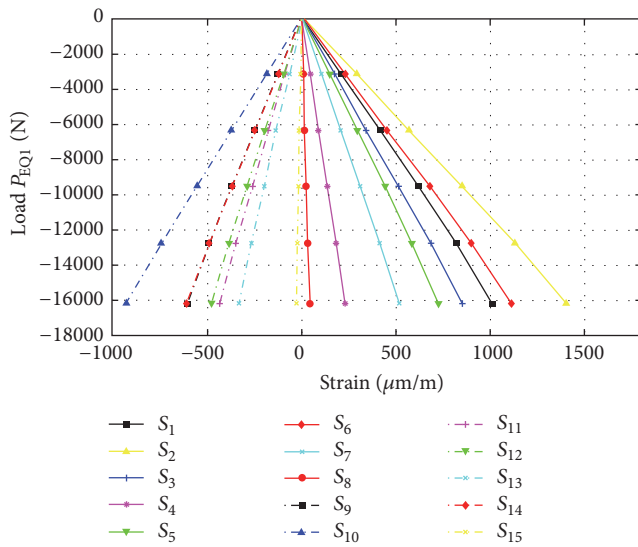


FIGURE 17: Load versus strain curve of experimental data.

Acknowledgments

The authors would like to thank Piaggio Aerospace S.p.A. for its support and contribution to experimental tests.

References

[1] M. Bossak and J. Kaczkowski, “Global/local analysis of composite light aircraft crash landing,” *Computers and Structures*, vol. 81, no. 8-11, pp. 503–514, 2003.

[2] T. C. Wittenberg, T. J. Van Baten, and A. De Boer, “Design of fiber metal laminate shear panels for ultra-high capacity aircraft,” *Aircraft Design*, vol. 4, no. 2-3, pp. 99–113, 2001.

[3] P. Linde, A. Schulz, and W. Rust, “Influence of modelling and solution methods on the FE-simulation of the post-buckling behaviour of stiffened aircraft fuselage panels,” *Composite Structures*, vol. 73, no. 2, pp. 229–236, 2006.

[4] G. Frulla and E. Cestino, “Design, manufacturing and testing of a HALE-UAV structural demonstrator,” *Composite Structures*, vol. 83, no. 2, pp. 143–153, 2008.

[5] F. Romano, J. Fiori, and U. Mercurio, “Structural design and test capability of a CFRP aileron,” *Composite Structures*, vol. 88, no. 3, pp. 333–341, 2009.

[6] E. Armentani, R. Citarella, and R. Sepe, “FML full scale aeronautic panel under multiaxial fatigue: experimental test and DBEM Simulation,” *Engineering Fracture Mechanics*, vol. 78, no. 8, pp. 1717–1728, 2011.

[7] R. Citarella and G. Cricri, “Three-dimensional BEM and FEM submodelling in a cracked FML full scale aeronautic panel,” *Applied Composite Materials*, vol. 21, no. 3, pp. 557–577, 2014.

[8] R. Citarella, V. Ascione, M. Lepore, and C. Cali, “Fatigue crack propagation using the dual boundary element method in a fiber metal laminates aeronautic full scale panel,” in *Proceedings of the 7th International Conference on Engineering Computational Technology*, Valencia, Spain, September 2010.

[9] J. Schön, T. Nyman, A. Blom, and H. Ansell, “Numerical and experimental investigation of a composite ENF-specimen,” *Engineering Fracture Mechanics*, vol. 65, no. 4, pp. 405–433, 2000.

[10] R. Jones and H. Alesi, “On the analysis of composite structures with material and geometric non-linearities,” *Composite Structures*, vol. 50, no. 4, pp. 417–431, 2000.

[11] F. Caputo, A. De Luca, and R. Sepe, “Numerical study of the structural behaviour of impacted composite laminates subjected to compression load,” *Composites Part B: Engineering*, vol. 79, pp. 456–465, 2015.

[12] R. Sepe, A. De Luca, G. Lamanna, and F. Caputo, “Numerical and experimental investigation of residual strength of a LVI damaged CFRP omega stiffened panel with a cut-out,” *Composites Part B: Engineering*, vol. 102, pp. 38–56, 2016.

[13] B. R. Gebart, “Permeability of unidirectional reinforcements for RTM,” *Journal of Composite Materials*, vol. 26, no. 8, pp. 1100–1133, 1992.

[14] R. S. Hansen, “RTM Processing and Applications,” EM 90-214, SME Technical Paper, 1990.

[15] Piaggio Aero Industries S.p.A., P1XX Program—Empennage FE Analysis, Centro di ricerca e sviluppo Piaggio Aero Industries S.p.A., Pozzuoli (NA), 2010.

- [16] G. Lamanna, R. Sepe, and A. Pozzi, "Tensile testing of hybrid composite joints," in *Proceedings of the 3rd International Conference on Materials Engineering and Automatic Control (ICMEAC '14)*, vol. 575 of *Applied Mechanics and Materials*, pp. 97–100, Tianjin, China, May 2014.
- [17] C. L. Lawson and R. J. Hanson, *Solving Least Squares Problems*, Prentice-Hall, Englewood Cliffs, NJ, USA, 1974.

Research Article

Shear Strength Reduction Factor of Prestressed Hollow-Core Slab Units Based on the Reliability Approach

Hae-Chang Cho,¹ Min-Kook Park,¹ Hyunjin Ju,¹ Jae-Yuel Oh,¹
Young-Hun Oh,² and Kang Su Kim¹

¹Department of Architectural Engineering, University of Seoul, 163 Seoulsiripdae-ro, Dongdaemun-gu, Seoul 02504, Republic of Korea

²Department of Medical Space Design & Management, Konyang University, 158 Gwanjeodong-ro, Seo-gu, Daejeon 35365, Republic of Korea

Correspondence should be addressed to Kang Su Kim; kangkim@uos.ac.kr

Received 10 February 2017; Revised 9 May 2017; Accepted 13 June 2017; Published 17 July 2017

Academic Editor: Paulo M. S. T. De Castro

Copyright © 2017 Hae-Chang Cho et al. This is an open access article distributed under the Creative Commons Attribution License, which permits unrestricted use, distribution, and reproduction in any medium, provided the original work is properly cited.

This study investigated the shear design equations for prestressed hollow-core (PHC) slabs and examined the suitability of strength reduction factors based on the structural reliability theory. The reliability indexes were calculated for the shear strength equations of PHC slabs specified in several national design codes and those proposed in previous studies. In addition, the appropriate strength reduction factors for the shear strength equations to ensure the target reliability index were calculated. The results of the reliability index analysis on the ACI318-08 equation showed that the shear strengths of the members with the heights of more than 315 mm were evaluated to be excessively safe, whereas some members with low depths did not satisfy the target reliability index.

1. Introduction

The prestressed hollow-core (PHC) slabs are made in the form of hollow sections with a circular or elliptical shape, as shown in Figure 1, to make them lighter and maximize the sectional efficiency. The prestress is commonly introduced to the PHC slabs by the placing of prestressing tendons, which leads them to have excellent flexural resistance. In addition, they have been widely used as a lightweight floor structural system in Europe and North America due to their excellent economic efficiency and constructability [1–3]. However, since the PHC slab members are typically formed by extruder machines that cast concrete while moving in the longitudinal direction of the members, it is very difficult to place shear reinforcements which are to be placed in the vertical direction. Moreover, the PHC slabs have thin webs due to the hollow-cores inside, and thus their shear strengths are typically dominated by the web-shear strength at the ends of the members. The method of enhancing their shear strength is truly very limited, compared to what can

be done to enhance their flexural strengths, for which their member strengths are governed by the web-shear strength in most cases [2, 3]. In particular, the previous experimental studies [1, 3] reported that, for the PHC slabs with the depths of greater than 315 mm (12.5 in.), the shear strengths were somewhat overestimated by the web-shear strength specified in ACI318-05. On that basis, the shear provision in ACI318-08 was substantially revised to reduce the shear strength of the PHC slabs greater than 315 mm depth with no minimum shear reinforcement by half [3–6]. As mentioned by Im [7] and Palmer and Schultz [6, 8], however, the revised shear provision can provide very conservative shear strengths for the PHC slabs thicker than 315 mm, and it can thus serve as a limiting factor for their wide applications. Therefore, more detailed analyses and deep examinations on the shear strengths of the PHC slabs are necessary. In the authors' previous study [9], the shear strength equations in the current design codes [4, 5, 10–13] and by a research group [14] were examined in detail comparing to the experimental results of the PHC slab members collected from literature. Then, they

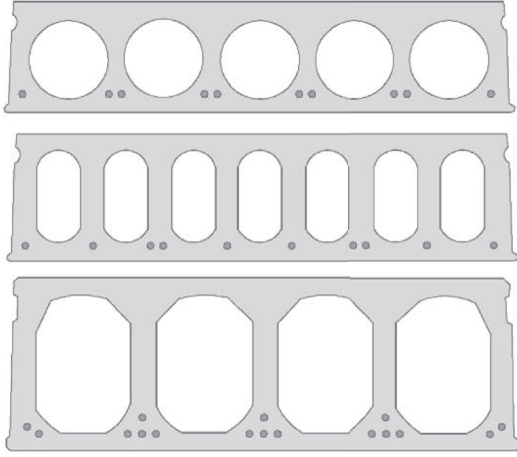


FIGURE 1: Various types of prestressed hollow-core slabs.

proposed an equation to calculate the web-shear strengths of the PHC slabs which is simple but provides a proper margin of safety.

In the design codes, based on the ultimate strength design approach, the design strength (ϕR_n) is calculated by multiplying the nominal strength (R_n) of the member and the strength reduction factor (ϕ) that is less than 1, depending on the importance and failure mode of the member to take into account the variability of materials and dimensions, the construction errors, the uncertainties of code equations, and so on. Macgregor et al. [15] determined the strength reduction factor (ϕ) by performing structural reliability analyses on the experimental results available at that time. In the current ACI 318 design code (2014) [16], however, the shear strength reduction factor is 0.75 for both reinforced concrete (RC) and prestressed concrete (PSC) members even though the construction errors and the uncertainties of the code equations for the RC and PSC members are not the same. In particular, Lee et al. [9] reported that the web-shear strength equation for PSC members overestimated the shear strengths of the PHC slabs with the heights of less than 315 mm (thin PHC slabs, hereafter) as well as those of greater than 315 mm (thick PHC slabs, hereafter). Thus, it is necessary to reexamine the current reduction factor for the shear strengths of PHC slabs. In this regard, this study examined the suitability of the shear strength reduction factor of 0.75 specified in the current ACI 318 design code (2014), based on the structural reliability analysis on the experimental results of the PHC slabs collected from literature including the authors' previous study.

2. Web-Shear Strength

The shear failures of PSC members without shear reinforcements are generally divided into the web-shear and flexural-shear failures [20–22]. The shear failure of PHC slabs that have a thin web due to the hollow-cores in the section is dominated by web-shear strength in most cases [3, 6–9, 23–25]. In most design codes [4, 5, 11], two assumptions are

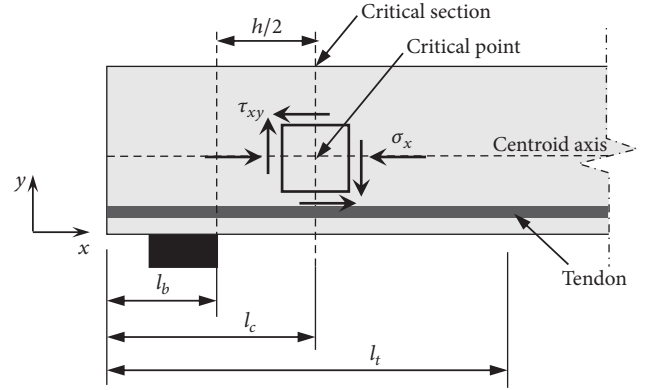


FIGURE 2: Description of transfer length (l_t), bearing length (l_b), and critical section (l_c).

introduced to simplify the calculations of web-shear strength; as shown in Figure 2, the critical section is located at a certain distance (l_c) away from the support, and the vertical normal stress (σ_y) at the centroid of the section is negligible. Then, the shear strength (τ_{xy}) and the longitudinal stress (σ_x) at the centroid axis of the critical section can be represented as follows:

$$\sigma_x = \alpha \frac{f_{pe} A_{ps}}{A_c}, \quad (1)$$

$$\tau_{xy} = \frac{S}{b_w I_g} V_y, \quad (2)$$

where α is the ratio of the prestress at the critical section to the fully effective prestress of the strands, which can be estimated as the distance (l_c) from the member end to the critical section divided by the transfer length (l_t) as shown in Figure 2. Also, f_{pe} is the effective prestress, A_{ps} and A_c are the cross-sectional area of the strands and the member, respectively, S is the moment of area, I_g is the moment of inertia of gross section, b_w is the sum of the web width, and V_y is the shear force acting on the section. According to the theory of elasticity [26], the principal tensile stress (σ_1) at the critical section can be represented as follows:

$$\sigma_1 = \frac{\sigma_x}{2} + \sqrt{\frac{\sigma_x^2}{4} + \tau_{xy}^2}. \quad (3)$$

The point at which the principal tensile stress (σ_1) on the web reaches the tensile strength of the concrete (f_{ct}) is considered as the shear cracking strength of the PSC member. The shear cracking strength and the shear strength of the member can be different, but they are assumed to be the same because their difference is very small especially when no shear reinforcements are placed. Therefore, by substituting (1) and (2) into σ_x and τ_{xy} in (3), respectively, the web-shear strength (V_{cw}) can be represented as follows:

$$V_{cw} = \frac{I_g b_w}{S} \sqrt{f_{ct}^2 + \alpha f_{pe} f_{ct} \frac{A_{ps}}{A_c}}. \quad (4)$$

In Eurocode 2 [11] and FIP recommendations [12], (4) is used to calculate the web-shear strength of PSC members. Eurocode 2 also presents the web-shear strength ($V_{Rd,c}$) of PSC members in a similar form as follows:

$$V_{Rd,c} = \frac{I \cdot b_w}{S} \sqrt{f_{ctd}^2 + \alpha_l \sigma_{cp} f_{ctd}}, \quad (5)$$

where f_{ctd} is $\alpha_{ct} 0.7 f_{ctm} / \gamma_c$. Here, α_{ct} is a coefficient to take account of long term effects on the tensile strength and unfavorable effects depending on the patterns of applied loads, and the recommended value is 1.0 in most cases. Also, γ_c is the partial safety factor for concrete, and 1.5 was used. f_{ctm} is the mean value of axial tensile strength of concrete, where $0.3(f'_c)^{2/3}$ was applied when the compressive strength of concrete (f'_c) is less than 50 MPa and $2.12 \ln(1 + (f'_c + 8)/10)$ when f'_c exceeds 50 MPa. In addition, α_l is l_x / l_{pt2} , which shall not be greater than 1.0, where l_x is the distance of the critical section from the starting point of the transfer length (equals to l_c), and l_{pt2} is the upper bound value of the transfer length (equal to l_t), which is calculated to be $\alpha_1 \alpha_2 d_b f_{pi} / \eta_{p1} \eta_1 f_{ctd}$. Here, α_1 is 1.25, α_2 is 0.19, η_{p1} is 3.2, η_1 is 1.0, d_b is the diameter of strands, and f_{pi} is the stress of strands right after release. σ_{cp} is the concrete compressive stress at the centroid axis due to axial loading and/or prestressing (equals to f_{pc}).

Walraven and Mercx (1983) proposed the web-shear strength (V_{cw}) of PHC slabs by applying the overall reduction factor of 0.75 to Eurocode 2 equation, as follows:

$$V_{cw} = 0.75 \frac{I b_w}{S} \sqrt{f_{ct}^2 + \alpha_{ie} \sigma_{cp} f_{ct}}, \quad (6)$$

where α_{ie} is as follows:

$$\alpha_{ie} = 1 - \left[\frac{(l_t - l_b)}{l_t} \right]^2 \quad (7)$$

and f_{ct} is $0.05 f_{cu} + 1$, and l_b is the bearing length.

The FIP recommendation [12] suggests the web-shear strength (V_{Rd12}) as follows:

$$V_{Rd12} = \frac{I b_w}{S} \sqrt{f_{ctd}^2 + 0.9 \alpha \sigma_{cp} f_{ctd}}. \quad (8)$$

In (5), compared to (8), the reduction factor of 0.9 was additionally considered. Also, $0.3(f'_c)^{2/3}$ presented in the CEB-FIP Model Code [12] is used for f_{ctd} , and the value α_{ie} presented by Walraven and Mercx [14] in (7) is also applied for α . In JSCE (2007), the web-shear strength (V_{wcd}) of the prestressed member without shear reinforcements is presented as follows:

$$V_{wcd} = \frac{f_{wcd} b_w d}{\gamma_b}, \quad (9)$$

where f_{wcd} is $1.25 \sqrt{f'_c}$, γ_b is the member factor that is generally taken to the value of 1.3, and d is the effective member depth.

ACI318-08 and AASHTO-LRFD simplified method [10] assumes the shear stress distribution as the mean shear stress ($\tau_{xy,a}$), as follows:

$$\tau_{xy,a} = \frac{V_y}{b_w d_p}. \quad (10)$$

Accordingly, the web-shear strength (V_{cw}) is presented in ACI318-08 (same as ACI318-14) and AASHTO-LRFD simplified method, respectively, as follows:

$$V_{cw} = \left(0.29 \sqrt{f'_c} + 0.3 f_{pc} \right) b_w d_p + V_p, \quad (11)$$

$$V_{cw} = \left(0.16 \sqrt{f'_c} + 0.3 f_{pc} \right) b_w d_v + V_p, \quad (12)$$

where d_p is the distance from the extreme compression fiber to the centroid of prestressing steel, d_v is the effective shear depth, and V_p is the vertical component of prestressing force. However, since most of the PHC slabs without shear reinforcements fail in shear soon or right after diagonal cracks occur in the web, mostly having no flexural cracks at the end region, it is not suitable to calculate the web-shear strength by assuming the shear stress as the mean stress value of a cracked section. Therefore, in the authors' previous study [9], they considered the shear stress distribution as a parabolic shape and proposed the web-shear strength (V_{cw}) as follows:

$$V_{cw} = \left(0.29 \lambda \sqrt{f'_c} + 0.3 f_{pc} \right) \frac{b_w I}{S} + V_p, \quad (13)$$

where the web-shear strength presented in ACI318-05 was lowered as much as the ratio of the average to the parabolic shear stress; that is, $[I_g / (S d_p)]$. In addition, a more simplified version of (13) was also proposed by applying the mean value of $I_g / (S d_p)$ of the collected specimens as 0.76, as follows:

$$V_{cw} = \left(0.22 \sqrt{f'_c} + 0.23 f_{pc} \right) b_w d_p. \quad (14)$$

Even in the authors' previous study (Lee et al., 2014), they recommended reducing the shear strength, calculated by (14), of the PHC slab members having more than 500 mm depth by half to ensure a proper margin of safety.

As shown in Table 1, a total of 155 experimental data sets were collected from Lee et al. [9] and Im [7] in order to validate the accuracy and reliability of the shear strength equations of design codes or previous studies. Table 3 presents the strength ratios ($V_{cw,Cal} / V_{cw,Test}$) of the shear strengths calculated by design codes and previous researchers to the test results on the specimens collected in this study. Note that no material or strength reduction factor was applied in the calculation only to check the accuracies of their shear strengths. It seems that the web-shear strength equation of ACI318-05 provided a good accuracy with a mean of 0.955 and a COV (coefficient of variation) of 0.251. Lee et al. [9] reported, however, that the shear strength by ACI318-05 provided unsafe results for a large number of specimens as shown in Figure 3(a), and a similar observation was also made in the cases of FIP and JSCE. As shown in Figure 3(b), the

TABLE 1: Dimensions and material properties of shear test data collected from literature [7, 9].

| Authors | Specimens name | Void type | Geometry | | | | Prestress reinforcement | | | Loading | | | |
|---|----------------------------|-----------|----------------|-------------|-------------|--------------------------|------------------------------------|-----------------------------|----------------|----------------|-----------|----------|----------------|
| | | | f_{tk} (MPa) | b_w (mm) | d_p (mm) | A_g (mm ²) | $I \cdot b_w/S$ (mm ³) | A_{ps} (mm ²) | f_{pu} (MPa) | f_{pc} (MPa) | a/d (—) | L (m) | V_{est} (kN) |
| Walraven and Merx (1983) | — | C, NC | 64.0 | 250.0~294.0 | 225.0~260.0 | 171000~199000 | 59601~60490 | 470.0~940.0 | 1860.0 | 2.7~6.3 | 1.7~6.7 | 6.0 | 181.6~286.3 |
| Becker and Buettner (1985) | — | NC | 41.4 | 337.8~431.8 | 170.0~215.9 | 140645~165806 | 43658~44528 | 449.0~1032.2 | 1722.5 | 2.9~5.3 | 3.5~6.7 | 4.6~10.4 | 115.3~271.9 |
| Pajari (2005) | — | C | 41.0~72.6 | 215.0~335.0 | 200.0~500.0 | 119000~300000 | 36333~125833 | 372.0~1953.0 | — | 2.2~8.3 | 2.4~4.6 | 4.0~11.0 | 80.0~528.0 |
| TNO Building and Constructions Research (2005) [17] | — | I, C | 59.9~113.9 | 241.0~449.0 | 255.0~400.0 | 172000~261000 | 49073~114927 | 853.7~1684.4 | — | 4.2~10.4 | 2.5 | 4.0~6.0 | 224.0~652.0 |
| Bertagnoli and Mancini(2009) | — | I | 55.7~65.7 | 215.0~444.0 | 151.0~497.0 | 116000~293000 | 41425~130089 | 249.1~1440.3 | 1860.0 | 2.4~8.0 | 2.3~3.0 | 4.1~7.0 | 157.0~714.0 |
| Celal (2011) | — | C | 62.9~67.9 | 219.0~283.0 | 158.0~255.0 | 132887~180414 | 34246~42359 | 502.5~888.3 | 1860.0 | 5.4~6.9 | 3.0~3.8 | — | 163.0~297.0 |
| Rahman et al. (2010) | — | C | 40.0 | 315.7~325.4 | 212.0~262.0 | 151812~179115 | 47304~70400 | 592.2~789.6 | 1960.0 | 4.0~4.7 | 2.3~2.8 | — | 198.5~298.9 |
| Im (2015) | ST200 | C | 60.0 | 247.0 | 175.0 | 121590 | 37839.5 | 504.8 | 1860.0 | 5.0 | 3.00 | 7.8 | 73.8 |
| | ST200R | C | 60.0 | 247.0 | 175.0 | 121590 | 37839.5 | 504.8 | 1860.0 | 5.0 | 3.00 | 7.8 | 171.8 |
| | ST265 | NC | 60.0 | 257.0 | 230.0 | 151120 | 52853.4 | 504.8 | 1860.0 | 4.0 | 3.00 | 7.8 | 111.3 |
| | ST265R | NC | 60.0 | 257.0 | 230.0 | 151120 | 52853.4 | 504.8 | 1860.0 | 4.0 | 3.00 | 7.8 | 208.4 |
| | ST4N-1 | NC | 60.0 | 260.0 | 360.0 | 212114 | 81201.8 | 899.6 | 1860.0 | 5.1 | 2.50 | 6.4 | 268.5 |
| | ST4N-2 | NC | 60.0 | 260.0 | 360.0 | 212114 | 81201.8 | 899.6 | 1860.0 | 5.1 | 2.50 | 6.4 | 250.6 |
| | ST4N-3 | NC | 60.0 | 260.0 | 360.0 | 212114 | 81201.8 | 899.6 | 1860.0 | 5.1 | 2.50 | 6.4 | 283.3 |
| | ST5N-1 | NC | 60.0 | 286.0 | 455.0 | 255405 | 111867.8 | 1097.0 | 1860.0 | 5.2 | 2.50 | 6.4 | 417.5 |
| | ST5N-2 | NC | 60.0 | 286.0 | 455.0 | 255405 | 111867.8 | 1097.0 | 1860.0 | 5.2 | 2.50 | 6.4 | 444.8 |
| | ST5N-3 | NC | 60.0 | 286.0 | 455.0 | 255405 | 111867.8 | 1097.0 | 1860.0 | 5.2 | 2.50 | 6.4 | 359.6 |
| | <i>Total 155 specimens</i> | | | | | | | | | | | | |

Cf. void type: NC (noncircular), C (circular), and I (I shape); f_{pu} : specified tensile strength of prestressing steel; f_{pc} : compressive stress in concrete at the centroid of the section due to effective prestress.

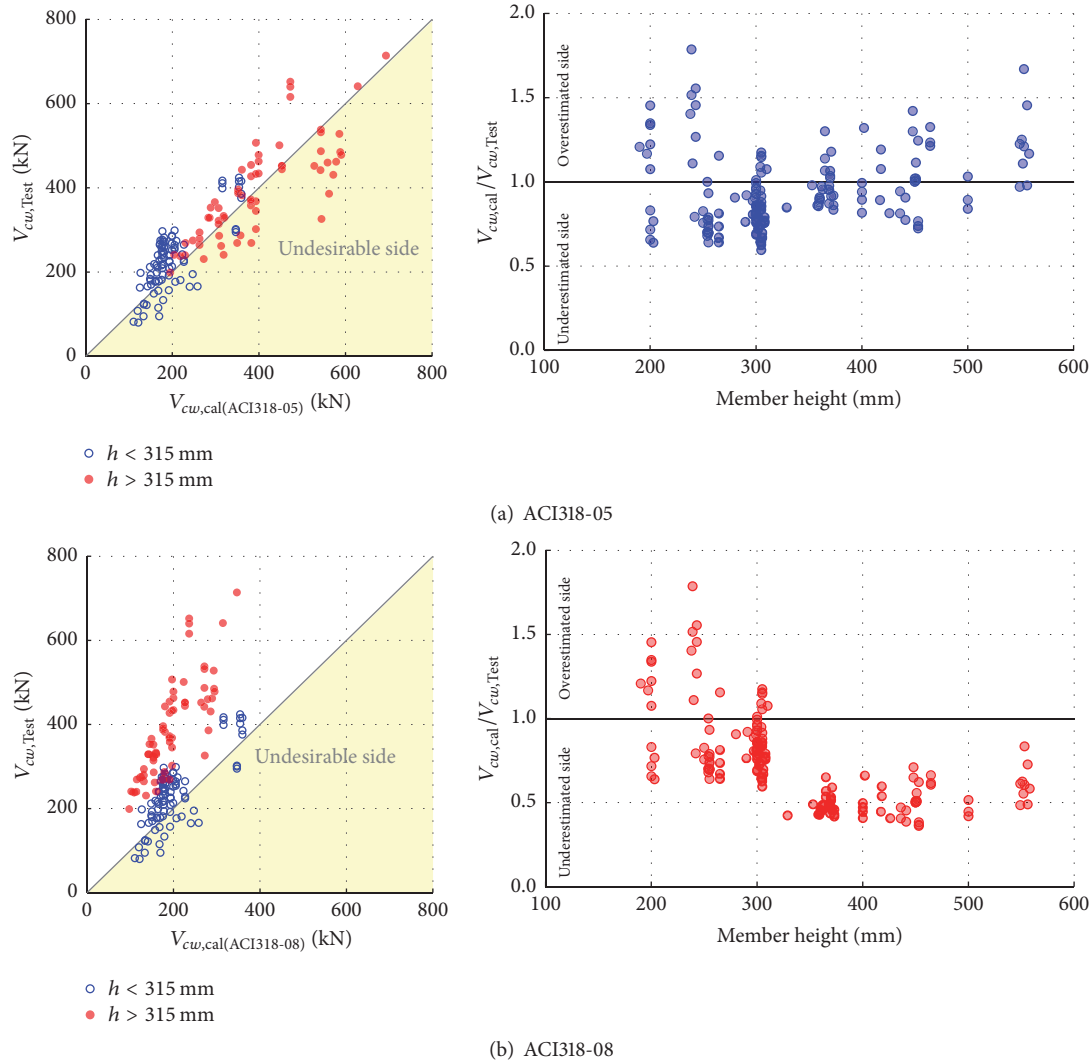


FIGURE 3: Shear strength ratios by design codes of ACI318-05 and ACI318-08.

ACI318-08, revised from ACI318-05, provided very conservative estimation on the shear strength of the PHC slabs having more than 315 mm depth. Compared to these shear strength equations, the proposed equations by Walraven and Merx [14] and Lee et al. [9] showed a better accuracy, as will be examined in detail later in the section on the shear strength reduction factor for PHC slabs. In particular, the equation proposed by Lee et al. [9] is fairly easy to apply in practical design because of its simple form.

3. Strength Reduction Factor

Many researches have been conducted to ensure the structural safety by considering the uncertainties of structural materials and members [18, 27], which required a lot of time and efforts since they are based on the vast amount of experimental results and statistical data. Macgregor [27] collected the experimental results of reinforced concrete and prestressed concrete members, based on which they

performed statistical analysis to investigate the uncertainties of the materials and members and derived the relationship between the strength reduction factor and the load factor based on the predetermined target reliability index (β_t). The target reliability is an index set to ensure a certain level of safety. In general, the probabilistic approaches to evaluate the structural safety by applying the structural reliability theory [28, 29] are divided into three types, that is, Level I, Level II, and Level III [30]. Level III is the most accurate approach, in which numerous random values are generated through a Monte Carlo simulation based on the mean and variance of each random variable and then substituted into the limit state function to directly calculate the number of failure cases. This method requires a significantly large number of trials, which is very disadvantageous. Level II is an approximate approach that estimates the failure probability through the reliability methods such as the First-Order Reliability Method (FORM) and the Second-Order Reliability Method (SORM). The limit state function can be linearized by the FORM, and

the reliability index is then estimated in a simple manner. The limit state function can be approximated in a quadratic form by the SORM, and the probability of failure is then estimated at the quadratic failure surface. These methods have an advantage in that the time required for analysis is relatively shorter than Level III. Level I is a method that determines the safety factor so that the reliability index (β), based on the design strength, exceeds the target reliability (β_t) [31]. The target reliability can be determined by considering the safety margin and the consequences of failure. Macgregor [27] performed statistical analysis of the relationship between the strength reduction factor and the load factor, based on which he determined β_t as 3.0 to satisfy the failure probability of 0.13%, and decided the load factors for the combination of dead loads, live loads, and snow loads, as follows:

$$\begin{aligned} U &= 1.2D + 1.6L, \\ U &= 1.2D + 1.6S, \\ U &= 1.4D, \end{aligned} \quad (15)$$

where U is the factored load, D is the dead load, L is the live load, and S is the snow load. In addition, when a wind load and earthquake load are applied, β_t was set to 2.5 and 2.0, respectively, and the load combinations were determined, as follows:

$$\begin{aligned} U &= 1.2D + 1.3W + 0.5L, \\ U &= 1.2D + 1.5E + (0.5L \text{ or } 0.2S), \\ U &= 0.9D - (1.3W \text{ or } 1.5E), \end{aligned} \quad (16)$$

where W is the wind load and E is the earthquake load. The failure probability varies greatly depending not only on the variability of the loads but also on the failure modes of the members. For the case of shear, the differences between the actual failure loads and the member strengths calculated by code equations are relatively large, and thus it should be designed to be safer compared to the case of flexure. Therefore, Macgregor [27] proposed different strength reduction factors according to failure modes so as to satisfy β_t with the load factors. In ACI318-83, the strength reduction factors were 0.85 for flexure, 0.70 for shear and torsion, and 0.70 and 0.65 for the spiral and the tied columns under compression, respectively, which were then revised a few times later up to the current version of ACI318-14.

In recent years, however, the uncertainties of the material and member strengths have been reduced with the development of material production and processing technology and structural design and construction technology. Accordingly, the design of concrete members by applying the strength reduction factors based on previous statistical data on the materials and members can lead to becoming excessively conservative, which may cause restraining economic efficiency. Nowak and Szerszen [18, 19] conducted a research on the strength reduction factors by setting β_t to 3.5 based on the recent statistics data, that is, mean, variance, and coefficient of variation of material, and proposed the strength reduction factors of 0.9 and 0.85 for flexural and shear, respectively,

which are equal to or greater than those of 0.9 and 0.75 presented in ACI318-14. This is, as previously mentioned, because the uncertainties are reduced due to a decrease in the variation of the material and member strengths and an enhanced accuracy of their strength estimation. Thus, a more reasonable strength reduction factor, which is on the safe side, was proposed by setting higher β_t .

In accordance with the recent researches, the target reliability for shear in PHC slabs was set to 3.5 in this study. The strength reduction factor for the shear and torsion in RC members is 0.75 in ACI318-14, which applies equally to PHC slabs. As mentioned previously, because PHC slabs are mostly manufactured in a factory, the quality of materials and members is consistently good, and the uncertainties of the member strengths are relatively small compared to typical RC members. In addition, the PHC slab members have hollow-cores in the section and relatively small depths, compared to the typical PSC beam members, and thus they have different deviations of the material and member strengths from those PSC beams. Therefore, a detailed analysis is necessary to check the suitability of 0.75 as the strength reduction factor for the shear design of PHC slabs when they are designed by applying the shear strength equations used for the general PSC members.

3.1. Shear Failure Probability of PHC Slabs. In order to investigate whether it is appropriate to apply the shear strength reduction factor of 0.75 in calculating the shear strengths of PHC slabs, the reliability index (β) was estimated for 155 data pieces collected in this study, based on the First-Order Reliability Method [30]. For the load combination of $1.2D + 1.6L$, the nominal strength (ϕR_n) should be designed to be equal to or greater than the required strength ($Q_{1.2D+1.6L}$), which can be expressed as follows:

$$\phi R_n \geq Q_{1.2D+1.6L}, \quad (17)$$

where the safety factor (SF) can be defined as follows:

$$\text{SF} = \frac{(1.2D + 1.6L) / \phi}{D + L}. \quad (18)$$

Considering $D + L$ in (18) as the load at shear failure of the specimen, the limit state function (g) can be defined as follows:

$$g = \text{SF} \cdot V_n - V_{\text{test}} < 0, \quad (19)$$

where V_n is the shear strength calculated by the code equations or other proposed equations by researchers and V_{test} is the experimental value. The shear strength (V_n) of the PHC slab is a function of several random variables. As shown in (11), that is, the ACI code equation, the compressive strength of concrete (f'_c), the compressive stress in concrete at the centroid of the cross section (f_{pc}), and the shape of the PHC slab (b_w , d_p) are the random variables. The moment of inertia of gross section (I_g) and section modulus (Q) can be additional random variables in Eurocode (see (5)). The bias factors and COVs for each random variable refer to the study of Nowak and Szerszen [18] as shown in Table 2. Since f_{pc} is

TABLE 2: Statistical parameters for variables [18, 19].

| Parameters | Nominal value (MPa) | Bias factor | COV | Distribution |
|------------|---------------------|-------------|-------|--------------|
| f_{ck} | 48 | 1.19 | 0.115 | Normal |
| | 55 | 1.09 | 0.090 | Normal |
| | 62 | 1.16 | 0.100 | Normal |
| | 69 | 1.13 | 0.115 | Normal |
| | 83 | 1.04 | 0.105 | Normal |
| f_{pe} | — | 0.9 | 0.16 | Normal |
| b_w | — | 1.00 | 0.06 | Normal |
| d_p | — | 1.00 | 0.06 | Normal |

TABLE 3: Summary of shear strength ratios.

| Standards and authors | Mean ($V_{cw,Cal}/V_{cw,Test}$) | Standard deviation | COV |
|----------------------------------|-----------------------------------|--------------------|-------|
| Eurocode 2 | 1.111 | 0.290 | 0.260 |
| FIP recommendation | 1.185 | 0.293 | 0.247 |
| JSCE | 1.104 | 0.291 | 0.263 |
| AASHTO-LRFD | 0.600 | 0.153 | 0.255 |
| ACI 318-05 | 0.955 | 0.239 | 0.251 |
| ACI 318-08 | 0.735 | 0.281 | 0.383 |
| Walraven and Mercx | 0.913 | 0.227 | 0.249 |
| Lee et al. (simplified equation) | 0.710 | 0.175 | 0.246 |

a function of the combinations of several random variables, such as the effective prestress (f_{pe}), sectional area of tendon (A_{ps}), and sectional area of the PHC slab ($A_g = b_w d_p$), this study assumed a normal distribution of these variables (f_{pe} , b_w , d_p) and then generated 1.0×10^6 random numbers for each random variable through a Monte Carlo simulation to determine the COV and bias factor of f_{pc} . The First-Order Reliability Method (FORM) analysis was performed using the limit state function presented in (19) and the probability distribution of the influencing variables on the shear strength, based on which the reliability index (β) was calculated for all the specimens. In case the limit state function is linear, β can be estimated by calculating the minimum distance between the origin and the limit state function in a plane where each random variable (X_1, X_2) is changed to standard normal distribution random variables (X'_1, X'_2) as shown in Figure 4. That is, the point that orthogonally comes in contact with the limit state function is the most probable failure point (MPP), and the distance between the origin and the MPP (β) can be expressed as a function of the mean and variance of each random variable as follows [30]:

$$\beta = \frac{\mu_{X_1} - \mu_{X_2}}{\sqrt{\sigma_{X_1}^2 + \sigma_{X_2}^2}}. \quad (20)$$

When the limit state function is nonlinear, it is very difficult to calculate the β value, and it can be thus simplified by the

first-order approximation. The limit state function can be expanded by the Taylor series, as follows:

$$\begin{aligned} g(X_1, X_2, \dots, X_n) &= g(x_1^*, x_2^*, \dots, x_n^*) \\ &+ \sum_{i=1}^n (X_i - x_i^*) \left(\frac{\partial g}{\partial X_i} \right) \\ &+ \sum_{j=1}^n \sum_{i=1}^n \frac{(X_i - x_i^*)(X_j - x_j^*)}{(\partial g / \partial X_i \partial X_j)} \\ &+ \dots, \end{aligned} \quad (21)$$

where g is a limit state function, X_i is a random variable, and x_i^* is a random variable at the MPP. By the FORM, the first-order term of (21) can be taken as follows:

$$g(X_1, X_2, \dots, X_n) = \sum_{i=1}^n (X'_i - x_i'^*) \left(\frac{\partial g}{\partial X'_i} \right), \quad (22)$$

where X'_i and $x_i'^*$ are reduced variates and taken as follows, respectively:

$$X'_i = \frac{X_i - \mu_{X_i}}{\sigma_{X_i}}, \quad (23a)$$

$$x_i'^* = \frac{x_i^* - \mu_{X_i}}{\sigma_{X_i}}. \quad (23b)$$

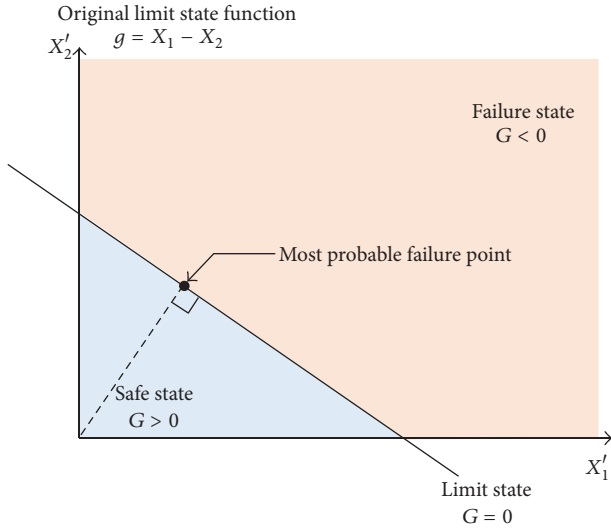


FIGURE 4: Space of reduced variates X'_1 and X'_2 .

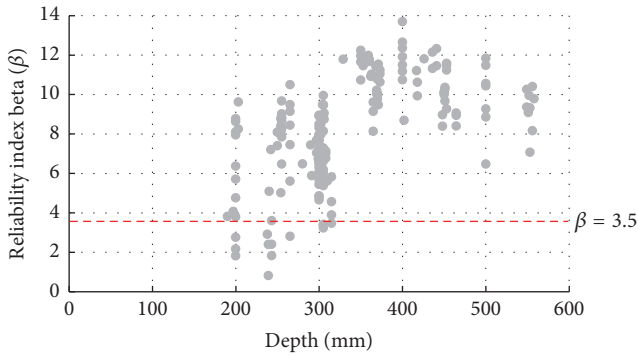


FIGURE 5: Web-shear strength failure probability of PHC slabs in ACI318-08.

From the first-order approximation, the mean value and variance (μ_g and σ_g^2) of the function $g(X)$ can be presented, as follows:

$$\mu_g \approx -\sum_{i=1}^n x_i'^* \left(\frac{\partial g}{\partial X_i'} \right), \quad (24a)$$

$$\sigma_g^2 \approx \sum_{i=1}^n \left(\frac{\partial g}{\partial X_i'} \right)^2. \quad (24b)$$

As mentioned previously, the reliability index can be expressed as a function of the mean and standard deviation, and thus the reliability index of FORM becomes

$$\beta = \frac{\mu_g}{\sigma_g} = \frac{-\sum_{i=1}^n x_i'^* \left(\frac{\partial g}{\partial X_i'} \right)}{\sqrt{\sum_{i=1}^n \left(\frac{\partial g}{\partial X_i'} \right)^2}}. \quad (25)$$

Figure 5 shows the reliability index (β) for 155 specimens, which were calculated by applying the ACI318-08 equation

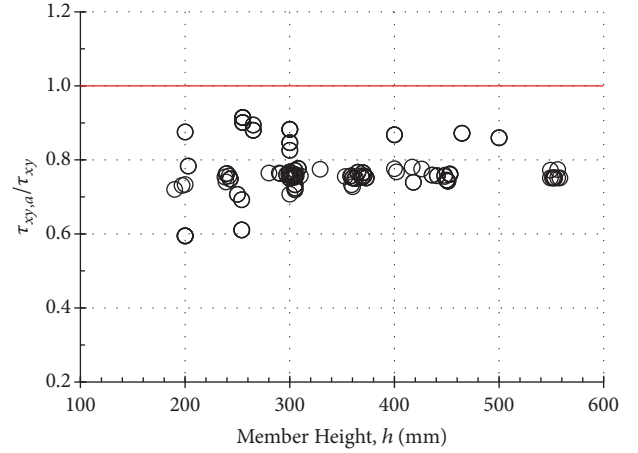


FIGURE 6: Ratio of average shear stress to parabolic shear stress.

to the limit state function with a strength reduction factor of 0.75 and a live load ratio to dead load of 0.5. The ACI318-08 equation showed significantly greater reliability index values in the cases of the PHC members with more than 315 mm depth because it allows only half the shear strengths of the members, and it confirms that the shear strengths by the ACI318-08 equation are excessively conservative for those thick members. Therefore, the shear strength reduction factor of 0.75 for the thick PHC slabs could result in a very uneconomical design. In addition, there were many cases that did not satisfy the target reliability ($\beta_t = 3.5$) in the PHC members with less than 315 mm depth. This is because the ACI318-08 equation is based on the assumption of the average shear stress distribution as shown in (10), and thus, as shown in Figure 6, the shear strength is underestimated by about 80% compared to the shear strength obtained by assuming the parabolic distribution of shear stress on the web. In contrast, as shown in Figure 7, the shear strength by Lee et al.'s [9] and Walraven and Mercx's [14] models in which the shear stress distribution of the PHC slab is considered to be a parabolic was found to secure the reliability index more than the target reliability (β_t) for most PHC slab members including the members with more than 315 mm depth. In Lee et al.'s [9] and Walraven and Mercx's [14] models, however, the reliability index values (β) for most of the data were greater than 4.5, which means that the failure probability is lower than $3.4 \times 10^{-4}\%$. Therefore, if the PHC slabs are designed by these approaches, the shear strength reduction factor of 0.75 could result in a very uneconomical design.

3.2. Shear Strength Reduction Factor for PHC Slabs. This study derived the relationship between the strength reduction factor of the PHC slab and reliability index (β) by using the shear strength estimation model proposed by the authors' previous study [9]. In order to consider various load conditions applied to the structures, as shown in Figure 8, the reliability indexes (β) were calculated according to the ratio of the dead load to the sum of dead load and live load ($D/(D + L)$). The load ratios $D/(D + L)$ ranged from 0.9, in which

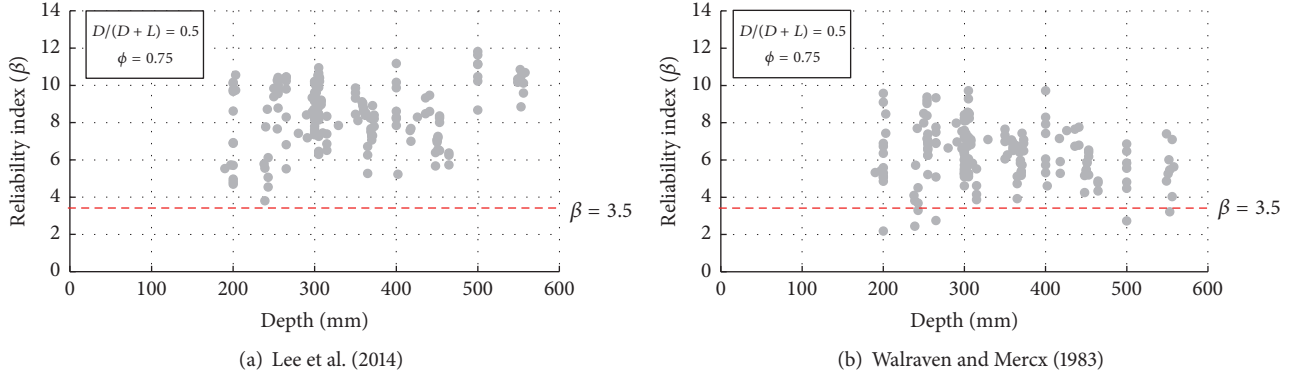


FIGURE 7: Reliability index values of PHC slabs.

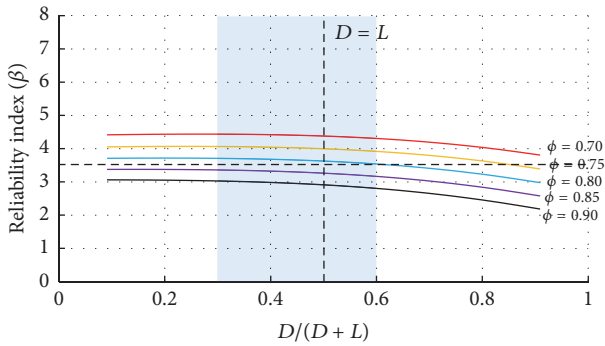


FIGURE 8: Reliability index for Lee et al.'s model.

the live load is very small, to 0.09 where the live load is very large. The reliability index (β) is expressed as follows:

$$\beta = \frac{\mu_{Lee} - \mu_D - \mu_L}{\sqrt{\sigma_{Lee}^2 + \sigma_D^2 + \sigma_L^2}}, \quad (26)$$

where μ_{Lee} and σ_{Lee} are the mean and variance of Lee et al.'s model, respectively. In this study, a normal distribution was assumed for the variables used in Lee et al.'s model and 1.0×10^6 random numbers were then generated for each random variable through the Monte Carlo simulation to determine the COV and bias factor (λ) of Lee et al.'s model. The sectional and material properties of PHC slabs were referred from Im tests shown in Table 1, and their bias factors and COVs were referred from Nowak and Szerszen [18] as shown in Table 2. In (26), μ_D and μ_L are the mean values of the dead and live loads, respectively, and σ_D^2 and σ_L^2 are the variances of the dead and live loads, respectively. The statistical data for the loads used in this study is also based on the study by Nowak and Szerszen [18] as presented in Table 4. The mean values of μ_{Lee} , μ_D , and μ_L can be expressed as follows:

$$\mu_{Lee} = \lambda_{Lee} R, \quad (27a)$$

$$\mu_D = \lambda_D D, \quad (27b)$$

$$\mu_L = \lambda_L L, \quad (27c)$$

TABLE 4: Statistical parameters for loads [18, 19].

| Load component | Bias | COV | Distribution |
|----------------|------|------|--------------|
| Dead load | 1.03 | 0.08 | Normal |
| Live load | 1.00 | 0.18 | Normal |

where λ_{Lee} , λ_D , and λ_L are the bias factors of Lee et al.'s model, dead loads, and live loads, respectively. By using (17) and the ratios of dead load to dead load plus live load ($D/(D+L)$), (26) can be rearranged as a function of μ_D .

When the dead load and live load are the same (i.e., $D/(D+L) = 0.5$), if the shear strength reduction factor of 0.75 is used, the reliability index was about 4.0, which is on the safe side. For the strength reduction factor of 0.8, the reliability index was about 3.5 which is almost equal to the target reliability (β_t). According to Nowak and Szerszen [18, 19], the load ratio $D/(D+L)$ was reported to range generally from 0.3 to 0.7 in beams, from 0.3 to 0.6 in slabs, and from 0.4 to 0.9 in columns. Therefore, when the strength reduction factor of 0.75 is applied for the cases of load ratios ranging from 0.3 to 0.6, which is typical in slabs, the reliability index (β) ranges from 3.90 to 4.07, which means being very safe. When the strength reduction factor of 0.8 is applied, the reliability index (β) ranges from 3.51 to 3.71, which is slightly greater than the target reliability index (β_t). This suggests that the use of the strength reduction factor of 0.8 makes it possible to perform an economic design, while satisfying the target reliability index. As mentioned previously, however, a large number of results of ACI318 equation do not satisfy the target reliability index (β_t) for the members with less than 315 mm depth; thus, it is desirable to slightly lower the shear strength reduction factor for the design of the PHC slabs based on ACI318-08.

4. Conclusion

This study evaluated the accuracy on the web-shear strength equations of various codes and researchers by comparing to the experimental results of PHC slabs failed in web-shear and examined the shear strength reduction factors suitable for

the shear design of the PHC slabs. The following conclusions were obtained from this study.

- (1) The reliability analysis showed that the ACI318-08 equation is excessively conservative for the PHC members with greater than 315 mm depth; the shear strength reduction factor of 0.75 for the thick PHC slabs could result in a very uneconomical design.
- (2) The ACI318-08 equation did not satisfy the target reliability ($\beta_f = 3.5$) for the PHC slabs with less than 315 mm depth, and thus it is desirable to slightly lower the shear strength reduction factor for the design of the PHC slabs based on ACI318-08.
- (3) The models by Walraven and Mercx and Lee et al. provided a good accuracy on the shear strengths of PHC slabs, but they provided very conservative results when the shear strength reduction factor of 0.75 was used.
- (4) The reliability analysis of Lee et al.'s shear strength equation showed that the strength reduction factor of 0.8 works well, leading to an economic design, while satisfying the target reliability index.

Conflicts of Interest

The authors declare that they have no conflicts of interest.

Acknowledgments

This research was supported by Basic Science Research Program through the National Research Foundation of Korea (NRF) funded by the Ministry of Education (2016R1D1A3B03932214).

References

- [1] R. J. Becker and D. R. Buettner, "Shear Tests of Extruded Hollow-Core Slabs," *PCI Journal*, vol. 30, no. 2, pp. 40–54, 1985.
- [2] D. R. Buettner and R. J. Becker, *PCI Manual for the Design of Hollow-Core Slabs, Precast/Prestressed Concrete Institute, ILLINOIS, Chicago*, 2nd edition, 1998.
- [3] N. M. Hawkins and S. K. Ghosh, "Shear strength of hollow-core slabs," *PCI Journal*, vol. 51, no. 1, pp. 110–115, 2006.
- [4] ACI Committee 318, *Building Code Requirements for Structural Concrete (ACI 318-05) and Commentary*, American Concrete Committee, Farmington Hills, MI, USA, 2005.
- [5] ACI Committee 318, Ed., *Building Code Requirements for Structural Concrete (ACI 318-08) and Commentary*, American Concrete Committee, Farmington Hills, MI, USA, 2008.
- [6] K. D. Palmer and A. E. Schultz, "Factors affecting web-shear capacity of deep hollow-core units," *PCI Journal*, vol. 55, no. 2, pp. 123–146, 2010.
- [7] J. H. Im, *Web shear strength of prestressed hollow-core slab [Ph.D. thesis]*, University of Seoul, 2015.
- [8] K. D. Palmer and A. E. Schultz, "Experimental investigation of the web-shear strength of deep hollow-core units," *PCI Journal*, vol. 56, no. 4, pp. 83–104, 2011.
- [9] D. H. Lee, M.-K. Park, J.-Y. Oh, K. S. Kim, J.-H. Im, and S.-Y. Seo, "Web-shear capacity of prestressed hollow-core slab unit with consideration on the minimum shear reinforcement requirement," *Computers and Concrete*, vol. 14, no. 3, pp. 211–231, 2014.
- [10] *AASHTO LRFD Bridge Design Specifications, American Association of State Highway and Transportation Officials*, Washington, DC, USA, 4th edition, 2007.
- [11] European Committee for Standardization (CEN), Eurocode 2: Design of Concrete Structure. Part 1-1: General Rules and Rules for Buildings, EN 1992-1-1:2004, Brussels, 2004.
- [12] FIP Recommendations, *Precast Prestressed Hollow Core Floors: FIP Commission on Prefabrication*, London, UK, 1988.
- [13] Concrete Committee of JSCE, Ed., *Standard Specifications for Concrete Structures Design, Japan Society of Civil Engineers*, Tokyo, Japan, 2007.
- [14] J. C. Walraven and W. P. M. Mercx, "The Bearing Capacity of Prestressed Hollow-Core Slabs," *Heron*, vol. 28, no. 3, pp. 1–4, 1983.
- [15] J. G. Macgregor, S. A. Mirza, and B. Ellingwood, "Statistical analysis of resistance of reinforced and prestressed concrete members," *ACI Journal*, vol. 80, no. 16, pp. 167–176, 1983.
- [16] ACI Committee 318, "Building code requirements for reinforced concrete (ACI 318-56) and commentary," *American Concrete Committee*, 2014.
- [17] TNO Building and Constructions Research, TNO Report: Standard Shear Tests on Prestressed Hollow Core Slabs according to EN 1168, TNO Building and Constructions Research, Hague, 2005.
- [18] A. S. Nowak and M. M. Szerszen, "Calibration of design code for buildings (ACI 318): part 1 – statistical models for resistance," *ACI Structural Journal*, vol. 100, no. 41, pp. 377–382, 2003.
- [19] M. M. Szerszen and A. S. Nowak, "Calibration of design code for buildings (ACI 318): part 2 – reliability analysis and resistance factors," *ACI Structural Journal*, vol. 100, no. 42, pp. 383–391, 2003.
- [20] M. P. Collins and D. Mitchell, *Prestressed Concrete Structures*, Prentice Hall, 1991.
- [21] D. A. Kuchma, N. M. Hawkins, S.-H. Kim, S. Sun, and K. S. Kim, "Simplified shear provisions of the AASHTO LRFD bridge design specifications," *PCI Journal*, vol. 53, no. 3, pp. 53–73, 2008.
- [22] D. H. Lee, S.-J. Han, and K. S. Kim, "Dual potential capacity model for reinforced concrete beams subjected to shear," *Structural Concrete*, vol. 16, no. 3, pp. 443–456, 2016.
- [23] G. Bertagnoli and G. Mancini, "Failure analysis of hollow-core slabs tested in shear," *Structural Concrete*, vol. 10, no. 3, pp. 139–152, 2009.
- [24] M. Pajari, "Resistance of prestressed hollow core slabs against web shear failure," Research Notes 2292, Technical Research Centre of Finland (VTT), Espoo, Finland, 2005.
- [25] M. Pajari, "Web shear failure in prestressed hollow core slabs," *Journal of Structural Engineering*, vol. 42, no. 4, pp. 207–217, 2009.
- [26] A. C. Ugural and S. K. Fenster, *Advanced strength and applied Elasticity*, Prentice Hall, 2003.
- [27] J. G. Macgregor, "Load and Resistance Factors for Concrete Design," *ACI Journal*, vol. 80, no. 27, pp. 279–287, 1983.
- [28] M. Mayer, "Die Sicherheit der Bauwerke und ihre Berechnung nach Grenzkraften anstatt nach zulässigen Spannungen," *J. Springer*, vol. 66, 1962.

- [29] A. M. Freudenthal, "The Safety of Structure," *ASCE Transactions*, vol. 112, pp. 383–391, 1947.
- [30] A. H. Ang and W. H. Tang, *Probability Concepts in Engineering Planning and Design*, Wiley, 1990.
- [31] P. Chetchotisak, J. Teerawong, S. Yindeesuk, and J. Song, "New strut-and-tie-models for shear strength prediction and design of RC deep beams," *Computers and Concrete*, vol. 14, no. 1, pp. 19–40, 2014.

Research Article

Experimental Investigation of Delamination Growth in Composite Laminates under a Compressive Load

A. Riccio,¹ R. Cristiano,¹ G. Mezzacapo,¹ M. Zarrelli,² and C. Toscano³

¹*Dipartimento di Ingegneria Industriale e dell'Informazione, Università degli Studi della Campania "Luigi Vanvitelli", Via Roma 29, 81031 Aversa, Italy*

²*Institute for Composite and Biomedical Materials, National Research Council (CNR), Portici, Italy*

³*CIRA Italian Aerospace Research Centre, Via Maiorise s/n, Capua, Italy*

Correspondence should be addressed to A. Riccio; aniello.riccio@unicampania.it

Received 8 February 2017; Revised 19 April 2017; Accepted 2 May 2017; Published 5 July 2017

Academic Editor: Paulo M. S. T. De Castro

Copyright © 2017 A. Riccio et al. This is an open access article distributed under the Creative Commons Attribution License, which permits unrestricted use, distribution, and reproduction in any medium, provided the original work is properly cited.

This paper focuses on the use of no-contact experimental techniques for monitoring the interlaminar damage evolution in composite laminates. Indeed, Infrared Thermography and Digital Image Correlation are adopted to investigate, in composite plates with artificial delamination, the influence of the delamination initial position on the delamination growth. The paper also investigates the feasibility of using a no-contact experimental technique for the measurement of displacement and strain during mechanical tests, such as the Digital Image Correlation, to evaluate, by means of indirect measurements, the delamination growth as a function of the applied load.

1. Introduction

Carbon fiber reinforced polymer (CFRP) laminates are being studied widely in aerospace and naval application due to their low specific weight and high corrosion resistance with respect to the metallic alloys [1]. However, carbon fiber/epoxy laminates can experience damage formation or imperfections arising during the manufacture and assembly phases or during their service life. Indeed, carbon fiber/epoxy laminates are susceptible to develop, as a consequence of low velocity impacts [2–5], critical damage mechanisms (fiber failure, matrix cracking, and delamination) which are hardly detectable by visual inspection [6–10] and then very dangerous in terms of load carrying capability reduction especially under compressive loading conditions. Moreover, geometrical and material imperfections make the structure prone to the buckling phenomenon, as investigated in [11]. Hence, the study of the compressive behavior of impacted composite structures becomes of main concern for ensuring the fulfilment of integrity and safety structural requirements [12, 13].

In order to assess the internal defects and to monitor the damage initiation and propagation in composite structures, widespread experimental techniques are adopted. Among others, Infrared Thermography (IRT) and Digital Image Correlation (DIC), whose combination has been used in [14] to study plastic deformations, can be considered effective and reliable no-contact experimental techniques able to assess the integrity of composite structures. The Infrared Thermography technique is usually adopted to evaluate the temperature field [15–17], while the Digital Image Correlation technique has been found able to satisfy the increasing demand of experimental detailed information connected to a deformation problem [18–23]. The advantages related to these two techniques are the real-time measures, the high precision, and the absence of any contact or interference with the measured samples.

The Infrared Thermography is also used for detection of material defects in structures [24, 25] being particularly useful when no-contact inspection is needed, for example, when the investigated structural component is hot and dangerous to inspect with contact sensors or when parts are

difficult to reach or disconnect or more in general could be damaged by contact. Indeed, the Infrared Thermography is able to reveal heat patterns in the infrared wavelength spectrum, which helps to visualize the damaged elements, using an infrared camera that captures the thermal images in specific ranges of temperatures (i.e., parts of the electromagnetic spectra). Among thermographic techniques, the active approach requires to induce a temperature gradient between the inspected body and the environment, generally warming up or cooling down the material. In the case of the used Lock-In method, the component is warmed up by a modulated heat wave while the emitted heat by the component is acquired by the thermal camera and processed by a software whose algorithm is FFT based. [26, 27]. Infrared thermocameras are being continuously developed in terms of both pixel resolution/noise level [28] and Lock-In technique [29] for various applications on solar cells, integrated circuits, and gate oxide integrity defects.

The DIC is one of the most popular no-contact techniques thanks to its ease of implementation, solution accuracy, and cheapness. It is an optical technique, which works by using cameras for recording digital photographs at different loading stages to be compared in order to obtain stress and strain fields. Indeed, according to the DIC technique, random and unique blocks of pixels are tracked to obtain strain and stress measurements.

Many researches have adopted the DIC technique to measure the strain field and the surface displacements in the last years. The local least squares fitting method to calculate the true strain field in presence of holes or crack areas has been investigated in [30] while the detection of strain singularity due to artificial delamination by using the DIC technique has been considered in [31, 32]. The DIC technique has been used to study the crack growth behavior in [33], the impact induced damage in composite structures under compressive load in [34], and finally, holes in composite laminates and the bonded repairs performance also under tensile load in [35].

In the present paper, the combination of DIC and IRT techniques is used to provide the displacements and the internal damage development in delaminated composite plates during a compressive test. The main aim is to investigate the influence of delamination position on the delamination growth in composite plates. The paper also investigates the feasibility of using the DIC, to evaluate, by means of indirect measurements of strain and displacement fields, the delamination growth as a function of the applied load.

In Sections 2 and 3, the IRT and DIC techniques are, respectively, introduced briefly explaining their working principles. In Section 4, the tested specimen characteristics and the test procedures and setup are presented. Finally, in Section 5, the experimental results are introduced and critically discussed.

2. Infrared Camera and Lock-In Thermography

Every object at temperature T , greater than the absolute zero (i.e., $T > 0$ K), emits electromagnetic radiations. These

radiations mainly fall into the infrared portion of the electromagnetic spectrum. The latter, called also infrared radiations or thermal radiations, propagates from one place to another through the electromagnetic waves. Infrared Thermography offers no-contact fast inspection of extensive areas and can be used as an alternative or complement to other inspection technologies because the infrared imaging device reveals features that are not visible to the naked eye.

Thermography is a nondestructive evaluation (NDE) tool that allows detecting imperfections or characterizing the materials and measuring temperature changes on the material surface due to stress generated thermal fields (SGTF) or externally applied thermal fields (EATF). A sensitive infrared camera, capable of detecting temperature changes less than 0.05 mK, is used to detect anomalies in the material heat transfer characteristics related to imperfections.

Materials must be thermally excited to show imperfections. Excitation sources can be applied by external thermal fields or by mechanical tools. In both cases, the produced thermal field depends on the investigated material emissivity. The emissivity, ε , in (1), is defined as the ratio between the thermal radiation, E , emitted from a real surface, and the thermal radiation, E_B , related to a blackbody at the same conditions (temperature, T , wavelength, λ , and direction):

$$\varepsilon(\lambda, T) = \frac{E(\lambda, T)}{E_B(\lambda, T)}. \quad (1)$$

Infrared detectors are transducers of incident radiant energy. The most used infrared detectors (Figure 1) are

- (i) thermal detectors;
- (ii) quantum/photon detectors.

They can be classified into *cooled* and *uncooled* infrared.

Cooled detectors have to be cooled down under ambient temperature in order to obtain a very rapid scanning rate, high sensitivity, and low thermal noise. The FLIR™ thermal camera used for this work is provided with a *Stirling cycle* cooling system. The InSb photovoltaic sensor is effective within the 3–5 μm wavelength transmission window, that is, Medium Infrared part of the spectra. Lock-In Thermography is based on the solution of the Fourier equation obtained taking into account the hypothesis that a homogeneous semi-infinite solid body is impinged by a sinusoidal thermal wave of temperature T propagating along x direction with *modulation frequency*, ω , and initial temperature, T_0 ,

$$T(x, t) = T_0 e^{-x/\mu} \cos\left(\omega t - \frac{x}{\mu}\right). \quad (2)$$

Equation (2) describes the harmonic part of that solution as a thermal wave, with the same modulation frequency as the exciting heat source, delayed by a phase lag $\varphi = x/\mu$ and with an amplitude damped by a factor depending on the so-called *diffusion length* $\mu = (2\alpha/\omega)^{1/2}$, where α is the thermal diffusivity.

According to the Lock-In Thermography technique, a series of thermal images representing the time evolution of

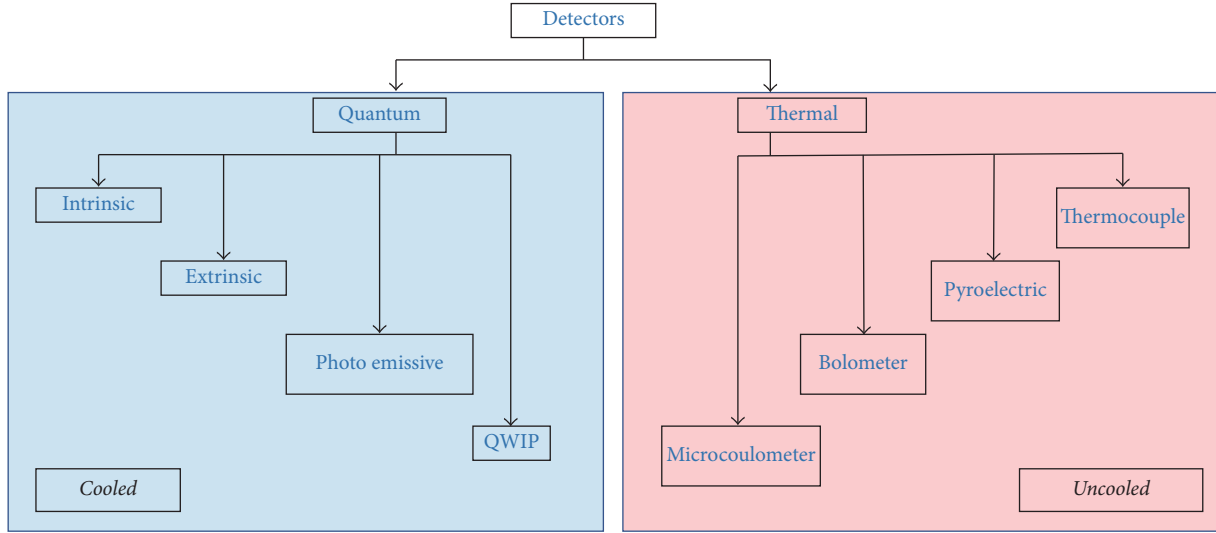


FIGURE 1: Types of IR detectors.

the surface temperature of the inspected body are collected and “compared” with the reference signal given by the excitation thermal wave taken as a reference. So, as in Lock-In amplifiers through the FFT the phase lag between the waves as well as the final amplitude can be obtained. From a computational point of view, if the two signals are both of sine-type, the same can be obtained with at least 4 equidistant (or even three) data points per modulation cycle (S_1 to S_4 in Figure 2) [26].

Therefore, for each pixel, amplitude A (see (3)) and phase φ (see (4)) can be calculated by means of already four thermal images taken during one modulation cycle:

$$A(x) = \sqrt{(S_3 - S_1)^2 + (S_4 - S_2)^2}, \quad (3)$$

$$\varphi(x) = \arctg\left(\frac{S_3 - S_1}{S_4 - S_2}\right). \quad (4)$$

From an experimental point of view, the excitation heat source is made by a halogen lamp which emits light modulated by a function generator. So it is possible to choose the frequency and the amplitude of the heat source. Both the reference signal and the heat reemitted by the inspected body are acquired by the thermal camera. The Lock-In software provides two maps in false colour related to A and φ . The phase maps are particularly interesting due to the possibility of investigating deeper within the thickness of the specimen; the smaller the frequency is the deeper it probes. Since the phase is dependent also on μ , if the body has local discontinuities with different thermal response they will give different phase values, easily represented onto the phase maps with different colours with respect to the surrounding areas.

3. Digital Image Correlation

The DIC technique uses a couple of digital cameras for capturing stereoisimages related to the examined structure

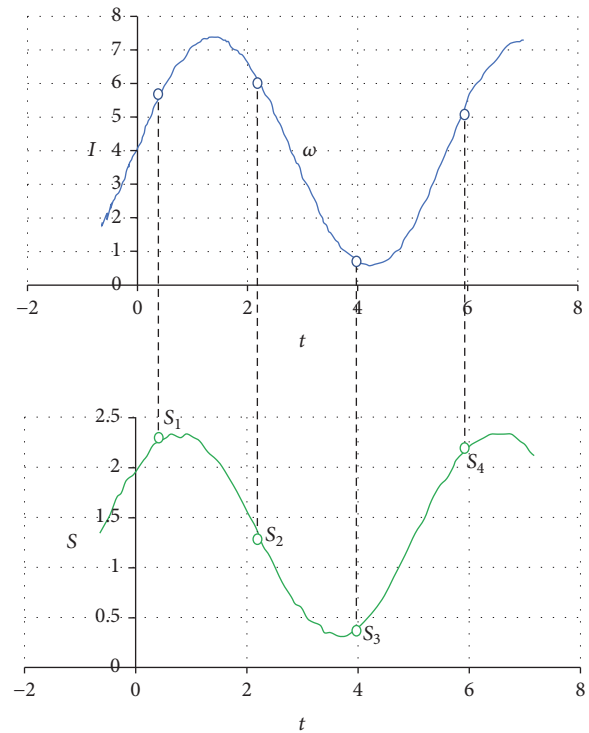


FIGURE 2: Amplitude and phase obtained by a sinusoidal thermal excitation.

under different loading conditions and so it allows estimating the unknown displacement (also out of the plane) and strain fields by comparing the recorded images to the initial nondeformed configuration [36]. The main DIC benefit is the capability of analyzing large displacements and deformations areas with no need of attaching sensors if compared with the conventional measuring methods.



FIGURE 3: Specimen preparation for DIC.

Figure 3 shows the specimen's surface preparation for DIC application. The surface is marked with a black dots pattern on a white background to increase the capability to distinguish locations on the specimen surface. Indeed, the black dots have to be absolutely randomly positioned and of random size, depending on the specimens' dimensions. The images of the specimens, acquired during testing, are elaborated by splitting the surface and the pattern in many subsets. 50 substeps with step 2-3 and strain gauge length of 1 mm were automatically selected by the VIC 3D device in order to minimize the influence on the displacement and strain field, according to the selected region of interest and to the random black dot size and position.

The black pattern on a white background is conceived to make easier and quicker the algorithm work in recording and elaborating the captured images. Indeed, integer values from 0 (black) to 100 (white), according to the current gray gradation, within the pattern are used. During the test, the pattern substep will move to a new position and the software is able to recognize this new position for the displacement calculation. This process is described in Figure 4.

In order to evaluate the displacement field, a correlation method is needed. There are three main correlation methods, which belong to the *sum of squared differences criteria* group. All the suggested criteria are used to evaluate the displacements. The strains field is evaluated by derivatives of the computed displacement field.

(i) *Sum of Squared Differences Criterion*

$$C_{SSD} = \sum_i^N \sum_j^N [f(x_i, y_i) - g(x'_i, y'_i)]^2, \quad (5)$$

where f and g are the values before and after the motion, (x_i, y_i) are the pixel coordinate in the reference image before the motion, and (x'_i, y'_i) are the pixel coordinate in the reference image after the motion. It is a particularly fast criterion, even if it is not very robust because it is very sensitive to brightness changes.

(ii) *Normalized Sum of Squared Differences Criterion*

$$C_{NSSD} = \sum_i^N \sum_j^N \left[\frac{f(x_i, y_i)}{\bar{f}} - \frac{g(x'_i, y'_i)}{\bar{g}} \right]^2 \quad (6)$$

with

$$\bar{f} = \sqrt{\sum_i^N \sum_j^N [f(x_i, y_i)]^2}, \quad (7)$$

$$\bar{g} = \sqrt{\sum_i^N \sum_j^N [g(x'_i, y'_i)]^2}.$$

This criterion seems to be more robust than the previous one because it is not sensitive to the brightness scale variation.

(iii) *Zero-Normalized Sum of Squared Differences Criterion*

$$C_{ZNSSD} = \sum_i^N \sum_j^N \left[\frac{f(x_i, y_i) - f_m}{\Delta f} - \frac{g(x'_i, y'_i) - g_m}{\Delta g} \right]^2 \quad (8)$$

with

$$\Delta f = \sqrt{\sum_i^N \sum_j^N [f(x_i, y_i) - f_m]^2}, \quad (9)$$

$$\Delta g = \sqrt{\sum_i^N \sum_j^N [g(x'_i, y'_i) - g_m]^2},$$

where f_m and g_m are the average gray values of the respective subset. This is the most robust formulation because it is not sensitive to both brightness scale and brightness changes [26].

In order to correctly evaluate the displacements and the strains, it is necessary to know the specimen position according to a 3D scanning system. The camera parameters and relative orientation should be also calibrated to extract the specimen position in the chosen reference coordinate system by means of an arbitrary calibrated rigid target (white grid with equally spaced black dots in Figure 5).

The target does not need to be exactly flat (even if a rather flat calibration target is adopted), but the distance between two points has to be clearly known. In order to guarantee the grid covering the entire image, in particular close to the boundaries, distortions become really important. These distortions are calibrated by short lenses which require a substantial number of images.

4. Tested Specimen and Test Procedures Description

4.1. Tested Specimen Description. As already mentioned, the IRT and DIC techniques have been used to track damage propagation and strain/displacements fields in delaminated composite plates.

The tested specimens are composite plates made of G1157/RTM6 material. The material properties have been evaluated by means of a full experimental material characterization campaign performed by CNR (Italian National Research Council). The system plies have been arranged according to the stacking sequence $[0, 90, 90, 0]_{4S}$. An artificial circular delamination with 40 mm diameter has been

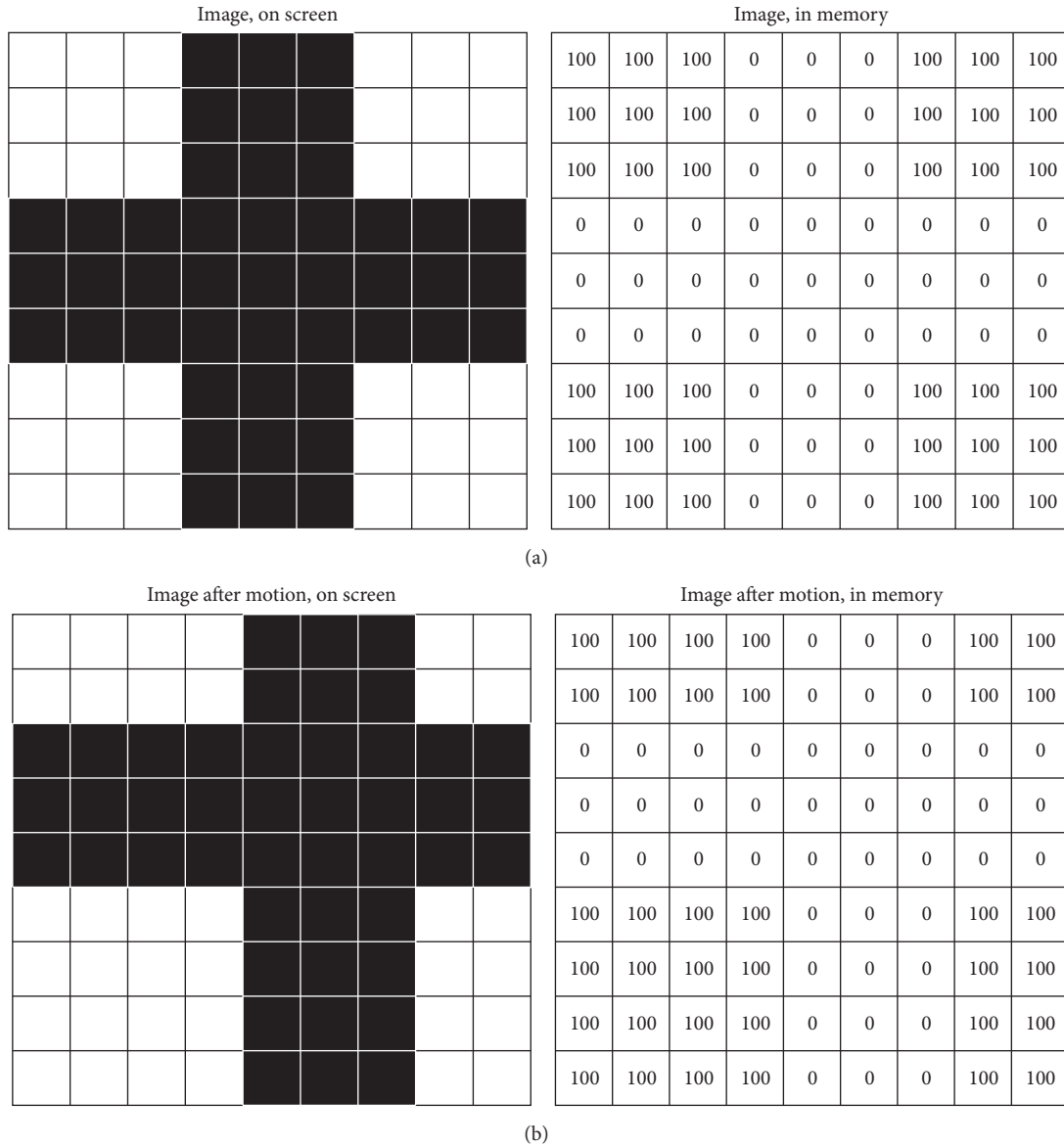


FIGURE 4: (a) Grayscale values (nondeformed configuration). (b) Grayscale values (deformed configuration).

placed between the second and the third ply by means of a Teflon insert during manufacturing with a negligible thickness. In this paper only one thickness (t) and one radius (R) values have been examined. Further studies could evaluate the thickness and the delamination radius changes influence. Two geometrical configurations with central and side delamination have been tested. The geometrical configuration is described in Figure 6 while the geometrical description of the tested specimens and the properties of the material system are presented in Tables 1 and 2, respectively.

Figure 7 shows phase maps taken from a preliminary IRT inspection on the two delaminated panels in order to detect the artificial defect.

The infrared camera and the DIC cameras are placed framing, respectively, the opposite sides of the same specimen. This caution is due to the presence of the black and white

pattern on one side of the sample, which could be responsible for an emissivity degradation of the surface, making IRT less effective. First, the thinner sublaminates have been analyzed as shown in Figure 8.

The DIC and the IR measurements have been carried out simultaneously. Indeed, the heat from the lighting system of the DIC optical setup is negligible if compared to the heat from the halogen lamps used during Lock-In Thermography inspection. Hence, it has been easily verified during the tests.

In order to investigate the influence of the delamination position on the compressive mechanical behavior of the specimen, including delamination growth, the specimen has been subjected to an increasing compressive axial displacement. The compressive displacement has been applied in steps. In order to check for delamination growth, the IRT test has been performed at the end of each load step by

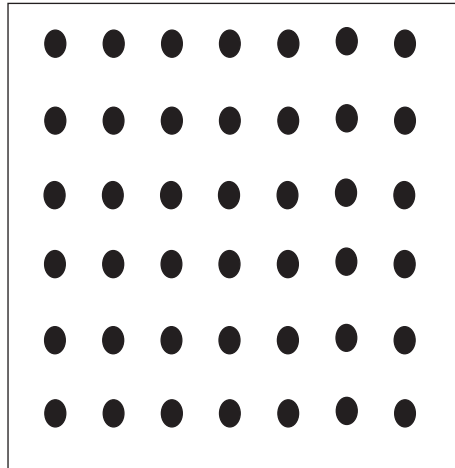


FIGURE 5: Example of the calibration grid.

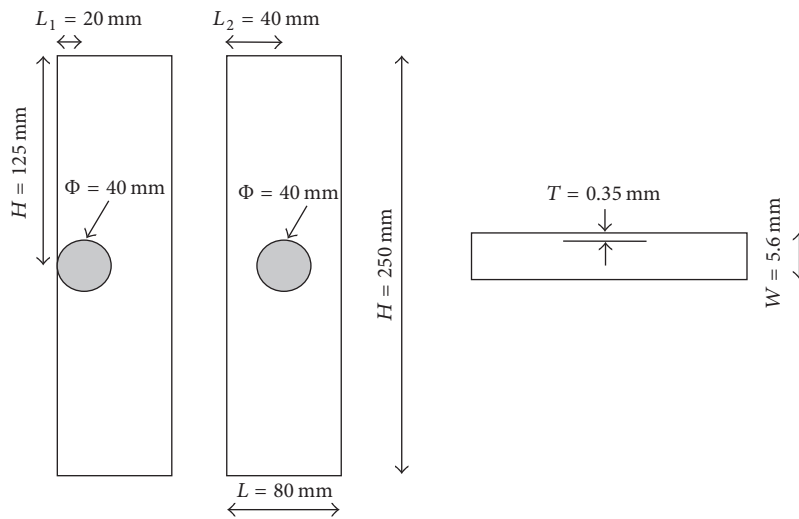


FIGURE 6: Geometrical description of the two tested specimens.

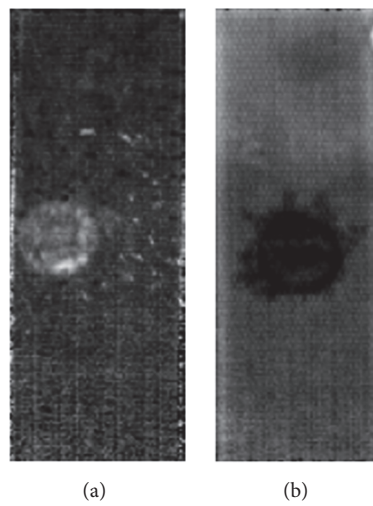


FIGURE 7: Two specimens' initial delamination position; (a) side delamination; (b) central delamination.

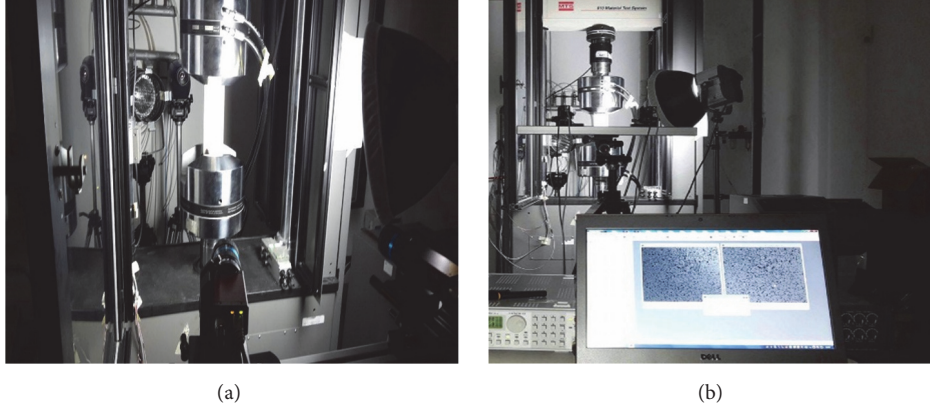


FIGURE 8: IRF and DIC test setup; (a) IRT and DIC cameras on the opposite side of the tested specimen; (b) complete test setup.

TABLE 1: Geometrical description of the tested specimens.

| | |
|---|---------|
| Specimens height (H) | 250 mm |
| Specimens length (L) | 80 mm |
| Specimens width (W) | 5.6 mm |
| Delamination position through the thickness (t) | 0.35 mm |
| Delamination position in plan (h) | 125 mm |
| Delamination position in plan ($L1$) | 20 mm |
| Delamination position in plan ($L2$) | 40 mm |
| Delamination diameter (Φ) | 40 mm |
| Specimens landing lengths | 45 mm |

TABLE 2: Material properties.

| Properties | Value |
|--------------------|--|
| Ply thickness | 0.175 mm |
| Elastic properties | $E_1 = 130.05$ GPa; $E_2 = E_3 = 11.55$ GPa; $G_{12} = G_{13} = G_{23} = 6$ GPa; $\nu_{12} = \nu_{13} = 0.312$; $\nu_{23} = 0.48$; |
| Strength [MPa] | $X_t = 1460.7$ MPa; $X_c = 876.42$ MPa; $Y_t = Z_t = 77.145$ MPa; $Y_c = Z_c = 241.43$ MPa; $S_{12} = S_{13} = 30$ MPa; $S_{23} = 40$ MPa; |
| Fracture toughness | $G_{Ic} = 180$ J \times m ⁻² ; $G_{IIc} = G_{IIIc} = 500$ J \times m ⁻² ; |

pausing the loading process without unloading the specimen. Then the specimen is unloaded and a new step is started, applying an increasing level of displacement. On the other hand, during the same experimental analysis, the DIC test has been performed continuously by recording every out-of-plane surface displacement of the specimen when increasing the load within each step. The adopted infrared camera is a FLIR silver SC5500, while the DIC has been performed by using the VIC-3D™ system provided with two high resolution cameras. The compression test has been carried out using the *810 Material Testing System* (MTS) hydraulic machine in a statistical regime. The test has been performed setting the parameters reported in Table 3.

TABLE 3: Test parameters.

| | |
|-----------------------------------|---------------------------|
| DIC | 1 Hz (1 image per second) |
| Infrared camera (frame frequency) | 103 Hz |
| Lamp (heat excitation frequency) | 0.5 Hz |
| LOA velocity | 0.3 mm/min (compression) |

TABLE 4: Load conditions for the side delamination.

| Step | Displacement [mm] | Load [kN] |
|------|-------------------|---------------------------|
| 1 | 0.61 | -40 |
| 2 | 0.645 | -42.2 |
| 3 | 0.76 | -42.7 |
| 4 | 0.83 | -42.7 |
| 5 | 0.9 | -42.4 |
| 6 | 1.03 | -41.9 \rightarrow -41.5 |
| 7 | 1.13 | -41.1 \rightarrow -40.6 |
| 8 | 1.2 | -40 \rightarrow -39.5 |
| 9 | 1.75 | -29 \rightarrow -25 |

5. Experimental Results

As already mentioned, in order to be able to investigate the delamination growth during the compressive test, the test has been performed by applying 9 increasing levels of displacement, as shown in Tables 4 and 5 for the specimen with side and central delamination.

At the end of each load step, without unloading the specimen, the Lock-In method is applied to check for the delamination growth by observing edges modification of the artificial defect onto the phase maps. Then the specimen is unloaded and a new step is performed up to the next level of displacement. On the other hand the DIC has been performed continuously during each loading step when applying the compressive displacement.

Figures 9 and 10 show the force-displacement curves, obtained at each step, respectively, for the specimen with side and central delamination. The slope reduction passing

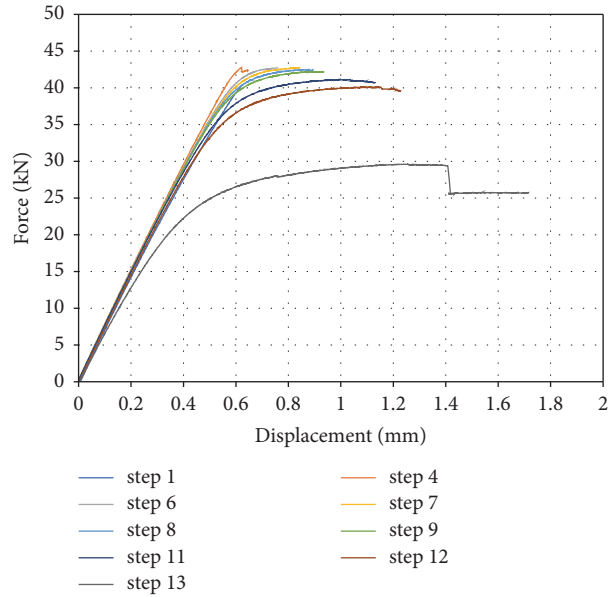


FIGURE 9: Force-displacement curves for the side delamination.

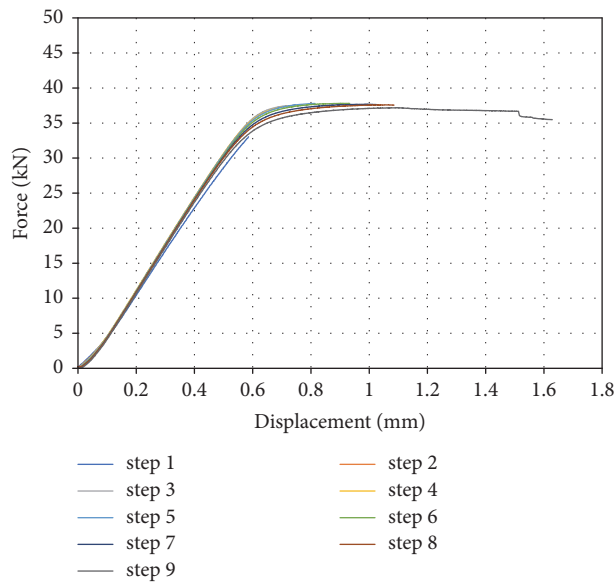


FIGURE 10: Force-displacement curves for the central delamination.

from one step to the next can be considered representative of the damage evolution experienced by the specimens during compression.

From Figures 9 and 10, both the specimens experience the buckling phenomenon leading to a constant value of the load while increasing the compressive displacements. The side delamination appears to be clearly affected by a reduction of the stiffness between one step and another with a clear decrease of the buckling load value. On the other hand, the specimen with central delamination seems to be not affected by stiffness or buckling load reduction from one step to another for all the performed compressive steps up to specimen failure.

Figures 11 and 12 show the DIC contour plot of the surface strain in the loading direction, respectively, for the specimen with side and central delamination at the end of the loading step. These images have been taken from the thicker sublaminar side. It is worth noting that all the DIC measurements have been taken in a 4000×4000 pixels (100 pixels = 1 mm) windows centered with respect to the specimen center. In a cyclic experimental test the variation of the local strain field distribution could be of course associated with localized damage effects. However, this phenomenon has been not analyzed because out of the scope of the present paper. Future works could be focused on the correlation between local damage and strain distribution.

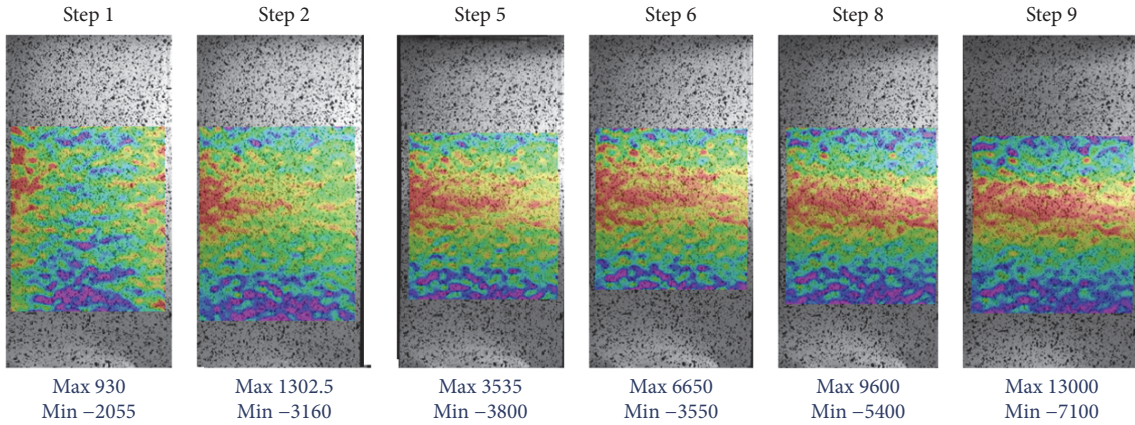


FIGURE 11: Surface strain-principal step-side delamination specimen [$\mu\epsilon$].

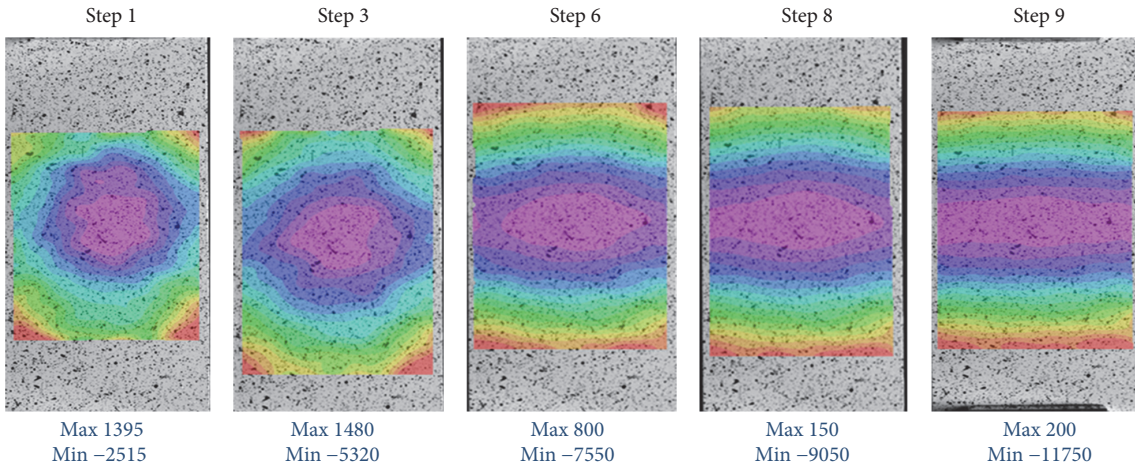


FIGURE 12: Surface strain-principal step-central delamination specimen [$\mu\epsilon$].

TABLE 5: Load conditions for the central delamination.

| Step | Displacement [mm] | Load [kN] |
|------|-------------------|-------------------------|
| 1 | 0.61 | -33.75 |
| 2 | 0.645 | -35.4 |
| 3 | 0.76 | -38.13 |
| 4 | 0.83 | -38.3 |
| 5 | 0.9 | -38.45 |
| 6 | 1.03 | -38.3 |
| 7 | 1.13 | -38.3 |
| 8 | 1.2 | -38.3 \rightarrow -38 |
| 9 | 1.75 | -37.9 \rightarrow -36 |

The influence of delamination position on the strain distribution can be clearly observed in Figures 11 and 12 at the end of the first load steps. Indeed, increasing the applied displacement from one step to another the global buckling shape can be clearly distinguished.

The DIC surface strain distributions are plotted for each step along x and y symmetry axes for the specimen with side

and central delamination, respectively, in Figures 13 and 14. The considerations made for Figures 11 and 12 apply.

The DIC out-of-plane displacements contours for both the studied specimens at the end of the loading steps are shown in Figures 15 and 16.

The effect of local delamination buckling on the out-of-plane displacements for the side delamination can be appreciated from the first steps images reported in Figure 15. On the other hand, Figure 16 shows that the central delamination buckling profile can be hardly distinguished from the first steps images.

The effects of the global buckling of the specimen on the out-of-plane displacements distribution can be observed from the last step images for both configurations. It is worth noting that, under compressive load, the two tested specimens undergo different deformed buckling shapes. Indeed, the specimen with side delamination buckles in the opposite direction with respect to thinner sublaminate while the central delaminated specimen buckles toward the direction of the thinner sublaminate.

The DIC out-of-plane displacements distributions are plotted for each step along x and y axes for the specimen with

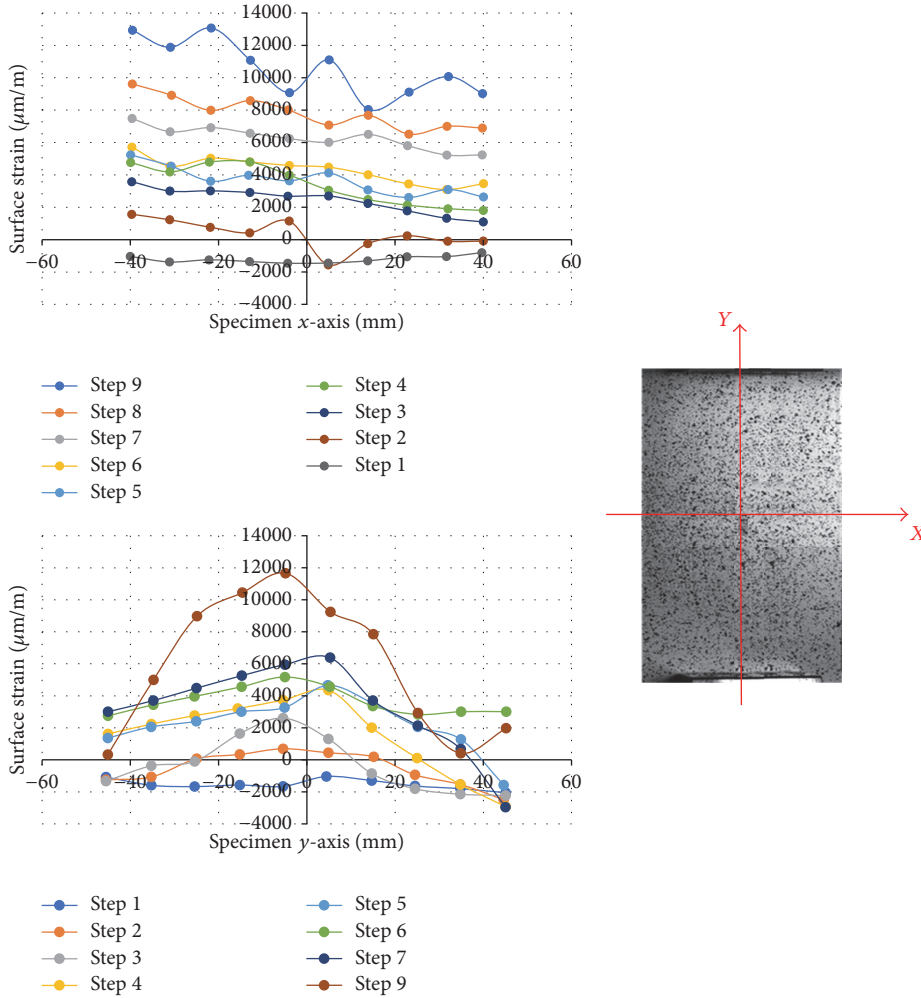


FIGURE 13: Surface strain-principal values along symmetry axes-side delamination specimen.

side and central delamination, respectively, in Figures 17 and 18. The considerations made for Figures 15 and 16 apply.

Tridimensional representations of the out-of-plane displacement distributions obtained with the DIC are presented in Figures 19 and 20, respectively, for the specimen with side and central delamination.

In these figures a comparison between the tridimensional distributions of the out-of-plane displacements obtained at the end of the first step and at the end of the last step is introduced. As it can be observed in Figure 19, even if the noise level is quite relevant in the first step images, the influence of the side positioned delamination on the out-of-plane displacements of the specimen is clearly distinguishable. The same cannot be said for Figure 20 where the central buckling delamination profile seems not to be completely developed. The global buckling profile is, again, clearly observable for both the specimen configurations. The difficulty in detecting the local buckling of delamination is due to the position of the DIC apparatus. Indeed the DIC apparatus, as already mentioned, has been located on the thicker sublaminar side. Hence, all we can appreciate from this position is the effect of the delamination buckling on the

global out-of-plane and strain distributions of the specimen. The effect of delamination buckling on the global strain and displacement distributions seems to be more relevant for the side delamination with respect to the central delamination.

The Lock-In method has allowed evaluating the delamination growth during the compressive static tests.

The delamination evolution as a function of the increasing compressive load is shown in the following phase maps. In Figure 21 the specimen with side delamination is shown as a circular red shape juxtaposed to blue background and in Figure 22 the phase maps of the specimen with the central delamination can be seen (also in this case as circular red shape on a blue background).

Figure 21 shows that the side delamination specimen is interested by a relevant delamination growth. Indeed, the side delamination area grows from 1256 mm² to 2045 mm² from the first step up to the specimen failure. On the other hand, Figure 22 shows that the central delamination growth is almost negligible (central delamination area, from the first step up to the specimen failure, grows from 1256 mm² to 1471 mm²). This behavior can be explained by the different global buckling shape in terms of out-of-plane

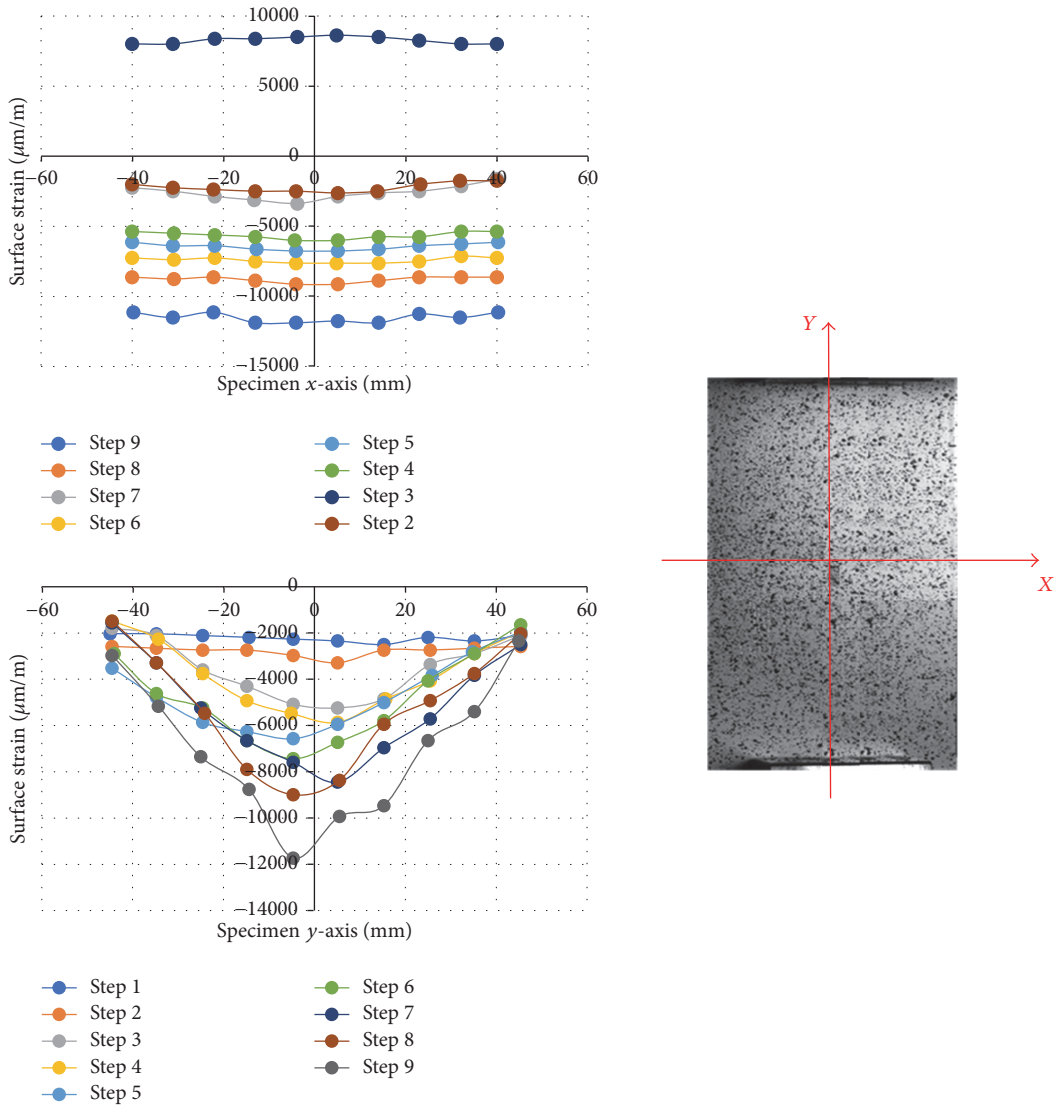


FIGURE 14: Surface strain-principal values along symmetry axes-central delamination specimen.

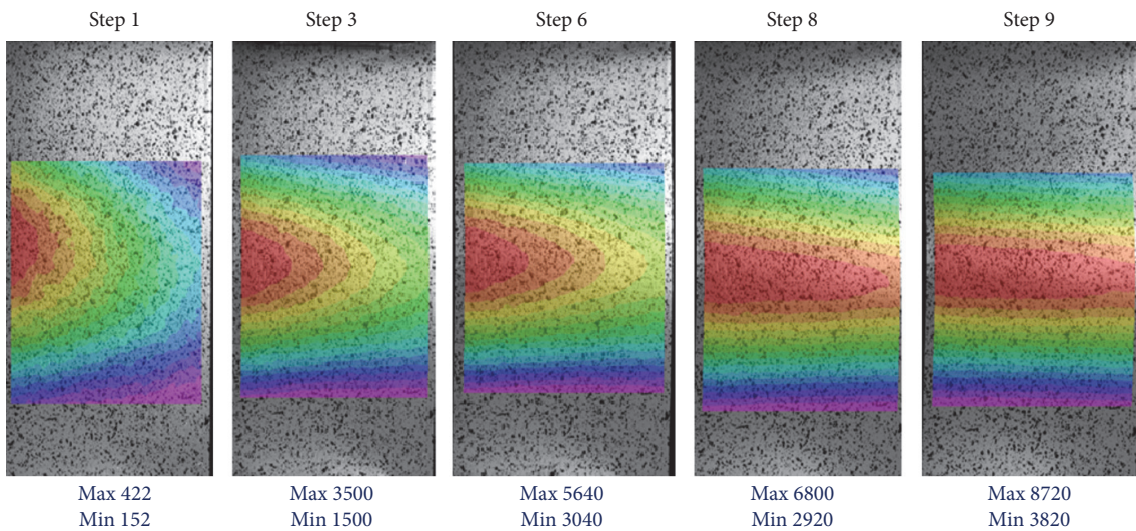


FIGURE 15: Out-of-plane displacement-principal step-side delamination specimen [$\mu\epsilon$].

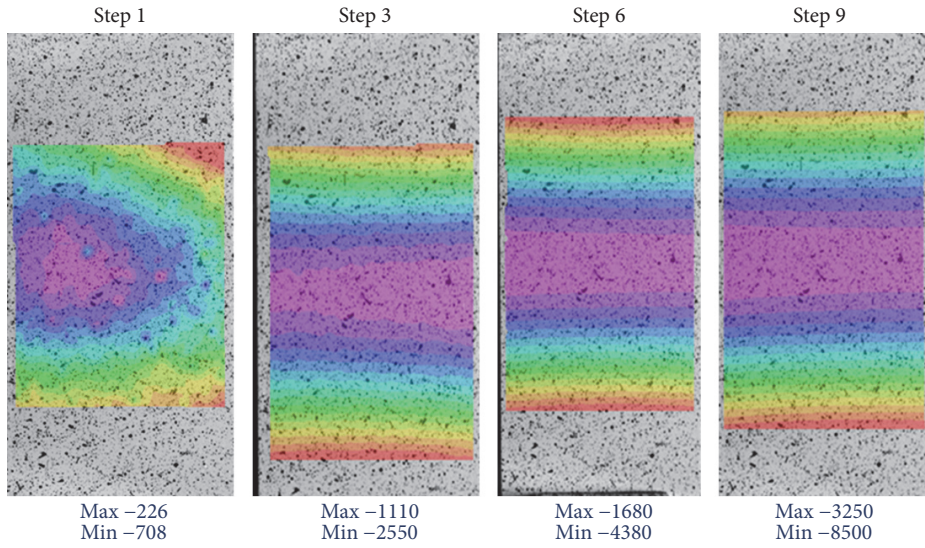


FIGURE 16: Out-of-plane displacement-principal step-central delamination specimen $[\mu\epsilon]$.

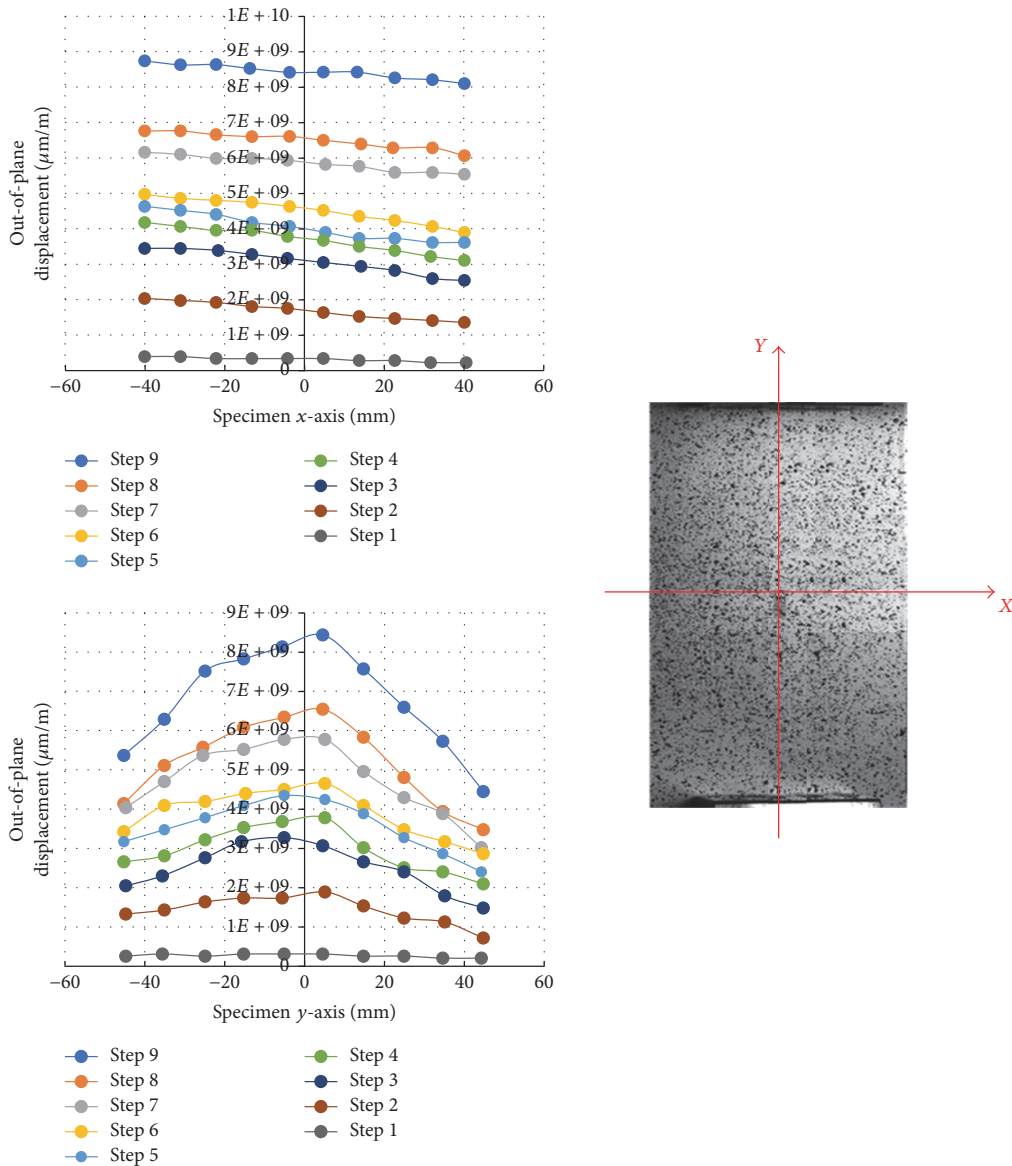


FIGURE 17: Out-of-plane displacement values along symmetry axes-side delamination specimen.

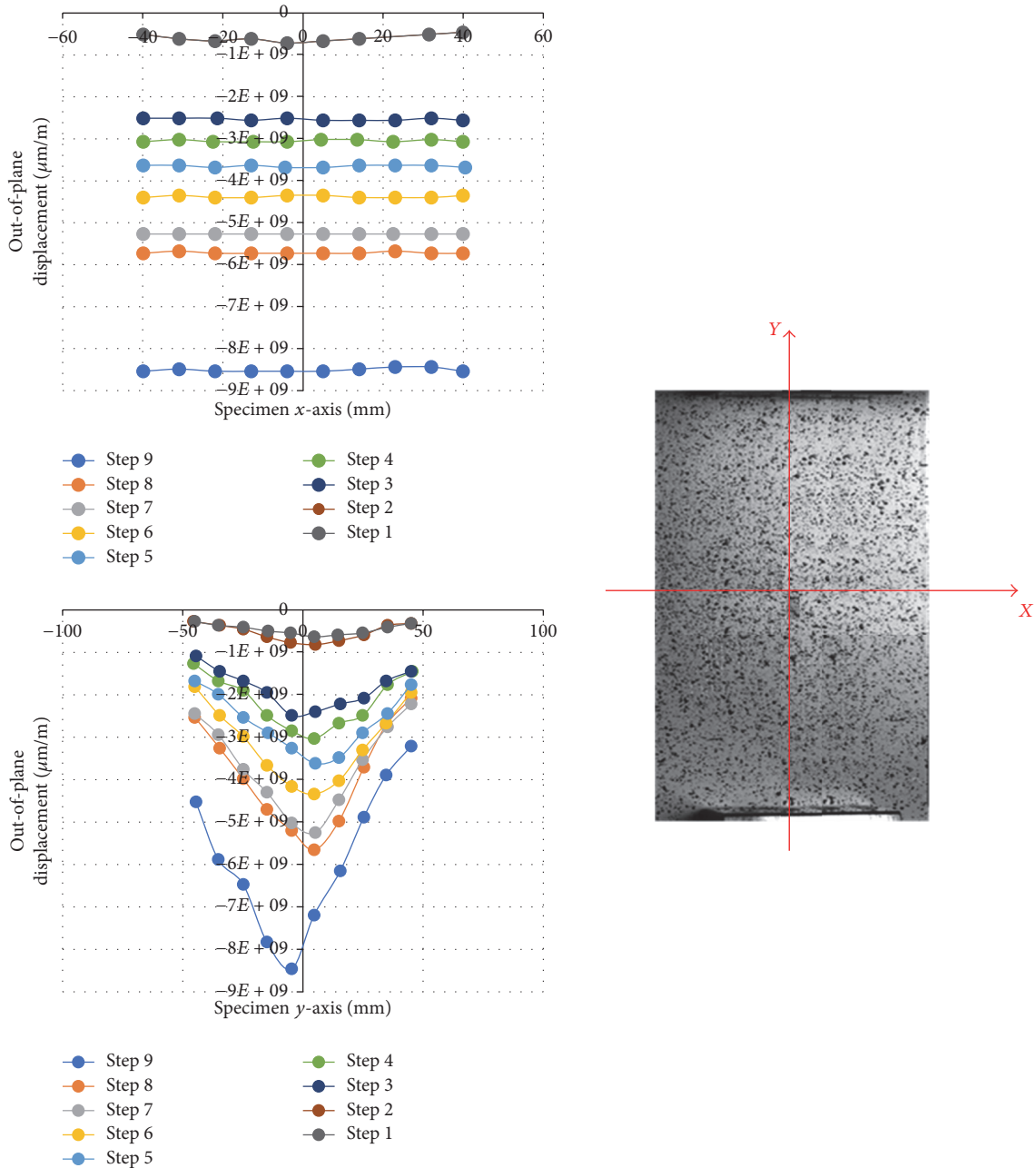


FIGURE 18: Out-of-plane displacement values along symmetry axes-central delamination specimen.

direction observed for the two specimens. Indeed, for the side delamination specimen, the thinner sublaminates are under compression and the local buckling turns out to be a natural consequence. For the central delamination specimen, the thinner sublaminates are under traction, and hence it is not prone to the local buckling. The growth trend as a function of the applied compressive displacements, for the two types of delamination, is reported in Figure 23. For this figure, the differences in terms of growth between the two analyzed configurations can be clearly noticed. Indeed, for the side delamination, a constant growth can be appreciated with a

sudden increase of delamination size at the global buckling displacement. On the contrary, the central delamination does not substantially grow up to the global buckling displacement where an instantaneous small increase of delaminated area can be noticed.

These experimental observations on the delamination size changes during compressive displacements application can be easily related to the load displacement curves recorded during the load steps and shown in Figures 9 and 10, respectively, for the side and the central delamination configuration. Indeed the delamination growth experienced by the side

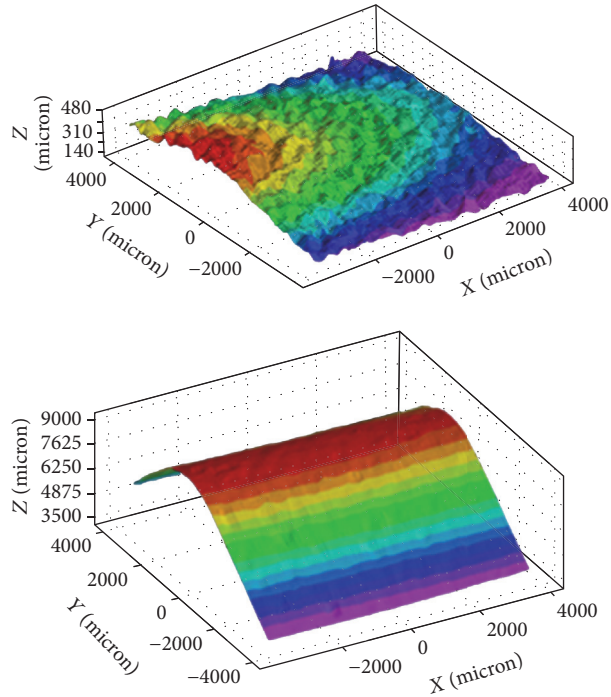


FIGURE 19: DIC: First and last step-3D plot-side delamination specimen.

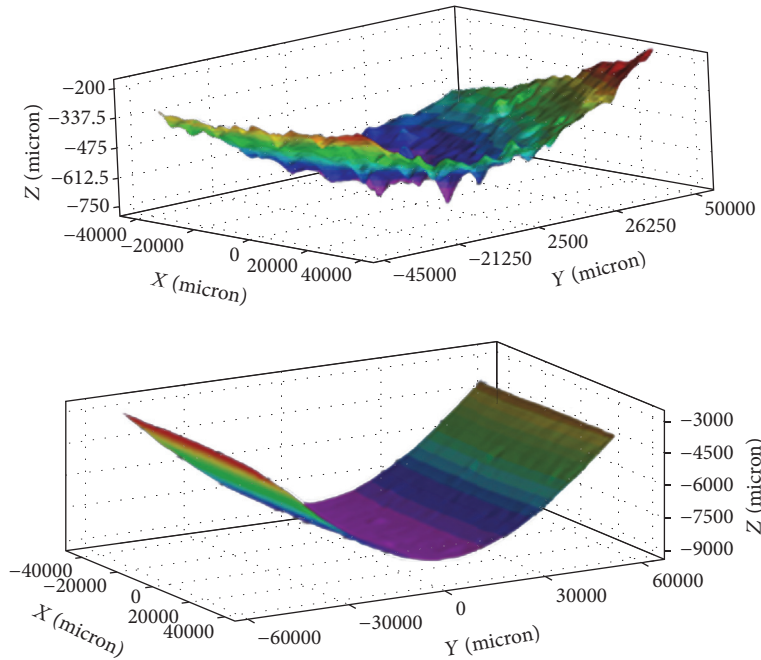


FIGURE 20: DIC: First and last step-3D plot-central delamination specimen.

delamination seems to influence the global stiffness and the global buckling load of the specimen (see Figure 9). On the other hand, the specimen with the central delamination, which does not propagate, seems to not experience stiffness and buckling load reductions. As an example, in Figure 24 the deformation of the specimen with central delamination at buckling is shown.

In the frame of this paper, due to need of elevated emissivity values for Lock-In performing, the DIC measurements have been taken on the opposite side with respect to surface closer to the artificial delamination. Hence, from the presented DIC measurements nothing can be derived concerning the delamination growth status. Indeed only the effects of delamination propagation on the global strain and

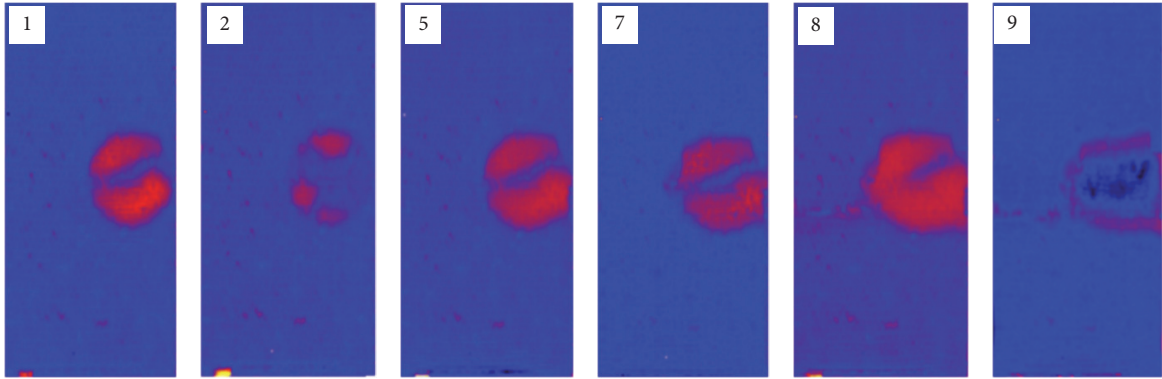


FIGURE 21: Delamination development-principal step-side delamination specimen.

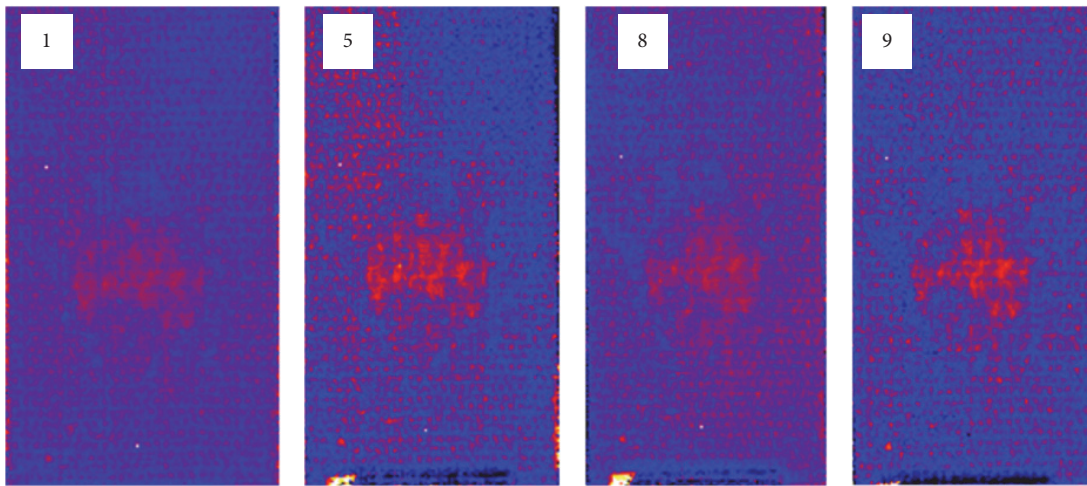


FIGURE 22: Delamination development-principal step-central delamination specimen.

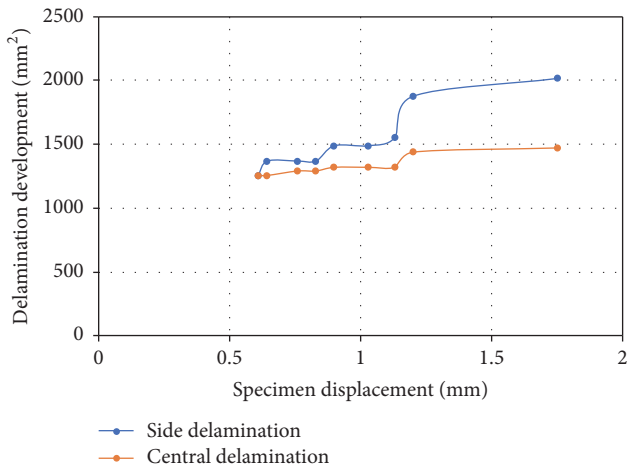


FIGURE 23: Delaminated area as a function of the applied compressive displacement, comparison between side and central delamination configuration.

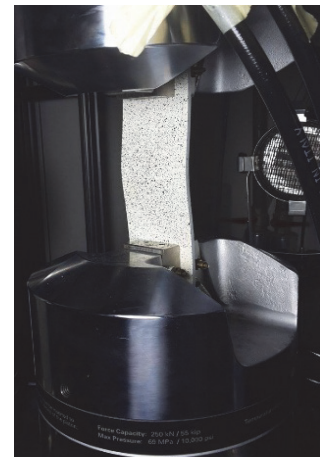


FIGURE 24: Specimen deformation at buckling, specimen with central delamination.

out-of-plane displacements on the opposite side with respect to delamination have been evaluated. However, the details of

the obtained experimental results in terms of out-of-plane displacements (even in the first compressive steps when the delamination buckling can be relevant) suggest an alternative

use for the Digital Image Correlation. As a matter of facts, the use of DIC measurements, taken on the delaminated surface, for its capability to determine with accuracy the strain and displacements in the delamination plane, could provide useful indirect no-contact information in terms of delamination buckling shape size.

6. Conclusions

In this paper, an experimental investigation on the delamination growth in composite plates under compressive load, by using two different experimental techniques (Infrared Thermography via Lock-In method and Damage Image Correlation), is presented. Two specimens with different delamination locations (side and central) have been investigated in order to understand the influence of delamination position on their global compressive behavior. The infrared camera has been used to monitor the internal damage development and the Digital Image Correlation (DIC) method has been used to obtain surface strain and out-of-plane displacements fields.

IRF and DIC measurements showed that, during test, the compressive behavior of the specimen with side delamination has been found mostly influenced by the delamination growth both in terms of stiffness and buckling load variations. On the contrary, no growth has been detected for the central delamination up to the final failure of the specimen. The influence of the local buckling of the delamination on the final surface strains and out-of-plane displacements distribution has been also appreciated for the two analyzed configurations. The obtained results suggest the use of DIC outputs, in terms of out-of-plane displacements, for the indirect measurement of the delamination size with a very easy implementation and without the need of contact with the specimen surface.

Conflicts of Interest

The authors declare that there are no conflicts of interest regarding the publication of this paper.

References

- [1] L. Couchman and A. Mouritz, *Modeling of Naval Composite Structures in Fire*, Acclaim Printing Services, Victoria, Australia, 2006.
- [2] S. Abrate, *Impact on Composite Structures*, Cambridge University Press, 1998.
- [3] A. Raimondo and A. Riccio, "Inter-laminar and intra-laminar damage evolution in composite panels with skin-stringer debonding under compression," *Composites Part B: Engineering*, vol. 94, pp. 139–151, 2016.
- [4] A. Riccio, M. Damiano, A. Raimondo, G. Di Felice, and A. Sellitto, "A fast numerical procedure for the simulation of inter-laminar damage growth in stiffened composite panels," *Composite Structures*, vol. 145, pp. 203–216, 2016.
- [5] R. Borrelli, A. Riccio, A. Sellitto, F. Caputo, and T. Ludwig, "On the use of global-local kinematic coupling approaches for delamination growth simulation in stiffened composite panels," *Composites Science and Technology*, vol. 115, pp. 43–51, 2015.
- [6] D. D. Symons and G. Davis, "Fatigue testing of impact-damaged T300/914 carbon-fibre-reinforced plastic," *Composites Science and Technology*, vol. 60, no. 3, pp. 379–389, 2000.
- [7] A. A. Baker, R. Jones, and R. J. Callinan, "Damage tolerance of graphite/epoxy composites," *Composite Structures*, vol. 4, no. 1, pp. 15–44, 1985.
- [8] G. Cricri and M. Perrella, "Investigation of mode III fracture behaviour in bonded pultruded GFRP composite joints," *Composites Part B: Engineering*, vol. 112, pp. 176–184, 2017.
- [9] G. Cricri, M. Perrella, S. Sessa, and N. Valoroso, "A novel fixture for measuring mode III toughness of bonded assemblies," *Engineering Fracture Mechanics*, vol. 138, pp. 1–18, 2015.
- [10] R. Citarella and G. Cricri, "Three-dimensional BEM and FEM submodelling in a cracked FML full scale aeronautic panel," *Applied Composite Materials*, vol. 21, no. 3, pp. 557–577, 2014.
- [11] G. Cricri, M. Perrella, and C. Cali, "Experimental and numerical post-buckling analysis of thin aluminium aeronautical panels under shear load," *Strain*, vol. 50, no. 3, pp. 208–222, 2014.
- [12] S. Sanchez-Saez, E. Barbero, R. Zaera, and C. Navarro, "Compression after impact of thin composite laminates," *Composites Science and Technology*, vol. 65, no. 13, pp. 1911–1919, 2005.
- [13] A. Shipsha and D. Zenkert, "Compression-after-impact strength of sandwich panels with core crushing damage," *Applied Composite Materials*, vol. 12, no. 3–4, pp. 149–164, 2005.
- [14] X. Wang, J.-F. Witz, A. El Bartali, and C. Jiang, "Infrared thermography coupled with digital image correlation in studying plastic deformation on the mesoscale level," *Optics and Lasers in Engineering*, vol. 86, pp. 264–274, 2016.
- [15] G. Gaussorgues, *Infrared Thermography*, Chapman & Hall, London, UK, 1994.
- [16] S. Datcu, L. Ibos, Y. Candau, and S. Mattei, "Improvement of building wall surface temperature measurements by infrared thermography," *Infrared Physics and Technology*, vol. 46, no. 6, pp. 451–467, 2005.
- [17] M. Poncelet, J.-F. Witz, H. Pron, and B. Watrisse, "A study of IRFPA camera measurement errors: Radiometric artefacts," *Quantitative InfraRed Thermography Journal*, vol. 8, no. 1, pp. 3–20, 2011.
- [18] M. A. Sutton, J. J. Orteu, and H. Schreier, *Image Correlation for Shape, Motion and Deformation Measurements: Basic Concepts, Theory and Applications*, Springer, New York, NY, USA, 2009.
- [19] B. Pan, K. Qian, H. Xie, and A. Asundi, "Two-dimensional digital image correlation for in-plane displacement and strain measurement: a review," *Measurement Science and Technology*, vol. 20, no. 6, article 062001, 2009.
- [20] B. Pan, A. Asundi, H. Xie, and J. Gao, "Digital image correlation using iterative least squares and pointwise least squares for displacement field and strain field measurements," *Optics and Lasers in Engineering*, vol. 47, no. 7–8, pp. 865–874, 2009.
- [21] B. Pan and K. Li, "A fast digital image correlation method for deformation measurement," *Optics and Lasers in Engineering*, vol. 49, no. 7, pp. 841–847, 2011.
- [22] B. Pan, J. Yuan, and Y. Xia, "Strain field denoising for digital image correlation using a regularized cost-function," *Optics and Lasers in Engineering*, vol. 65, no. 0, pp. 9–17, 2014.
- [23] C. Cofaru, W. Philips, and W. Van Paepegem, "A three-frame digital image correlation (DIC) method for the measurement of small displacements and strains," *Measurement Science and Technology*, vol. 23, no. 10, article 105406, 2012.
- [24] W. T. Kim, M. Y. Choi, and J. H. Park, "Diagnosis of defect points in materials using infrared thermography," *Key Engineering Materials*, vol. 297–300, pp. 2169–2175, 2005.

- [25] J.-H. Park, M.-Y. Choi, and W.-T. Kim, "Infrared thermography and modeling to the concrete deck with internal defects as a non-destructive testing," *Key Engineering Materials*, vol. 270-273, pp. 938-943, 2004.
- [26] G. Busse, D. Wu, and W. Karpen, "Thermal wave imaging with phase sensitive modulated thermography," *Journal of Applied Physics*, vol. 71, no. 8, pp. 3962-3965, 1992.
- [27] O. Breitenstein and M. Langenkamp, "Lock-in contact thermography investigation of lateral electronic inhomogeneities in semiconductor devices," *Sensors and Actuators, A: Physical*, vol. 71, no. 1-2, pp. 46-50, 1998.
- [28] <http://thermosensorik.com/>.
- [29] S. Huth, O. Breitenstein, A. Huber, D. Dantz, U. Lambert, and F. Altmann, "Lock-in IR-thermography—a novel tool for material and device characterization," *Solid State Phenomena*, vol. 82-84, pp. 741-746, 2002.
- [30] B. Pan and H. Xie, "Full-field strain measurement based on least-square fitting of local displacement for digital image correlation method," *Acta Optica Sinica*, vol. 27, no. 11, pp. 1980-1986, 2007.
- [31] M. Wisnom, F. Pierron, C. Devivier, and D. Thompson, "Correlation between full-field measurements and numerical simulation results for multiple delamination composite specimens in bending," *Applied Mechanics and Materials*, vol. 24, pp. 109-114, 2010.
- [32] C. Devivier, F. Pierron, and M. R. Wisnom, "Damage detection in composite materials using deflectometry, a full-field slope measurement technique," *Composites Part A: Applied Science and Manufacturing*, vol. 43, no. 10, pp. 1650-1666, 2012.
- [33] L. Yang, P. Zhang, S. Liu, P. R. Samala, M. Su, and H. Yokota, "Measurement of strain distributions in mouse femora with 3D-digital speckle pattern interferometry," *Optics and Lasers in Engineering*, vol. 45, no. 8, pp. 843-851, 2007.
- [34] F. Laurin, J.-S. Charrier, D. Lévêque, J.-F. Maire, A. Mavel, and P. Nuñez, "Determination of the properties of composite materials thanks to digital image correlation measurements," in *Proceedings of the IUTAM Symposium on Full-Field Measurements and Identification in Solid Mechanics*, pp. 106-115, July 2011.
- [35] M. A. Caminero, M. Lopez-Pedrosa, C. Pinna, and C. Soutis, "Damage monitoring and analysis of composite laminates with an open hole and adhesively bonded repairs using digital image correlation," *Composites Part B: Engineering*, vol. 53, no. 24, pp. 76-91, 2013.
- [36] G. Musotto, *Digital Image Correlation: applicazione di tecniche convenzionali e sviluppo di soluzioni innovative per la stima e l'incremento dell'accuratezza [M.S. thesis]*, Politecnico di Milano, Facoltà di Ingegneria Industriale, Corso di Laurea in Ingegneria Meccanica, 2012.

Research Article

Stochastic Effect of Grain Elongation on Nanocrystalline Materials Strain and Strain Rate Produced by Accumulative Roll-Bonding and Equal Channel Angular Pressing

P. Baonhe Sob,¹ A. Alfayo Alugongo,¹ and T. Ba Bob Tengen²

¹Department of Mechanical Engineering, Faculty of Engineering and Technology, Vaal University of Technology, Private Bag X021, Vanderbijlpark 1900, South Africa

²Department of Industrial Engineering and Operations Management, Faculty of Engineering and Technology, Vaal University of Technology, Private Bag X021, Vanderbijlpark 1900, South Africa

Correspondence should be addressed to P. Baonhe Sob; baonhe_sob@rocketmail.com

Received 20 February 2017; Accepted 3 May 2017; Published 12 June 2017

Academic Editor: Paulo M. S. T. De Castro

Copyright © 2017 P. Baonhe Sob et al. This is an open access article distributed under the Creative Commons Attribution License, which permits unrestricted use, distribution, and reproduction in any medium, provided the original work is properly cited.

Severe plastic deformation techniques are acknowledged to produce elongated grains during fabrication of nanostructured materials. Previous models relating grain size to mechanical properties considered only equivalent radius, thus ignoring other approaches of measuring grain sizes such as semiminor axis, semimajor axis, and major axis radii that determine true grain shape. *In this paper, stochastic models of nanomaterials mechanical properties that include the ignored parameters have been proposed.* The proposed models are tested with data from nanocrystalline aluminum samples. The following facts were experimentally observed and also revealed by the models. Grain elongates to a maximum value and then decreases with further grain refinement due to grain breakages. Materials yield stress increases with elongation to a maximum and then decreases continuously. The varying approaches of measuring grain radius reveal a common trend of Hall-Petch and Reverse Hall-Petch Relationship but with different critical grain sizes. Materials with high curvature grains have more enhanced yield stress. Reducing strain rates leads to materials with more enhanced yield stress, with critical strain rates values beyond which further reductions do not lead to yield stress enhancement. It can be concluded that, by considering different approaches of measuring grain sizes, reasons for different yield stress for nanomaterials that were observed but could not be explained have been dealt with.

1. Introduction

Amongst the severe plastic deformation (SPD) techniques developed and tested, the Equal Channel Angular Pressing (ECAP) and Accumulative Roll-Bonding (ARB) are unique due to their abilities to produce nanomaterials with ultrafine grain structures and high shear strains [1, 2]. The ECAP produces high shear strain without changing the sample shape or dimension [1, 2]. Its main shortcoming is that only small quantities of nanomaterials can be produced during experimentation, which makes it not suitable for industrial application. However, the ARB solves this “small quantity” problem due to its ability to improve on productivity of bulk nanostructure. Both ECAP and ARB are unique and similar since both methods involve large misorientation-angle grain

boundaries that lead to very high strains during the deformation of nanostructures [3, 4].

Materials are called nanomaterials because of their refined grain sizes, and most nanomaterials properties have been characterized as a function of their grain sizes or sizes of the constituent structures. The sizes of 3D grain can be described by the equivalent radius r , semiminor axis radius r_2 , semimajor axis radius r_1 , and major axis radius r_3 . Hillert [5] initially established the model for evolution of grain size or grain growth assuming spherical grains while employing the Theory of Second Phase Particle Coarsening. Tengen [6] further states that the theoretical and experimental investigations reveal that grain growth not only is brought about by Grain Boundary Migration (GBM), but also is accompanied by Grain Rotation-Coalescence (GRC)

mechanism. Tengen [6] modified the Hillert Model [5] so as to consider GRC mechanism, the random or stochastic nature of grain size by adding fluctuation terms that account for random fluctuations due to GBM and GRC processes, and variable grain boundary energy.

Despite these modifications of the models for grain size evolutions, most nanomaterials mechanical properties are given as functions of spherical grains [7, 8] although with random size distribution. The relationship between grain size (i.e., equivalent radius) and yield stress was first proposed by Hall and Petch [7, 8]. The Hall-Petch Relationship (HPR) states that as the average size of the grains in materials gets finer, the yield stress increases. This relationship has its shortcoming since infinite refinement does not lead to infinite yield stress. The HPR model was modified by Zhao and Jiang [9] to reveal the Reverse Hall-Petch Relationship (RHPR), which was later modified by Tengen et al. [10] to consider the stochastic nature of grain size.

It should be noted that all the above-mentioned modified models dealt only with the equivalent radius r or made the assumptions that the grains in nanomaterials are spherical in nature. Experimentally, this spherical shape of all the grains in nanomaterials is not the case; in fact, majority of the grains in nanomaterials are not nearly spherical nature. Thus, the models that consider that the grains in nanomaterials are spherical ignore other important parameters such as semiminor axis radius r_2 , semimajor axis radius r_1 , and the major axis radius r_3 , which can be used to closely define elongation and shape. It must be remarked here that a grain undergoing elongation during nanomaterial refinement might not change in equivalent radius (with equivalent radius defined as the radius of an equivalent sphere or circle obtained by the displacement method of volume/area measurement). As such, the impacts of grain elongation on nanomaterials mechanical properties cannot be properly addressed with the use of equivalent radius only. *Therefore a stochastic model of grain elongation for 3D grain undergoing severe plastic deformation that considers the various approaches of measuring grain size is necessary, which has been proposed in the current report.* The impacts of the different approaches of measuring grain sizes and the impacts of grain elongations on nanomaterials are then dealt with in this report. The proposed models are tested with data from grain deformation in nanocrystalline aluminum.

2. Methodology

2.1. Experimental Procedure of Accumulative Roll-Bonding (ARB). The experimental setup for ARB is shown schematically in Figure 1(a). The ARB technology made use of conventional rolling facility. In this report two shafts were placed horizontally so that they were free to rotate by means of a mechanically automated operation. Three gauges (load gauge, temperature gauge, and a time gauge or a stop watch) were used during experimentation. One measured the applied force, which caused the deformation; the second gauge measured the temperature at the time of experiment; and the third gauge measured the time of deformation. All rotating shafts were mounted on the support roll cage with roller

bearings to prevent friction during motion. Extra support shafts were mounted to ensure stability of the system during operation. Power was transferred from the power generator to the gearbox by a shaft. Drive was also transferred from the gearbox to the rotating beam by a chain drive. During experimentation a plunger connected to another motor was used to force or feed the AA6082-T6 Aluminum (Al) through the rotating shafts. The purpose of this second motor was to control the feed rate or deformation rate or strain rate. The rotating shafts gripped the AA6082-T6 Aluminum sample and forced the sample through the rollers in the first pass.

The deformed AA6082-T6 Aluminum was cut in two pieces and stacked together. Before stacking, the entire surfaces of the strips were degreased with tetrachlorethylene and wire-brushed (stainless steel brush) to achieve good bonding. The materials were joined together in the corners using aluminum wires and subsequently rolled. The whole sequence of “rolling, cutting, face-brushing, degreasing, and stacking” was repeated again for several “passes” until nanomaterials with required characteristics were obtained.

The samples with the deformed microstructures were examined using Transmission Electron Microscopy (TEM). The microstructure was observed to lengthen along the semimajor axis r_3 , semimajor axis r_1 , and semiminor axis r_2 . The observed nanostructures are presented in Figure 1(b).

2.2. Experimental Procedure of Equal Channel Angular Pressing (ECAP). The experiments were carried out as demonstrated by the routes in Figures 2(a) and 2(b) using samples of AA6082-T6 Aluminum. The ECAP die tunnels were designed to intersect “internally” at angle ϕ ($\phi = 90^\circ$) but subtended by the arc or curved “external” surface. During fabrication of nanomaterials, a 50-ton hydraulic press was used to press the aluminum sample through the ECAP die shown in Figures 2(a)–2(c). Since it was very difficult to force the AA6082-T6 Aluminum sample through the ECAP die at the point where the two tunnels meet, the AA6082-T6 Aluminum samples were heat-treated before each ECAP pass to enable the sample to pass through the ECAP die, as recommended by other researchers [1]. It was observed that heating the AA6082-T6 Aluminum sample led to grain growth and subjecting the material through the ECAP die led to grain refinement. The samples with the deformed microstructures were examined using TEM to obtain values of semiminor axis radius, semimajor axis radius, and major axis radius.

2.3. Justifications for Material Used for ARB and ECAP Experimentations. In the current study AA6082-T6 was used for the experimentations. Aluminum material is the most used material in domestic and industrial applications. There are several reasons why aluminum material is widely used in severe plastic deformation process. Some of the reasons are that it is easy to deform aluminum material when compared with other materials. It is also easy to bend aluminum samples to the desired shape during experimentations. Aluminum material is lighter and cheaper when compared to other materials. However, since most severe plastic deformations have been carried out on aluminum material, it is therefore easy

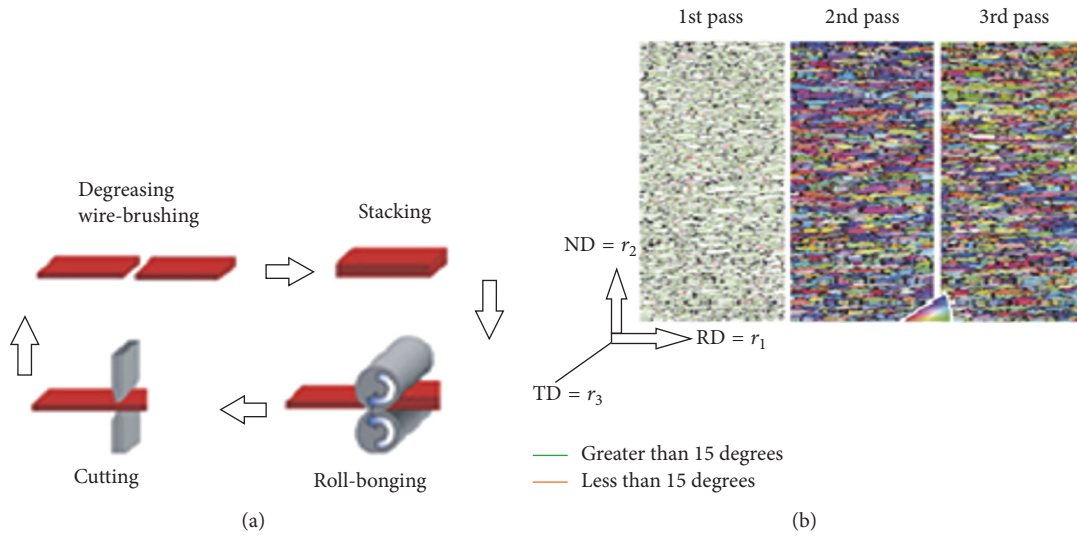


FIGURE 1: (a) Schematic of ARB experimental setup [11] and (b) microscopic observation.

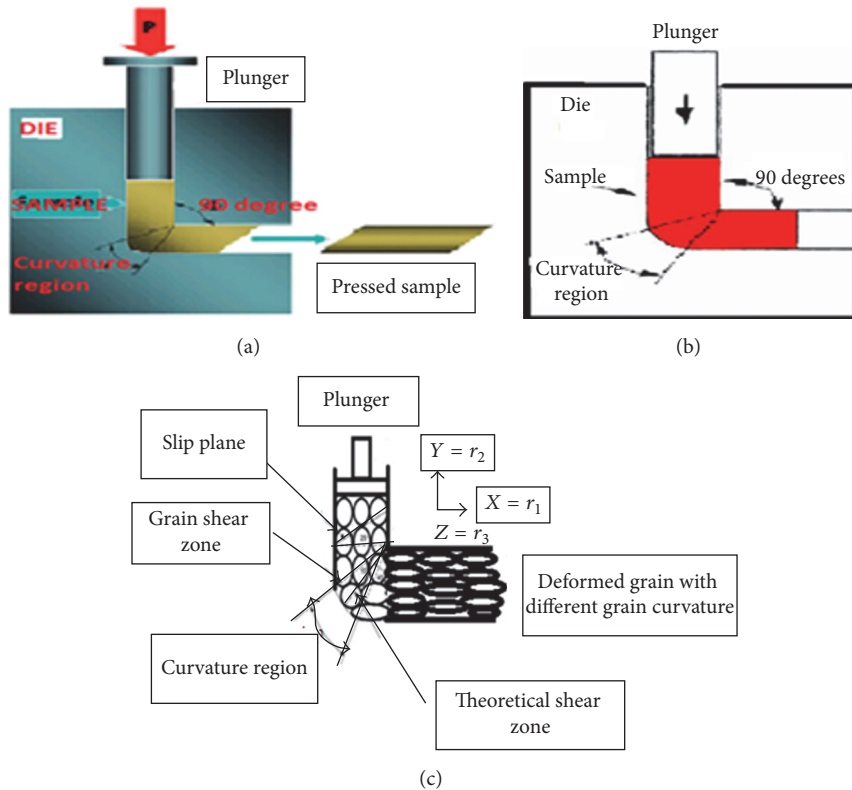


FIGURE 2: Schematic of ECAP processing routes by Estrin and Vinogradov [1], (a) illustration of material deformation, (b) schematic of material deformation, and (c) schematic of grain refinement.

to compare and validate experimental results and theoretical results, which is critical aspect.

2.4. *Sample Preparation for TEM Examination.* Standard TEM thin foils that were 3 mm in diameter were prepared by electrolytic twin jet polishing (at -30°C , 30 V) in Struers Tenupol 2 filled with 6% solution of perchloric acid in

methanol. The 3D observations were carried out at 200 KV with JEOL JEM 2000FX microscope equipped with an X-ray energy dispersive spectrometer (XEDS) LINKAN 10000.

2.5. *Schematic of Experimental Observation Needed for Models Derivations.* The material dealt with in this research had grains that were assumed to be initially closely spherical as

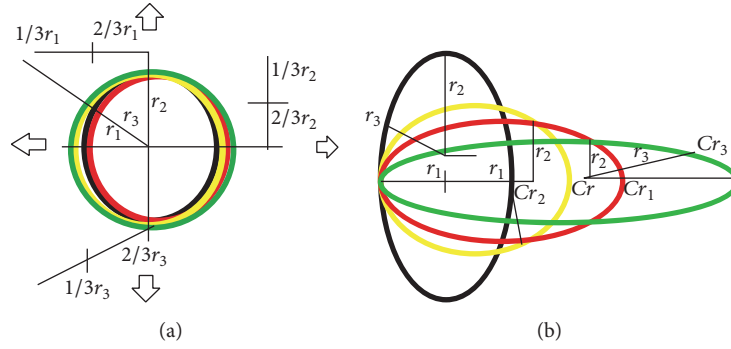


FIGURE 3: (a) Initially spherical grains before deformation and (b) elongated grains due to deformation.

shown in Figure 3(a). As the materials were subjected to deformation it was observed that the semimajor axis radius r_1 and major axis radius r_3 initially increased (as shown in Figure 3(b)) and then decreased since grain breakages took place in these directions. As a result of this repeated lengthening and grain breakage processes the effective lengths of r_1 and r_3 decreased during grain refinement. It was also observed during grain refinement that the equivalent radius axis r and semiminor axis radius r_2 decrease continuously. It was further observed that r_2 and r_3 evolved as proportions or fractions of r and r_1 , respectively.

2.6. Models Derivation. The model for grain elongation in 2D [12] can be modified to be applicable to 3D grain from the previous work of Sob et al. [13] for grain elongation in 2D to grain elongation in 3D grain by relating the cross-sectional area A of a 2D grain given in the previous model [12] from [13] to the volume in 3D grain of [13] since in 3D the density of a material is determined by its volume. This relationship is given as $A = V^{2/3}$. Thus the expression of elongation as defined by Nash [12] is modified to

$$\text{Elongation} = \frac{Pr_0}{V^{2/3}E}, \quad (1)$$

where r_0 is initial length, E is Young's modulus, and P is the applied force.

The model for Young's modulus (E) of nanomaterials as defined by Sob et al. [14] is given as

$$E = \left(\frac{P}{d}\right) \left(\frac{r^3}{192I}\right), \quad (2)$$

where it can be inferred that the moment of inertial is $I = \pi r_1^4/64$, $d = dr = (r - r_0)$, and r is length or equivalent radius of nanocrystalline grain.

It is experimentally observed during grain size evolution that at any instant the radii can be related to the equivalent volume of the grain through $(4/3)\pi r^3 = V = (4/3)\pi r_1 r_2 r_3$. This gives

$$r^3 = r_1 r_2 r_3. \quad (3)$$

By substituting expressions (2) and (3) into expression (1), the derived model of elongation for 3D grain is given as

$$\text{Elongation} = \frac{3\pi r_0 r_1^4}{r_2 r_3 r^3} (r - r_0). \quad (4)$$

By employing the different experimental observations for r , r_1 , r_2 , and r_3 during grain refinement, the following set of grain size variant evolutions (given in expressions (5)–(8)) were established for 3D grain as defined by Sob et al. [14] as follows.

Since r_1 increased and instantaneously decreased after breakage, the evolution of r_1 during grain refinement can be represented as

$$dr_1 = M \left(\frac{1}{r_{c1}} - \frac{1}{r_1} \right) dt + r_1^{1/2} D dW(t) - Z r_1 V_1 d(t), \quad (5)$$

where r_{c1} is local critical grain size, Z and D are constants, $dW(t)$ is change of the Wiener process, $V_1 = \tau_1 r_1^2$ defines rate of grain breakage, $M = M_0(1 + CD/r_1)$, $CD = 4(Hm)(h_0)/((k)(T))$, $T_m = T\{\ln(M_{o1}/M)\}$, and $M_0 = M_{O1} \exp\{(\ln)/T\}$ as given by [6, 10].

Since r_3 evolves (i.e., decreases) as a fraction or proportion (Ratio_1) of r_1 during grain refinement, r_3 can be represented by

$$dr_3 = \text{Ratio}_1 (dr_1). \quad (6)$$

Since equivalent radius r decreases continuously during grain refinement, r can be represented by

$$dr = -O r dt + I dW(t), \quad (7)$$

where O and I are constants.

For r_2 that evolves or decreases as a fraction (Ratio_2) of r during grain refinement, r_2 can be represented by

$$dr_2 = \text{Ratio}_2 (dr). \quad (8)$$

Moving now to other mechanical properties, the model of the yield stress given by Reversed Hall-Petch Relationship (RHPR) as modified by Zhao and Jiang [9] is given by

$$\sigma(r) = \sigma'_0 + A(r^{-1/2}) - B(r^{-1}) - C(r^{-3/2}), \quad (9)$$

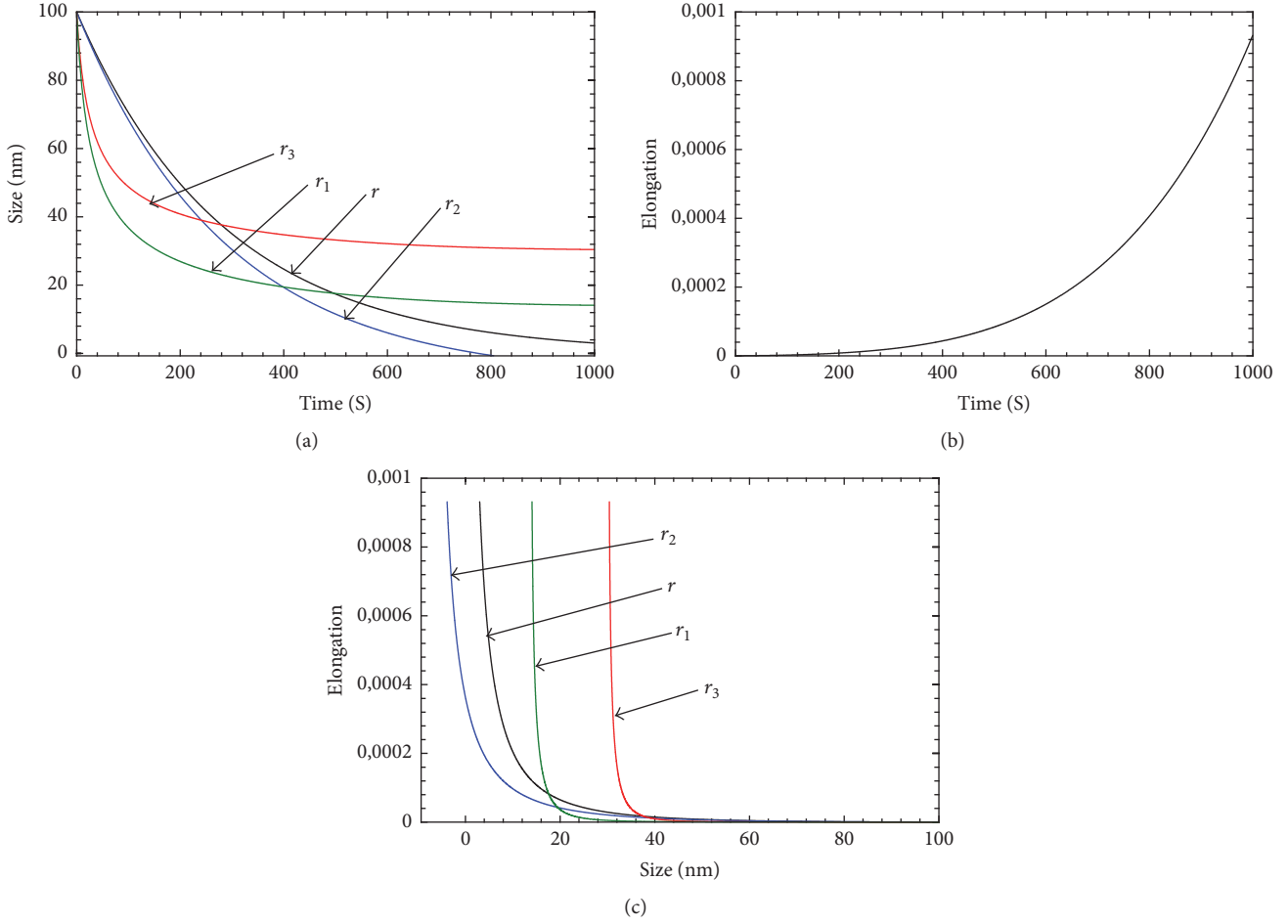


FIGURE 4: (a) Time evolution of size, (b) time evolution of elongation, and (c) evolution of elongation as function of size.

where $\sigma'_0 = \sigma_0 + K_t$ is bulk yield stress, $A = K_d$ is HPR proportionality constant, $B = K_t[2hH_m/RT_r]$, $C = K_d[2hH_m/RT_r]$, K_t is a constant, h is atomic diameter in the case of metal, H_m is the bulk melting enthalpy, R is ideal gas constant, and T_r is the room temperature, $K_d \gg 100K_t$ and $\sigma_0 \gg 10K_t$.

The models of strain evolution for nanocrystalline material for the different approaches of measuring grain size evolution given in expressions (5)–(8) as defined by Sob et al. [14] are as follows:

$$d\varepsilon_1 = d \left[\frac{dr_1}{r_1} \right]$$

$$= d \left(M \left(\frac{1}{r_{1c}} \right) \left(\frac{1}{r_1} \right) - \frac{1}{r_1^2} \right) dt + \frac{CDdW(t)}{r_1} - \frac{ZV_1r_1^2d(t)}{r_1},$$

$$d\varepsilon_3 = d \left[\frac{dr_3}{r_3} \right] = d \left(\frac{\text{Ratio}_1 dr_1}{r_3} \right),$$

$$d\varepsilon_r = d \left[\frac{dr}{r} \right] = d \left(\frac{-Ord t + IdW(t)}{r} \right),$$

$$d\varepsilon_2 = d \left[\frac{dr_2}{r_2} \right] = d \left(\frac{\text{Ratio}_2 dr}{r_2} \right). \quad (10)$$

Equations (1) to (10) are solved simultaneously using Engineering Equation Solver software (F-Chart Software, Madison, WI53744, USA) while employing the lognormal distribution of grain size.

3. Results and Discussion

To test the models proposed in this paper, the data from (nanocrystalline) aluminum sample (some of which are found in other papers [6]) are used, which are $M'_0 = 0.01 \text{ nm}^2 \text{ s}^{-1}$, $m = 4$, $CC = 12$, $a = 0.90$, $D = 10^{-4}$, $h_0 = 0.25 \text{ nm}$, $T_m(\infty) = 933.47 \text{ K}$, $CV_0 = 0.3$, $H_m(\infty) = 10.71 \text{ KJmol}^{-1}$, $\sigma'_0 = 16.7 \text{ MPa}$, $K_t = 1.3$, $\sigma_0 = 15.40 \text{ MPa}$, $K_d = 1301.77 \text{ MPa} \cdot \text{nm}^{1/2}$, $R = 8.31 \text{ JK}^{-1} \text{ mol}^{-1}$, and $T_r = 300 \text{ K}$. The additional data obtained for this work are $O = 0.0035$, $I = 1.1$, $r_{c1} = 1.95r$, $r_0 = 100 \text{ nm}$, $Z = 0.4$, $\text{Ratio}_1 = 0.81$, $\text{Ratio}_2 = 1.071$, and $\tau_1 = 0.000008$. The obtained results are presented in Figures 4(a), 4(b), and 4(c).

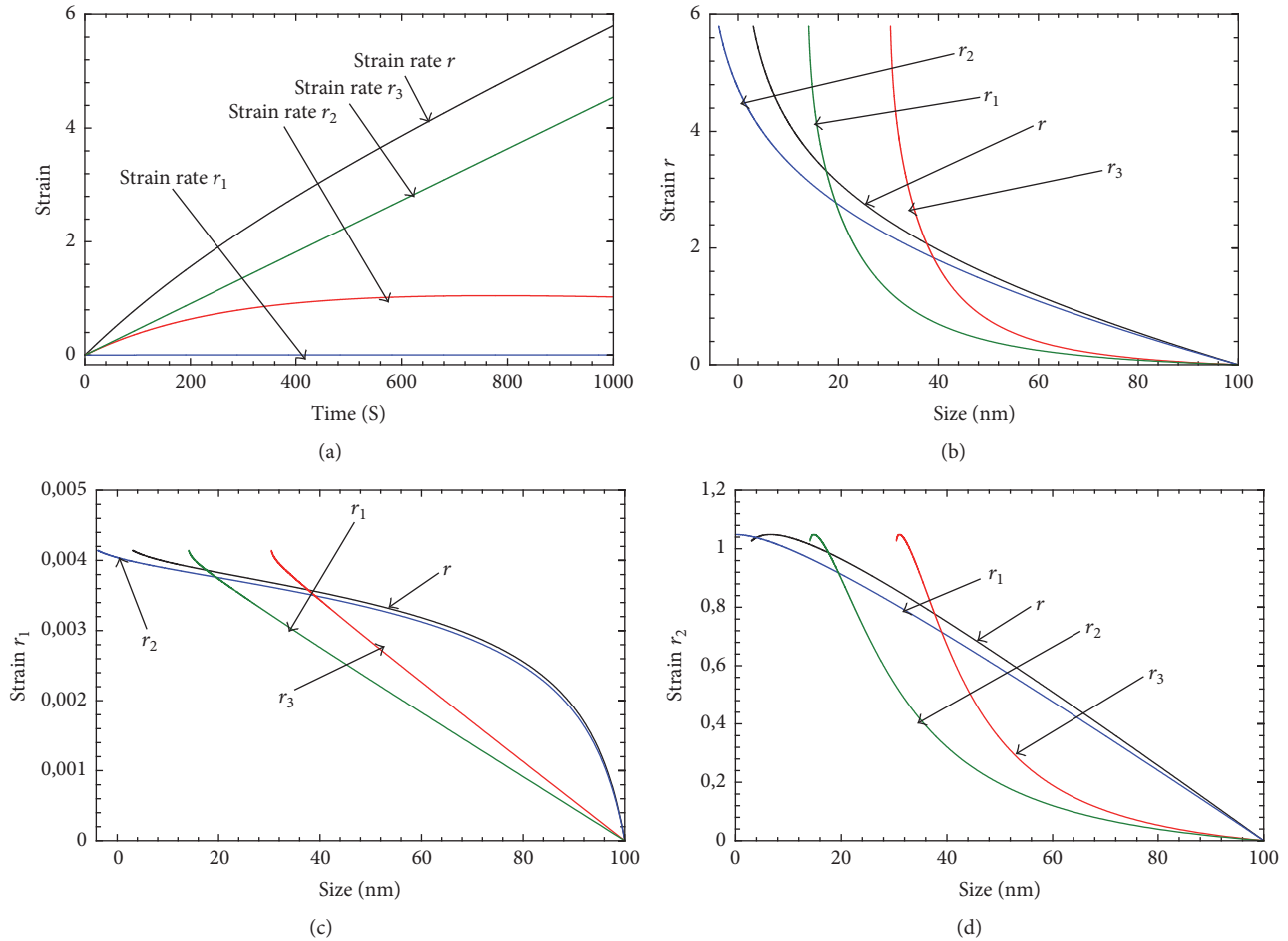


FIGURE 5: (a) Time evolutions of strains and ((b)-(d)) strain evolutions as functions of grain size variants (nm).

It should be observed from Figure 4(a) that the natures of decrease of the different approaches of measuring grain sizes are typical of experimental revelations of 3D grains. The different approaches of measuring grain size such as r_1 , r_2 , r_3 , and r have different characteristics and hence different properties (yield stress) due to different grain orientation and grain curvatures as shown in Figures 3(a) and 3(b). Since grain breakage rotation, grain migration, and grain rotation coalescence events take place during grain refinement by ARB and ECAP whose rates depend on grain curvature or elongation, different material yield stresses are being reported as shown in Figures 3(a) and 3(b). It should be observed from Figure 4(a) that r_2 decrease as lower value when compared to r throughout the deformation process, and, similarly, r_1 decrease as lower value when compared with r_3 throughout the deformation range. It was also observed that both r_1 and r_3 initially started with breakage and as such smaller grain sizes, which then lengthened and became larger than the sizes of r and r_2 . The increase in grain elongation with time as shown in Figure 4(b) or with decreasing grain size as shown in Figure 4(c) can be explained by the fact that, during grain refinement, new high angle grain boundaries are generated. It is noted further from Figure 4(c) that, depending on the approach of measuring grain size or observing the grain size,

the elongation values can become so large at larger grain size or the elongation values become larger at smaller grain size.

It is shown from Figure 5(a) that, at a time of, for example, 600 sec, different strains are obtained for the different approaches of measuring grain size. The nature of the evolution of strains depends on the direction along which the grain size is measured, as shown in Figures 5(b)–5(d). The reasons for this nature of evolution of strain values with respect to the different directions of observation (of the grain size) are that it was noted experimentally that, along the axial (r_1) and lateral (r_3) directions, both change-in-grain size and grain size varied proportionately with both either increasing or decreasing simultaneously, while, along the normal direction (r_2) or equivalent radius measured (r), the increasing change-in-grain sizes were accompanied by reductions in the grain sizes making the strains approach infinite values.

From Figure 6 it is observed that yield stress evolved as predicted by Hall-Petch to Reversed Hall-Petch Relationship (HPR-RHPR) when measured as functions of time, different approaches of measuring grain size, elongation, strain, and strain rate. The yield stress generally tended to increase with decreasing gain size since it is reported [14, 15] to be a result of dislocation motion from grain interiors to grain

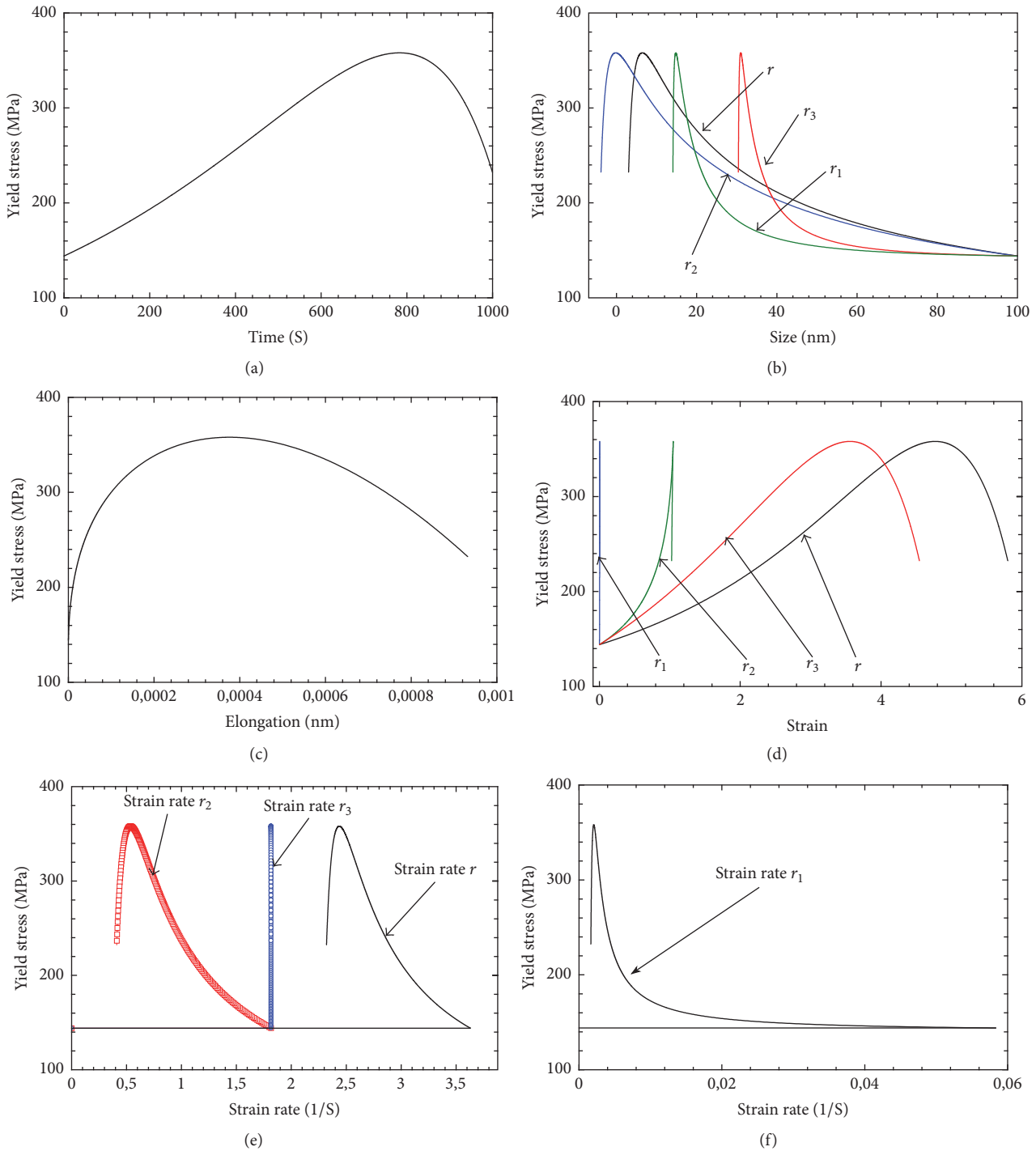


FIGURE 6: Plots of yield stress as a function of (a) time, (b) size, (c) elongation, (d) strain, and ((e)-(f)) strain rate.

boundaries and subsequent dislocation pile-ups at the grain boundaries. It was observed that, in the directions whereby the sizes increased and subsequently decreased due to grain breakage (i.e., r_1 and r_3), there were more material flow in those directions, which can without loss of generality be claimed that there were more dislocation motions and pile-ups towards those directions and hence more grain boundary

curvatures in those directions. As a result the yield stress when measured as a function of grain size and strain with size measured along the r_1 and r_3 directions show more rapid enhanced properties (see Figures 6(b) and 6(d)). Since elongation can be termed lengthening, it can be concluded that materials with elongated grains have more enhanced properties which rapidly drop with continuous lengthening

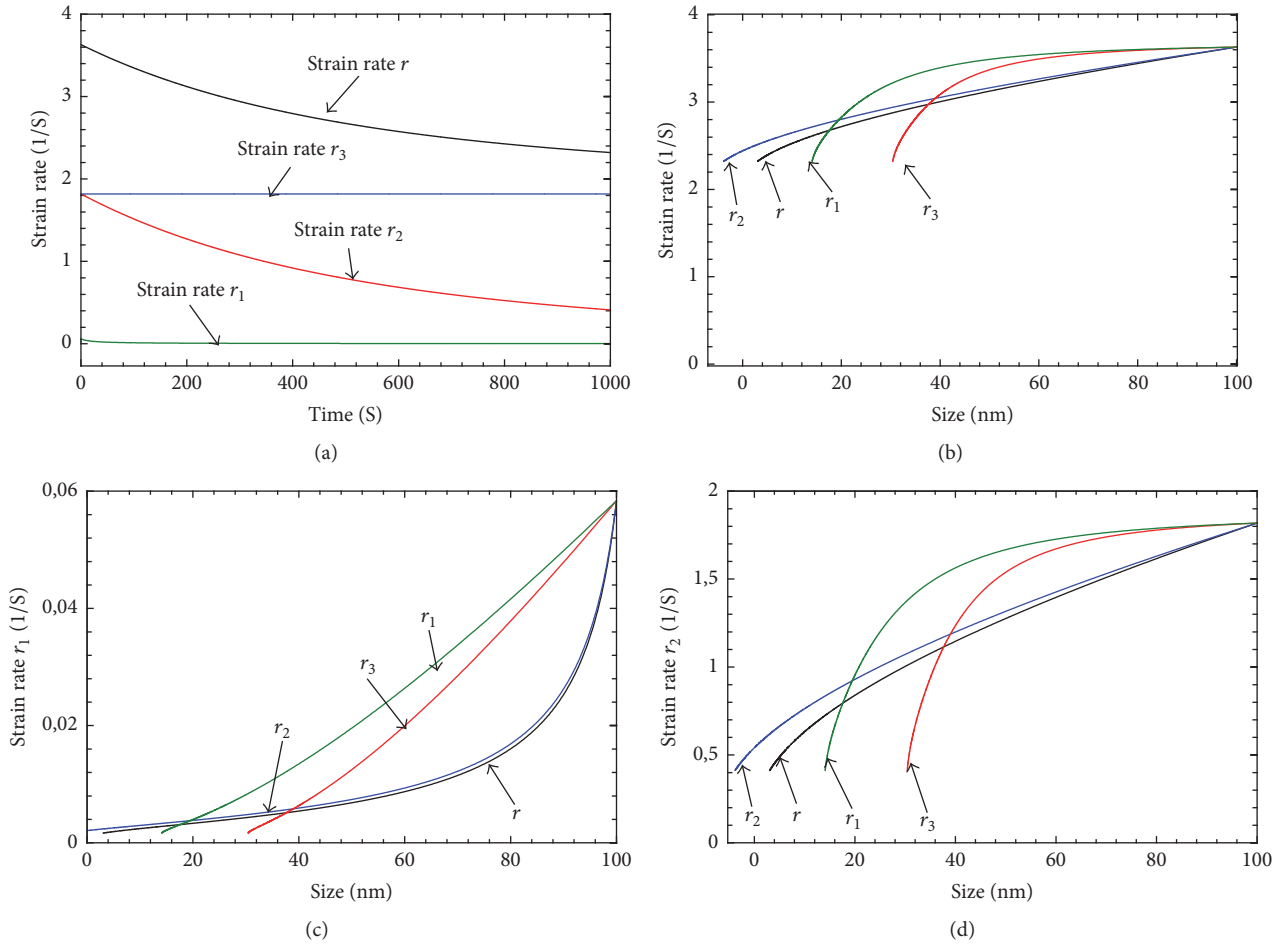


FIGURE 7: Plots of strain rate as a function of (a) time and (b)–(d) size (nm).

of grains, as revealed in Figures 6(b), 6(c), and 6(d) and for most ARB processes at rolling facilities. The reason for the subsequent decrease in yield stress with further decrease in grain size was that low plastic deformation occurred resulting in low materials hardness and properties. Extreme plastic straining led to distorted structures where the grain boundaries and grain curvatures were in “nonequilibrium” states. At these nonequilibrium states the grain boundaries and grain curvatures are characterized by more grain boundary energy, enhanced free volume, and the presence of long range elastic stresses [16].

Studying the effect of curvature on properties, reference is made to Figure 6(b). From the figure it is noted that, at grain size of 35 nm, the material has the most enhanced property (i.e., yield stress) for radius measured along r since the grain curvature of Cr is higher than the grain curvature of Cr_1 , Cr_2 , and Cr_3 at that 35 nm. When the material gets more refined at a size of 30 nm, the material has the most enhanced property for the radius measured along r_3 since grain curvature for Cr_3 is higher than the grain curvature of Cr_1 , Cr_2 , and Cr . Furthermore, it has been revealed as shown in Figure 6(b) that different critical grain sizes exist for r_1 , r_2 , r_3 , and r but give the same yield stress value at those different critical grain

sizes. It is observed from Figure 6(d) that the yield stresses for the grain size variants increase with increasing strains due to different misorientation angles and the grain curvatures (Cr_1 , Cr_2 , Cr_3 , and Cr) during grain deformation.

The different strain rates observed in Figures 6(e) and 6(f) have a general trend. This implied that in order to increase the material yield stress the rate of straining the material had to be reduced, similar to observations made by other researchers [16–18]. This is required so as to allow the material to relax and accommodate more plastic strain. Furthermore, it is observed that indefinite reduction in strain rate or feed rate does not lead to more property enhancement since it was becoming difficult for the material to be gripped by the rollers and get deformed. It was also noted that the rate of straining the material depended on the direction of observation or measuring the grain size. Figure 7 shows that in order to have more grain refinements the strain rates have to be decreased.

4. Conclusions

The current work was aimed at investigating the impacts of elongation or grain shapes on nanomaterials properties. To achieve that, the model for elongation that has been

previously given for 2D was modified to be applicable to 3D grains. Furthermore, the stochastic natures of the grain size variants (i.e., different approaches of measuring or observing grain sizes) were also taken into consideration.

It was observed that the stochastic effect of grain elongation led to different mechanical properties when studied as functions of different grain size variants due to different grain curvatures. It was shown that the properties varied in different ways with equivalent radius, semiminor axis radius, semimajor axis radius, and major axis radius. The present analysis revealed that the material has the most enhanced property for radius measured with higher grain curvature and less enhanced property for radius with low grain curvature. It has also been revealed that in order to increase the material yield stress the rate of straining the material has to be reduced. It was also observed that materials with elongated grains have more enhanced properties that rapidly drop with continuous lengthening of grains. The present analysis for 3D grain shows more properties for nanomaterials that were not revealed from the models that dealt only with the equivalent radius. These findings provide valuable insights into the possibility of tailoring sample dimensions to elicit desired property.

Disclosure

The abstract of this manuscript was approved at the international conference of composites materials held in Istanbul 2015 but the full paper was not submitted for journal consideration at the conference.

Conflicts of Interest

The authors declare that they have no conflicts of interest.

Acknowledgments

This paper is based on the work which is supported financially by the National Research Foundation (NRF) and Vaal University of Technology (VUT).

References

- [1] Y. Estrin and A. Vinogradov, "Extreme grain refinement by severe plastic deformation: a wealth of challenging science," *Acta Materialia*, vol. 61, no. 3, pp. 782–817, 2013.
- [2] M. Saravanan, R. M. Pillai, B. C. Pai, M. Brahmakumar, and K. R. Ravi, "Equal channel angular pressing of pure aluminium-an analysis," *Bulletin of Materials Science*, vol. 29, no. 7, pp. 679–684, 2006.
- [3] N. Tsuji, Y. Saito, S.-H. Lee, and Y. Minamino, "ARB (accumulative roll-bonding) and other new techniques to produce bulk ultrafine grained materials," *Advanced Engineering Materials*, vol. 5, no. 5, pp. 338–344, 2003.
- [4] A. Rosochowski, L. Olejnik, J. Richert, M. Rosochowska, and M. Richert, "Equal channel angular pressing with converging billets-experiment," *Materials Science and Engineering A*, vol. 560, pp. 358–364, 2013.
- [5] M. Hillert, "On the theory of normal and abnormal grain growth," *Acta Metallurgica*, vol. 13, no. 3, pp. 227–238, 1965.
- [6] T. B. Tengen, *Analysis of Characteristic of Random Microstructures of Nanomaterials [PhD. Thesis]*, Witwatersrand Johannesburg, 2008.
- [7] E. O. Hall, "The deformation and ageing of mild steel: III discussion of results," *Proceedings of the Physical Society Section B*, vol. 64, no. 9, pp. 747–753, 1951.
- [8] N. J. Petch, "The cleavage strength of polycrystals," *Journal of the Iron and Steel Institute*, vol. 174, pp. 25–28, 1953.
- [9] M. Zhao and Q. Jiang, "Reverse hall-petch relationship of metals in nanometer size," in *Proceedings of the 2006 IEEE Conference on Emerging Technologies—Nanoelectronics*, pp. 472–474, Singapore, January 2006.
- [10] T. B. Tengen, T. Wejrzanowski, R. Iwankiewicz, and K. J. Kurzydowski, "Stochastic modelling in design of mechanical properties of nanometals," *Materials Science and Engineering A*, vol. 527, no. 16-17, pp. 3764–3768, 2010.
- [11] M. Lewandowska, "Malgorzata lewandowska: fabrication methods of nanomaterials," in *Structure and Properties of Nanomaterials*, pp. 1–54, 2006.
- [12] W. A. Nash, *Strength of Materials*, McGraw-Hill, New York, NY, USA, 4th edition, 1998.
- [13] P. B. Sob, A. A. Alugongo, and T. B. Tengen, "Stochastic effect of grain elongation on nanocrystalline material yield stress produced by accumulative roll bonding," in *Proceeding of the 9th South African Conference of Computational and Applied Mechanics (SACAM '14)*, Somerset West, South Africa, 2014.
- [14] P. B. Sob, A. A. Alugongo, and T. B. Tengen, *Modelling Strain Rate Sensitive Nanomaterials Mechanical Properties: The Effects of Varying Definition. MTECH, [MS thesis]*, Vaal University of Technology, Vanderbijlpark, South Africa, 2016.
- [15] G. Wang and L. Xiaodong, "Predicting the young's modulus of nanowire from first principle calculations on their surface and bulk materials," *Journal of Applied Physics*, vol. 104, no. 11, Article ID 113517, pp. 1–33, 2008.
- [16] K. M. Rahman, V. A. Vorontsov, and D. Dye, "The effect of grain size on the twin initiation stress in a TWIP steel," *Acta Materialia*, vol. 89, pp. 247–257, 2015.
- [17] L. S. Toth and C. Gu, "Ultrafine-grain metals by severe plastic deformation," *Materials Characterization*, vol. 92, pp. 1–14, 2014.
- [18] I. Sabirov, M. R. Barnett, Y. Estrin, and P. D. Hodgson, "The effect of strain rate on the deformation mechanisms and the strain rate sensitivity of an ultra-fine-grained Al alloy," *Scripta Materialia*, vol. 61, no. 2, pp. 181–184, 2009.

Research Article

Experimental and Numerical Evaluation of Rock Dynamic Test with Split-Hopkinson Pressure Bar

Kang Peng,^{1,2} Ke Gao,³ Jian Liu,³ Yujiao Liu,³ Zhenyu Zhang,^{1,2} Xiang Fan,⁴ Xuyan Yin,¹ Yongliang Zhang,⁵ and Gun Huang^{1,2}

¹State Key Laboratory of Coal Mine Disaster Dynamics and Control, Chongqing University, Chongqing 400044, China

²College of Resources and Environmental Science, Chongqing University, Chongqing 400030, China

³College of Safety Science and Engineering, Liaoning Technical University, Liaoning 125105, China

⁴School of Highway, Chang'an University, Xi'an 710064, China

⁵Automotive School, Qingdao Technological University, Qingdao, Shandong 266520, China

Correspondence should be addressed to Kang Peng; pengkang@cqu.edu.cn

Received 12 January 2017; Revised 4 May 2017; Accepted 14 May 2017; Published 12 June 2017

Academic Editor: Francesco Caputo

Copyright © 2017 Kang Peng et al. This is an open access article distributed under the Creative Commons Attribution License, which permits unrestricted use, distribution, and reproduction in any medium, provided the original work is properly cited.

Feasibility of rock dynamic properties by split-Hopkinson pressure bar (SHPB) was experimentally and numerically evaluated with ANSYS/LS-DYNA. The effects of different diameters, different loading rates, and different propagation distances on wave dispersion of input bars in SHPB with rectangle and half-sine wave loadings were analyzed. The results show that the dispersion effect on the diameter of input bar, loading rate, and propagation distance under half-sine waveform loading is ignorable compared with the rectangle wave loading. Moreover, the degrees of stress uniformity under rectangle and half-sine input wave loadings are compared in SHPB tests, and the time required for stress uniformity is calculated under different above-mentioned loadings. It is confirmed that the stress uniformity can be realized more easily using the half-sine pulse loading compared to the rectangle pulse loading, and this has significant advantages in the dynamic test of rock-like materials. Finally, the Holmquist-Johnson-Concrete constitutive model is introduced to simulate the failure mechanism and failure and fragmentation characteristics of rock under different strain rates. And the numerical results agree with that obtained from the experiment, which confirms the effectiveness of the model and the method.

1. Introduction

Understanding the dynamic characteristics of rocks under higher strain rate is significant for either engineering stability or rock fragmentation efficiency. Since the first use of split-Hopkinson pressure bar (SHPB) system by Kolsky (1949), extensive studies have been performed to investigate dynamic mechanical properties of different materials. So far, SHPB experimental technique has been widely used in geotechnical evaluations and substantial efforts have been made to study dynamic mechanical properties of rocks [1–9]. The result shows that the dynamic compressive strength and dynamic tensile strength of lands measurement using SHPB are valid and reliable by Dai et al. [10]. Currently, there is an increasing demand for better experimental equipment and higher experimental accuracy on this aspect. Numerical

simulation is an important way to improve and optimize the SHPB experimental technique. Firstly, the SHPB experiment technology can be perfected and supplemented by using numerical simulation. The sensitivity coefficient of the strain gauge attached to SHPB bars needs to be statically calibrated prior to relevant tests. By comparing the accurate numerical result with the experimental waveform, the coefficient can be obtained to reduce the number of errors. Xu et al. confirmed the validity of this DEM model to reproduce the dynamic fracturing and the feasibility to simultaneously measure key dynamic rock fracture parameters, including initiation fracture toughness, fracture energy, and propagation fracture toughness [11]. The damage and rupture process of coal-rock is accompanied by acoustic emission (AE) by Wen et al. [12]; the results show that coal-rock's size influences the uniaxial compressive strength, peak strain, and elastic modulus of



FIGURE 1: Striker of SHPB measurement equipment (φ , 50 mm).

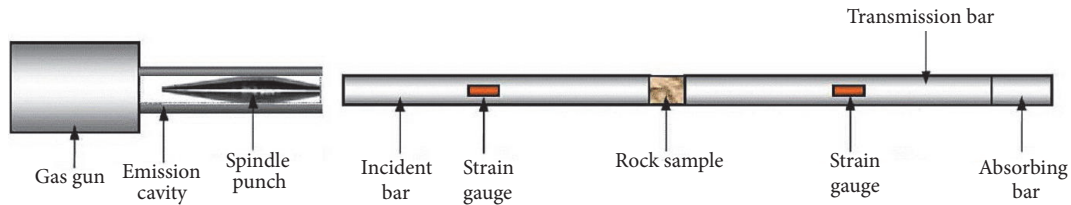


FIGURE 2: Typical SHPB testing device.

itself. Assessing via discrete element method shows that the loading-rate-dependent cracking profiles of chevron-notched specimens cannot be ignored in order to determine accurately the fracture toughness of rock in dynamic mode I [13]. The bedding effect on the coal behavior at static strain rate is more prominent than that at dynamic strain rate [14]. A two-dimensional axisymmetric numerical analysis is used to compute all components of the stress, strain, and strain rate tensors at each mesh point within the specimen and the elastic bars by Bertholf and Karnes [15]. The result shows that inertia and friction between the specimen and the elastic bars affected the response of specimen differently because of different length-to-diameter ratios, and serious stress and strain nonuniformity exists when the ends are not lubricated. To efficiently study and analyze the mechanism behind major stope disasters, a method based on monitoring the stress and displacement of stopes was adopted, and a method of ascertaining stope stability based on qualitative identification of the dynamics was further proposed. At the same time, the relations and differences between rockburst in the coal mine and rockburst in the metal mine were studied. Coal mine rockburst is divided into two types: static loading type during roadway excavation process and dynamic loading type during mining face advancing [16–18]. Secondly, the shape of the pulse and the materials of the bars have attracted attention recently [19, 20]. The result shows that, by virtue of the ramped wave loading, the force equilibrium of the specimen can be effectively achieved and the rupture is precisely measured to synchronize with the peak force, both of which guarantee the quasi-static data reduction method employed to determine the dynamic flexural strength by Xu et al. [21]. A series of rock cutting tests were performed to investigate the influence of back rake angle on the critical failure mode transition depth by Zhou et al. [22]. It is found that the critical failure mode transition depth increases with the back rake angle. This suggests that the brittle fracture failure induced at large depth of cut can be inhibited by increasing the back rake angle. Cutting at a small back rake

angle, on the other hand, is desirable if minimization of the cutting energy is required in the application.

Although the results of numerical simulation demonstrate that rectangular wave and trapezoidal wave applied performed perfectly, simulation analysis was still complicated. It barely takes action to load with sine wave. In this study, the dynamic compressive properties of rocks were experimentally and numerically evaluated using ANSYS/LS-DYNA. And for numerical simulation analysis, an approach, which uses sine wave, was put into use.

2. Experimental Apparatus

2.1. Impact Ram. The rectangular waveform loading was adopted in the conventional SHPB experiment on rocks, and the obtained curves were smoothly processed. However, large experimental errors exist for rock-like materials [7]. In order to eliminate this error, Li et al. [23, 24] proposed a half-sine waveform loading instead of the conventional rectangular waveform loading in SHPB tests. The novel striker (Figure 1) was designed by back-design method and Numerical Simulation Software [8, 25–28], whose material is the same as the bars.

2.2. Experimental Apparatus and Principle. A typical test system consists of a gas gun, an input bar, an output bar, and the specimen as shown in Figure 2. Figure 3 shows the sketch of the experiment devices.

When the striker impacts the free end of the input bar, an elastic compressive stress pulse is produced which propagates in the input bar toward the specimen. When the pulse reaches the specimen, it is partially reflected, with one part back into the input bar and the rest transmitted into the output bar through the specimen.

3. Computational Model and Method

3.1. FEM Model. In the SHPB apparatus, the bars and specimens are designed into cylinders, and they are coaxial.



FIGURE 3: The sketch of the experiment devices (1, stress transfer device, 2, axial compression load outreach framework, 3, axial compression loading device, and 4, bearing of the axial compression loading outreach framework).

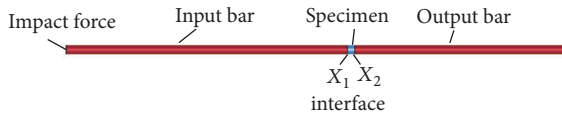


FIGURE 4: Modeling of the SHPB apparatus.

The input and output bars are made by 40 Cr alloy and the length is 200 mm and 150 mm, respectively. The diameter and the length of the specimens can be changed according to different needs. Surface contacts are adopted between bars and specimens on condition that the effect of friction is neglected.

3.2. Numerical Modeling Development. The model is discretized by three-dimensional 8-node elements with reduced integration and hourglass control (SOLID164). Totally, 37042 elements and 46293 nodes are constructed in the model (Figure 4), 21600 elements for the input bar, 16200 elements for the output bar, and 1080 elements for the specimen.

3.3. Computational Method. Because the yield strength of the Hopkinson bars outclasses that of specimen, the finite element models of the Hopkinson bars are assumed to be a linear elastic material. Poisson ratio, density, and elastic modulus for the bars are 0.30, 7795 kg/m³, and 210 GPa, respectively.

Rock is a typical quasi-brittle, flaws-embedded material. The deformation failure of rock is usually accompanied with nonuniform, noncontinuous, and large deformation which makes it a very complex highly nonlinear problem because of the particularity and complexity of the rock material.

The Holmquist-Johnson-Concrete constitutive equation is used to model rock-like material in the finite element simulation, which makes it possible to simulate large strains,

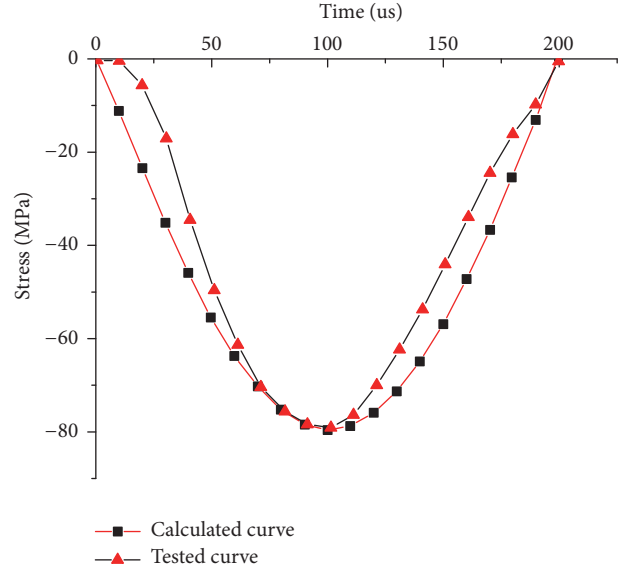


FIGURE 5: The incident pulse.

TABLE I: Mechanical properties of the rock.

| Properties | value |
|-------------------------------------|----------------------|
| Type of rock | Sandstone |
| ρ (kg/m ³) | 2630 |
| G /GPa | 6.00 |
| A | 0.71 |
| B | 1.84 |
| C | 0.007 |
| N | 1.00 |
| $\dot{\epsilon}_0$ /s ⁻¹ | 2.9×10^{-5} |
| ϵ_{fmin} | 0.01 |
| S_{max} | 5.0 |
| P_{cr} /GPa | 0.035 |
| μ_{cr} | 8.0×10^{-4} |
| P_{lock} /GPa | 1.035 |
| μ_{lock} | 0.100 |
| D_1 | 0.045 |
| D_2 | 1.00 |
| Tensile strength/MPa | 13.8 |
| f_c /MPa | 91.36 |
| K_1 /GPa | 85 |
| K_2 /GPa | -171 |
| K_3 /GPa | 208 |

A : standard cohesion strength; B : standard pressure hardening coefficient; C : the coefficient of strain rate; N : pressure hardening index; D_1/D_2 : damage constant; P_{cr}/P_{lock} : Elastic peak point/the pressure of crack compaction point; μ_{cr}/μ_{lock} : bulk strain; K_1 , K_2 , and K_3 : rock constant; f_c : compressive strength; S_{max} : ultimate strength; ϵ_{fmin} : the minimum tensile strain at break; $\dot{\epsilon}_0$: reference rate of strain.

high strain rates, and high pressure in rock-like materials. Mechanical properties used for the specimens are listed in Table 1 [29].

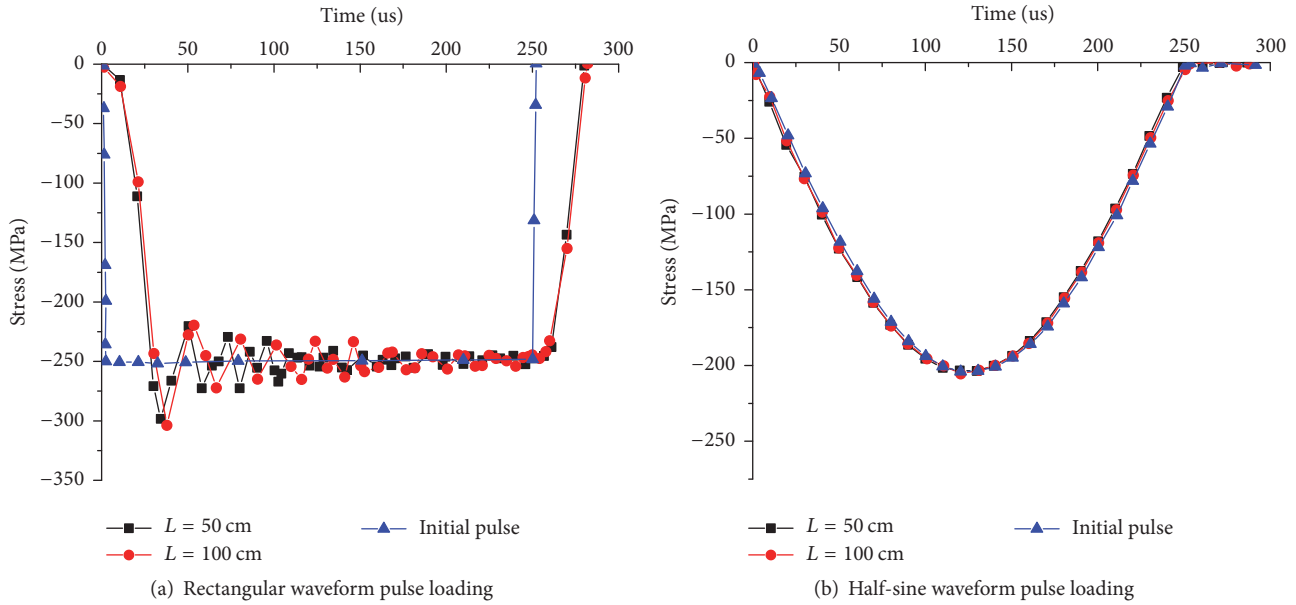


FIGURE 6: Time-history of stress pulses at different propagation distances (L) away from the impact end of the input bar.

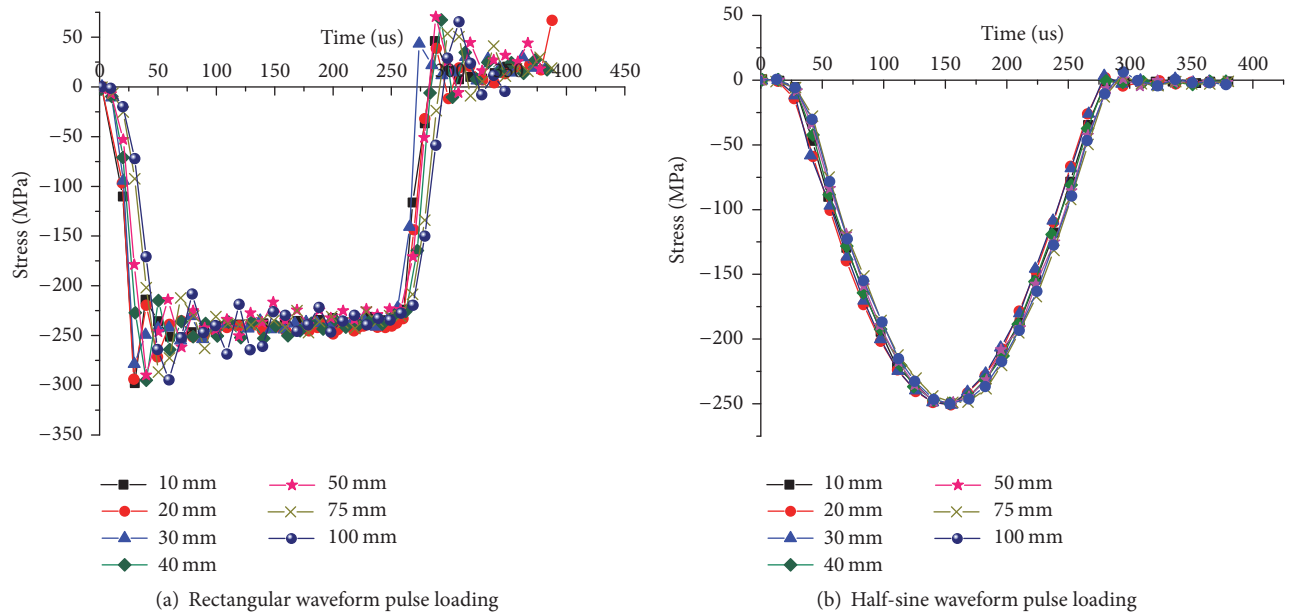


FIGURE 7: Time-history of stress pulses at different diameters ($L = 100$ mm).

3.4. Loading and Constraint. The constraint is applied on the symmetrical surfaces. The axial constraint is applied on the center nodes of the bars and specimens. Other surfaces of the coaxial system of the model are all stress-free.

In the SHPB test, the incident pulse is normally provided by the effect of a striker on the incident bar. The incident wave is determined by the shape of the striker. While the length of the striker can change that of the incident pulse, it has limited impact on the incident wave. In order to easily control the waveform and facilitate the analysis, the direct

stress loading mode, pulse duration, and stress amplitude are designed for different needs (Figure 5). In this study, two waveforms, rectangular waveform and half-sine waveform, are used for analogy calculation.

4. Results and Analysis

4.1. The Choice of the Rational Waveform Loading of Rock with SHPB. In order to investigate the rational waveform loading of rock with SHPB, both rectangle and half-sine

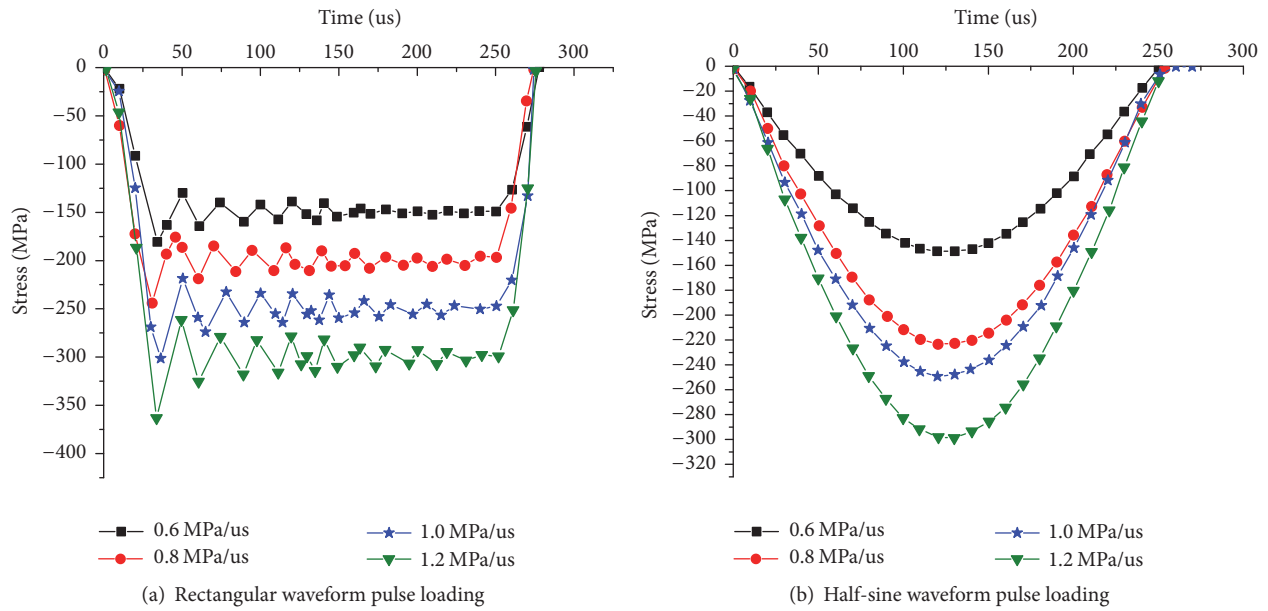


FIGURE 8: Time-history of stress pulses at different loading rates.

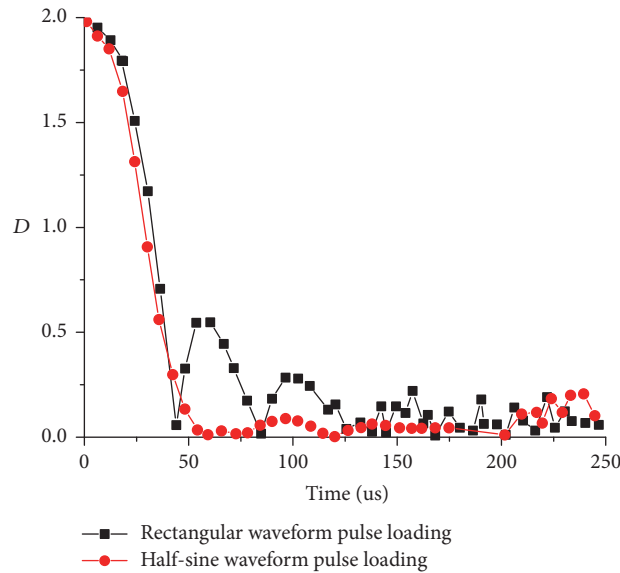


FIGURE 9: Variation curve of stress equilibrium equations factor (the diameter is 50 mm, and the length-diameter ratio of specimen is 1).

waveform loadings are chosen. The wave dispersion and the stress uniformity process under two input wave loadings are analyzed by conducting large-diameter SHPB test.

4.1.1. Numerical Analysis of Wave Dispersion. It is shown that the dispersion phenomenon occurs when the stress pulse transmits along the input bar in conventional SHPB, which can cause severe oscillation of the ultimate dynamic constitutive response of materials [7, 15, 30, 31]. Merle and Zhao suggest a correct method, which can find potential error of frequency components [32]. Zhao and Gary proposed a direct calculation of dispersion relations, which can

accurately analyze the dispersion effect and not consider the stress uniformity [33]. To study the influence of wave dispersion on the stress distribution across the bar section at different radii (10 mm, 20 mm, 30 mm, 40 mm, 50 mm, 75 mm, and 100 mm), the stress distribution in input bar (2.0 m in length) under different loadings was numerically analyzed. The material parameters used in the finite element model (Figure 4) for the bar are listed in Table 1. The time-stress curves are recorded at two positions which are 50 cm and 100 cm from the loading interface, respectively.

Figure 6 shows typical stress pulses recorded under both rectangle and half-sine waveform loadings. It is apparent

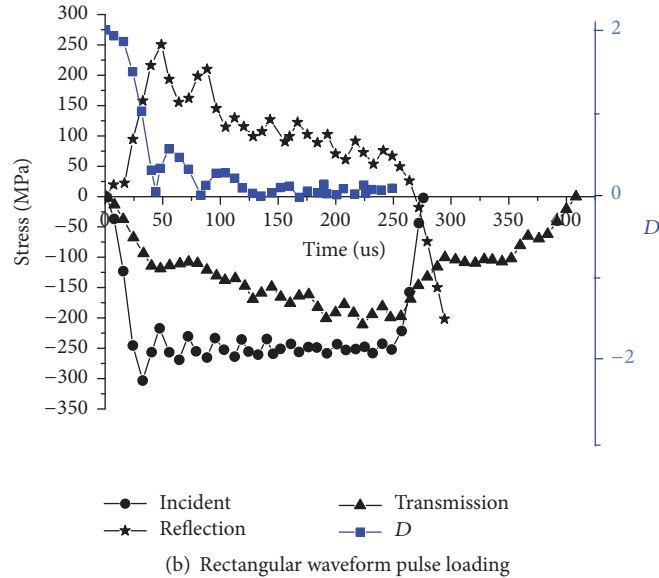
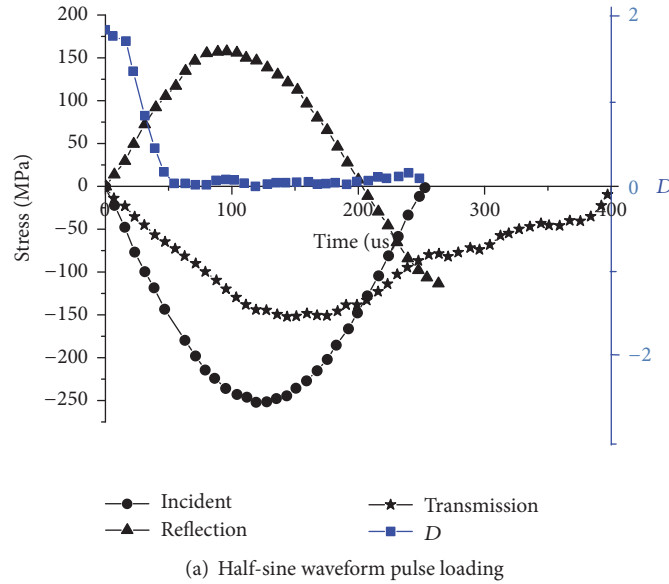


FIGURE 10: Stress pulses and stress equilibrium equations factor.

that both the rise time of the stress front and oscillation amplitude increased with the wave propagation distance as shown in Figure 6(a), and the high frequency oscillations and oscillation amplitude of wave became stronger with the increase of bar diameter.

It is also shown in Figure 7 that the higher the loading rate is, the more serious the P-C oscillation is, thus making it impossible to obtain proper dynamic mechanical properties. However, the oscillation can be eliminated when the half-sine waveform pulse is loaded (see Figure 8), and there was absence of oscillation in the incident wave with the range of loading rate.

The reason of the dispersion phenomenon is that rectangular wave is of many different frequencies and harmonics.

Supposing that the time period is τ , which denotes the rectangular wave, the formula can be expanded to the following equation according to Fourier class [34]:

$$\sigma_{\tau}(t) = \frac{4}{\pi} \sum_{i=1}^n \sin \left[\frac{2i-1}{\tau} \pi t \right] \quad i = 1, 2, \dots, n \quad (1)$$

$$w_i = \frac{(2i-1)}{\tau} \pi \propto f \left(\frac{1}{\lambda_i} \right).$$

For this waveform, even the front main harmonic can guarantee that $r/\lambda \leq 1$ ($i = 1, 2, \dots, k$); there will always be numerous high-harmonic items behind, where velocity $c_p < c_0$ will occur at the time of high-frequency items; then

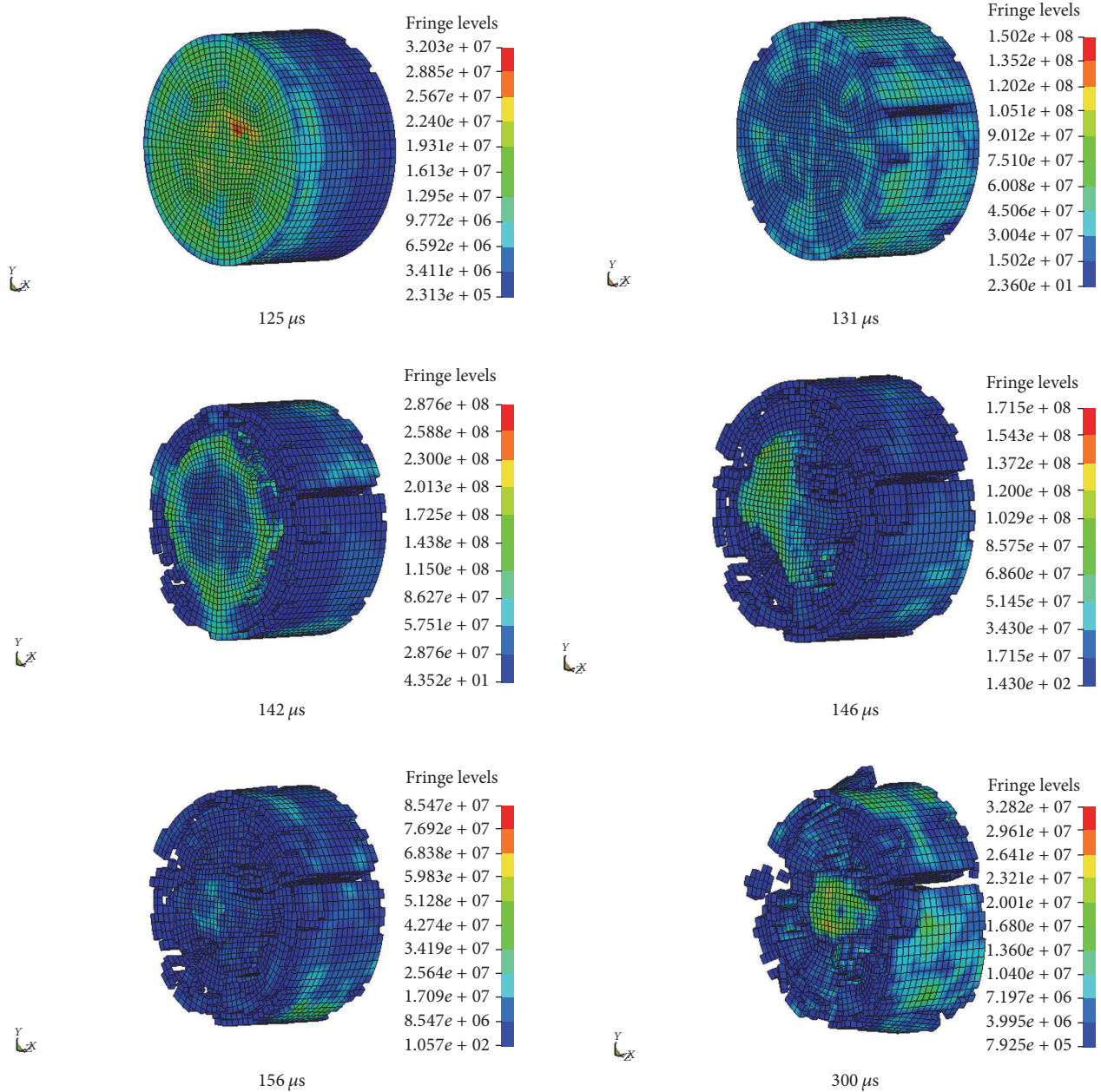


FIGURE 11: Numerical fracture process (the average strain rate is 52 s^{-1}).

during the rod transmission process, it will certainly lead to the high-frequency dispersion at the first part of the wave. Meanwhile the single-frequency half-sine waves, as long as the bar radius meets the one-dimensional stress conditions (when $r/\lambda \ll 1$, $c_p \approx c_0$, that is, to meet the one-dimensional stress conditions), will not produce geometric dispersion during the wave propagation.

4.1.2. *Correlation between the Stress Uniformity and the Incident Pulse.* Accuracy of the SHPB test is based on the assumption of stress and strain uniformity within the specimen, which, however, is not always satisfied in an actual

SHPB test due to the existence of some unavoidable negative factors, for example, friction and specimen size effects.

To quantify the stress uniformity process, the coefficient of the axial stress uniformity, which was proposed by Zencker and Clos [35], is defined as

$$D = 2 \left| \frac{\sigma_z^{(a)} - \sigma_z^{(b)}}{\sigma_z^{(a)} + \sigma_z^{(b)}} \right|, \quad (2)$$

where $\sigma_z^{(a)}$ and $\sigma_z^{(b)}$ describe the stress at X_1 -interface and X_2 -interface of specimen, respectively.

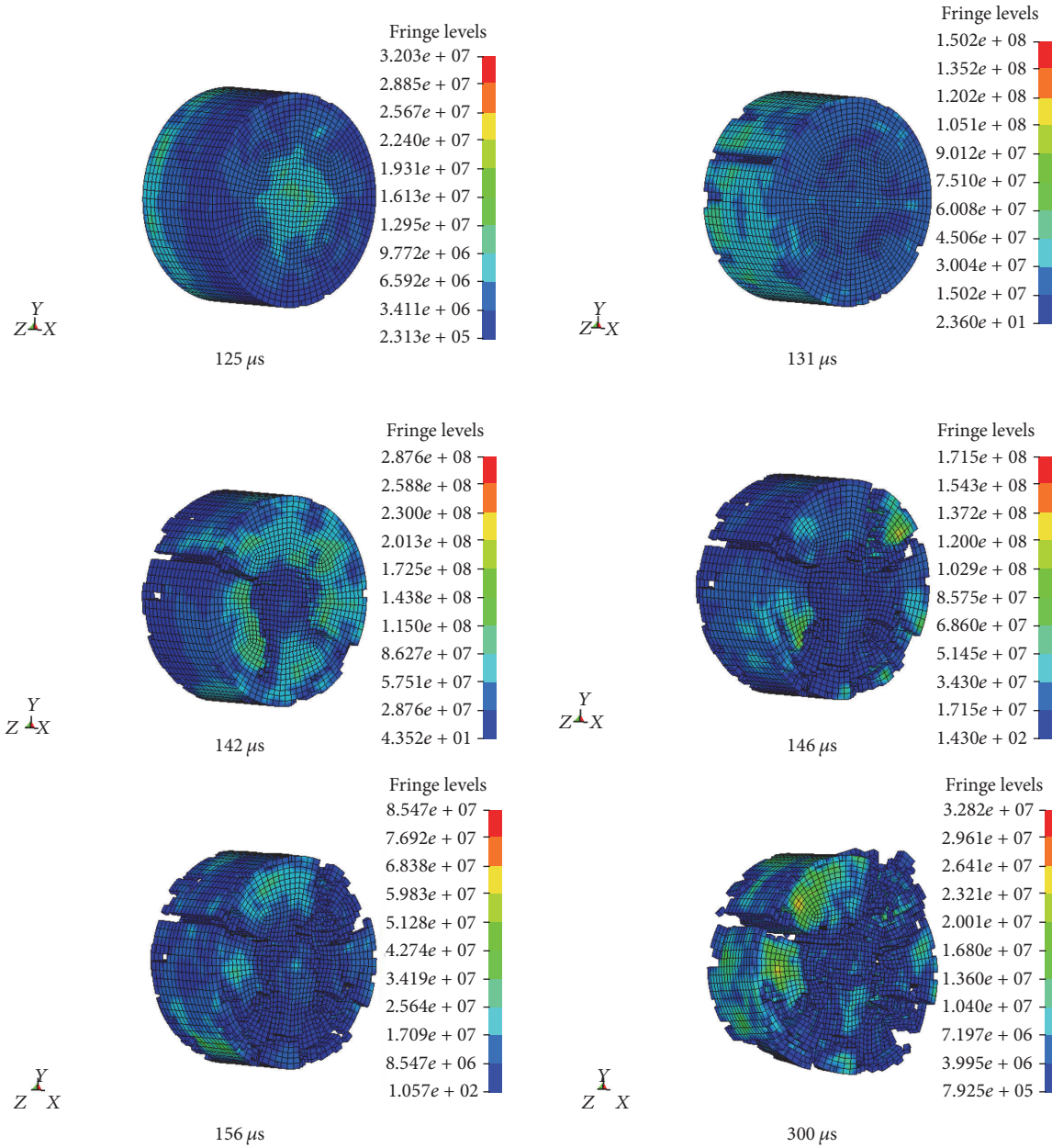


FIGURE 12: Numerical fracture process (the average strain rate is 52 s^{-1}).

Figure 9 presents a typical curve of stress equilibrium equations factor versus loading time received in this study by using pulse shaping technique. If $D \leq 0.05$, as can be seen from Figure 9, the stress within the specimen is uniform at 50 μs when the half-sine waveform loading is adopted. When it is assumed that the failure strain is 5000 μs at 100/s for rock, the total loading time before the failure is 100 μs . It is clear that the stress distribution along the radius is uniform during the loading period, which is very important for SHPB experiment. While the rectangular waveform loading is adopted, good equilibrium effect is achieved when the time is above 125 μs after the stress reaches its maximum (Figure 10).

4.2. Numerical Analysis on the Failure Process of Rock. The mechanical behavior of rock, including its fracture characteristics, has become more and more important in recent years [36].

The pressure loading shape is half-sine. The stress level is 150 MPa and 250 MPa, respectively. The rising is 125 μs , and the duration is 250 μs . The tensile stress of 13.8 MPa is set as failure point of the element in numerical simulation. The rock is gripped between incident bar and transmission bar, and the process of damage of the specimen is shown in Figures 11, 12, 13, and 14. It is clear that its main damage is mostly in the form of tensile splitting failure along the axial direction. There was no damage in the front-end unit of specimen in

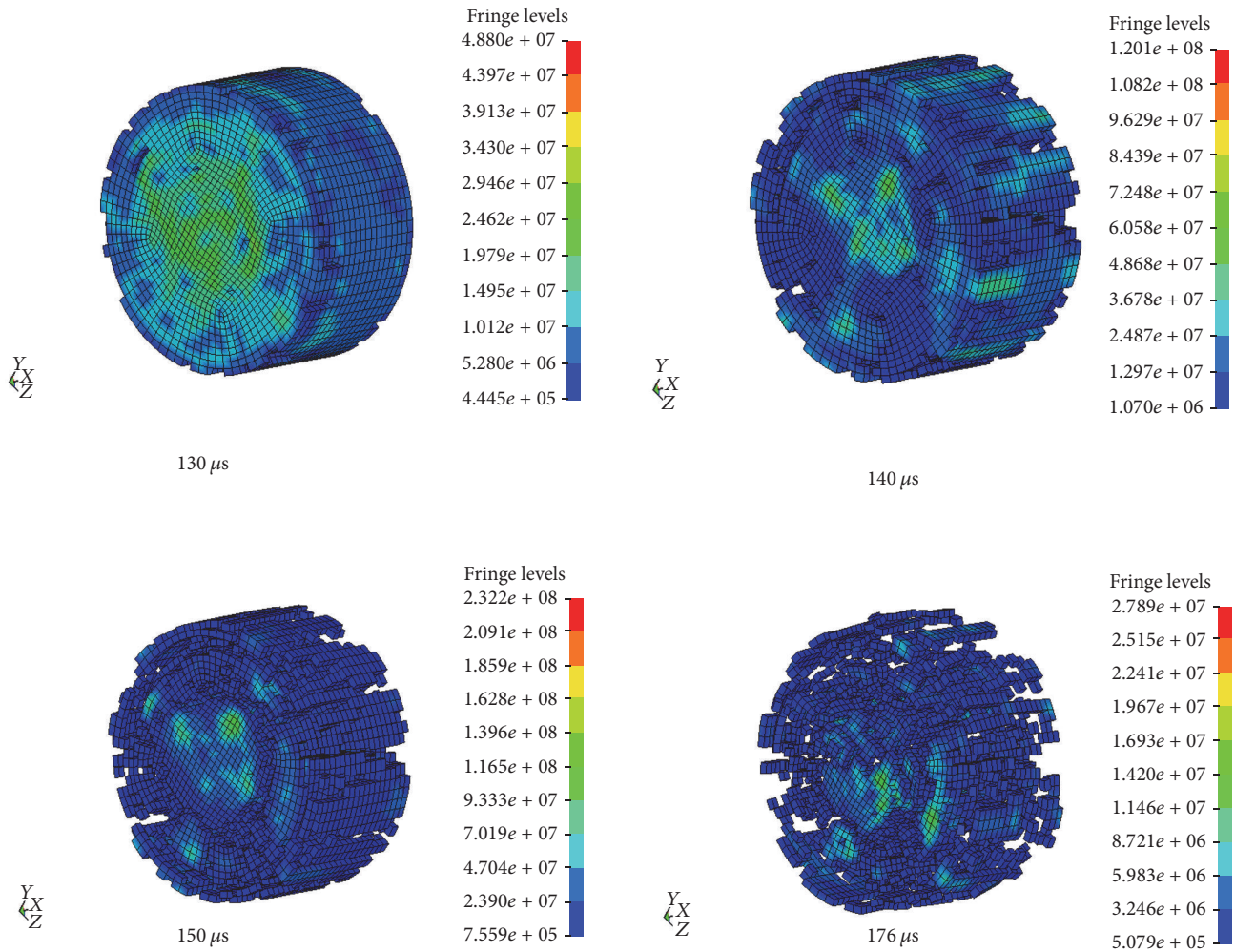


FIGURE 13: Numerical fracture process (the average strain rate is 130 s^{-1}).

the initial loading stage, while some cracks developed at some certain locations, such as the sides, finally leading to specimen collapse. This is because the lateral face is free; when the compression wave converts into tensile wave after reflection, it easily leads to tensile failure for rock-like material, even if the tension is not so strong.

It is also observed from numerical results that the failure modes transformed from fragmentation to pulverization. With the increase of strain rate, the number of broken pieces increased, as shown in Figure 13. Figure 14 summarizes the process of damage in high-speed photographs for SHPB experiments, and it is evident that the main crack orientation is axial, that is, parallel to the direction of wave propagation.

Figures 15 and 16 show the photos of failure modes of specimens, which are similar to the simulation results (Figures 11 and 13). The failure strength (as can be seen from the stress versus strain profiles in Figure 17) of rock is shown to have positive strain rate sensitivity. These results are satisfactory, showing the strain rate's effect on the degree of fragmentation accurately.

5. Conclusions

Feasibility of rock dynamic properties by split-Hopkinson pressure bar (SHPB) was experimentally and numerically evaluated with ANSYS/LS-DYNA.

It is found that the time required to achieve a uniform stress state in a specimen for the half-sine incident pulse is noticeably shorter than that for the perfectly rectangular incident pulse. Therefore, the half-sine wave is an optimum incident pulse shape that can make the measured data reliable and valid.

The numerical modeling indicates the existence of some relationship between compressive fracture process and strain rate of rock material. This is similar to experimental investigation. It is also found that there is a good agreement between numerical stress-strain curves and experimental stress-strain curves. This study provides evidence that half-sine pulse decreases dispersion in wave propagation.

Conflicts of Interest

The authors declare that there are no conflicts of interest.

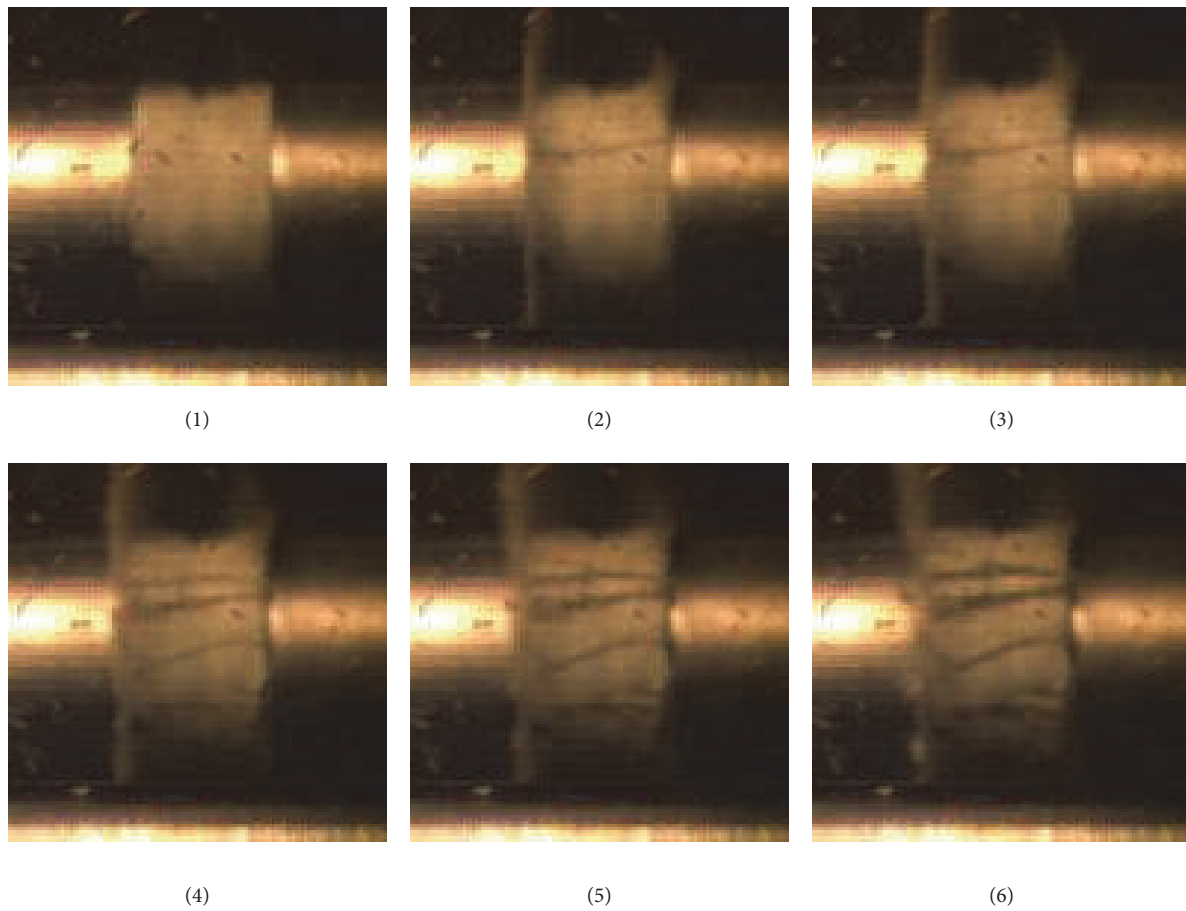


FIGURE 14: Photograph of fracture process from tests (the length-diameter ratio of specimen is 0.5, and the average strain rate is 119 s^{-1}).



FIGURE 15: Failure modes of specimens in the SHPB test (the length-diameter ratio of specimen is 0.5, and the average strain rate is 75.3 s^{-1}).



FIGURE 16: Failure modes of specimens in the SHPB test (the length-diameter ratio of specimen is 0.5, and the average strain rate is 162 s^{-1}).

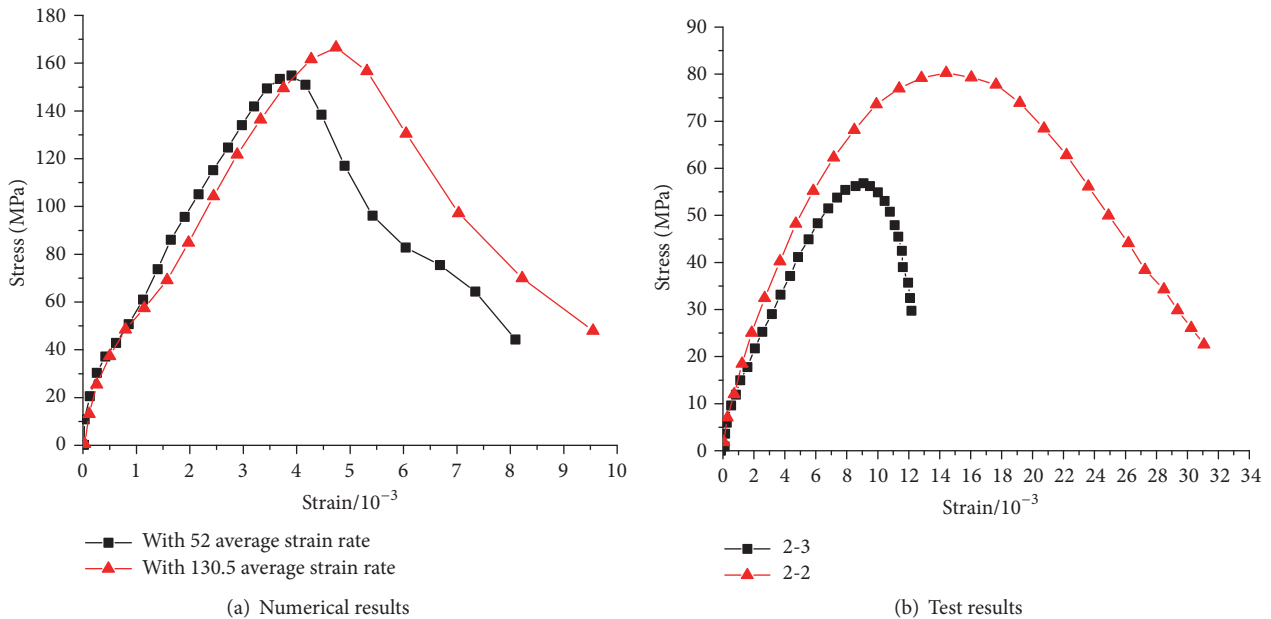


FIGURE 17: Stress-strain curves.

Acknowledgments

The study reported in the paper is supported by National Natural Science Foundation of China (51504044 and 51404126), the Research Fund of Chongqing Basic Science and Cutting-Edge Technology Special Projects (cstc2016jcyjA1861), China Postdoctoral Science Foundation (2015M570607), and the Independent Subject of State Key Laboratory of Coal Mine Disaster Dynamics and Control (2011DAI05287-MS201503).

References

[1] J. S. Rinehart, “Dynamic fracture strength of rocks,” in *Proceedings of the 7th US Symposium on Rock Mechanics*, pp. 205–213, Society of Mining, Metallurgical and Petroleum Engineers, Pennsylvania, Pa, USA, 1965.

[2] A. Kumar, “The effect of stress rate and temperature on the strength of basalt and granite,” *Geophysics*, vol. 33, no. 3, pp. 501–510, 1968.

[3] U. S. Lindholm, L. M. Yeakley, and A. Nagy, “The dynamic strength and fracture properties of dresser basalt,” *International Journal of Rock Mechanics and Mining Sciences & Geomechanics Abstracts*, vol. 11, no. 5, pp. 181–191, 1974.

[4] T. L. Blanton, “Effect of strain rates from 10^{-2} to 10 sec^{-1} in triaxial compression tests on three rocks,” *International Journal of Rock Mechanics and Mining Sciences & Geomechanics Abstracts*, vol. 18, no. 1, pp. 47–62, 1981.

[5] Z. P. Bažant, B. Shang-Ping, and G. Ravindra, “Fracture of rock: effect of loading rate,” *Engineering Fracture Mechanics*, vol. 45, no. 3, pp. 393–398, 1993.

[6] X. B. Li, T. S. Lok, and J. Zhao, “Dynamic characteristics of granite subjected to intermediate loading rate,” *Rock Mechanics and Rock Engineering*, vol. 38, no. 1, pp. 21–39, 2005.

- [7] H. B. Li, J. Zhao, and T. J. Li, "Micromechanical modelling of the mechanical properties of a granite under dynamic uniaxial compressive loads," *International Journal of Rock Mechanics and Mining Sciences*, vol. 37, no. 6, pp. 923–935, 2000.
- [8] L. Dong, J. Wesseloo, Y. Potvin, and X. Li, "Discrimination of mine seismic events and blasts using the fisher classifier, naive bayesian classifier and logistic regression," *Rock Mechanics and Rock Engineering*, vol. 49, no. 1, pp. 183–211, 2016.
- [9] L. Dong, X. Li, and G. Xie, "Nonlinear methodologies for identifying seismic event and nuclear explosion using random forest, support vector machine, and naive Bayes classification," *Abstract and Applied Analysis*, vol. 2014, Article ID 459137, 8 pages, 2014.
- [10] F. Dai, S. Huang, K. Xia, and Z. Tan, "Some fundamental issues in dynamic compression and tension tests of rocks using split Hopkinson pressure bar," *Rock Mechanics and Rock Engineering*, vol. 43, no. 6, pp. 657–666, 2010.
- [11] Y. Xu, F. Dai, N. W. Xu, and T. Zhao, "Numerical investigation of dynamic rock fracture toughness determination using a semi-circular bend specimen in split hopkinson pressure bar testing," *Rock Mechanics and Rock Engineering*, vol. 49, no. 3, pp. 731–745, 2016.
- [12] Z. Wen, X. Wang, L. Chen, G. Lin, and H. Zhang, "Size effect on acoustic emission characteristics of coal-rock damage evolution," *Advances in Materials Science and Engineering*, vol. 2017, Article ID 3472485, 8 pages, 2017.
- [13] F. Dai, Y. Xu, T. Zhao, N.-W. Xu, and Y. Liu, "Loading-rate-dependent progressive fracturing of cracked chevron-notched Brazilian disc specimens in split Hopkinson pressure bar tests," *International Journal of Rock Mechanics and Mining Sciences*, vol. 88, pp. 49–60, 2016.
- [14] X. Liu, F. Dai, R. Zhang, and J. Liu, "Static and dynamic uniaxial compression tests on coal rock considering the bedding directivity," *Environmental Earth Sciences*, vol. 73, no. 10, pp. 5933–5949, 2015.
- [15] L. D. Bertholf and C. H. Karnes, "Two-dimensional analysis of the split hopkinson pressure bar system," *Journal of the Mechanics and Physics of Solids*, vol. 23, no. 1, pp. 1–19, 1975.
- [16] Z.-J. Wen, M. Rinne, Z. Song, Z.-Z. Han, and J.-H. Wen, "Research on modelling of spatial dynamic structural mechanics and spatio-temporal evolution of coal mine stopes," *Tehnicki Vjesnik*, vol. 22, no. 3, pp. 607–613, 2015.
- [17] Z. Wen, X. Wang, Y. Tan, H. Zhang, W. Huang, and Q. Li, "A study of rockburst hazard evaluation method in coal mine," *Shock and Vibration*, vol. 2016, Article ID 8740868, 9 pages, 2016.
- [18] S. F. Sun, X. T. Xu, and H. P. Li, "Numerical simulation of effects of specimen size and shape in SHPB experiment," *Chinese Journal of Hefei University of Technology*, vol. 31, no. 9, pp. 1509–1512, 2008.
- [19] T. S. Lok, X. B. Li, D. Liu, and P. J. Zhao, "Testing and response of large diameter brittle materials subjected to high strain rate," *Journal of Materials in Civil Engineering*, vol. 14, no. 3, pp. 262–269, 2002.
- [20] X. He and C. Xu, "Specific energy as an index to identify the critical failure mode transition depth in rock cutting," *Rock Mechanics and Rock Engineering*, vol. 49, no. 4, pp. 1461–1478, 2016.
- [21] Y. Xu, F. Dai, N.-W. Xu, T. Zhao, and C. Zhou, "Discrete element simulation of dynamic semi-circular bend flexure tests of rocks using split Hopkinson pressure bar," *Arabian Journal of Geosciences*, vol. 9, no. 9, article 543, 2016.
- [22] Z. Zhou, X. Li, Y. Zou, Y. Jiang, and G. Li, "Dynamic Brazilian tests of granite under coupled static and dynamic loads," *Rock Mechanics and Rock Engineering*, vol. 47, no. 2, pp. 495–505, 2014.
- [23] X. B. Li, D. S. Gu, and H. H. Lai, "On the reasonable loading stress waveforms determined by dynamic stress-strain curves of rocks by SHPB," *Chinese Explosion and Shock Waves*, vol. 13, no. 2, pp. 125–130, 1993.
- [24] X. B. Li, T. S. Lok, J. Zhao, and P. J. Zhao, "Oscillation elimination in the Hopkinson bar apparatus and resultant complete dynamic stress-strain curves for rocks," *International Journal of Rock Mechanics and Mining Sciences*, vol. 37, no. 7, pp. 1055–1060, 2000.
- [25] Z. Wen, Y. Tan, Z. Han, and F. Meng, "Construction of time-space structure model of deep stope and stability analysis," *Polish Journal of Environmental Studies*, vol. 25, no. 6, pp. 2633–2640, 2016.
- [26] M. K. C. Roberts and R. K. Brummer, "Support requirements in rockburst conditions," *Journal of the South African Institute of Mining and Metallurgy*, vol. 88, no. 3, pp. 97–104, 1988.
- [27] T. J. Holmquist, G. R. Johnson, and W. H. Cook, "A computational constitutive model for concrete to large strains, high strain rates, and high pressures," in *Proceeding of the Fourteenth International Symposium on Ballistics*, pp. 591–600, Quebec, Canada, 1995.
- [28] "Ls-dyna Keyword User's Manual, Version 970," LSTC, April 2003.
- [29] Y.-S. Tai and C.-C. Tang, "Numerical simulation: the dynamic behavior of reinforced concrete plates under normal impact," *Theoretical and Applied Fracture Mechanics*, vol. 45, no. 2, pp. 117–127, 2006.
- [30] Z. Tang and L. Wang, "Computational data processing system of SHPB," *Explosion Shock Waves*, vol. 6, no. 4, pp. 320–327, 1986.
- [31] H. Zhao, G. Gary, and J. R. Klepaczko, "On the use of a viscoelastic split Hopkinson pressure bar," *International Journal of Impact Engineering*, vol. 19, no. 4, pp. 319–330, 1997.
- [32] R. Merle and H. Zhao, "On the errors associated with the use of large diameter SHPB, correction for radially non-uniform distribution of stress and particle velocity in SHPB testing," *International Journal of Impact Engineering*, vol. 32, no. 12, pp. 1964–1980, 2006.
- [33] H. Zhao and G. Gary, "On the use of SHPB techniques to determine the dynamic behavior of materials in the range of small strains," *International Journal of Solids and Structures*, vol. 33, no. 23, pp. 3363–3375, 1996.
- [34] X. B. Li and D. S. Gu, "Effective method of eliminating the oscillation of rock dynamic stress-strain-strain rate curves," *Journal of Central South University Technology*, vol. 36, pp. 457–460, 1995.
- [35] U. Zencker and R. Clos, "Limiting conditions for compression testing of flat specimens in the split Hopkinson pressure bar," *Experimental Mechanics*, vol. 39, no. 4, pp. 343–348, 1999.
- [36] W. Goldsmith, J. L. Sackmn, and C. Ewert, "Static and dynamic fracture strength of barre granite," *International Journal of Rock Mechanics and Mining Sciences & Geomechanics Abstracts*, vol. 13, no. 11, pp. 303–309, 1976.

Research Article

Chloride Diffusivity and Life Prediction of Cracked RC Beams Exposed to Different Wet-Dry Ratios and Exposure Duration

Jieqiong Wu,¹ Bo Diao,^{1,2} Yinghua Ye,¹ and Xiaoning Zheng^{1,2}

¹*School of Transportation Science and Engineering, Beihang University, Beijing 100083, China*

²*State Laboratory of Subtropical Building Science, South China University of Technology, Guangzhou 510640, China*

Correspondence should be addressed to Bo Diao; diaobo@buaa.edu.cn

Received 6 February 2017; Revised 31 March 2017; Accepted 4 May 2017; Published 11 June 2017

Academic Editor: Francesco Caputo

Copyright © 2017 Jieqiong Wu et al. This is an open access article distributed under the Creative Commons Attribution License, which permits unrestricted use, distribution, and reproduction in any medium, provided the original work is properly cited.

Effects of crack width, wet-dry ratio, and exposure duration of wet-dry cycles on chloride ingress of RC beams were experimentally studied. Crack widths of 40, 70, 90, and 120 microns were, respectively, induced by three-point flexural loading and four wet-dry ratios (seawater spraying 1 d in one wet-dry cycle) of 1:3, 1:7, 1:11, and 1:15 were selected. Chloride contents of RC beams were tested every 32 d (or 16 d) of wet-dry cycles. Results show that chloride content increased significantly when crack width was larger than 90 microns and wet-dry ratio was 1:3, and it increased slightly when crack width was 120 microns and wet-dry ratio was 1:7, 1:11, and 1:15. The chloride content on steel bar surface became the largest when crack width was less than 90 microns and wet-dry ratio was 1:7, and while crack width was equal to or greater than 90 microns and wet-dry ratio was 1:3, it was the largest. Based on the testing results, chloride diffusion model and prediction model of residual service life of RC beams were suggested considering combined effects of crack width and exposure duration. The predicted residual service lives were corresponding well with experimental results and they decreased as crack width increased.

1. Introduction

The attack of chloride corrosion is one of the major factors that reduce durability of existing reinforced concrete (RC) structures in coastal region; these structures are normally worked with cracks induced by service loading. The corrosive medium (e.g., chloride, oxygen, and water) could penetrate into concrete through these cracks. So RC structures in coastal region normally suffered the combined action of cracks and chloride corrosion [1]. There are many experiments about chloride ingress of concrete structures exposed to the environment of seawater wet-dry cycles, but few experiments investigated the difference of chloride diffusion when RC structures are exposed to chloride environments with different ratios of wetting time and drying time.

Hong and Hooton [2] immersed plain concrete specimens in 1.0 mol/L NaCl solution for 6 h, and then these specimens were dried for 18 h (one-day cycle) or 66 h (three-day cycle). After 1, 4, 9, 16, 25, and 36 cycles (one-day cycle) and 1, 4, 9, 16, and 25 cycles (three-day cycle), the testing

results of chloride content showed that prolonging the drying time could increase the rate of chloride ingress and there existed a good relationship between the depth of chloride penetration and the square root of the number of cycles. C. Li and K. Li [3] experimentally studied the law of chloride diffusion in the process of wet-dry cycles. The exposed surface of specimens contacted 1.0 mol/L NaCl solution for 12 h and then dried at 20°C, RH 70%. Wet-dry ratios were 1:6; 1:13; 1:27, respectively. It was indicated that when wet-dry ratio was 1:6 and 1:13, the content of acid-soluble chloride ion was relatively larger. Gang et al. [4] immersed specimens in 7% (by weight) NaCl solution, and wet-dry ratios were 1:1, 3:1, 5:1, 1:3, and 1:5, respectively, and cycling time was 48 h. The testing results of chloride content showed that, with the decrease of wet-dry ratio, the peak concentration of convection became higher. These indicated that chloride diffusion in uncracked concrete was significantly influenced by wet-dry ratios. But few experiments investigated the effect of wet-dry ratios on chloride diffusion of cracked RC structures.

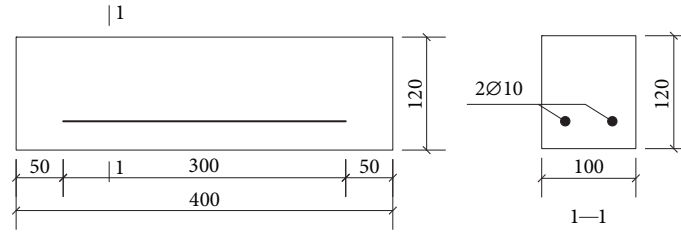


FIGURE 1: Dimensions and reinforcements of RC beams.

Apparent chloride diffusion is time-dependent, and it decays with time for the reason that pore structure is being more compact as the continuous hydration of concrete and the repulsive effect of anions on chloride ion [5]. Mangat and Molloy [6] placed concrete specimens in the tidal zone at Aberdeen beach for up to 3.3 years and tested the chloride content of concrete. The testing results showed that as the exposure duration increased, the chloride content increased but the increasing rate reduced; that is, chloride diffusion coefficient reduced. Moradillo et al. [7] measured the surface chloride content of concrete with different surface coatings in tidal zone during five years. It was found that surface chloride content of most specimens increased and chloride diffusion coefficient decreased as exposure duration increased.

Şahmaran [8] studied the effect of cracks, where specimens were immersed in NaCl solution for 30 d at concrete age of 43 d. Results showed that when crack width was less than 135 microns, the effect of cracks on chloride diffusion coefficient could be neglected; and when crack width was larger than 135 microns, the diffusion coefficient increased obviously. Win et al. [9] applied a bending load to induce four widths of cracks (100, 200, 300, and 500 microns) in concrete specimens. Then the specimens were immersed in NaCl solution for 1 month. The results of Electron Probe Microanalysis showed that the chloride penetration profile around the crack was more than twice that in the uncracked surface. Lei et al. [10] tested the chloride content of RC columns after 100 wet-dry cycles and calculated chloride diffusion coefficients. Immersing for 8 h and naturally drying for 16 h acted as one wet-dry cycle. Results showed that when crack width was less than 100 microns, chloride content and diffusion coefficient changed little. When $100 \text{ microns} \leq \text{width} \leq 140 \text{ microns}$, the chloride content on steel bar surface increased slightly while diffusion coefficient increased significantly. Li [11] sprayed NaCl solution to specimens for 8 h, and then these specimens were naturally dried at 25°C and RH 60% for 1 d and then dried at 50°C and RH 20% for 1 d. After the designed wet-dry cycles, chloride contents of concrete with three widths of cracks (less than 50 microns, 100 microns, and 200 microns) were tested. It was shown that when crack width was greater than 100 microns, cracks had significant effect on chloride content of concrete. Existing experiments mainly considered the effect of single factor such as crack width, or wet-dry ratio, or exposure duration on chlorine ion permeability, but few considered the combined effects of crack width, wet-dry ratio, and exposure duration.

TABLE 1: Concrete mixture composition (kg/m^3).

| | |
|---------------------|------|
| 425 Portland cement | 315 |
| Water | 170 |
| River sand | 661 |
| Coarse aggregates | 1284 |

Note. 425 Portland cement refers to a cement class in China; its compressive strength at age of 28 d was 42.5 MPa.

The working conditions of RC structures in coastal region were stimulated in lab and the evolution of crack widths, chloride diffusivity, and service life were experimentally investigated considering different wet-dry ratios (1:3, 1:7, 1:11, and 1:15), different crack widths (0~120 microns), and different exposure durations (32 d~160 d). Based on the research, the model of chloride diffusion and life prediction of RC beams, where the combined effects of crack width and exposure duration were considered, were proposed.

2. Specimen and Testing Program

2.1. Specimens. The working conditions of RC structures in coastal region were stimulated in lab and the combined effects of crack width, wet-dry ratio, and exposure duration on evolution of crack widths, chloride diffusivity, and service life were experimentally investigated. The testing environments in the current study included seawater wet-dry environment and laboratory natural environment. Total 150 RC beam specimens with same sizes and same reinforcements were made, where 102 beam specimens were exposed in the environment of seawater wet-dry cycles, and 21 beams were placed in lab atmosphere environment as reference group. The rest of 27 beam specimens were used as to study how to induce the designed width of cracks and acted as spare specimens in the wet-dry cycles.

The reinforcement arrangements of RC beam specimens are showed in Figure 1. The dimension of the rectangular cross-section was $100 \text{ mm} \times 120 \text{ mm}$, and the length of the beam specimen was 400 mm. The diameter of longitudinal tensile steel bar was 10 mm and concrete cover was 30 mm. The mixtures of concrete included 425 Portland cement, river sand, and coarse aggregates. The maximum size of aggregate was 10 mm and the water-cement ratio was 0.54. The concrete mixture composition in per cubic meter is given in Table 1. The average compressive strength of the concrete used for the

TABLE 2: Names of RC beam specimens (Group A = 1:3, or B = 1:7, or D = 1:15).

| Crack width | Duration | | | | | | |
|-------------|----------|---------|----------|----------|-----------|----------|-----------|
| | 32 d | 48 d | 64 d | 96 d | 128 d | 144 d | 160 d |
| 00 microns | A-00-32 | A-00-48 | A-00-64 | A-00-96 | A-00-128 | A-00-144 | A-00-160 |
| 40 microns | A-40-32 | A-40-48 | A-40-64 | A-40-96 | A-40-128 | A-40-144 | A-40-160 |
| 70 microns | A-70-32 | — | A-70-64 | A-70-96 | A-70-128 | — | A-70-160 |
| 90 microns | A-90-32 | — | A-90-64 | A-90-96 | A-90-128 | — | A-90-160 |
| 120 microns | A-120-32 | — | A-120-64 | A-120-96 | A-120-128 | — | A-120-160 |

TABLE 3: Names of RC beam specimens (Group C = 1:11).

| Crack width | Duration | | | | | | |
|-------------|----------|----------|------|----------|-------|-----------|-------|
| | 32 d | 48 d | 64 d | 96 d | 128 d | 144 d | 160 d |
| 00 microns | — | C-00-48 | — | C-00-96 | — | C-00-144 | — |
| 40 microns | — | C-40-48 | — | C-40-96 | — | C-40-144 | — |
| 70 microns | — | C-70-48 | — | C-70-96 | — | C-70-144 | — |
| 90 microns | — | C-90-48 | — | C-90-96 | — | C-90-144 | — |
| 120 microns | — | C-120-48 | — | C-120-96 | — | C-120-144 | — |

150 RC beam specimens was 41 MPa, as determined on the prisms at an age of 28 days.

2.2. Testing Program. All tests were performed in the Civil Engineering Laboratory at Beihang University in Beijing. Based on the wet-dry ratios, 102 beam specimens were classified into A, B, C, and D four groups, and the wet-dry ratio is as follows: Group A = 1:3, Group B = 1:7, Group C = 1:11, and Group D = 1:15, which means that the beam specimens were subjected to seawater spraying for 1 d and then atmosphere drying in lab environment for 3, 7, 11, and 15 d, respectively. Within each group, the beam specimens were further divided by five crack widths (0, 40, 70, 90, and 120 microns) and seven exposure durations (32 d, 48 d, 64 d, 96 d, 128 d, 144 d, and 160 d). The beam specimens of Groups A, B, and D are summarized in Table 2, named as group number-crack width-exposure duration; for example, A-00-32 means Group A, crack width of 00 microns, and exposure duration 32 d, and so on. And beam specimens of Group C are summarized in Table 3.

All beam specimens were demolded after 24 h of casting and were cured under standard temperature and moisture conditions. At the age of 28 d, three-point flexural loading was performed on RC beam specimens to induce different widths of flexural cracks, where loading increment was controlled by mid-span deflection. The loading equipment was shown in Figure 2. The maximum crack width was measured and recorded with a crack detector after two hours of the beam specimens unloading and classified into five crack widths (0, 40, 70, 90, and 120 microns), as listed in Tables 2 and 3.

To simulate the combined actions of crack width, wet-dry ratio, and exposure duration, the beam specimens of Group A, B, C, and D were sprayed with seawater for 1 d and then atmosphere dried in lab environment for 3 d (Group A), 7 d (Group B), 11 d (Group C), and 15 d (Group D), respectively,



FIGURE 2: Loading equipment.



FIGURE 3: Spraying device.

as one round of wet-dry cycle. This procedure was repeated until the designed exposure duration as listed in Tables 2 and 3.

Automatic device of seawater spraying was shown in Figure 3; the seawater here was artificially made with 3.5% (by

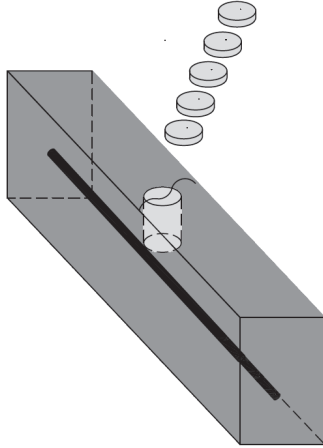


FIGURE 4: Sampling from tensile side of RC beam specimens.

weight) NaCl. In order to ensure one-dimensional diffusion in the process of wet-dry cycles, all beam specimens were coated with waterproof paint except for the testing surface.

After accomplishment of designed exposure duration of wet-dry cycles, a cylinder concrete sample was drilled at tensile side of RC beam specimens, as shown in Figure 4. The diameter and depth of the cylinder sample was 50 mm and 30 mm, respectively. The cylinder sample was then subdivided into 5 slices along the depth. Each slice was ground into fine powder and the free chloride content in each slice was tested by the Ion Selective Electrode Method [12] according to the standard JTJ 270-98 [13].

3. Results and Discussion

The initial cracks on RC beam specimens were induced by three-point flexural loading at the age of 28 d, and then the load was removed. The beam specimens with different crack widths were exposed to the designed wet-dry ratios and cycles. During the period of wet-dry cycles, the evolution of crack width was monitored. After the designed duration of wet-dry cycles completed, the chloride contents of cracked and uncracked concrete at depths of 0~6 mm, 6~12 mm, 12~18 mm, 18~24 mm, and 24~30 mm were tested. The experimental results of crack width and chloride content are briefly introduced as the following.

3.1. Self-Healing Effect of Concrete Cracks. The crack photos of initial widths 120 microns on beam specimens in Groups A, B, C, and D, before ($t = 0$) and after wet-dry cycles, were shown in Figure 5. It can be seen from Figure 5, when initial width was 120 microns after designed wet-dry cycles, self-healing effect of cracks in Group A (wet-dry ratio 1:3) was quite obvious, and Group B (wet-dry ratio 1:7) was next, and Groups C and D (wet-dry ratios 1:11 and 1:15) were not obvious. Therefore, as wet-dry ratio decreased from 1:3 to 1:15, self-healing effect of concrete cracks weakened.

Figure 6 shows the photos of cracks on RC beam specimens in Group B, with different initial crack widths of 40, 70, 90, and 120 microns, before ($t = 0$) and after

TABLE 4: Crack width of four groups (A = 1:3, B = 1:7, C = 1:11, and D = 1:15) after wet-dry cycles.

| Initial width ($t = 0$) | $t = 160$ d (microns) | | | |
|------------------------------|-----------------------|---------|-----------------|---------|
| | Group A | Group B | Group C (144 d) | Group D |
| 40 microns | 00 | 00 | 00 | 00 |
| 70 microns | 00 | 30 | 45 | 50 |
| 90 microns | 00 | 70 | 75 | 75 |
| 120 microns | 40 | 70 | 90 | 90 |

TABLE 5: Cracks evolution of Group B (1:7) after designed exposure duration.

| Initial width | Duration | | | | |
|---------------|----------|------|------|-------|-------|
| | 32 d | 64 d | 96 d | 128 d | 160 d |
| 40 microns | 40 | 35 | 25 | 5 | 00 |
| 70 microns | 70 | 65 | 60 | 40 | 30 |
| 90 microns | 90 | 90 | 85 | 70 | 70 |
| 120 microns | 120 | 120 | 100 | 80 | 70 |

($t = 160$ d) wet-dry cycles. After 160 d of wet-dry cycles, as shown in Figure 6, when initial crack width was 40 or 70 microns, the crack nearly disappeared due to self-healing effect of concrete materials, while when initial crack width was 90 or 120 microns, self-healing effect was not quite obvious. The conclusion was that as the width of initial cracks increased from 40 microns to 120 microns, self-healing effect of concrete cracks gradually weakened.

The testing results of crack widths after designed wet-dry cycles for four groups are listed in Table 4. It was indicated that self-healing effect of crack surface was the best where the wet-dry ratio was 1:3 (Group A). And when initial crack width was 40 microns, the crack in concrete surface of four groups disappeared after the designed wet-dry cycles. Besides, as the wet-dry ratio decreased from 1:3 to 1:15 and crack widths increased from 40 microns to 120 microns, self-healing effect gradually weakened.

The testing results of crack widths in Group B with different initial crack widths and exposure durations were listed in Table 5. It can be seen from Table 5 that as the exposure duration increased from 0 d to 160 d, the self-healing effects of concrete cracks were observed to be gradually obvious, and as the width of initial crack increased from 40 microns to 120 microns, the self-healing effects of concrete cracks were monitored to be gradually weaken.

In the exposure duration of wet-dry cycles, the self-healing effect of concrete cracks mainly comes from two aspects. On one hand, the white deposit (CaCO_3) blocked the crack [14, 15], which was chemically formed by CO_2 from the air and the alkaline component from concrete. On the other hand, the beam specimens in Group A suffered the longest duration of seawater spraying, which result in sufficient hydration of concrete and obvious self-healing of concrete cracks after 160 d wet-dry cycles.

3.2. Testing Results of Chloride Content and Discussion. When the designed duration of wet-dry cycles was finished, cylinder

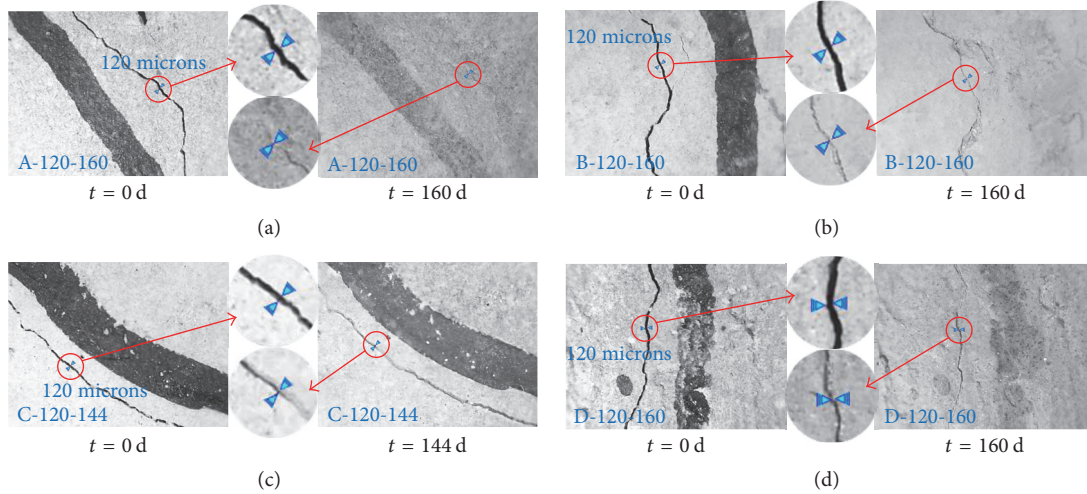


FIGURE 5: Cracks in Groups A, B, C, and D (initial width 120 microns) before and after wet-dry cycles: (a) Group A; (b) Group B; (c) Group C; (d) Group D.

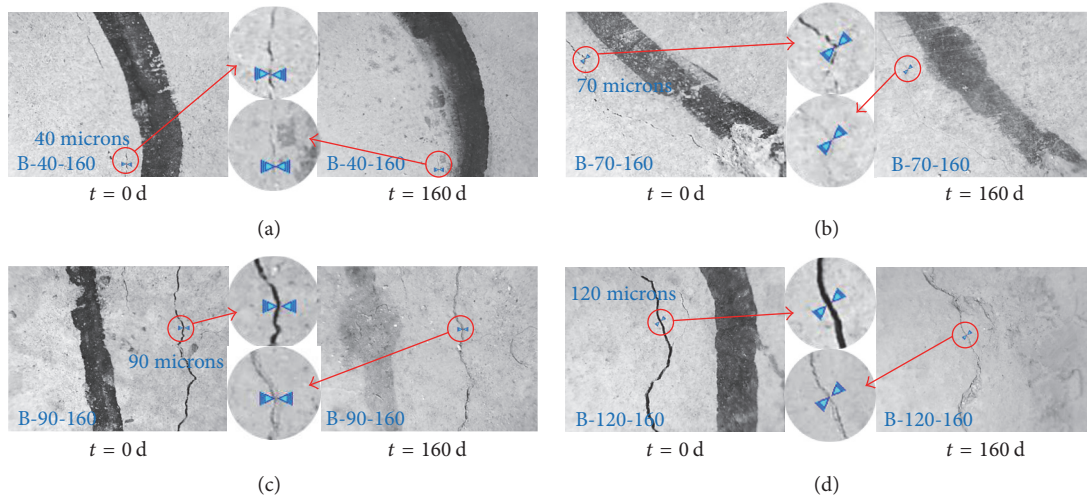


FIGURE 6: Self-healing of cracks in Group B (initial width = 40, 70, 90, and 120 microns) before and after wet-dry cycles: (a) 40 microns; (b) 70 microns; (c) 90 microns; (d) 120 microns.

samples were drilled at tensile side of RC beam specimens, as shown in Figure 4. The chloride contents along the depth of concrete cover with different crack widths in four groups were tested. The relationship of the chloride content with the crack width, wet-dry ratio, and exposure duration will be discussed in the following sections.

3.2.1. Effect of Crack Widths on Chloride Content. The chloride contents along the depth of the concrete covers with different widths of crack in Group A were plotted in Figure 7, when the exposure duration 160 d was finished. As can be seen from Figure 7, the chloride content decreased as the depth increased from surface to 30 mm, where the chloride content decreased rapidly as the depth increased from surface to 15 mm, and the chloride content decreased slowly as the depth increased from 15 mm to 30 mm. It can be seen from

Figure 7 that the chloride content increased as the crack widths increased and when the crack width was 120 microns, the chloride content was obviously larger.

The chloride contents at different depths of concrete cover with different crack widths in Groups A, B, C, and D are shown in Figures 8(a), 8(b), 8(c), and 8(d), respectively. Since the chloride content at depth 0~6 mm showed a large discreteness, the data at this depth was abandoned here.

As shown in Figures 8(a), 8(b), 8(c), and 8(d), the chloride content at the same depth increased as the crack width increased from 0 to 120 microns. As can be seen from Figure 8(a), the chloride content changed little when crack width was less than 90 microns, and the chloride content increased significantly when the crack width was larger than 90 microns. As can be seen from Figures 8(b), 8(c), and 8(d), with the wet-dry ratios of 1:7, 1:11, and 1:15, the chloride

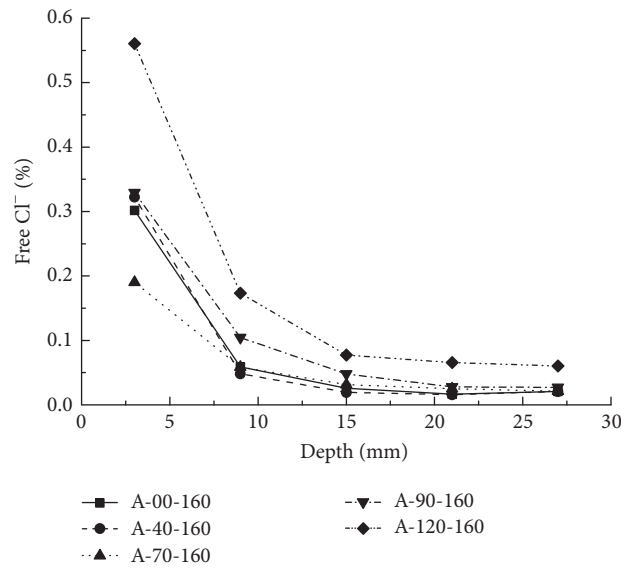


FIGURE 7: Chloride contents along the depth of concrete cover with different crack widths in Group A.

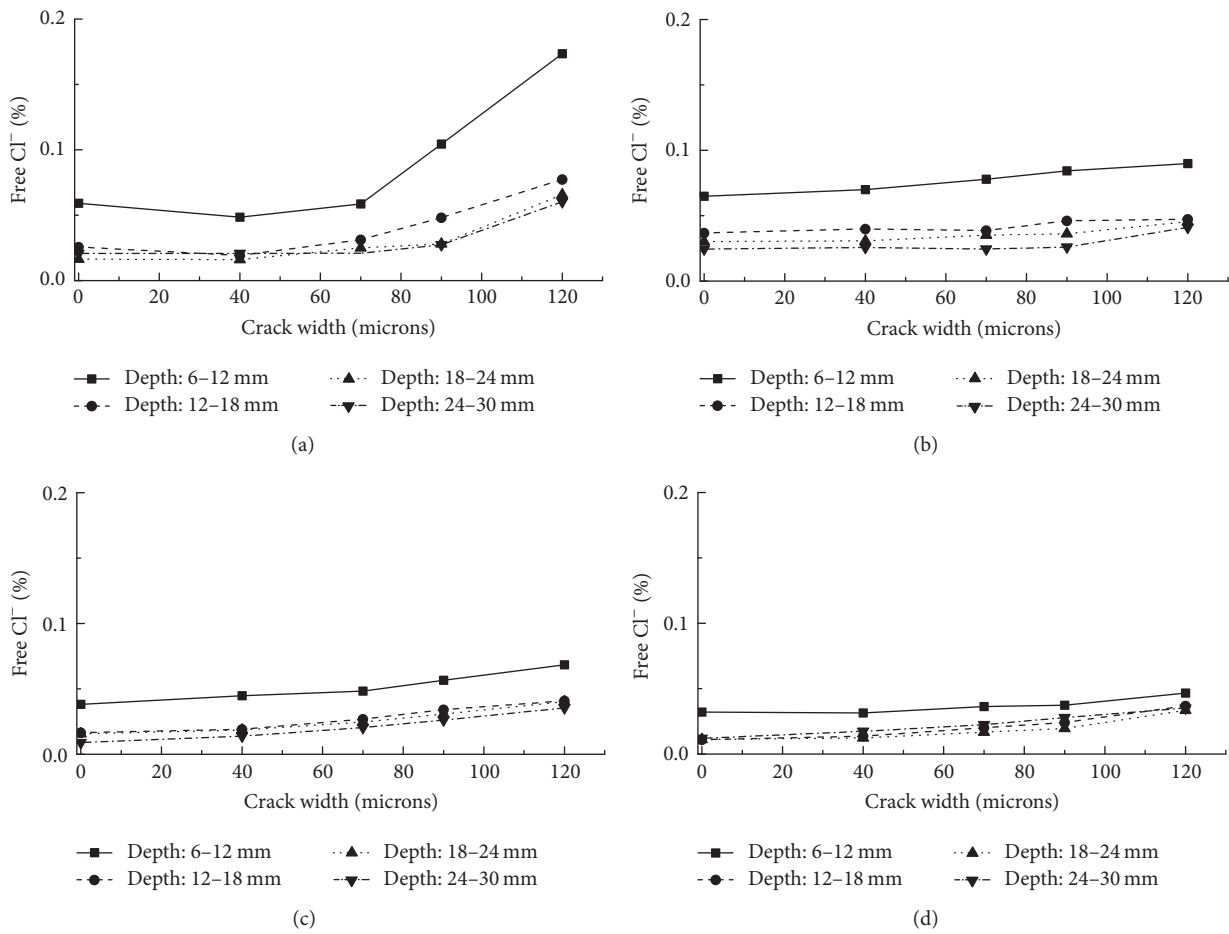


FIGURE 8: Chloride content with different crack widths and different wet-dry ratios. (a) Group A (1 : 3); (b) Group B (1 : 7); (c) Group C (1 : 11); (d) Group D (1 : 15).

TABLE 6: Chloride content on steel bar surface (%) and its increment compared with uncracked concrete (%).

| Crack width (microns) | Chloride content A (160 d) | Incr. A (160 d) | Chloride content B (160 d) | Incr. B (160 d) | Chloride content C (144 d) | Incr. C (144 d) | Chloride content D (160 d) | Incr. D (160 d) |
|-----------------------|----------------------------|-----------------|----------------------------|-----------------|----------------------------|-----------------|----------------------------|-----------------|
| 00 | 0.0208 | 0.00 | 0.0245 | 0.00 | 0.0090 | 0.00 | 0.0121 | 0.00 |
| 40 | 0.0217 | 4.33 | 0.0257 | 4.90 | 0.0138 | 53.33 | 0.0174 | 43.80 |
| 70 | 0.0226 | 8.65 | 0.0254 | 3.67 | 0.0204 | 126.67 | 0.0225 | 85.95 |
| 90 | 0.0279 | 34.13 | 0.0260 | 6.12 | 0.0262 | 191.11 | 0.0270 | 123.14 |
| 120 | 0.0604 | 190.38 | 0.0411 | 67.76 | 0.0354 | 293.33 | 0.0352 | 190.91 |

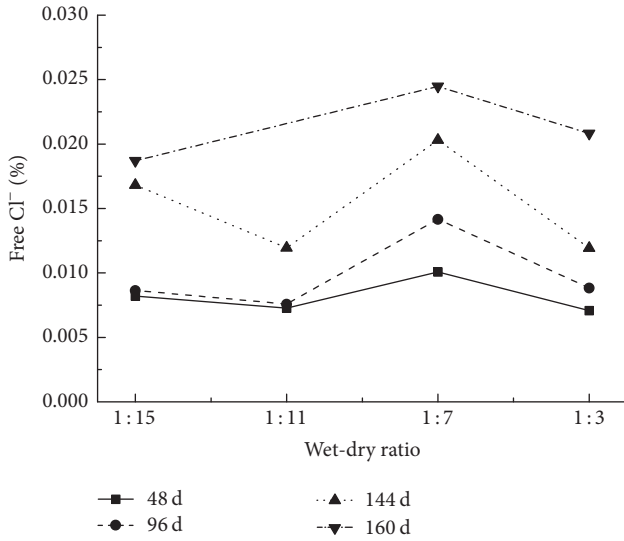


FIGURE 9: Chloride content on steel bar surface of uncracked concrete with different wet-dry ratios and different durations.

content changed little when crack width was equal to or less than 90 microns and the chloride content increased slightly when the crack width was 120 microns.

In conclusion, when wet-dry ratio was 1:3, the chloride content along the depth of concrete cover increased significantly as crack width was larger than 90 microns and when wet-dry ratios were 1:7, 1:11, and 1:15, chloride content increased slightly as crack width increased from 0 to 120 microns. A possible explanation was that the evaporation of pore solution influenced the concentration difference along the depth of concrete cover, which leads to different penetration rate of chloride ion during wetting process.

3.2.2. Effect of Wet-Dry Ratios on Chloride Content. The chloride content on steel bar surface of uncracked concrete with different wet-dry ratios (Groups A, B, C, and D) and different exposure durations are plotted in Figure 9. As shown in Figure 9, for the same duration, when wet-dry ratio increased from 1:15 to 1:3, the chloride content on steel bar surface changed and reached the largest value when the wet-dry ratio was 1:7, and the chloride content on steel bar surface increased as the exposure duration increased from 48 d to 160 d.

The chloride contents on steel bar surface and the increments of chloride content compared with uncracked concrete in the same group were listed in Table 6, where wet-dry ratios of four groups were A (1:3), B (1:7), C (1:11), and D (1:15), respectively. As shown in Table 6, for the same group, the chloride content on steel bar surface increased as the crack width increased. And the increment of chloride content also increased as the crack width increased, compared with the chloride content of uncracked RC beam specimens in the same group. When crack width was 120 microns, the chloride content on steel bar surface was the largest and the increment was 190.38%, 67.76%, 293.33%, and 190.91% for Groups A, B, C, and D, respectively. When wet-dry ratio was 1:3 or 1:7, the increment of the chloride content on steel bar surface with crack width of 40 microns or 70 microns was smaller than 10%, while the increment of the chloride content on steel bar surface increased sharply when crack width was greater than 90 microns. When wet-dry ratio was 1:11 or 1:15 and crack width was 40 microns, the increment of chloride content was 53.33% or 43.80%, respectively, while the chloride content was relatively small. This indicated that as the wet-dry ratio decreased to 1:11 or 1:15, cracks had significant effect on the increment of the chloride content.

A possible explanation of the results in Figure 9 and Table 6 was that convection zone increased due to the extension of wet-dry cycles [4]. Based on the “inkbottle effect” and “hysteresis” [15, 16], the water evaporation rate in the drying process was obviously lagging behind the penetration rate of liquid in the wetting process. And when the drying duration was not enough for evaporation of the pore solution, diffusion played the major role and convection effect was not evident during the next wetting process [4], while the penetration rate would be accelerated because of wide concentration difference between the inside and outside solution [2]. As wet-dry ratio decreased from 1:3 to 1:15, the drying duration became longer and chloride penetration was accelerated, while the duration of concrete surface exposed to NaCl solution was shortened, which led to a decrease of the total chloride ion in concrete. So moderate drying duration was more conducive to chloride diffusivity.

The chloride contents on steel bar surface with different crack widths in different groups of wet-dry ratios were plotted in Figure 10, where the chloride content of exposure duration 96 d was shown in Figure 10(a) and that of exposure duration 160 d was shown in Figure 10(b). The ratios of chloride content in four groups and chloride content in reference group were listed in Table 7, where the wet-dry ratios of

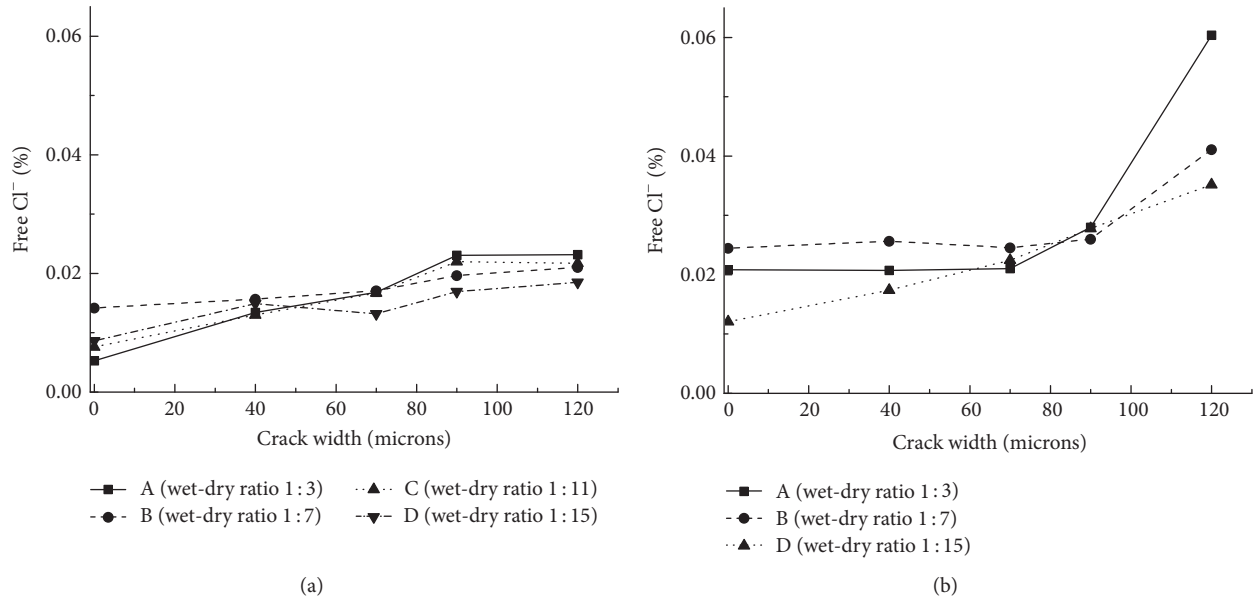


FIGURE 10: Chloride content on steel bar surface with different wet-dry ratios and different crack widths: (a) exposure duration 96 d; (b) exposure duration 160 d.

TABLE 7: Ratio of chloride content on steel bar surface of Groups A, B, C, and D and reference group.

| Group | A (160 d) | B (160 d) | C (144 d) | D (160 d) |
|-------------|-------------|-------------|-----------|-----------|
| 00 microns | 3.22 | 3.79 | 1.39 | 1.87 |
| 40 microns | 3.36 | 3.98 | 2.14 | 2.69 |
| 70 microns | 3.50 | 3.93 | 3.16 | 3.48 |
| 90 microns | 4.32 | 4.02 | 4.06 | 4.18 |
| 120 microns | 9.35 | 6.36 | 5.48 | 5.45 |

four groups were A = 1 : 3, B = 1 : 7, C = 1 : 11, and D = 1 : 15, respectively, and the duration of wet-dry cycles for Groups A, B, and D was 160 d and for Group C was 144 d.

As can be seen from Figure 10 and Table 7, when crack width was less than 90 microns, chloride content of Group B (wet-dry ratio 1 : 7) was the largest of four groups. And when crack width was equal to or greater than 90 microns, chloride content of Group A (wet-dry ratio 1 : 3) was the largest.

A possible explanation was that when crack width was 90 or 120 microns, the wider crack was conducive to evaporation of pore solution and led to a wide concentration difference between the inside and outside solution, even the wet-dry ratio was 1 : 3 (Group A). And when crack widths were less than 90 microns, the wetting duration in Group B (wet-dry ratio 1 : 7) was shorter than Group A, and the chloride diffusivity was improved due to less hydration of cement and less self-healing effect of crack, which indicated that moderate drying duration was more conducive to chloride diffusivity.

3.2.3. Effect of Exposure Duration on Chloride Content. The time dependency of chloride content on steel bar surface in four groups with wet-dry ratios of 1 : 3, 1 : 7, 1 : 11, and 1 : 15 were

plotted in Figures 11(a), 11(b), 11(c), and 11(d), respectively. It can be seen from Figure 11(a), in Group A (wet-dry ratio 1 : 3), that the chloride content changed little when exposure duration was shorter than 96 d and the chloride content increased significantly when exposure duration increased from 96 d to 160 d. It can be seen from Figures 11(b), 11(c), and 11(d), in the rest of the three groups, that the chloride content changed little when the exposure duration was less than 96 d, and the chloride content increased significantly when crack width was larger than 90 microns and the exposure duration was larger than 96 d.

In conclusion, chloride content on steel bar surface increased sharply when exposure duration was larger than 96 d and crack width was larger than 90 microns for all four groups.

4. Apparent Chloride Diffusion Coefficient (D_w) and Service Life Prediction

4.1. Effect of Exposure Duration on Chloride Diffusion Coefficient. Based on Fick's second law and related research of chloride diffusion of concrete, surface chloride content (C_s) and apparent chloride diffusion coefficient (D_w) were obtained by regression analysis using (1) as to result into the best fit curve [17]. Because (1) only considered the effect of diffusion, the convection zone was removed in the fitting process.

$$C(x, t) = C_s \left[1 - \operatorname{erf} \left(\frac{x}{2\sqrt{D_w t}} \right) \right], \quad (1)$$

where $C(x, t)$ is the chloride content of concrete at the depth x and the exposure duration t .

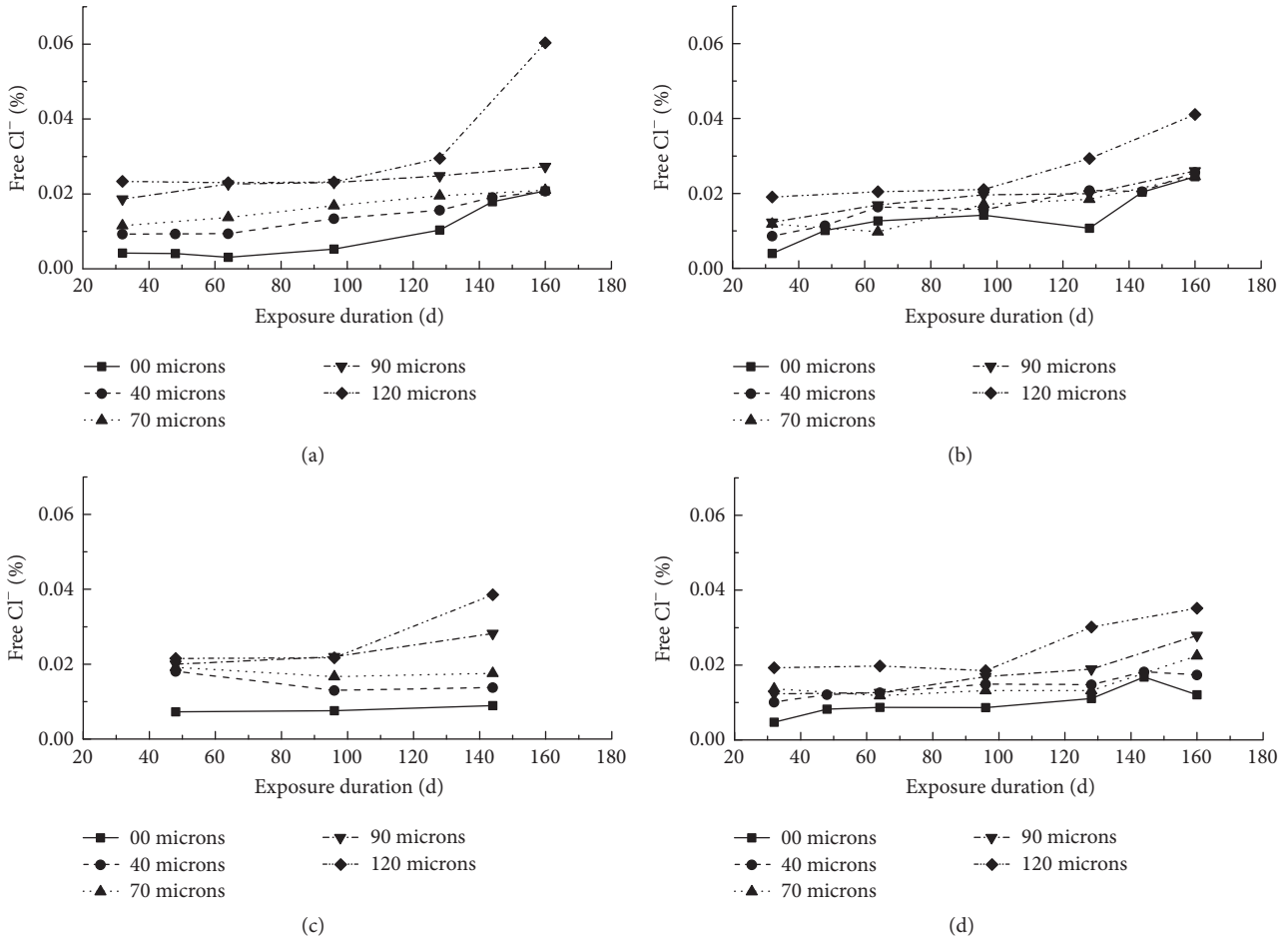


FIGURE 11: Chloride content on steel bar surface with different exposure durations and different crack widths. (a) Group A (1:3); (b) Group B (1:7); (c) Group C (1:11); (d) Group D (1:15).

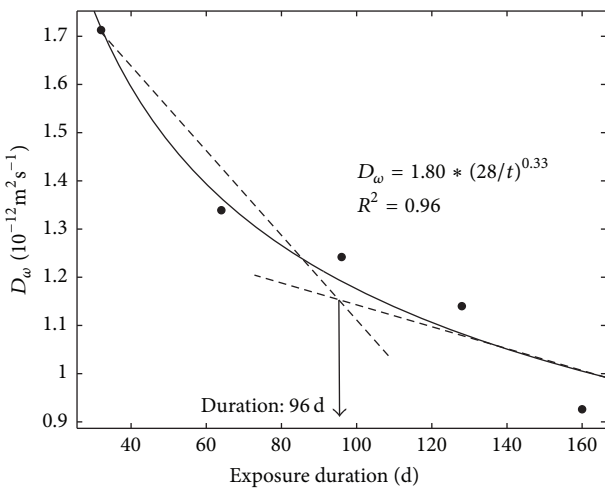


FIGURE 12: D_ω versus exposure duration.

The time-dependent change of D_ω in uncracked concrete of Group B is given in Figure 12. According to the study of

Thomas and Bamforth [18], the time dependency of D_ω can be described as follows [7]:

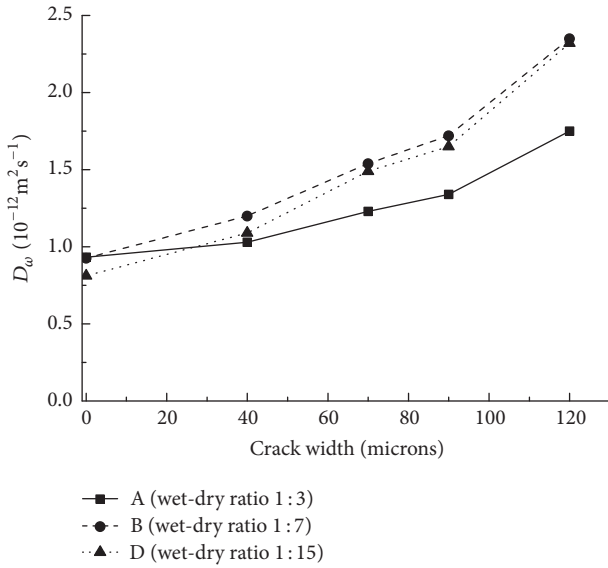
$$D_\omega(t) = D_{28} \left(\frac{28}{t} \right)^{\alpha_t} \quad (2)$$

where $D_\omega(t)$ is the apparent chloride diffusion coefficient ($10^{-12} \text{ m}^2/\text{s}$); t is the exposure duration of wet-dry cycles (day); D_{28} is the apparent chloride diffusion coefficient at age of 28 d ($10^{-12} \text{ m}^2/\text{s}$); α_t is the time decay factor.

As can be seen from Figure 12, D_ω decreased from 1.72×10^{-12} to almost $1.01 \times 10^{-12} \text{ m}^2/\text{s}$ as exposure duration increased to 160 d. In Figure 12, two time-dependent trends of D_ω were observed and they were represented by two dashed lines. The intersection of two dashed lines was 96 d, which implied that exposure duration 96 d was a critical value. When exposure duration increased from 32 d to 96 d, D_ω decreased sharply from 1.72×10^{-12} to almost $1.20 \times 10^{-12} \text{ m}^2/\text{s}$. When exposure duration increased from 96 d to 160 d, D_ω decreased slowly from almost 1.20×10^{-12} to almost $1.01 \times 10^{-12} \text{ m}^2/\text{s}$. The relationship between D_ω and exposure duration was regressed and the result was given by solid line in Figure 12. The coefficient of determination (R^2) was 0.96, which indicated correlation was well.

TABLE 8: D_{28} and α_ω of different crack widths.

| Crack width | D_{28} ($10^{-12} \text{m}^2/\text{s}$) | α_ω |
|-------------|---|-----------------|
| 00 microns | 1.80 | 1.00 |
| 40 microns | 1.83 | 1.02 |
| 70 microns | 1.95 | 1.08 |
| 90 microns | 2.83 | 1.57 |
| 120 microns | 5.64 | 3.13 |

FIGURE 13: D_ω versus crack width (160 d).

4.2. *Effect of Crack Widths and Wet-Dry Ratios on Chloride Diffusion Coefficient.* After 160 d of wet-dry cycles, D_ω in Groups A, B, and D are plotted in Figure 13. As shown in Figure 13, D_ω increased as crack width increased and D_ω increased slowly as crack width increased from 0 to 90 microns and increased sharply as crack width increased from 90 to 120 microns. It implied that width of 90 microns was a critical value to consider the effect of crack width on chloride diffusion coefficient.

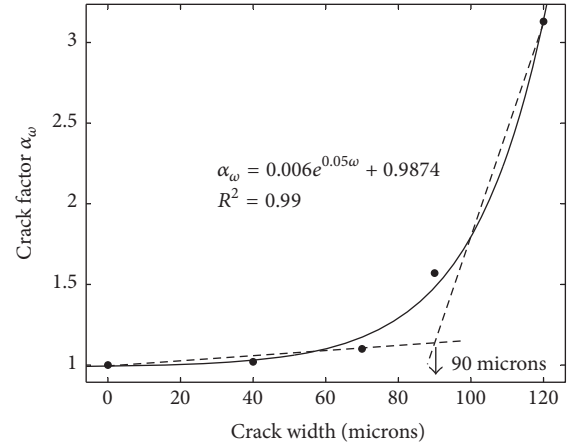
Besides, as shown in Figure 13, when crack width was 0 and 40 microns, wet-dry ratio had little influence on D_ω ; and D_ω achieved the largest values when wet-dry ratio was 1:7 for all crack widths. This means that moderate ratio of wetting and drying duration would be conducive to the chloride ingress; that is, wet-dry ratio 1:7 was the critical wet-dry ratio for lab accelerated test.

The crack factor α_ω was introduced to consider the effect of initial crack. The apparent chloride diffusion coefficient of concrete at 28 d in Group B (wet-dry ratio 1:7) was obtained by (2) and the ratio of this apparent chloride diffusion coefficient between cracked concrete (D_c) and uncracked concrete (D_0) was listed in Table 8. Crack factor α_ω was calculated by (3) and the result of α_ω was given in Figure 14 and Table 8.

$$\alpha_\omega = \frac{D_c}{D_0}. \quad (3)$$

TABLE 9: C_s and decrement.

| Group | λ | λ_t | R^2 | C_s (160 d) | Decrement |
|------------------|------------------|-------------|-------|---------------|-----------|
| A (wet-dry 1:3) | $1.42 * 10^{-5}$ | 0.065 | 0.91 | 0.55 | 1 |
| B (wet-dry 1:7) | $1.29 * 10^{-5}$ | 0.065 | 0.92 | 0.50 | 9.1% |
| D (wet-dry 1:15) | $0.57 * 10^{-5}$ | 0.065 | 0.83 | 0.22 | 60.0% |

FIGURE 14: α_ω versus crack width.

As can be seen from Figure 14, α_ω increased from 1 to 3.13 as crack width increased to 120 microns. In Figure 14, two development trends of α_ω were observed and they were represented by two dashed lines. The intersection of two dashed lines was 90 microns, which implied that crack width of 90 microns was a critical value. When crack width increased from 0 to 90 microns, α_ω increased slowly from 1 to almost 1.53. When crack width increased from 90 to 120 microns, α_ω increased sharply from almost 1.53 to 3.13. The relationship between α_ω and crack width was regressed and the result was given by solid line in Figure 14. The coefficient of determination (R^2) was 0.99, which indicated correlation was well.

4.3. *Effect of Exposure Duration and Wet-Dry Ratios on C_s .* As mentioned above, (1) was used to obtain the surface chloride content (C_s) by curve fitting. In this paper, the specimen surface was under unsaturated state because of seawater wet-dry cycles and subsequently C_s increased as exposure duration increased. To describe the time dependency of the surface chloride content (C_s), (4) [5] was obtained by regression based on the results of the surface chloride content (C_s) from Groups A, B, and D.

$$C_s = \lambda \cdot e^{(\lambda_t \cdot t)}, \quad (4)$$

where λ is an environmental parameter; λ_t is a time-dependent parameter; t is the exposure duration of wet-dry cycles (day).

Table 9 gives the value of the surface chloride content (C_s) from (1) and the regression results of λ , λ_t , and its determination coefficient (R^2) from Groups A, B, and D as well as the decrement of C_s compared with C_s of Group

A. As can be seen from Table 9, compared with C_s of Group A, C_s in Groups B and D decreased by 9.1% and 60.0%, respectively. It was indicated that C_s was significantly affected by the environment; that is, with the decrease of the proportion of wetting time, surface chloride content significantly decreased.

4.4. Life Prediction considering Cracks, Wet-Dry Ratios, and Exposure Durations

4.4.1. *Model of Life Prediction.* Recently, in order to calculate the chloride profile resulting from ingress of penetrating chlorides, many researches have adopted model of chloride transmission in concrete proposed by Collepardi et al. [19] according to Fick's second law of one-dimensional unsteady flowing [20], and its mathematical expression is

$$\frac{\partial C(x, t)}{\partial t} = D \frac{\partial^2 C(x, t)}{\partial x^2}, \quad (5)$$

where x is the depth; t is exposure duration; $C(x, t)$ is the chloride content of concrete at the depth x and exposure duration t ; D is the apparent chloride diffusion coefficient at duration t .

Collepardi et al. [19] assumed the initial and boundary conditions ($C(x, t = 0) = 0$ and $C(x = 0, t) = C_s$) and simplified (5) into (6) through the function (erf).

$$C(x, t) = C_s - (C_s - C_i) \cdot \operatorname{erf}\left(\frac{x}{2\sqrt{D_w \cdot t}}\right), \quad (6)$$

where C_s is surface chloride content and C_i is initial chloride content.

In the theory of life prediction of chloride diffusion, the end point of the durability life of structures is that the chloride content on steel surface reaches critical value (C_{cr}) [21]. Thus, in this study, it is assumed that time to corrosion initiation was reached when the chloride content on the steel surface has reached the critical chloride content C_{cr} . With America ACI222 [22] and Europe BS-EN206 [23] as reference, $C_{cr} = 0.063\%$ (g/cm^3); that is, 0.2% of cement weight was adopted in this paper.

As it was concluded in Section 4.1, the chloride diffusion coefficient (D_w) decreased as exposure duration increased in

service life. Stanish and Thomas [24] used (7) to describe the time-dependent change of chloride diffusion coefficient,

$$D_t = D_{\text{ref}} \left(\frac{t_{\text{ref}}}{t}\right)^m, \quad (7)$$

where D_t is chloride diffusion coefficient at time t , D_{ref} is the chloride diffusion coefficient at reference time t_{ref} ($t_{\text{ref}} = 28$ d), and m is the so-called ageing factor.

According to study of Stanish and Thomas [24], the relationship between D_t and t can be expressed as follows:

$$D_t = \begin{cases} D_{\text{ref}} \left(\frac{t_{\text{ref}}}{t}\right)^m & t \leq t_R \\ D_{\text{ref}} \left(\frac{t_{\text{ref}}}{t_R}\right)^m = D_{t_R} & t > t_R, \end{cases} \quad (8)$$

where t_R is the time after which the diffusion coefficient is assumed to remain constant and t_R is generally assumed to be 30 years [12].

Tang and Gulikers [25] substitute (8) into (9) to get T . Consequently, T can be expressed by (10),

$$T = \int_{t_1}^{t_2} D_t dt \quad (9)$$

T

$$= \begin{cases} \frac{D_{\text{ref}} (t_{\text{ref}})^m}{(1-m)} (t_2^{1-m} - t_1^{1-m}) & t_2 \leq t_R \\ D_{\text{ref}} \left[\frac{(t_{\text{ref}})^m (t_R^{1-m} - t_1^{1-m})}{(1-m)} + \left(\frac{t_{\text{ref}}}{t_R}\right)^m (t_2 - t_R) \right] & t_2 > t_R, \end{cases} \quad (10)$$

where t_1 is the start of exposure period and t_2 is the end of exposure period.

In this paper, crack factor (α_w) was introduced to consider the effect of cracks and (3) was used to take the place of D_t in (9), referring to Section 4.2. And time decay factor (α_t) was introduced to take the place of m , referring to Section 4.1. So T can be calculated by (11) which are derived from (10). Based on C_s and D_{ref} of each sample, substituting the critical chloride content $C_{cr} = 0.063\%$, concrete cover $x = 30$ mm, $t_1 = t_{\text{ref}} = 28$ d, $t_R = 30$ year, and each C_i , α_w , and α_t into (12), the magnitude of t_2 could be calculated as calculated service life.

$$T = \begin{cases} \alpha_w \frac{D_{\text{ref}} (t_{\text{ref}})^{\alpha_t}}{(1-\alpha_t)} (t_2^{1-\alpha_t} - t_1^{1-\alpha_t}) & t_2 \leq t_R \\ \alpha_w D_{\text{ref}} \left[\frac{(t_{\text{ref}})^{\alpha_t} (t_R^{1-\alpha_t} - t_1^{1-\alpha_t})}{(1-\alpha_t)} + \left(\frac{t_{\text{ref}}}{t_R}\right)^{\alpha_t} (t_2 - t_R) \right] & t_2 > t_R \end{cases} \quad (11)$$

$$C_{\text{cr}} = C_s - (C_s - C_i) \cdot \operatorname{erf}\left(\frac{x}{2\sqrt{t}}\right). \quad (12)$$

4.4.2. *Prediction of Residual Service Life.* Figure 15 shows the residual service life of RC beam specimens in Groups A,

B, and D. As can be seen from Figure 15, as crack width increased to 120 microns, the residual service life of RC beam

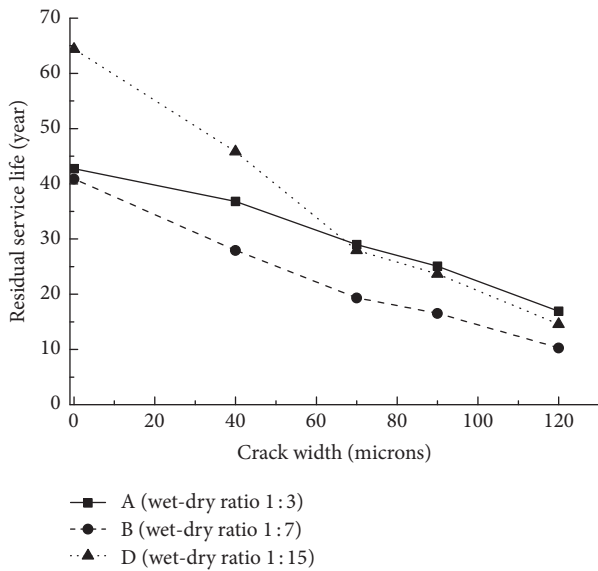


FIGURE 15: Residual service life of RC beams with the increase of crack widths.

specimens decreased from 43 years to 17 years in Group A (wet-dry ratio 1:3), 41 years to 10 years in Group B (wet-dry ratio 1:7), and 64 years to 15 years in Group D (wet-dry ratio 1:15), respectively. As mentioned above, chloride diffusivity of Group B (wet-dry ratio 1:7) was accelerated most and subsequently Group B (wet-dry ratio 1:7) showed the shortest residual service life, compared with Group A (wet-dry ratio 1:3) and Group D (wet-dry ratio 1:15).

5. Conclusion

This study investigated the combined effects of crack width, wet-dry ratio, and exposure duration of wet-dry cycles on chloride ions diffusion of RC beams to simulate working conditions of RC structures. The chloride diffusion model was obtained based on the experiments, which considered crack width, wet-dry ratio, and exposure duration. The life prediction model of RC structures and critical value of chloride ion content were also concluded. Conclusions specifically are as follows:

- (1) The chloride content along the depth of concrete cover increased significantly when crack width was larger than 90 microns and wet-dry ratio was 1:3, and the chloride content increased slightly as crack width increased from 0 to 120 microns when wet-dry ratios were 1:7, 1:11, and 1:15, respectively.
- (2) When crack width was less than 90 microns and wet-dry ratio was 1:7, the chloride content on steel bar surface was the largest of four wet-dry ratios (1:3, 1:7, 1:11, and 1:15). And when crack width was equal to or greater than 90 microns and wet-dry ratio was 1:3, the chloride content on steel bar surface was the largest.
- (3) Based on the testing results of chloride content on steel bar surface and the analysis results of chloride

diffusion coefficient, the suitable ratio of wetting and drying duration was 1:7, which was conducive to the chloride ingress for the cracked RC structures of working conditions.

- (4) The chloride diffusion model and prediction model of residual service life of RC beams were suggested, taking the combined effects of crack width and exposure duration into consideration. The predicted residual service life decreased with the increase of crack width and the residual service lives of RC structures predicted here were corresponding well with the experimental results.

Conflicts of Interest

The authors declare that there are no conflicts of interest regarding the publication of this paper.

Acknowledgments

This work was financially supported by the National Natural Science Foundation of China (Grant no. 51678021) and the Open Project of State Key Laboratory of Subtropical Building Science, South China University of Technology (2016ZA03).

References

- [1] B. Diao, Y. Sun, S. Cheng, and Y. Ye, "Effects of mixed corrosion, freeze-thaw cycles, and persistent loads on behavior of reinforced concrete beams," *Journal of Cold Regions Engineering*, vol. 25, no. 1, pp. 37–52, 2010.
- [2] K. Hong and R. D. Hooton, "Effects of cyclic chloride exposure on penetration of concrete cover," *Cement and Concrete Research*, vol. 29, no. 9, pp. 1379–1386, 1999.
- [3] C. Li and K. Li, "Chloride ion transport in cover concrete under drying-wetting cycles: theory, experiment and modeling," *Journal of the Chinese Ceramic Society*, no. 4, pp. 581–589, 2010 (Chinese).
- [4] X. Gang, L. Yun-Pan, S. Yi-Biao, and X. Ke, "Chloride ion transport mechanism in concrete due to wetting and drying cycles," *Structural Concrete*, vol. 16, no. 2, pp. 289–296, 2015.
- [5] W. Jin, *Theory and Design Method of Durability of Concrete Structures in Chloride Environment*, The Science Publishing Company, Beijing, China, 2011, (Chinese).
- [6] P. S. Mangat and B. T. Molloy, "Prediction of long term chloride concentration in concrete," *Materials and Structures*, vol. 27, no. 6, pp. 338–346, 1994.
- [7] M. K. Moradillo, M. Shekarchi, and M. Hoseini, "Time-dependent performance of concrete surface coatings in tidal zone of marine environment," *Construction and Building Materials*, vol. 30, pp. 198–205, 2012.
- [8] M. Şahmaran, "Effect of flexure induced transverse crack and self-healing on chloride diffusivity of reinforced mortar," *Journal of Materials Science*, vol. 42, no. 22, pp. 9131–9136, 2007.
- [9] P. P. Win, M. Watanabe, and A. Machida, "Penetration profile of chloride ion in cracked reinforced concrete," *Cement and Concrete Research*, vol. 34, no. 7, pp. 1073–1079, 2004.
- [10] Y. Lei, Y. Ye, B. Shen et al., "Effect of crack widths on durability of RC columns under seawater wet-dry cycles," *Concrete*, no. 5, pp. 18–22, 2015.

- [11] C. Q. Li, "Initiation of chloride-induced reinforcement corrosion in concrete structural members—experimentation," *Structural Journal*, vol. 98, no. 4, pp. 502–510, 2001.
- [12] B. Shen, Y. Ye, B. Diao, and X. Zheng, "Mechanical performance and chloride diffusivity of cracked Rc specimens exposed to freeze-thaw cycles and intermittent immersion in seawater," *Advances in Materials Science and Engineering*, vol. 2016, Article ID 5973467, 10 pages, 2016.
- [13] JTJ 270-98, "Testing code of concrete for port and waterwog engineering," Tech. Rep., China Communications Press, Beijing, China, 1998, (Chinese).
- [14] Z. Liu, B. Diao, and X. Zheng, "Effects of seawater corrosion and freeze-thaw cycles on mechanical properties of fatigue damaged reinforced concrete beams," *Advances in Materials Science and Engineering*, vol. 2015, Article ID 536487, 15 pages, 2015.
- [15] R. P. Chaube, T. Shimomura, and K. Maekawa, "Multiphase water movement in concrete as a multi-component system," in *Proceeding of the 5th RILEM International Symposium on Creep and Shrinkage in Concrete*, pp. 139–144, E & FN, Barcelona, Spain, 1993.
- [16] W. Jin, Y. Zhang, and Z. Lu, "Mechanism and mathematic modeling of chloride permeation in concrete under unsaturated state," *Journal of the Chinese Ceramic Society*, vol. 36, no. 10, pp. 1362–1369, 2008.
- [17] E. P. Nielsen and M. R. Geiker, "Chloride diffusion in partially saturated cementitious material," *Cement and Concrete Research*, vol. 33, no. 1, pp. 133–138, 2003.
- [18] M. D. A. Thomas and P. B. Bamforth, "Modelling chloride diffusion in concrete effect of fly ash and slag," *Cement and Concrete Research*, vol. 29, no. 4, pp. 487–495, 1999.
- [19] M. Collepardi, A. Marcialis, and R. Turriziani, "Penetration of chloride ions into cement pastes and concretes," *Journal of the American Ceramic Society*, vol. 55, no. 10, pp. 534–535, 1972.
- [20] M. Jiang, H. Lu, X. Kou et al., "Diffusion model study of chloride ion in concrete structure under chlorine salt corrosion environment," *Concrete*, no. 5, pp. 46–49, 2013 (Chinese).
- [21] S. J. Kwon, U. J. Na, S. S. Park, and S. H. Jung, "Service life prediction of concrete wharves with early-aged crack: probabilistic approach for chloride diffusion," *Structural Safety*, vol. 31, no. 1, pp. 75–83, 2009.
- [22] B. B. Hope and C. K. Nmai, *Protection of Metals in Concrete against Corrosion*, vol. 222, American Concrete Institute Committee, 2001.
- [23] EN T S. 206-1, *Concrete-Part 1: Specification, Performance, Production and Conformity*, Turkish Standards Institution, Ankara, Turkey, 2002.
- [24] K. Stanish and M. Thomas, "The use of bulk diffusion tests to establish time-dependent concrete chloride diffusion coefficients," *Cement and Concrete Research*, vol. 33, no. 1, pp. 55–62, 2003.
- [25] L. P. Tang and J. Gulikers, "On the mathematics of time-dependent apparent chloride diffusion coefficient in concrete," *Cement and Concrete Research*, vol. 37, no. 4, pp. 589–595, 2007.

Review Article

Micromechanics of Cracked Laminates under Uniaxial Load: A Comparison between Approaches

J. A. Rivera-Santana, A. Guevara-Morales, and U. Figueroa-López

Escuela de Ingeniería y Ciencia, Tecnológico de Monterrey, Campus Estado de Mexico, Carretera Lago de Guadalupe Km. 3.5, Margarita Maza de Juárez, 52926 Atizapán de Zaragoza, MEX, Mexico

Correspondence should be addressed to U. Figueroa-López; ufiguero@itesm.mx

Received 10 February 2017; Revised 20 April 2017; Accepted 9 May 2017; Published 5 June 2017

Academic Editor: Paulo M. S. T. De Castro

Copyright © 2017 J. A. Rivera-Santana et al. This is an open access article distributed under the Creative Commons Attribution License, which permits unrestricted use, distribution, and reproduction in any medium, provided the original work is properly cited.

This paper compares stiffness degradation models of cross-ply glass fiber/epoxy laminates based on four of the most commonly used approaches to micromechanical modelling: shear-lag, variational, McCartney, and synergistic damage mechanics (SDM). All of these include the process of defining $[0/90]_s$ laminate unit cell, from which governing differential equations and corresponding boundary conditions are stated. Afterwards, these boundary value problems (BVP) are solved in order to obtain a stress function which couples the initial and perturbation stresses, the latter being in function of crack density, thus related to material stiffness reduction. When compared against experimental results, shear-lag model presented accurate results however, additional differentiation and integration steps were required in order to obtain the final stress field. Hashin's variational method predicts correctly the boundary conditions at crack surfaces and gives out the complete stress field. McCartney's approach shows further improvement over the previous two models, taking into account thermal strains and stresses. Finally, SDM, which is designed for numerical experimentation, implying a more economical alternative in comparison to traditional physical experimentation, also presented very good agreement with experimental results and can be extended to arbitrary laminate stackings, going beyond the classical cross-ply.

1. Introduction

Composite laminates have found increased use in mechanical applications over the last years, especially in areas related to aerospace, civil, and mechanical systems. Efforts have been particularly intense on damage assessment of large composite structures. There are many models such as the ones developed by Shokrieh [1] that focus on the degradation of mechanical properties, relying on experimental curve fits which do not necessarily have a direct physical interpretation. This can represent a large obstacle for understanding the mechanisms of onset and propagation of damage over a component or structure.

Of these damage modes, matrix cracking has received the most attention, followed by delamination. After the material reaches certain level of crack density, there is progressively less space for transverse crack formation. This phenomenon is known as crack saturation [2] and the corresponding

density is known as Characteristic Damage State (CDS), but before this happens, delamination may occur. Delamination [3] is the mechanism of separation between plies caused by an interfacial weakening partially due to previously formed intralaminar cracks. Delamination proves to be more catastrophic than matrix cracking, because it could render the structure useless in a short amount of time driving it to failure [4].

Matrix cracking in 90-degree plies was first studied by Reifsneider [5], who experimentally investigated this phenomenon on $[0/\pm 45/90]_s$ laminates subjected to uniaxial quasistatic and cyclic tests. Although practical, physical experiments can become relatively expensive when less assumption is considered, especially when compared with ever-increasing computer capacity [6].

The first micromechanical model was shear-lag, introduced by Garrett and Bailey [7–9] and significantly improved by Cox [10]. Shear-lag model relies on the basic principle that

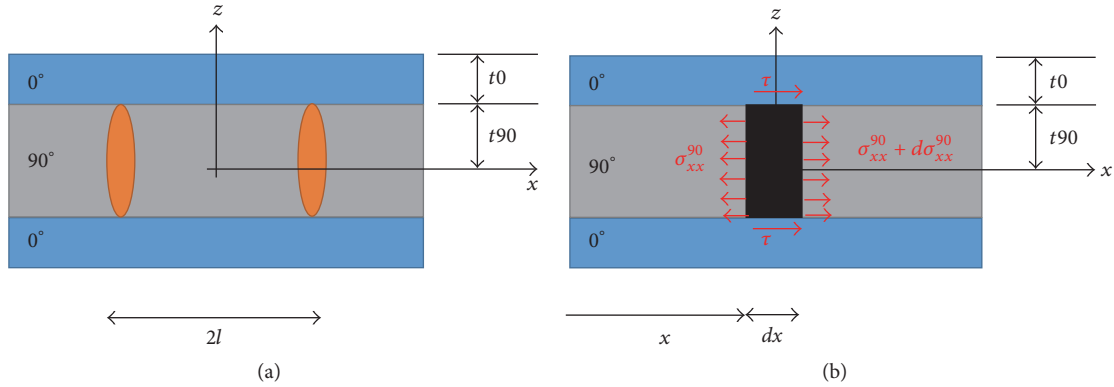


FIGURE 1: Unit cell for shear-load and variational methods. (a) Geometry. (b) Equilibrium. The crack is supposed to span all the laminate width, adapted from [12, 14].

relaxed stresses arising from the formation of intralaminar cracks transfer to ply interface [11] in form of shear stress, increasing in turn the occurrence of delamination. In the present review, Berthelot complete parabolic shear-lag model is used [12], which means a parabolic variation of axial displacement is introduced for both 0- and 90-degree layers (see (1a)-(1b)). Then, corresponding stress functions are obtained, which ultimately translate into stress accumulation and degradation mechanical properties, particularly stiffness [13].

Another family of micromechanical approaches is proposed by Hashin [14] who proposes a variational stress-perturbation function, departing from crack-free stress state. In order to achieve this, Hashin applied the minimum complementary energy principle and optimized it. Subsequently, the total stress field (crack-free plus perturbation) was recovered for cross-ply $(0/90_m)_s$ laminates. Similar to the first approach, the stresses formed cracks, which in turn translated in material degradation, chiefly stiffness reduction. Hashin's variational analysis has become a seminal work in the field of micromechanical damage analysis on composite materials [14]. For example, it has been used and adapted for predicting fatigue [15], random crack growth [16], and delamination [17]. Thereafter, McCartney [18] introduced his model based on Hashin's variational approach and classical elasticity, presenting three novelties: inclusion of the thermal expansion strains, explicit expressions for displacements, and a further expansion to three-dimensional stress evaluation that will not be reviewed in this work.

Continuum damage mechanics (CDM) is another family that has become more commonplace in literature over the last years due to increased computational capacity. These models are based on updating stiffness matrices in function of crack opening displacement (COD) or density. Their scheme may be iterative, such as the so-called self-consistent methods [19, 20] and the proposed by Barbero [21–23], or departing from an initial set of real-life [24] or virtual finite element simulations such as the Synergistic Damage Mechanics (SDM) model presented by Singh and Talreja [25–27], which expanded the scope of micromechanical modelling to laminates other than cross-ply.

Driven by aerospace and wind energy applications in which other laminate configurations such as the $[0/\pm 45/90]_s$

are preferred, recent models such as the ones proposed by Hajikazemi [28] and Adumitroaie [29] have also expanded to laminates other than cross-ply. However, as these models are usually extensions of previous models (Hashin's variational for the case of Hajikazemi's model and SDM for Adumitroaie's model), the main goal of this work is drawing a comparison between these four approaches (shear-lag, Hashin's variational, McCartney, and SDM) and highlighting the advantages and setbacks for each one. This comparison will be helpful for selecting the most appropriate matrix cracking approach for future works related to damage propagation in fiber-reinforced polymers for different applications. The nomenclature used throughout the article is summarized in the Nomenclature.

2. Models

2.1. Shear-Lag Model. As mentioned above, the shear-lag models were the first approaches on intralaminar cracking. The basic governing principle consists in stress redistribution along the loading direction causing an increase in interfacial shear-load due to crack onset. The basic unit cell is shown in Figure 1, representing a symmetric $(0/90)_s$ laminate element composed of two 0° -degree outer plies of thickness t_0 and a 90° -degree inner ply of thickness t_{90} . Total laminate thickness is thus $h = 2(t_0 + t_{90})$. In addition, x is loading direction, $2l$ is crack spacing, and ply interface is located along coordinate $z = t_{90}$.

Shear-lag model is considerably simple compared to the other approaches presented below because of the following assumptions: (a) plane stress and (b) longitudinal stresses σ_{xx} are assumed to be uniform across the thickness of 0° and 90° plies and (c) the tensile load applied to 0° plies is considered to be transmitted into the 90° ply by shear of the transverse ply [12].

However, these assumptions may compromise the accuracy of the model. For this reason, Berthelot [12] introduced parabolic profiles for x -direction displacements in 0- and 90-degree plies.

$$u_0(x, z) = A_0(x)z^2 + B_0(x)z + C_0(x) \quad (1a)$$

$$u_{90}(x, z) = A_{90}(x)z^2 + B_{90}(x)z + C_{90}(x), \quad (1b)$$

TABLE I: Comparison of boundary conditions of the four models analyzed in the present article.

| <i>Boundary conditions governing shear lag model [12]</i> | |
|---|--|
| (i) Traction free crack surfaces | $\bar{\sigma}_{xx}^{90}(l) = 0$ |
| (ii) Interlaminar shear stress symmetry condition | $\tau(0) = 0$ |
| <i>Boundary conditions governing variational model [14]</i> | |
| (i) Symmetry | $\sigma_{xz}^{90}(x, 0) = 0$ |
| (ii) Traction continuity | $\sigma_{xz}^{90}(x, t_{90}) = \sigma_{xz}^0(x, t_{90})$ $\sigma_{zz}^{90}(x, t_{90}) = \sigma_{zz}^0(x, t_{90})$ |
| (iii) Traction-free end | $\sigma_{xz}^0(x, h) = 0$ $\sigma_{zz}^0(x, h) = 0$ |
| (iv) Traction-free crack surfaces | $\sigma_{xx}^{90}(\pm a, z) = -\sigma_{90}$ $\sigma_{xz}^{90}(\pm a, z) = 0$ |
| <i>Boundary conditions governing McCartney model [18]</i> | |
| (i) Perfect interlaminar bonding | $\sigma_{xx}^m = \sigma_{xx}^f, \sigma_{xy}^m = \sigma_{xy}^f @ x = a, y \leq L$ $u_m = u_f, v_m = v_f @ x = a, y \leq L$ |
| (ii) Stress-free external surface of outer plies | $\sigma_{xx}^f = 0, \sigma_{xy}^f = 0 @ x = h, y \leq L$ |
| (iii) Symmetry about y -axis | $\sigma_{xy}^m = 0, u_m = 0 @ x = 0, y \leq L$ |
| (iv) Symmetry about x -axis | $\sigma_{xy}^m = 0, v_m = 0 @ y = 0, 0 \leq x \leq a$ $\sigma_{xy}^f = 0, v_f = 0 @ y = 0, a \leq x \leq h$ |
| (v) Stress-free crack surface | $\sigma_{yy}^m = 0, \sigma_{xy}^m = 0 @ y = L, 0 \leq x \leq a$ $\sigma_{xy}^f = 0 @ y = L, a \leq x \leq h$ |
| (vi) Bridging outer plies | $v_f = L e_x @ y = L, a \leq x \leq h$ |
| <i>Boundary conditions governing SDM model [25]</i> | |
| (i) Symmetry about midplane | $w = 0 @ z = 0$ |
| (ii) Displacement condition at right face | $u = u^0 @ x = 2l = s_\alpha$ |
| (iii) Fixture at left face | $u = 0 @ x = 0$ |

where A , B , and C are integration constants. These profiles are then introduced within the framework of classic equations for elasticity: first kinematics (strain-displacement), then compliance, and finally equilibrium within the unit cell shown in Figure 1(b) [12].

$$\frac{\partial \bar{\sigma}_{xx}^{90}}{\partial x} + \frac{\partial \sigma_{xz}^{90}}{\partial z} = 0. \quad (2)$$

This produces the boundary value problem (BVP) with governing equation in terms of average longitudinal stress in the 90-degree layer ($\bar{\sigma}_{xx}^{90}$)

$$\frac{d^2 \bar{\sigma}_{xx}^{90}}{dx^2} - \lambda^2 \bar{\sigma}_{xx}^{90} = -\lambda^2 \frac{E_{22}}{E_x^0} \sigma_c, \quad (3a)$$

where $\lambda^2 = 3G_{xy}^0(t_0 + t_{90})E_x^0/t_{90}^2 t_0 E_{11} E_{22}$, and the laminate stiffness constants for shear $G_{xy}^0 = G_{23}/(1 + t_0 G_{23}/t_{90} G_{12})$ and Young's modulus $E_x^0 = (t_0 E_{11} + t_{90} E_{22})/(t_0 + t_{90})$, subject to a global load σ_c .

This governing equation is subject to the boundary conditions (BCs) shown in Table 1.

Thus, the complete solution for x -direction stress field in 0-degree and 90-degree plies is given out by

$$\bar{\sigma}_{xx}^{90}(x) = \sigma_c \frac{E_{22}}{E_x^0} \left(1 - \frac{\cosh \eta a (x/l)}{\cosh \eta a} \right) \quad (4a)$$

$$\bar{\sigma}_{xx}^0(x) = \sigma_c \frac{E_{11}}{E_x^0} \left(1 + \frac{t_{90} E_{22}}{t_0 E_{11}} \frac{\cosh \eta a (x/l)}{\cosh \eta a} \right) \quad (4b)$$

$$\begin{aligned} \sigma_{xx}^0(x, z) = & \bar{\sigma}_{xx}^0(x) - \sigma_c \frac{E_{11}}{2G_{12}} \frac{E_{22}}{E_x^0} \frac{t_{90}}{t_0} \\ & \cdot \eta^2 \left[\left(\frac{z}{t_{90}} \right)^2 - 2(1 + \alpha) \frac{z}{t_{90}} + \frac{2}{3} \alpha^2 + 2\alpha + 1 \right] \\ & \cdot \frac{\cosh \eta a (x/l)}{\cosh \eta a} \end{aligned} \quad (4c)$$

$$\begin{aligned} \sigma_{xx}^{90}(x, z) = & \bar{\sigma}_{xx}^{90}(x) + \sigma_c \frac{E_{22}^2}{2G_{23} E_x^0} \eta^2 \left[\left(\frac{z}{t_{90}} \right)^2 - \frac{1}{3} \right] \\ & \cdot \frac{\cosh \eta a (x/l)}{\cosh \eta a} \end{aligned} \quad (4d)$$

$$a = \frac{l}{t_{90}} \quad (4e)$$

$$\eta^2 = \lambda^2 t_{90}^2 = \frac{3G_{xy}^0 (t_0 + t_{90}) E_x^0}{t_0 E_{11} E_{22}} \quad (4f)$$

$$\alpha = \frac{t_0}{t_{90}}, \quad (4g)$$

where (4e) expresses the aspect ratio a . This parameter is of great importance as it reflects the relationship of crack spacing to ply thickness, having a profound impact on the degradation model. Meanwhile, (4g) shows the stacking parameter α . Shear-lag method calculates in a straightforward fashion the interfacial shear-load that may be applied later to delamination models. The complete model for inter-laminar shear stress is also obtained as follows:

$$\tau(x) = \sigma_c \frac{E_{22}}{E_{11}} \eta \frac{\sinh \eta a (x/l)}{\cosh \eta a}. \quad (5)$$

The shear stress field is obtained introducing (4c)-(4d) into (2) and solving for σ_{xz} . Subsequently the z -direction axial stress field is obtained introducing this solution into equilibrium equation (6) and solving for σ_{zz} . This procedure is repeated for the 0-degree ply.

$$\frac{\partial \sigma_{xz}^{90}}{\partial x} + \frac{\partial \sigma_{zz}^{90}}{\partial z} = 0. \quad (6)$$

Finally, these stresses have an effect on the material, which is reflected in degradation rules such as the stiffness reduction formula obtained by Ogin [13]:

$$\frac{E_x}{E_x^0} = \frac{1}{1 + (t_{90}/t_0) (E_{22}/E_{11}) (1/\eta a) \tanh \eta a}. \quad (7)$$

2.2. Variational Method. In 1985, Hashin proposed another approach to solve the crack problem in a cross-ply laminate, already shown in Figure 1. The variational method is an energetic approach that consists in posing an internal energy formulation for a perturbation stress, which is considered a variation from the intact material stress, caused by crack onset. Because this is an equilibrium situation, total energy change is considered near zero, with this method being therefore soundly based on virtual work statics.

The assumptions taken for this approach are as follows:

- (i) The normal stress in external load direction is constant over ply thickness.
- (ii) Shear stresses develop only within a boundary layer of unknown thickness in between plies.
- (iii) Cracks remain sufficiently far apart so that their mutual interaction can be neglected.

Said this, the stresses in the cracked laminate are

$$\sigma_{ij}^m = \sigma_{ij,0}^m + \sigma_{ij,p}^m, \quad (8)$$

where i, j subscripts stand for x, z direction of the stresses. The index m represents the ply, whether 0- or 90-degree.

Finally, the subscript 0 represents the stress of the intact matrix and p , the perturbation stress generated by the crack. After applying the equilibrium equations obtained from basic elasticity over the region illustrated in Figure 1 and the boundary conditions listed in Table 1, the perturbation stress field in terms of intact 90-degree ply stress (σ_{90}) is found out.

$$\sigma_{xx,p}^0(x, z) = -\sigma_{90} \phi(x) \quad (9a)$$

$$\sigma_{xz,p}^0(x, z) = \sigma_{90} \phi'(x) z \quad (9b)$$

$$\sigma_{zz,p}^0(x, z) = \sigma_{90} \phi''(x) \frac{1}{2} (ht_{90} - z^2) \quad (9c)$$

$$\sigma_{xx,p}^{90}(x, z) = \sigma_{90} \left(\frac{t_{90}}{t_0} \right) \phi(x) \quad (9d)$$

$$\sigma_{xz,p}^{90}(x, z) = \sigma_{90} \left(\frac{t_{90}}{t_0} \right) \phi'(x) (h - z) \quad (9e)$$

$$\sigma_{zz,p}^{90}(x, z) = \sigma_{90} \left(\frac{t_{90}}{t_0} \right) \phi''(x) \frac{1}{2} (h - z)^2, \quad (9f)$$

where the perturbation function $\phi(x)$ is evaluated by the following formulation, provided that in most epoxy/carbon materials, $4q > p^2$:

$$\phi = A_1 \cosh \alpha_1 \xi \cos \alpha_2 \xi + A_2 \sinh \alpha_1 \xi \sin \alpha_2 \xi \quad (10a)$$

$$\xi = \frac{x}{t_{90}} \quad (10b)$$

$$A_1 = \frac{2(\alpha_1 \cosh \alpha_1 a \sin \alpha_2 a + \alpha_2 \sinh \alpha_1 a \cos \alpha_2 a)}{\alpha_1 \sin 2\alpha_2 a + \alpha_2 \sinh 2\alpha_1 a} \quad (10c)$$

$$A_2 = \frac{2(\alpha_2 \cosh \alpha_1 a \sin \alpha_2 a - \alpha_1 \sinh \alpha_1 a \cos \alpha_2 a)}{\alpha_1 \sin 2\alpha_2 a + \alpha_2 \sinh 2\alpha_1 a}, \quad (10d)$$

where $\alpha_1 = q^{1/4} \cos(1/2)\Theta$, $\alpha_2 = q^{1/4} \sin(1/2)\Theta$, and $\tan \Theta = \sqrt{4q/p^2 - 1}$. The material constants p and q may be evaluated as follows:

$$p = \frac{C_{02} - C_{11}}{C_{22}}; \quad (11a)$$

$$q = \frac{C_{00}}{C_{22}}$$

$$C_{00} = \frac{1}{E_{22}} + \frac{1}{\alpha E_{11}}; \quad (11b)$$

$$C_{02} = \left(\frac{\nu_{23}}{E_{22}} \right) \left(\alpha + \frac{2}{3} \right) - \frac{\nu_{12} \alpha}{3E_{11}}$$

$$C_{22} = \frac{(\alpha + 1)(3\alpha^2 + 12\alpha + 8)}{60E_{22}}; \quad (11c)$$

$$C_{11} = \frac{1}{3} \left(\frac{1}{G_{23}} + \frac{\alpha}{G_{12}} \right).$$

For the equations governing case $4q < p^2$, the reader is referred to Talreja [11]. As in the previous method, a stress

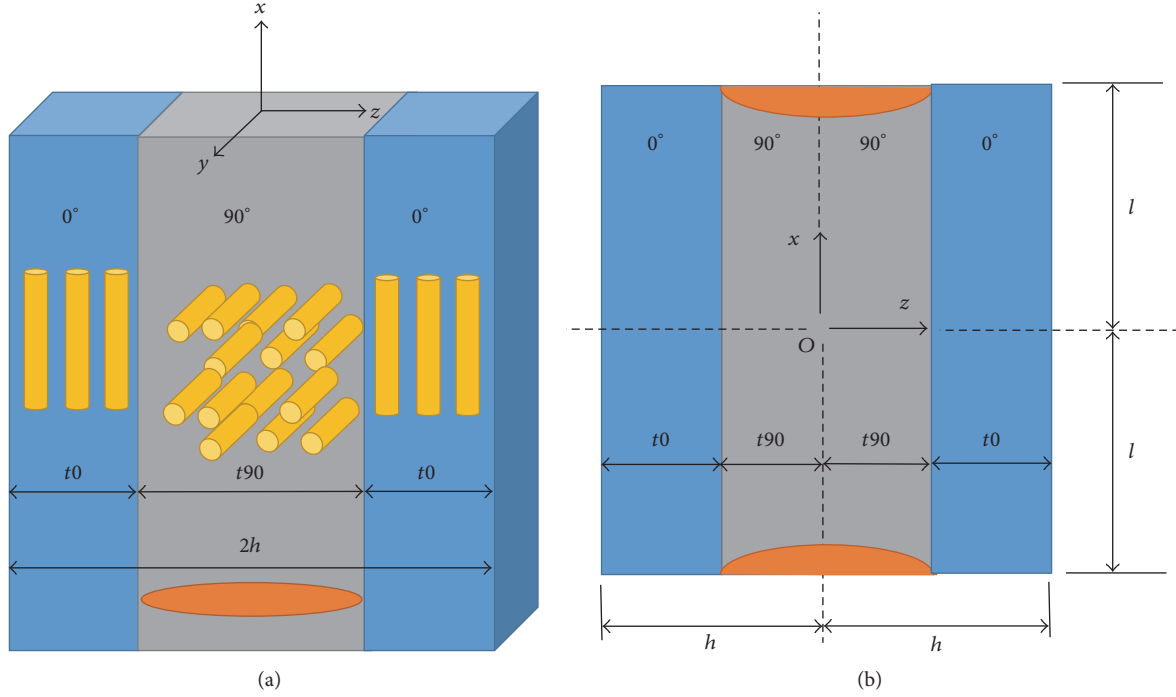


FIGURE 2: (a) Unit cell used to derive the equations of the McCartney model. (b) Coordinates for boundary conditions shown in Table 1. Adapted from [18].

field is recovered and then applied in a degradation rule that has an effect on material's elasticity.

$$\frac{1}{E_x} = \frac{1}{E_x^0} + \frac{1}{E_{22}} k_1^2 \frac{\mu(\alpha)}{a} \chi(a), \quad (12a)$$

where $k_1 = \sigma_{90}/\sigma_c$ and is obtained from traditional laminate analysis. The other functions are evaluated as follows:

$$\chi(a) = -\phi'''(\xi = a) \quad (12b)$$

$$\mu(\alpha) = \frac{(3\alpha^2 + 12\alpha + 8)}{60}. \quad (12c)$$

Finally, it is important to take into account the fact that this formulation is only applicable to equally spaced cracks. If the separation is arbitrary, a probabilistic distribution such as those used by Vinogradov [16] must be used.

2.3. McCartney Method. McCartney proposed another analytical method in 1992 [18]. Similar to variational approach, the method models the same phenomenon by optimizing an energetic expression. As in the previous two models, it only considers cross-ply laminates. Nevertheless, there are three noteworthy novelties. First of all, components of thermal expansion are taken into account for stain and stress modelling. Then, even though precision is similar to Hashin, McCartney model includes explicit expressions for displacement field. Finally, in contrast to shear-lag, the McCartney model satisfies exactly a more comprehensive set of boundary conditions. The basic unit cell of the laminate

between two cracks, subjected to uniaxial stress, is shown in Figure 2(a).

Then, from basic elasticity and including thermal strains, the field equations for generalized plane strain conditions are expressed by

$$\frac{\partial \sigma_{xx}}{\partial x} + \frac{\partial \sigma_{xz}}{\partial z} = 0,$$

$$\frac{\partial \sigma_{xz}}{\partial x} + \frac{\partial \sigma_{zz}}{\partial z} = 0$$

$$\begin{aligned} \epsilon_{xx} &= -\frac{\nu'_{12}}{E'_{11}} \sigma_{zz} + \frac{1}{E'_{11}} \sigma_{xx} + \alpha'_A \Delta T \\ &\quad - \nu_{12} \frac{E_{22}}{E_{11}} \epsilon_c^* = \frac{\partial u}{\partial x} \end{aligned} \quad (13)$$

$$\begin{aligned} \epsilon_{zz} &= \frac{1}{E'_{22}} \sigma_{zz} - \frac{\nu'_{12}}{E'_{11}} \sigma_{xx} + \alpha'_T \Delta T - \nu_{23} \epsilon_c^* \\ &= \frac{\partial w}{\partial z} \end{aligned}$$

$$\epsilon_{xz} = \frac{\sigma_{xz}}{2G_{12}} = \frac{1}{2} \left(\frac{\partial u}{\partial z} + \frac{\partial w}{\partial x} \right).$$

It is important to keep in mind that (13) actually represents two sets of equations, one for outer 0-degree plies and another one for inner 90-degree plies. Engineering elastic constants that feature an apostrophe are the modified moduli, which are shown in more details in [18]. The original moduli appear with no apostrophe. Finally, the development for the

uniform transverse strain in the cracked laminate ϵ_c^* is also shown in the referred paper. Assuming perfect interlaminar bonding, McCartney model is governed by the boundary conditions shown in Table 1 (cf. Figure 2(b)), where ϵ_c is the longitudinal strain experienced by the cracked composite and is also explained in further details in [18]. Now, assume that longitudinal stress components σ_{xx}^0 and σ_{xx}^{90} are independent of z and are of the form

$$\begin{aligned}\sigma_{xx}^0 &= C(x) + E'_{11} \left(\epsilon + \nu_{12} \frac{E'_{22}}{E'_{11}} \epsilon^* - \alpha'_A \Delta T \right) \\ &= C(x) + \sigma_0 \\ \sigma_{xx}^{90} &= -\frac{t_0}{t_{90}} C(y) + E'_{22} \left(\epsilon + \nu_{12} \epsilon^* - \alpha'_T \Delta T \right) \\ &= -\frac{t_0}{t_{90}} C(x) + \sigma_{90},\end{aligned}\quad (14)$$

where ϵ and ϵ^* are the corresponding longitudinal and transverse strains for the undamaged laminate. We now proceed to introduce (14) in field (1a) and (1b) with boundary conditions (Table 1) in order to obtain the following stress field:

$$\begin{aligned}\sigma_{xz}^0 &= C'(x)(h-z) \\ \sigma_{zz}^0 &= \frac{1}{2} C''(x)(h-z)^2 \\ \sigma_{xz}^{90} &= \frac{t_0}{t_{90}} C'(x)z \\ \sigma_{zz}^{90} &= \frac{1}{2} \frac{t_0}{t_{90}} C''(x)(ht_{90} - z^2).\end{aligned}\quad (15)$$

It is interesting to note the similarities between (10a), (10b), (10c), and (10d) from Hashin and (14) and (15) from McCartney. Now, the corresponding displacement field (16a), (16b), (16c), and (16d) is obtained

$$\begin{aligned}w_{90} &= \frac{t_0}{t_{90}} \frac{\nu'_{23}}{E'_{22}} C(x)z - \frac{1}{6} \frac{t_0}{t_{90}} \frac{1}{E'_{22}} C''(x)z(z^2 \\ &\quad - 3t_{90}h) - \left(\frac{\nu'_{23}}{E'_{22}} \sigma_{90} - \alpha'_T \Delta T + \nu_{12} \epsilon^* \right) z \\ w_0 &= \left[\frac{\nu'_{23}}{E'_{22}} t_0 - \frac{\nu'_{12}}{E'_{11}} (z - t_{90}) \right] C(x) \\ &\quad + \left\{ \frac{1}{6E'_{22}} [t_0^3 - (h-z)^3] + \frac{1}{3E'_{22}} t_0 t_{90} \left(h + \frac{1}{2} t_0 \right) \right\} \\ &\quad \cdot C''(x) - \left(\frac{\nu'_{12}}{E'_{11}} \sigma_0 - \alpha'_T \Delta T + \nu_{23} \epsilon^* \right) (z - t_{90}) \\ &\quad - \left(\frac{\nu'_{23}}{E'_{22}} \sigma_{90} - \alpha'_T \Delta T + \nu_{12} \epsilon^* \right) t_{90}\end{aligned}\quad (16a)$$

$$\begin{aligned}u_0 &= \left\{ \frac{\nu'_{12}}{2E'_{11}} (z - t_{90})^2 - \frac{\nu'_{23}}{E'_{22}} t_0 (z - t_{90}) \right. \\ &\quad \left. - \frac{1}{2G_{12}} [(z-h)^2 - t_0^2] \right\} C'(x) \\ &\quad - \left\{ \frac{1}{24E'_{22}} [(z-h)^4 + 4t_0^3(z-t_{90}) - t_0^4] \right. \\ &\quad \left. + \frac{1}{3E'_{22}} t_0 t_{90} \left(h + \frac{1}{2} t_0 \right) (z - t_{90}) \right\} C'''(x) + A(x)\end{aligned}\quad (16c)$$

$$\begin{aligned}u_{90} &= \frac{t_0}{2t_{90}} \left(\frac{1}{G_{23}} - \frac{\nu'_{23}}{E'_{22}} \right) (z^2 - t_{90}^2) C'(x) + \frac{1}{24E'_{22}} \\ &\quad \cdot \frac{t_0}{t_{90}} [z^4 - t_{90}^4 - 6t_{90}h(z^2 - t_{90}^2)] C'''(x) + A(x),\end{aligned}\quad (16d)$$

where $A(x)$ is the x -displacement at the interface of inner and outer plies

$$\begin{aligned}A(x) &= \frac{1}{E'_{11}} \bar{C}(x) - \left(\frac{\nu'_{12}}{3E'_{11}} - \frac{\nu'_{23}}{2E'_{22}} + \frac{1}{3G_{12}} \right) t_0^2 C'(x) \\ &\quad + \left[\frac{1}{20E'_{22}} + \frac{1}{12E'_{22}} \frac{t_{90}}{t_0} \left(2 \frac{t_{90}}{t_0} + 3 \right) \right] t_0^4 C'''(x) \\ &\quad + \epsilon x.\end{aligned}\quad (17)$$

And perturbation function $C(x)$, similar to Hashin's, is defined for most composites as

$$C(x) = P \cosh \frac{p_1 x}{t_0} \cos \frac{q_1 x}{t_0} + Q \sinh \frac{p_1 x}{t_0} \sin \frac{q_1 x}{t_0}\quad (18a)$$

$$p_1 = \sqrt{\frac{1}{2} \left(\frac{G}{2F} + \sqrt{\frac{H}{F}} \right)},\quad (18b)$$

$$q_1 = \sqrt{\frac{1}{2} \left| \frac{G}{2F} - \sqrt{\frac{H}{F}} \right|}$$

$$\begin{aligned}P &= \Lambda \left(q_1 \sinh \frac{p_1 l}{t_0} \cos \frac{q_1 l}{t_0} + p_1 \cosh \frac{p_1 l}{t_0} \sin \frac{q_1 l}{t_0} \right) \\ &\quad \cdot \frac{t_{90}}{t_0} \sigma_{90},\end{aligned}\quad (18c)$$

$$\begin{aligned}Q &= \Lambda \left(q_1 \cosh \frac{p_1 l}{t_0} \sin \frac{q_1 l}{t_0} - p_1 \sinh \frac{p_1 l}{t_0} \cos \frac{q_1 l}{t_0} \right) \\ &\quad \cdot \frac{t_{90}}{t_0} \sigma_{90}\end{aligned}$$

$$\frac{1}{\Lambda} = q_1 \sinh \frac{p_1 l}{t_0} \cosh \frac{p_1 l}{t_0} + p_1 \sin \frac{q_1 l}{t_0} \cos \frac{q_1 l}{t_0}.\quad (18d)$$

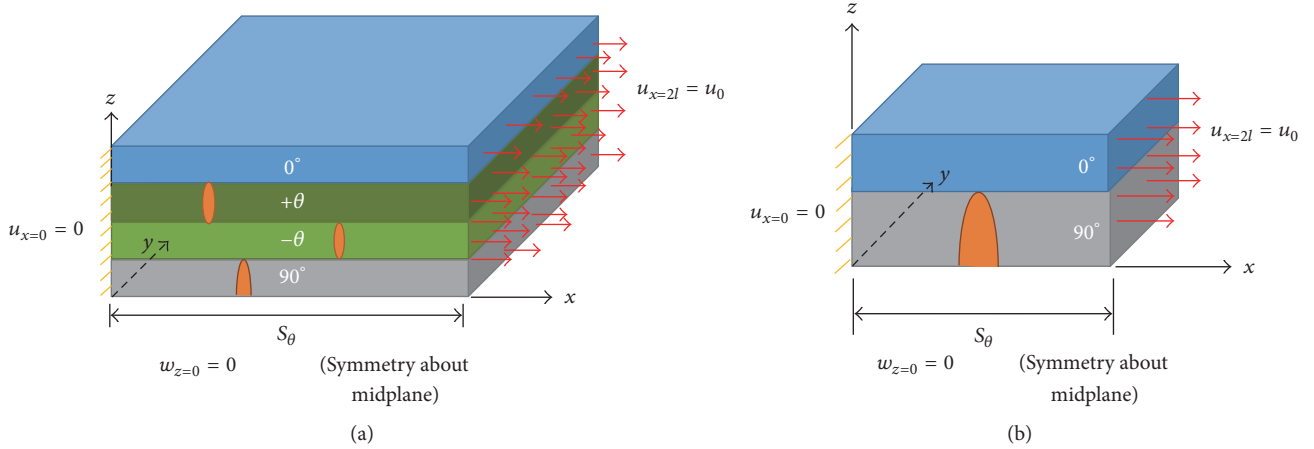


FIGURE 3: (a) Representative unit cell for a laminate under SDM micromechanics analysis, adapted from [25]. (b) Special case for cross-ply analysis, adapted from [24].

Here F , G , and H are constants dependent on geometry and material and are defined thoroughly in [18]. Then, the function $\bar{C}(x)$ is computed from the following integral:

$$\bar{C}(x) = \int_0^x C(x') dx'. \quad (19)$$

Once the perturbation function is obtained it is used to calculate stiffness reduction in the cracked laminate.

$$\frac{1}{E_x} = \frac{1}{E_x^0} + \frac{1}{\Xi} \left[\left(1 - \nu_{xy}^0 \nu_{12} \right) \frac{E'_{22}}{E_x^0} \right] \frac{t_{90}^2}{hl} H\Phi \quad (20a)$$

$$\Phi = \frac{2\Lambda p_1 q_1}{p_1^2 + q_1^2} \left(\cosh^2 \frac{p_1 l}{t_0} - \cos^2 \frac{q_1 l}{t_0} \right) \quad (20b)$$

$$\Xi = 1 - \left(\nu_{12} - \nu_{12} \frac{E_{22}}{E_{11}} \right)^2 \frac{t_0^2}{hl} \frac{\Phi}{HE_y^0}, \quad (20c)$$

where ν_{xy}^0 , E_x^0 , and E_y^0 are the longitudinal Poisson ratio and longitudinal and transverse Young's moduli of the undamaged laminate, respectively. Finally, in the same work, McCartney introduces a novel 3D version of the formerly explained model, which is not included in this analysis for the sake of comparison, and because the plane strain assumption under which the 2D model operates is enough for adequately modelling the mechanics of cracked composite plies.

2.4. Synergistic Damage Mechanics (SDM). Up to now, micromechanical models shown in Sections 2.1 to 2.3 refer to cracked composites limited to the cross-ply case, which has very limited applications. For most aerospace and wind energy applications, a $[0/\pm 45/90]_s$ configuration is more common. For this reason, Singh and Talreja developed the Synergistic Damage Mechanics (SDM) model [25], which is explained as follows.

The basic cell under which the SDM model operates is shown in Figure 3(a). The picture clearly shows that the

model is flexible for stacking more arbitrary ply orientations than those presented previously. For the sake of comparison against previous shown models, the basic cell used for simulations shown in Section 3 is also cross-ply [24], Figure 3(b); nevertheless, in this section the general case is described in order to discuss all the innovations the SDM model poses.

Of these innovations, the most important over the previous micromechanical models is that SDM can initiate and multiply cracks in any of the layers of the laminate, even if the probability of this occurring at 0° is relatively low. Each of these crack orientations is defined in SDM as damage modes, denoted by α . As it will be described, each of these modes will have their particular stress fields, stiffness changes, and damage tensors as each one of them contributes individually to the total damage state and stiffness reduction in the laminate.

The model starts with a damage state tensor \mathbf{D}_{ij}^α , with a given spacing (s^α), thickness (t^α), restriction parameter (κ^α), and orientation n_i, n_j for the damage mode α . Finally, the total laminate thickness is represented by t .

$$\mathbf{D}_{ij}^\alpha = \frac{\kappa^\alpha (t^\alpha)^2}{s^\alpha t} n_i n_j. \quad (21)$$

The normal orientation vector is expressed by $n_i = (\sin \theta, \cos \theta, 0)$. Meanwhile, the restriction parameter κ^α accounts for the constraining effect on ply cracks caused by adjacent plies in the laminate.

$$\kappa^\alpha = \frac{\bar{u}_n^\alpha}{\epsilon_{22} t^\alpha}, \quad (22)$$

where ϵ_{22} is the transformed applied strain component normal to the crack surface and \bar{u}_n^α is the normal average crack opening displacement (COD) for a given crack spacing. These averaged CODs are computed previously from a series of FE simulations using software such as ANSYS [30]. The micromechanical unit cell (Figure 3) is modelled by replicating the material stacking and elastic constants, defined by

the size of crack spacing, and three boundary conditions [25] shown in Table 1.

Another important quantity resulting from the model is the stiffness tensor and its reduction caused by the presence of the microcracks. For the case being [25], the damage stiffness tensors for each mode C_{pq}^α are expressed by

$$C_{pq}^1 + C_{pq}^2 = \frac{\kappa_\theta t_\theta}{s_\theta t} \begin{bmatrix} 2a_1^{1,2} & a_4^{1,2} & 0 \\ a_4^{1,2} & 2a_2^{1,2} & 0 \\ 0 & 0 & 2a_3^{1,2} \end{bmatrix} = D_\theta [a_i^{1,2}] \quad (23a)$$

$$C_{pq}^3 = \frac{\kappa_{90} t_{90}}{s_{90} t} \begin{bmatrix} 2a_1^3 & a_4^3 & 0 \\ a_4^3 & 2a_2^3 & 0 \\ 0 & 0 & 2a_3^3 \end{bmatrix} = D_{90} [a_i^3] \quad (23b)$$

$$C_{pq}^4 = \frac{\kappa_0 t_0}{s_0 t} \begin{bmatrix} 2a_1^4 & a_4^4 & 0 \\ a_4^4 & 2a_2^4 & 0 \\ 0 & 0 & 2a_3^4 \end{bmatrix} = D_0 [a_i^4]. \quad (23c)$$

This stiffness reduction scheme needs the determination of material constants a_{ij}^α . In order to obtain these constants, stiffness reduction curves are taken from previously described ANSYS simulations over $[0/90]_s$ laminates where the values of E_{11} , E_{22} , G_{12} , and ν_{12} are plotted against the value of crack spacing s^α for each ply. Finally, a curve fitting procedure is conducted in order to satisfy the following set of equations:

$$C_{pq} = \begin{bmatrix} \frac{E_x^0}{1 - \nu_{xy}^0 \nu_{yx}^0} & \frac{\nu_{xy}^0 E_y^0}{1 - \nu_{xy}^0 \nu_{yx}^0} & 0 \\ \frac{\nu_{xy}^0 E_y^0}{1 - \nu_{xy}^0 \nu_{yx}^0} & \frac{E_y^0}{1 - \nu_{xy}^0 \nu_{yx}^0} & 0 \\ 0 & 0 & G_{xy}^0 \end{bmatrix} - \sum_{\alpha} a_{\alpha} D_{\theta} [a_i^{\alpha}], \quad (24a)$$

where the 0-superscripted engineering constants correspond to those of the virgin laminate. For a $[0/\pm\theta/90]_s$ laminate, the total damage tensor is given by

$$\begin{aligned} \sum_{\alpha} a_{\alpha} D_{\theta} [a_i^{\alpha}] &= \sum_{\alpha} C_{pq}^{\alpha} \\ &= 2 \{C_{pq}^1 + C_{pq}^2\} + C_{pq}^3 + 2C_{pq}^4. \end{aligned} \quad (24b)$$

Once the model is ready, (24a) and (24b) is applied again, but now for the current crack separation parameter present

in the laminate. The final results are the degraded elasticity engineering constants of the material.

$$\begin{aligned} E_x &= \frac{C_{11}C_{22} - C_{12}^2}{C_{22}}, \\ E_y &= \frac{C_{11}C_{22} - C_{12}^2}{C_{22}}, \\ \nu_{xy} &= \frac{C_{12}}{C_{22}}, \\ G_{xy} &= G_{66}, \\ \nu_{yx} &= \nu_{xy} \frac{E_y}{E_x}. \end{aligned} \quad (25)$$

Subsequently, the resulting stress tensor is recalculated

$$\sigma_{ij}^{\alpha} = C_{ijkl} (D_{ij}^{\alpha}) \epsilon_{kl}. \quad (26)$$

As stated previously, even if Synergistic Damage Mechanics (SDM) model has the capability of analyzing stresses and stiffness degradation in laminates such as $[0/\pm 45/90]_s$, it is first necessary to perform simulations on cross-ply laminates. As in all other stiffness degradation models, SDM stiffness reduction for $[0/90]_s$ glass/epoxy laminates is plotted against crack density, which is also in terms of the reciprocal of crack spacing as per (27). This means that for each case of crack density ($s_\theta = 16, 8, 4, 2, 1, 0.75, 0.5, 0.2,$ and 0.1 mm) FE models were prepared and analyzed using ANSYS by applying loading, geometry, and boundary conditions as shown in Figure 3(b). An intact case simulated with highly spaced cracking ($s_\theta = 32$) was also prepared.

$$c = \frac{1}{s_\theta} = \frac{1}{2at_{90}}. \quad (27)$$

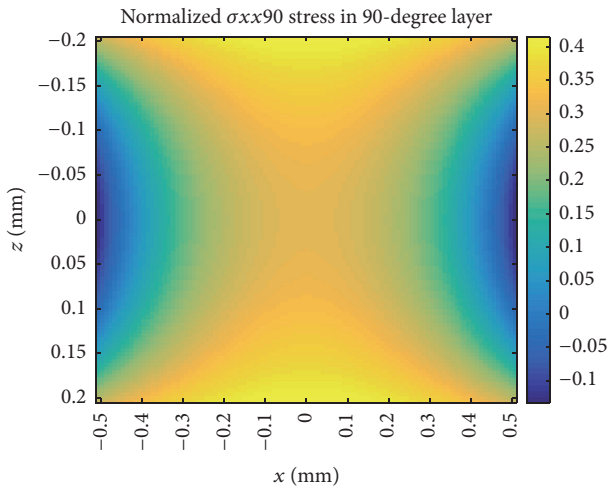
Boundary conditions for each crack spacing case remained the same, with applied displacement at right face of $(u)_{x=2l} = 5 \mu\text{m}$. Left face is fixed and there is a symmetry condition in the bottom face, along z -axis. Cracks were supposed to have grown throughout the width of the cell. Subsequently, each model was meshed using 10,000–25,000 3D tetrahedral elements. Then, stress field was recovered and averaged along the volume. At last, longitudinal Young's modulus is then obtained, according to [31], by applying the following equation:

$$E_x = \frac{\langle \sigma_{xx} \rangle}{\langle \epsilon_{xx} \rangle} = \frac{(1/V_{\text{RVE}}) \int_V \sigma_{xx} dV}{u_0/2l}, \quad (28)$$

where V_{RVE} is the volume of the whole unit cell, $\int_V \sigma_{xx} dV \sim \sum_i (\sigma_{xx,i} V_i)$, where $\sigma_{xx,i}$ and V_i are the normal axial stress and volume of element i ; u_0 is the applied displacement in the right face, as well. Finally, these curves can later be used for obtaining through fitting, materials constants a_{ij}^α , which can later be used in (24a) and (24b) in order to calculate stiffness degradation in stacking cases such as $[0/45/90]_s$.

TABLE 2: Elastic engineering constants for glass-fiber/epoxy and carbon fiber/epoxy composites [5].

| Property | GFRP | CFRP |
|--|------|-------|
| Longitudinal Young's modulus (E_{11}), GPa | 41.7 | 208.3 |
| Transverse Young's modulus (E_{22}), GPa | 13.0 | 6.5 |
| Longitudinal shear modulus ($G_{12} = G_{13}$), GPa | 3.4 | 1.65 |
| Transverse shear modulus (G_{23}), GPa | 4.58 | 2.3 |
| Longitudinal Poisson's ratio ($\nu_{12} = \nu_{13}$) | 0.3 | 0.255 |
| Transverse Poisson's ratio (ν_{23}) | 0.45 | 0.413 |

FIGURE 4: Normal longitudinal stress distribution σ_{xx} in 90-degree layer for a glass fiber/epoxy cross-ply $[0/90]_s$ laminate using Berthelot-modified shear-lag model [12].

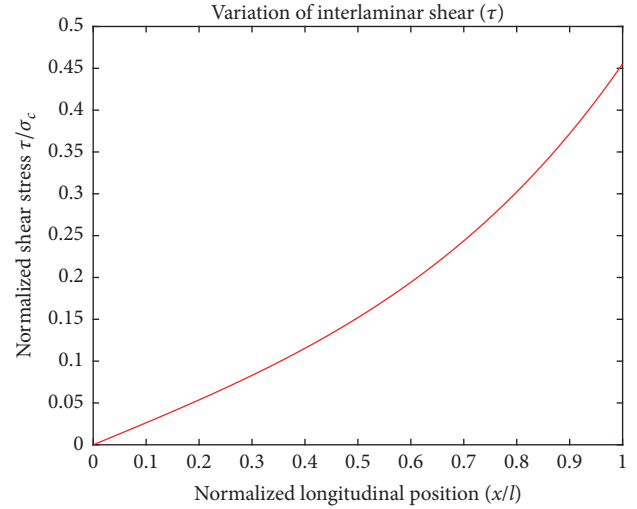
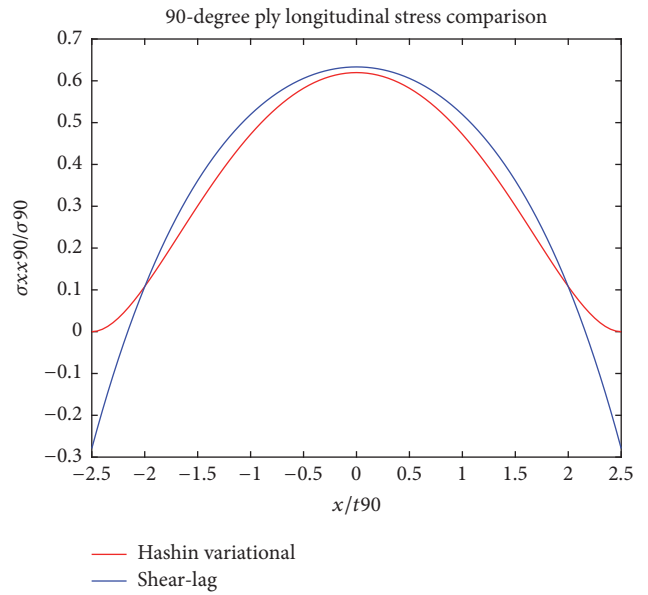
3. Results and Discussion

From the formulation explained in Section 2, stress distribution is drawn for longitudinal stress σ_{xx} in 90-degree layer for an E -glass fiber/epoxy laminate with material constants (Table 2) obtained from Highsmith and Reifsneider [5], with 90-ply thickness $t_{90} = 0.203$ mm, stacking parameter $\alpha = 1$, and aspect ratio of cracking $a = 2.5$ and $k_1 = 0.464$. Cracking aspect ratio and 90-ply thickness will be kept constant through results analysis; for other values their variation will be presented as needed.

It is seen from Figure 4 that minimum normal stress is zero and is found where the cracks are located; meanwhile the maximum longitudinal stress is found midway between consecutive cracks. Furthermore, it is observed from Figure 5 that crack onset has increased interlaminar shear.

Nevertheless, shear-lag method is at disadvantage when compared to variational micromechanics because the shear-lag assumption forces the model not to follow the zero-traction boundary condition, in stark comparison to Hashin formulation. This brings considerable error for the shear-lag method as it approaches the crack surface (Figure 6).

Taking the shear stress variation for the interface located between 0- and 90-degree plies from Hashin variational

FIGURE 5: Variation of interlaminar shear in 0/90 interface for a glass fiber/epoxy cross-ply $[0/90]_s$ composite using Berthelot-modified shear-lag model [12].FIGURE 6: Comparison of longitudinal stress obtained by shear-lag and variational methods for 90-degree ply in a glass fiber/epoxy cross-ply $[0/90]_s$ composite under longitudinal stress.

method (Figure 7(a)) [14], it is observed from Figure 7 that shear stress redistributes to somewhere in the middle between crack surface and the z -axis of symmetry because of the restriction imposed on crack surface. Again, this contrasts with Berthelot shear-lag model, which puts the maximum location of shear redistribution just above the cracking surface (Figure 5). Finally, a complete stress distribution field for σ_{xz}^{90} by Hashin method is illustrated in Figure 7(b), from where it is observed that σ_{xz}^{90} becomes progressively higher as it approaches the interlaminar interface.

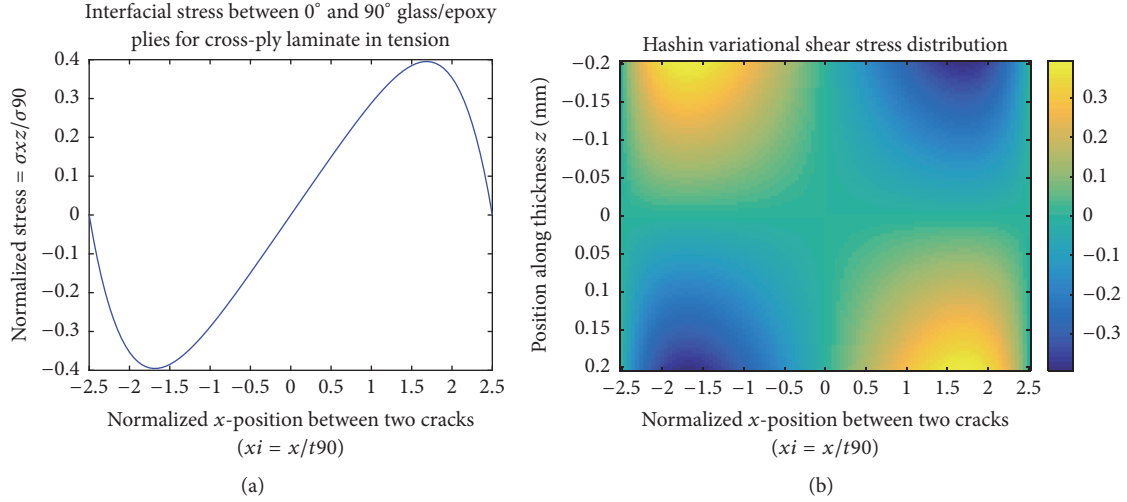


FIGURE 7: (a) Interfacial shear stress variation along the interface between 0 and 90 plies of a glass fiber/epoxy cross-ply $[0/90]_s$ laminate under longitudinal stress and (b) shear stress distribution for a glass fiber/epoxy cross-ply laminate under longitudinal stress, both using variational method [14].

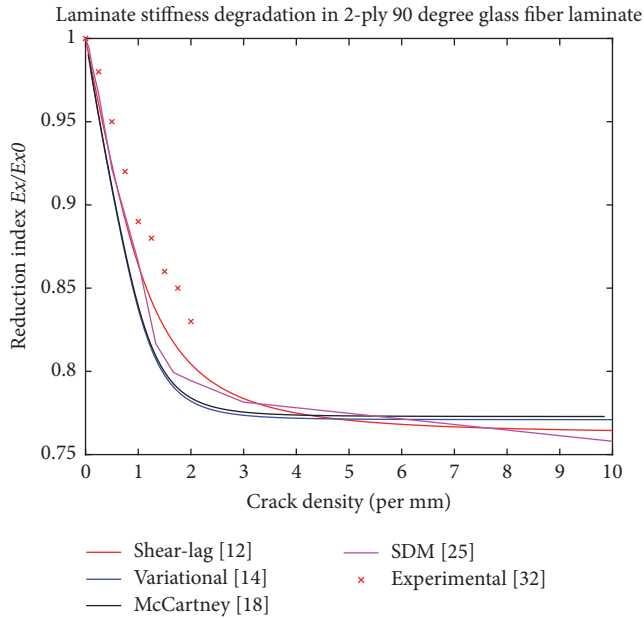


FIGURE 8: Curve comparing the four methods covered in this paper for longitudinal Young's modulus reduction on a $[0/90]_s$ glass fiber/epoxy laminate.

Afterwards, degradation of longitudinal Young's modulus $D = E_x/E_x^0$ against crack density c , (27) for $[0/90]_s$ glass/epoxy laminates ($\alpha = 1$, $k_1 = 0.464$), is plotted for all four stiffness reduction models (Figure 8). For shear-lag model used by Berthelot [12], Ogin model stiffness reduction curve is applied [13]. Meanwhile, for the Hashin variational method [14], Reifsneider formulation was employed instead [5]. McCartney [18] and SDM [25] incorporate their own stiffness reduction methods. As a first verification step, convergence for all four curves is verified against (29) proposed

by Reifsneider [5]; there is very good agreement between all model results.

$$\frac{1}{E_x} = \frac{1}{E_x^0} + \frac{k_1^2}{\alpha + 1} \left(\frac{1}{E_{22}} + \frac{1}{\alpha E_{11}} \right). \quad (29)$$

Regarding experimental results, a comparison was drawn between all four models and Smith and Wood experimentation [32]. Again, from Figure 8 it is seen that only shear-lag and SDM follow good agreement at initial cracking stages. Smith and Wood do not provide experimental results for advanced ($c > 2$ cracks/mm), nonetheless convergence has been proved with (29).

4. Conclusions

A comparison between four micromechanical models has been presented. From degradation rules, it is noticed that all four methods covered in this paper predicted convergence value quite accurately. From Hashin's variational method it is important to remark that it not only predicts correctly the boundary conditions at the surfaces of the crack but also readily gives out the complete stress field. Although limited by model assumptions, there are novel methods capable of analyzing arbitrary stacking [28] based on Hashin's approach. In contrast, shear-lag degradation model is more accurate when compared against experimental results [32] but it takes additional differentiation and integration steps in order to obtain the final stress field. However, the assumptions under which it is governed limit its application to cross-ply laminates.

McCartney's approach shows further improvement over the last two methods because it takes the generalized plane strain assumption, which soundly resonates with laminate mechanics. This model is also unique because it takes into account thermal strains and stresses. Furthermore,

this model is applied to multiaxial loading conditions. By last, McCartney provides explicit expressions for computing displacements throughout the laminate cell. However, McCartney model is computationally expensive because of higher order differentiation involved in the computation of stiffness reduction.

For the case of SDM, the model not only converges but also replicates experimental results with relative accuracy. Furthermore, SDM is designed for numerical experimentation, implying a more economical alternative in comparison to traditional physical experimentation. Damage mechanics models present the advantage of being flexible because they may be applied to a wider range of laminate stacking, going beyond the classical cross-ply case and thus proving more useful in practical cases that involve laminates of arbitrary stacking [23, 25], such as the widely used $[0/\pm 45/90]_s$ laminates. However, these modelling approaches may be computationally expensive and heavily dependent on mesh size for the case of virtual simulations.

Nomenclature

| | |
|------------------------------------|---|
| $A(x)$: | Interlaminar region displacement function (only McCartney model) |
| A_1, A_2 : | Integration constants (variational method) |
| A_0, B_0, C_0 : | Integration constants for parabolic displacement profile in 0-degree plies (shear-lag) |
| A_{90}, B_{90}, C_{90} : | Integration constants for parabolic displacement profile in 90-degree plies (shear-lag) |
| $C(x)$: | McCartney perturbation function |
| $C_{00}, C_{22}, C_{02}, C_{11}$: | Variational method material constants |
| C_{pq} : | Damaged stiffness tensor |
| C_{pq}^0 : | Undamaged stiffness tensor |
| D_{ij}^{α} : | SDM damage tensor |
| E_{11} : | Ply longitudinal Young's modulus |
| E_{22} : | Ply transverse Young's modulus |
| E_x^0 : | Intact laminate longitudinal Young's modulus |
| E_y^0 : | Intact laminate transverse Young's modulus |
| E_x : | Cracked laminate longitudinal Young's modulus |
| F, G, H : | McCartney material constants |
| G_{12} : | Ply in-plane shear modulus |
| G_{23} : | Ply out-of-plane shear modulus |
| P, Q : | McCartney integration constants |
| V_{RVE} : | Volume of unit cell |
| a : | Crack aspect ratio |
| a_{ij}^{α} : | SDM material constants for α ply |
| c : | Crack density |
| h : | Half-laminate thickness |
| k_1 : | Stress ratio in cross-ply laminates, obtained from classical lamination theory (CLT) |

| | |
|----------------------------------|--|
| l : | Half crack spacing |
| n_i, n_j : | Normal orientation vectors |
| p, q : | Variational method material constants |
| p_1, q_1 : | McCartney integration constants |
| s^{α} : | Crack spacing, that is, $s^{\alpha} = 2l$ |
| t_0, t_{90}, t : | Ply thickness |
| u, v, w : | Displacements |
| u_0 : | Applied displacement |
| \bar{u}_n : | Normal average crack opening displacement |
| x, y, z : | Positions |
| ΔT : | Temperature increase |
| Θ : | Variational method integration constant |
| Λ : | McCartney integration constant |
| Ξ, Φ : | McCartney material degradation constants |
| α : | Laminate stacking parameter |
| α_1, α_2 : | Variational method integration constants |
| α_A, α_T : | Longitudinal and transverse thermal expansion coefficients |
| ϵ, ϵ^* : | Longitudinal and transverse strains in undamaged laminates |
| ϵ_c, ϵ_c^* : | Longitudinal and transverse strains in cracked laminates |
| $\epsilon_{ii}, \epsilon_{ij}$: | Normal and shear strain |
| η : | Shear-lag integration constant |
| θ : | Ply orientation respect loading axis |
| κ : | SDM interlaminar restriction parameter |
| λ : | Shear-lag integration constant |
| ν_{12} : | In-plane ply Poisson's ratio |
| ν_{23} : | Out-of-plane ply Poisson's ratio |
| ν_{xy}^0 : | In-plane intact laminate Poisson's ration |
| ξ : | Normalized x -position coordinate |
| σ_0, σ_{90} : | Stress in intact 0- and 90-degree plies |
| σ_c : | Longitudinal load applied on laminate |
| σ_{ii} : | Normal stress |
| σ_{ij} : | Shear stress |
| $\bar{\sigma}_{xx}$: | Average longitudinal stress |
| $\tau(x)$: | Interlaminar shear stress function |
| ϕ : | Variation method perturbation function. |

Conflicts of Interest

The authors declare that there are no conflicts of interest regarding the publication of this paper.

References

- [1] M. M. Shokrieh and M. Esmkhani, "Fatigue life prediction of nanoparticle/fibrous polymeric composites based on the micromechanical and normalized stiffness degradation approaches," *Journal of Materials Science*, vol. 48, no. 3, pp. 1027–1034, 2013.
- [2] K. L. Reifsnider, "Some fundamental aspects of the fatigue and fracture response of composite materials," in *Proceedings of the Fourteenth Annual Meeting in Recent Advances in Engineering Science*, pp. 373–384, Bethlehem, Pa, USA, November 1977.

- [3] T. W. Kim, H. J. Kim, and S. Im, "Delamination crack originating from transverse cracking in cross-ply composite laminates under extension," *International Journal of Solids and Structures*, vol. 27, no. 15, pp. 1925–1941, 1991.
- [4] A. J. Brunner, S. Stelzer, G. Pinter, and G. P. Terrasi, "Cyclic fatigue delamination of carbon fiber-reinforced polymer-matrix composites: data analysis and design considerations," *International Journal of Fatigue*, vol. 83, pp. 293–299, 2016.
- [5] A. L. Highsmith and K. L. Reifsnider, "Stiffness-reduction mechanisms in composite laminates," in *Damage in Composite Materials: Basic Mechanisms, Accumulation, Tolerance, and Characterization*, ASTM International, 1982.
- [6] G. Dai and L. Mishnaevsky, "Damage evolution in nanoclay-reinforced polymers: a three-dimensional computational study," *Composites Science and Technology*, vol. 74, pp. 67–77, 2013.
- [7] K. W. Garrett and J. E. Bailey, "Multiple transverse fracture in 90° cross-ply laminates of a glass fibre-reinforced polyester," *Journal of Materials Science*, vol. 12, no. 1, pp. 157–168, 1977.
- [8] A. Parvizi, K. W. Garrett, and J. E. Bailey, "Constrained cracking in glass fibre-reinforced epoxy cross-ply laminates," *Journal of Materials Science*, vol. 13, no. 1, pp. 195–201, 1978.
- [9] M. G. Bader, J. E. Bailey, A. Parvizi, and P. T. Curtis, "The mechanisms of initiation and development of damage in multi-axial fibre-reinforced plastics laminates," *Mechanical Behaviour of Materials*, pp. 227–239, 1980.
- [10] H. L. Cox, "The elasticity and strength of paper and other fibrous materials," *British Journal of Applied Physics*, vol. 3, no. 3, pp. 72–79, 1952.
- [11] R. Talreja and C. V. Singh, *Damage and Failure of Composite Materials*, Cambridge University Press, 2012.
- [12] J.-M. Berthelot, P. Leblond, A. El Mahi, and J.-F. Le Corre, "Transverse cracking of cross-ply laminates: Part 1. Analysis," *Composites Part A: Applied Science and Manufacturing*, vol. 27, no. 10, pp. 989–1001, 1996.
- [13] S. L. Ogin, P. A. Smith, and P. W. R. Beaumont, "Matrix cracking and stiffness reduction during the fatigue of a (0/90)_s GFRP laminate," *Composites Science and Technology*, vol. 22, no. 1, pp. 23–31, 1985.
- [14] Z. Hashin, "Analysis of cracked laminates: a variational approach," *Mechanics of Materials*, vol. 4, no. 2, pp. 121–136, 1985.
- [15] J. A. Nairn, "The strain energy release rate of composite microcracking: a variational approach," *Journal of Composite Materials*, vol. 23, no. 11, pp. 1106–1129, 1989.
- [16] V. Vinogradov and Z. Hashin, "Probabilistic energy based model for prediction of transverse cracking in cross-ply laminates," *International Journal of Solids and Structures*, vol. 42, no. 2, pp. 365–392, 2005.
- [17] N. V. Akshantala and R. Talreja, "A micromechanics based model for predicting fatigue life of composite laminates," *Materials Science and Engineering: A*, vol. 285, no. 1-2, pp. 303–313, 2000.
- [18] L. N. McCartney, "Theory of stress transfer in a 0°-90°-0° cross-ply laminate containing a parallel array of transverse cracks," *Journal of the Mechanics and Physics of Solids*, vol. 40, no. 1, pp. 27–68, 1992.
- [19] J. Qu and K. Hoiseth, "Evolution of transverse matrix cracking in cross-ply laminates," *Fatigue and Fracture of Engineering Materials and Structures*, vol. 21, no. 4, pp. 451–464, 1998.
- [20] S. K. Kanaun and V. Levin, *Self-Consistent Methods for Composites*, vol. 1 of *Static Problems (Vol. 148)*, Springer Science & Business Media, 2007.
- [21] E. J. Barbero, T. M. Damiani, and J. Trovillion, "Micromechanics of fabric reinforced composites with periodic microstructure," *International Journal of Solids and Structures*, vol. 42, no. 9-10, pp. 2489–2504, 2005.
- [22] E. J. Barbero and D. H. Cortes, "A mechanistic model for transverse damage initiation, evolution, and stiffness reduction in laminated composites," *Composites Part B: Engineering*, vol. 41, no. 2, pp. 124–132, 2010.
- [23] M. Ghayour, H. Hosseini-Toudeshky, M. Jalalvand, and E. J. Barbero, "Micro/macro approach for prediction of matrix cracking evolution in laminated composites," *Journal of Composite Materials*, vol. 50, no. 19, pp. 2647–2659, 2016.
- [24] R. Joffe, A. Krasnikovs, and J. Varna, "COD-based simulation of transverse cracking and stiffness reduction in [S/90_n]s laminates," *Composites Science and Technology*, vol. 61, no. 5, pp. 637–656, 2001.
- [25] C. V. Singh and R. Talreja, "Analysis of multiple off-axis ply cracks in composite laminates," *International Journal of Solids and Structures*, vol. 45, no. 16, pp. 4574–4589, 2008.
- [26] C. V. Singh and R. Talreja, "A synergistic damage mechanics approach to mechanical response of composite laminates with ply cracks," *Journal of Composite Materials*, vol. 47, no. 20-21, pp. 2475–2501, 2013.
- [27] J. Montesano and C. V. Singh, "A synergistic damage mechanics based multiscale model for composite laminates subjected to multi-axial strains," *Mechanics of Materials*, vol. 83, pp. 72–89, 2015.
- [28] M. Hajikazemi, M. H. Sadr, and J. Varna, "Analysis of cracked general cross-ply laminates under general bending loads: a variational approach," *Journal of Composite Materials*, Article ID 0021998316682364, 2016.
- [29] A. Adumitroaie, E. J. Barbero, and M. Schagerl, "Matrix cracking in non-symmetric laminates under combined membrane and flexural loading," *International Journal of Materials, Mechanics and Manufacturing*, vol. 4, pp. 223–231, 2016.
- [30] ANSYS® Workbench, Release 17.1, <http://www.ansys.com/>.
- [31] C. V. Singh, *Multiscale modeling of damage in multidirectional composite laminates dissertation [Ph.D. Thesis]*, Texas A & M University, College Station, Tex, USA, 2008.
- [32] P. A. Smith and J. R. Wood, "Poisson's ratio as a damage parameter in the static tensile loading of simple crossply laminates," *Composites Science and Technology*, vol. 38, no. 1, pp. 85–93, 1990.

Research Article

Study on the High Temperature Friction and Wear Behaviors of Cu-Based Friction Pairs in Wet Clutches by Pin-on-Disc Tests

Er-Hui Zhao,¹ Biao Ma,^{1,2} and He-Yan Li^{1,2}

¹*School of Mechanical Engineering, Beijing Institute of Technology, Beijing, China*

²*Collaborative Innovation Center of Electric Vehicles in Beijing, Beijing, China*

Correspondence should be addressed to He-Yan Li; lovheyang@bit.edu.cn

Received 10 January 2017; Revised 2 May 2017; Accepted 8 May 2017; Published 29 May 2017

Academic Editor: Carlos Navarro

Copyright © 2017 Er-Hui Zhao et al. This is an open access article distributed under the Creative Commons Attribution License, which permits unrestricted use, distribution, and reproduction in any medium, provided the original work is properly cited.

This work is devoted to the study of the high temperature friction and wear behaviors of Cu-based friction pairs in wet clutches under different temperatures, rotation speeds, and loads. Pin-on-disc tests are carried out on the UMT-3. The friction coefficient, wear factor, and high temperature wear mechanism are primarily analyzed. The results show that as the temperature rises from 120°C to 420°C, the friction coefficient increases from 0.28 to 0.35 at first and then decreases to 0.30, when the vibration of friction coefficient is significantly identified. Meanwhile, the wear factor grows gradually from $K = 7.9 \times 10^{-8}$ g/Nm to $K = 41.8 \times 10^{-8}$ g/Nm at first and then grows sharply to $K = 112.2 \times 10^{-8}$ g/Nm. The main wear mechanisms are abrasive wear and ploughing wear when the temperature is below 345°C, and the wear seriously deteriorates when the temperature exceeds 345°C, when the wear mechanism changes to adhesive wear and delamination wear.

1. Introduction

Cu-based powder metallurgy friction pairs are widely used in the wet multidisc clutch, which is one of the main parts in tracked-vehicle integrated transmissions. As power switching and torque transfer devices, wet clutches often work under extremely atrocious conditions, such as high initial sliding velocity, rapid temperature rise, and high surface pressure. The failures of wet clutches due to the friction and wear problems have become a limiting factor for the use of integrated transmissions. Therefore, the friction and wear behaviors of Cu-based friction pairs in wet clutches have to be thoroughly investigated.

The friction and wear behaviors of Cu-based friction pairs in wet clutches crucially depend on the operating conditions. However, the operating conditions in wet clutches are complex and unstable. Gao et al. [1], Deur et al. [2], Ompusunggu et al. [3], and Iqbal et al. [4] proposed numerical models and tests to investigate the engagement of wet clutches. At the initial stage of engagement, friction plates are separated from the mating discs and rotate with a high relative speed. Then, asperity contacts emerge and the relative speed decreases

sharply. During the engagement of wet clutches, a large quantity of heat is generated intensively in 1 second, and the temperature rises rapidly at the interfaces of friction pairs. Researchers, such as Mansouri et al. [5], Jen and Nemecek [6], Ingram et al. [7], Seo et al. [8], and Wenbin et al. [9], investigated the heat transfer, temperature distribution, and thermal stresses of wet clutches by numerical models and experiments. The temperature distribution at the contact surfaces and the thermal stresses in the friction pairs are nonhomogeneous. The friction pairs can buckle due to the elevated temperatures and thermal stresses that occur during clutch engagements. Therefore, the friction and wear behaviors of Cu-based friction pairs will be influenced by the deterioration of operating conditions.

The friction and wear behaviors of wet clutches have long been investigated by numerical and experimental methods. Xiong et al. [10] investigated the effects of Fe and SiO₂ friction components on the friction and wear behaviors of the Cu-based friction materials by an experimental method, and the wear mechanisms were analyzed. Ost et al. [11] investigated the friction and wear behaviors of paper-based wet clutch friction pairs by both SAE#II and pin-on-disc tests, and the

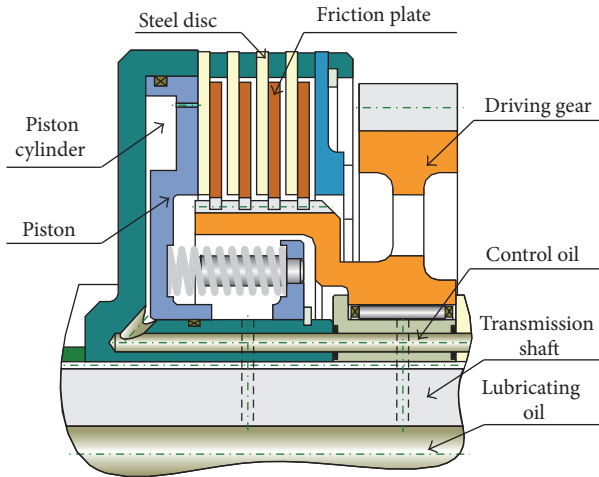


FIGURE 1: Structure diagram of wet multidisc clutch.

influences of material parameters and operating conditions on friction coefficient and wear rate were analyzed. Nyman et al. [12] investigated the influence of changes in the topography of the sintered friction material on the friction characteristics of wet clutches by an experimental method. Yao et al. [13] investigated the characteristics of a worn surface of Cu-based powder metallurgy brake materials after working under service condition, and the main mechanisms were discussed. Zhou et al. [14] investigated the drag torque in a two-speed dual clutch transmission by numerical and experimental methods. Li et al. [15] presented a methodology for prediction of wear in the friction lining of a wet clutch subjected to repeated engagement cycles. Pica et al. [16] provided a temperature and slip speed dependent model to investigate the torque characteristics of dry dual clutches. Gong et al. [17] investigated the wear behaviors of Cu-based friction wet clutches by ring-on-ring test, and the dominant wear mechanisms were discussed. Hoic et al. [18] investigated the wear behaviors of dry dual clutch by experimental characterization and mathematical model. However, the investigations presented above mainly focused on the friction and wear behaviors of wet clutch friction pairs under normal operating conditions, and few of them investigated the friction and wear behaviors of Cu-based friction pairs in wet clutches under severe operating conditions, especially the high temperature friction and wear behaviors.

In this paper, based on the Cu-based wet multidisc clutches used in tracked-vehicle integrated transmissions, as shown in Figure 1, pin-on-disc tests are conducted on the UMT-3 to investigate the friction and wear behaviors of Cu-based friction pairs under severe operating conditions, especially the high temperature friction and wear behaviors. The friction coefficient and wear factor under different operating conditions and the high temperature wear mechanisms are primarily analyzed.

2. Experimental Details

The friction and wear behaviors of Cu-based friction pairs in wet clutches crucially depend on the operating conditions.

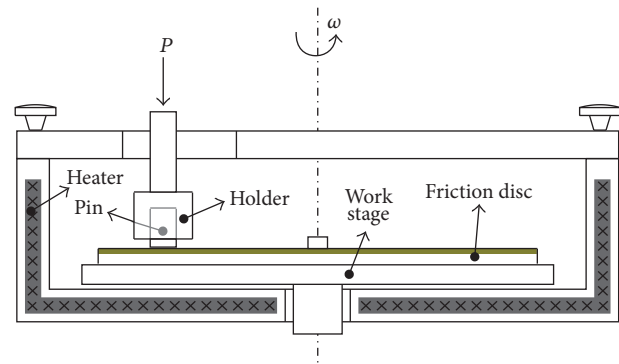


FIGURE 2: Elevated temperature chamber for rotary drives.

However, the local temperature, the local contact pressure, and the local relative sliding velocity are not constant on the contact surfaces of the friction pairs. Therefore, to better study the local friction and wear behaviors of Cu-based friction pairs under different operating conditions, pin-on-disc tests are conducted on a professional test apparatus, Universal Material Tester (UMT), the model of which used in this paper is UMT-3, provided by the Bruker Corporation in the United States. Generally, during the engagement of wet clutches, a large quantity of heat is generated intensively in 1 second, and the lubricant film can fail due to the rapid temperature rise. Therefore, in this paper, the high temperature friction and wear behaviors of Cu-based friction pairs are investigated by dry pin-on-disc tests, and there is no lubricant present during these experiments.

The structure of elevated temperature chamber for rotary drives is shown in Figure 2. The heating range of the elevated temperature chamber is 0~1000°C. The diameter of the steel pin is $d = 6$ mm, and the rotation radius of the sliding track on the friction disc is $r = 25$ mm. In the process of testing, the pin was fixed with the sensor module, and the friction disc rotated with the rotary chamber.

The steel pin was made of 65Mn steel, and the friction disc was made of Cu-based powder metallurgy material. Copper was the matrix material, and the iron powder (5% in weight), feldspar powder (5% in weight), carbon (6% in weight), and so forth were the additive materials. The RMS surface roughness of the friction disc was $0.61 \mu\text{m}$. When the friction coefficient was stable after running in, we started the tests. When the temperature stabilized at the target temperature, we carried out the test procedures: (1) pressure the pin against the friction disc; (2) bring the electromotor to the target rotation speed; (3) record the rotation speed, load, temperature, and friction coefficient; (4) stop the electromotor and separate the pin and friction disc; (5) change the pin and disc with brand new ones. Operating parameter settings in pin-on-disc tests and corresponding values in wet clutches are shown in Table 1.

3. Results and Discussion

In order to investigate the high temperature friction and wear behaviors of Cu-based friction pairs, the test results presented below are carried out with five different temperature levels,

TABLE 1: Parameter settings in pin-on-disc tests and corresponding values in wet clutches.

| Parameters | Values |
|---|------------------------------|
| Rotation speed in pin-on-disc tests (rpm) | 400, 500, 600, 700, 800 |
| Relative sliding velocity in wet clutches (mm/s) | 1047, 1309, 1571, 1833, 2095 |
| Load in pin-on-disc tests (N) | 60, 80, 100, 120, 140 |
| Average surface pressure in wet clutches (MPa) | 2.1, 2.8, 3.5, 4.2, 4.9 |
| Temperature in pin-on-disc tests ($^{\circ}\text{C}$) | 120, 195, 270, 345, 420 |
| Temperature in wet clutches ($^{\circ}\text{C}$) | 120, 195, 270, 345, 420 |

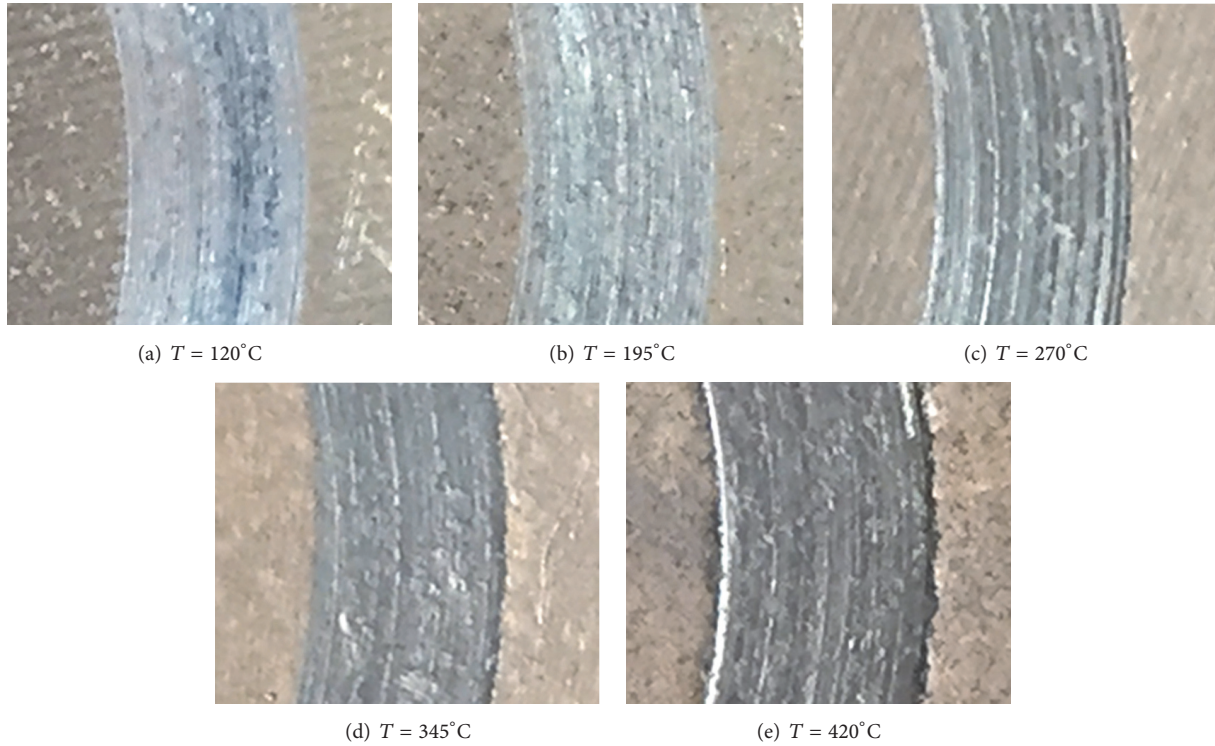


FIGURE 3: Friction discs after tests with different levels of temperature.

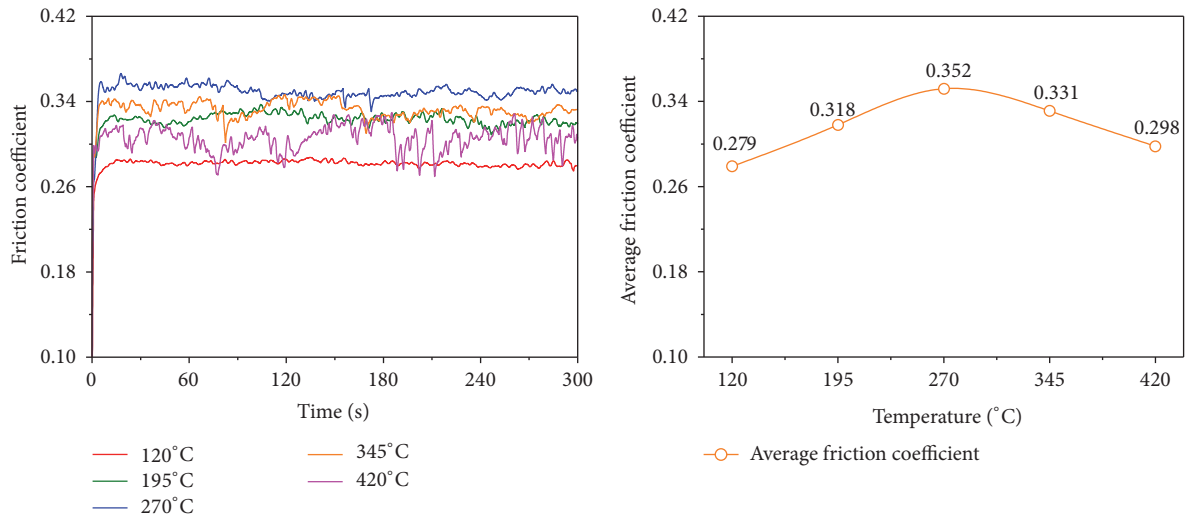
five different rotation speeds, and five different load levels. The test duration is 30 minutes. The friction coefficient, wear factor, and high temperature wear mechanism will be primarily analyzed in this part. The pin and the disc used in each experiment are brand new.

Figures 3(a)–3(e) show the surface state of the friction discs after tests with different temperatures. It is clear that the depth of wear groove increases significantly as the temperature rises. Furthermore, the friction condition and the wear mechanism of Cu-based friction pairs change in the process of temperature rising.

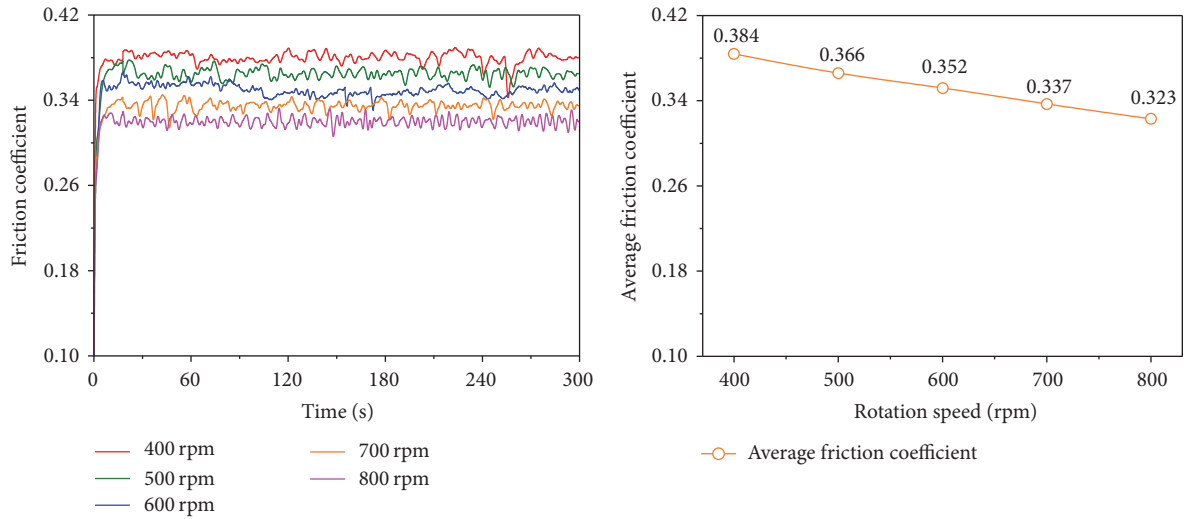
Figure 4(a) presents the test results of friction coefficient and average friction coefficient under different temperatures. It is clear that temperature rise has a significant influence on the friction coefficient of Cu-based friction pairs. When the temperature is $T = 120^{\circ}\text{C}$, the friction coefficient is stable and the mean value of friction coefficient is about 0.28. As the temperature rises to $T = 195^{\circ}\text{C}$, the friction coefficient has slight fluctuation and the mean value increases to about 0.32.

With the temperature $T = 270^{\circ}\text{C}$, the friction coefficient is the biggest, about 0.35, and begins to vibrate obviously. Then, as the temperature rises to $T = 345^{\circ}\text{C}$, the friction coefficient decreases to about 0.33 and fluctuates strongly. When the temperature rises to $T = 420^{\circ}\text{C}$, the vibration of friction coefficient is significantly identified, and the mean value of the friction coefficient decreases to about 0.30.

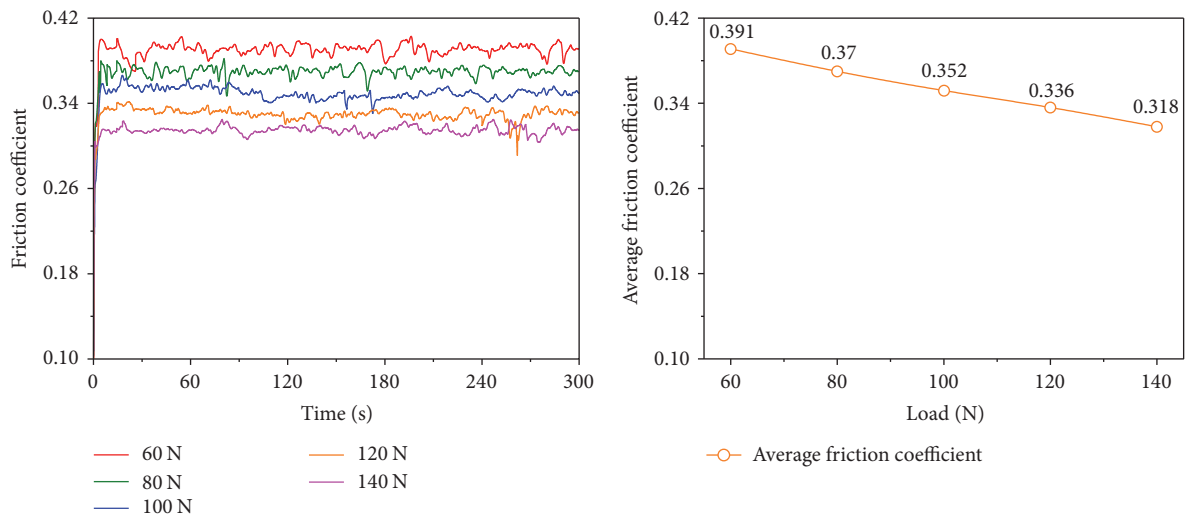
Figures 4(b) and 4(c) present the test results of friction coefficient and average friction coefficient under different rotation speeds and different loads. We can see that the effects of rotation speed and load on the friction coefficient of Cu-based friction pairs are also obvious. As the rotation speed increases from 400 rpm to 800 rpm, the average friction coefficient decreases gradually from about 0.38 to 0.32, and the vibration of the friction coefficient decreases at the same time. Similarly, as the load increases from 60 N to 140 N, the average friction coefficient decreases gradually from about 0.39 to 0.32, and there is no significant change in the vibration of the friction coefficient.



(a) Test results of friction coefficient under different temperatures



(b) Test results of friction coefficient under different rotation speeds



(c) Test results of friction coefficient under different loads

FIGURE 4: Test results of friction coefficient under different temperatures, rotation speeds, and loads.

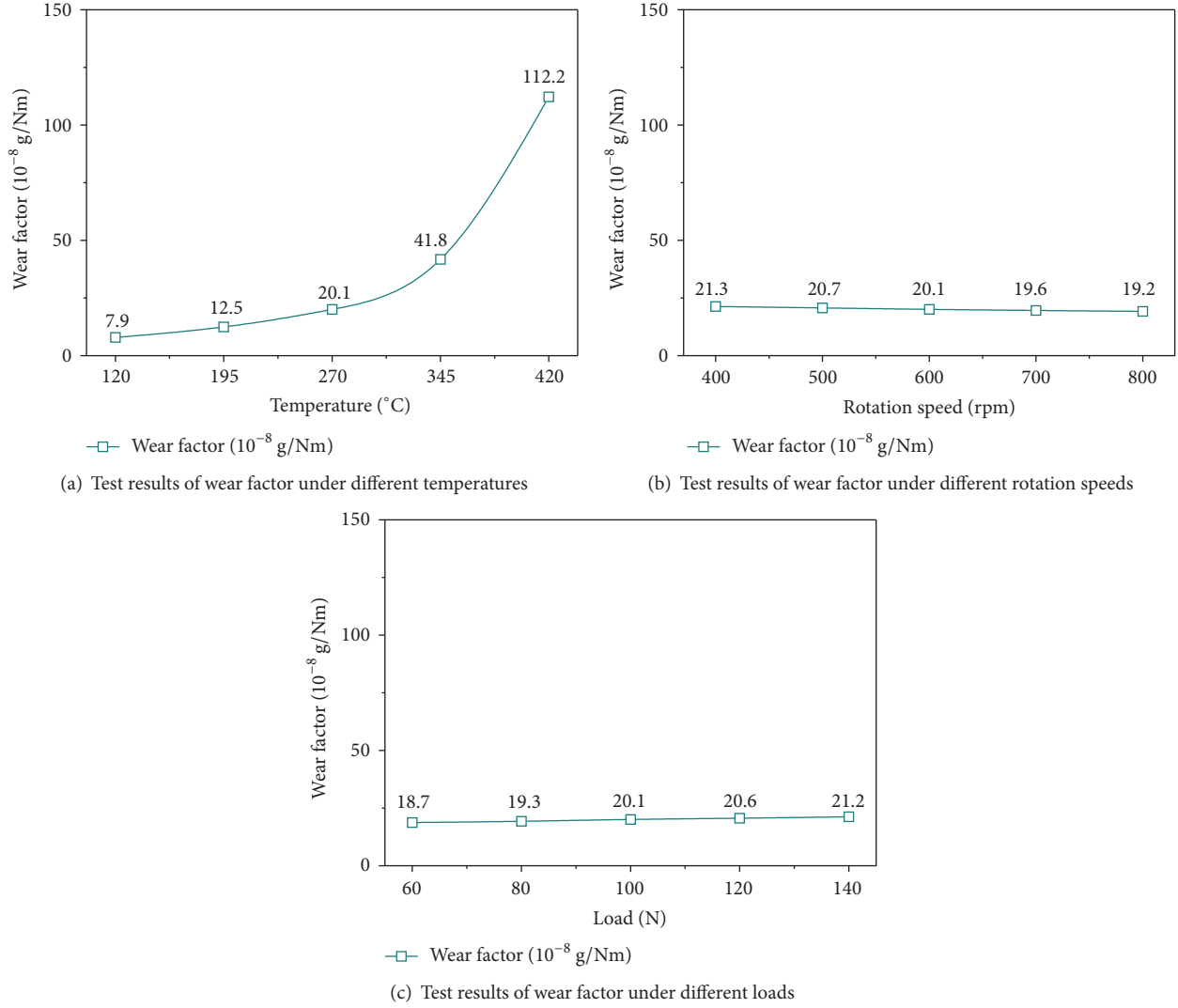


FIGURE 5: Test results of wear factor under different temperatures, rotation speeds, and loads.

The wear loss of the friction disc is measured by an electronic balance, and the wear factor can be calculated from the test result of weight loss by Archard's wear model:

$$K = \frac{W_{\text{test}}}{F_{\text{test}}S}, \quad (1)$$

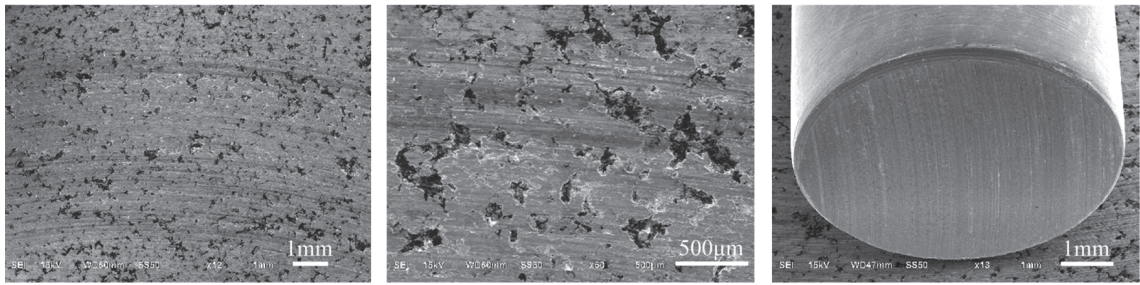
where W_{test} is the test result of weight loss (g); F_{test} is the load of pin-on-disc test (N); and S is the total relative sliding distance of the pin and the disc (m). The unit of the wear factor K is g/Nm.

Figure 5(a) shows the test results of wear factor under different temperatures. We can see that the wear of Cu-based friction pairs seriously deteriorates when the temperature exceeds 345°C. When the temperature is $T = 120^\circ\text{C}$, the wear of Cu-based friction pairs is slight, and the wear factor is about $K = 7.9 \times 10^{-8}$ g/Nm. As the temperature rises to $T = 270^\circ\text{C}$, the wear factor of Cu-based friction pairs grows gradually to about $K = 20.1 \times 10^{-8}$ g/Nm. When the temperature is higher than $T = 300^\circ\text{C}$, the growth of the wear factor becomes faster. When the temperature is $T = 345^\circ\text{C}$, the wear

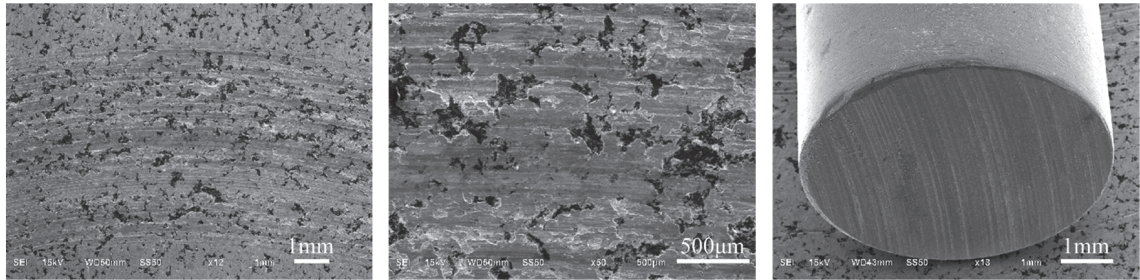
factor of Cu-based friction pairs grows significantly to about $K = 41.8 \times 10^{-8}$ g/Nm. However, as the temperature rises to $T = 420^\circ\text{C}$, the wear factor of Cu-based friction pairs grows sharply to about $K = 112.2 \times 10^{-8}$ g/Nm.

Figures 5(b) and 5(c) show the test results of wear factor under different rotation speeds and loads. We can see that there is no significant change in the wear factor of Cu-based friction pairs when the rotation speed or the load increases. As the rotation speed increases from 400 rpm to 800 rpm, the wear factor decreases slightly from about $K = 21.3 \times 10^{-8}$ g/Nm to $K = 19.2 \times 10^{-8}$ g/Nm. On the contrary, as the load increases from 60 N to 140 N, the wear factor of the Cu-based friction pairs increases slightly from about $K = 18.7 \times 10^{-8}$ g/Nm to $K = 21.2 \times 10^{-8}$ g/Nm.

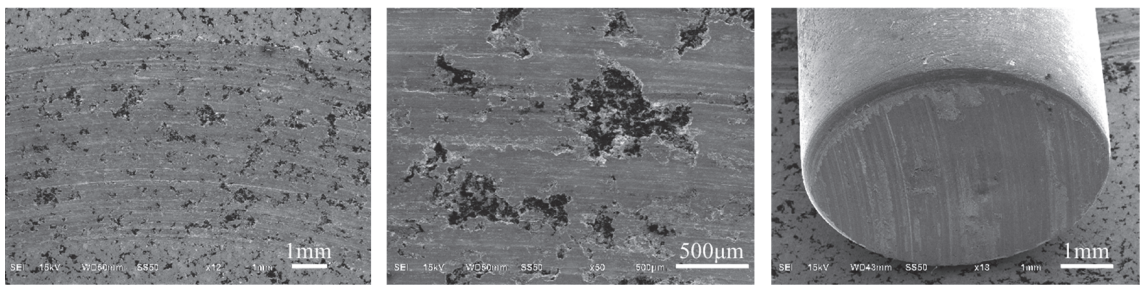
Figures 6(a)–6(e) provide the SEM micrographs of worn surfaces of Cu-based friction pairs after test under different temperatures. It is observed that the wear mechanism changes obviously as the temperature rises from $T = 120^\circ\text{C}$ to $T = 420^\circ\text{C}$. When the temperature is $T = 120^\circ\text{C}$, the wear of the friction surface is slight, and the wear mechanism is abrasive



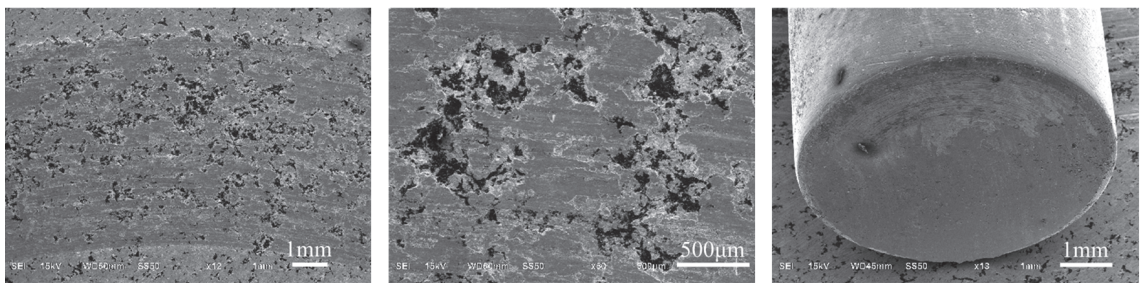
(a) $T = 120^{\circ}\text{C}$



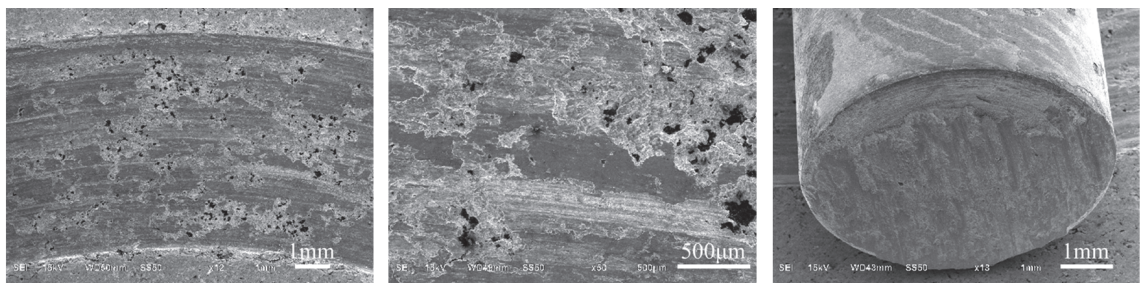
(b) $T = 195^{\circ}\text{C}$



(c) $T = 270^{\circ}\text{C}$



(d) $T = 345^{\circ}\text{C}$



(e) $T = 420^{\circ}\text{C}$

FIGURE 6: SEM micrographs of worn surfaces of Cu-based friction pairs after the test.

wear. As the temperature rises to $T = 195^{\circ}\text{C}$, the wear of the friction surface becomes more obvious, and the wear mechanism is still abrasive wear. When the temperature rises to $T = 270^{\circ}\text{C}$, some furrows emerge, and the wear mechanism becomes ploughing wear. As the temperature rises to $T = 345^{\circ}\text{C}$, the Cu-based powder metallurgy material begins to soften, and the main wear mechanism changes to adhesive wear. When the temperature rises continuously to extremely high $T = 420^{\circ}\text{C}$, the wear of Cu-based friction pairs deteriorates seriously, and there are massive exfoliations on the friction surface, when the wear mechanism changes to delamination wear.

4. Conclusions

The high temperature friction and wear behaviors of Cu-based friction pairs in wet clutches have been investigated based on pin-on-disc tests. The friction coefficient, wear factor, and high temperature wear mechanism have been primarily analyzed. The main conclusions are summarized as follows:

- (1) When the temperature is 120°C , the friction coefficient of Cu-based friction pairs is stable. As the temperature rises to 420°C , the friction coefficient begins to vibrate significantly. The friction coefficient increases from 0.28 to 0.35 when the temperature rises from 120°C to 270°C and decreases to 0.30 when the temperature continuously rises to 420°C .
- (2) When the temperature rises from 120°C to 270°C , the wear of Cu-based friction pairs is slight, and the wear factor grows gradually from $K = 7.9 \times 10^{-8} \text{ g/Nm}$ to $K = 20.1 \times 10^{-8} \text{ g/Nm}$. However, as the temperature rises from 345°C to 420°C , the wear factor grows sharply from $K = 41.8 \times 10^{-8} \text{ g/Nm}$ to $K = 112.2 \times 10^{-8} \text{ g/Nm}$.
- (3) When the temperature is lower than 345°C , the main wear mechanisms are abrasive wear and ploughing wear. As the temperature rises to higher than 345°C , the wear of Cu-based friction pairs seriously deteriorates, and the wear mechanism changes to adhesive wear and delamination wear.

Conflicts of Interest

The authors declare that they have no conflicts of interest regarding the publication of this paper.

Acknowledgments

The authors would like to express their appreciation for the continuous support from Professor Wen-zhong Wang at Beijing Institute of Technology. Furthermore, the authors acknowledge the financial support from the National Natural Science Foundation of China (no. 51575042).

References

- [1] H. Gao, G. C. Barber, and M. Shillor, "Numerical simulation of engagement of a wet clutch with skewed surface roughness," *Journal of Tribology*, vol. 124, no. 2, pp. 305–312, 2002.
- [2] J. Deur, J. Petric, J. Asgari, and D. Hrovat, "Modeling of wet clutch engagement including a thorough experimental validation," *SAE Technical Papers*, 2005.
- [3] A. P. Ompusunggu, P. Sas, and H. Van Brussel, "Modeling and simulation of the engagement dynamics of a wet friction clutch system subjected to degradation: An application to condition monitoring and prognostics," *Mechatronics*, vol. 23, no. 6, pp. 700–712, 2013.
- [4] S. Iqbal, F. Al-Bender, A. P. Ompusunggu, B. Pluymers, and W. Desmet, "Modeling and analysis of wet friction clutch engagement dynamics," *Mechanical Systems and Signal Processing*, vol. 60–61, pp. 420–436, 2015.
- [5] M. Mansouri, M. Holgersson, M. M. Khonsari, and W. Aung, "Thermal and dynamic characterization of wet clutch engagement with provision for drive Torque," *Journal of Tribology*, vol. 123, no. 2, pp. 313–323, 2001.
- [6] T.-C. Jen and D. J. Nemecek, "Thermal analysis of a wet-disk clutch subjected to a constant energy engagement," *International Journal of Heat and Mass Transfer*, vol. 51, no. 7–8, pp. 1757–1769, 2008.
- [7] M. Ingram, T. Reddyhoff, and H. A. Spikes, "Thermal behaviour of a slipping wet clutch contact," *Tribology Letters*, vol. 41, no. 1, pp. 23–32, 2011.
- [8] H. Seo, C. Zheng, W. Lim, S. W. Cha, and S. Han, "Temperature prediction model of wet clutch in coupling," in *Proceedings of the 7th IEEE Vehicle Power and Propulsion Conference, VPPC 2011*, pp. 1–4, IEEE, Chicago, IL, USA, September 2011.
- [9] L. Wenbin, H. Jianfeng, F. Jie, C. Liyun, and Y. Chunyan, "Simulation and application of temperature field of carbon fabric wet clutch during engagement based on finite element analysis," *International Communications in Heat and Mass Transfer*, vol. 71, pp. 180–187, 2016.
- [10] X. Xiong, J. Chen, P. Yao, S. Li, and B. Huang, "Friction and wear behaviors and mechanisms of Fe and SiO_2 in Cu-based P/M friction materials," *Wear*, vol. 262, no. 9–10, pp. 1182–1186, 2007.
- [11] W. Ost, P. De Baets, and J. Degrieck, "The tribological behaviour of paper friction plates for wet clutch application investigated on SAE#II and pin-on-disk test rigs," *Wear*, vol. 249, no. 5–6, pp. 361–371, 2001.
- [12] P. Nyman, R. Mäki, R. Olsson, and B. Ganemi, "Influence of surface topography on friction characteristics in wet clutch applications," *Wear*, vol. 261, no. 1, pp. 46–52, 2006.
- [13] P.-P. Yao, H.-C. Sheng, X. Xiong, and B.-Y. Huang, "Worn surface characteristics of Cu-based powder metallurgy bake materials for aircraft," *Transactions of Nonferrous Metals Society of China*, vol. 17, no. 1, pp. 99–103, 2007.
- [14] X. Zhou, P. Walker, N. Zhang, B. Zhu, and J. Ruan, "Numerical and experimental investigation of drag torque in a two-speed dual clutch transmission," *Mechanism and Machine Theory*, vol. 79, pp. 46–63, 2014.
- [15] M. Li, M. M. Khonsari, D. M. C. McCarthy, and J. Lundin, "On the wear prediction of the paper-based friction material in a wet clutch," *Wear*, vol. 334–335, pp. 56–66, 2015.
- [16] G. Pica, C. Cervone, A. Senatore, M. Lupo, and F. Vasca, "Dry dual clutch torque model with temperature and slip speed

- effects," *Intelligent Industrial Systems*, vol. 2, no. 2, pp. 133–147, 2016.
- [17] T. Gong, P. Yao, Y. Xiao et al., "Wear map for a copper-based friction clutch material under oil lubrication," *Wear*, vol. 328–329, pp. 270–276, 2015.
- [18] M. Hoic, N. Kranjcevic, Z. Herold, J. Deur, and V. Ivanovic, "Experimental characterization and modeling of dry dual clutch wear," *SAE International Journal of Passenger Cars-Mechanical Systems*, vol. 7, no. 1, pp. 326–337, 2014.

Research Article

Effects of Voids on Concrete Tensile Fracturing: A Mesoscale Study

Lei Xu and Yefei Huang

College of Water Conservancy and Hydropower Engineering, Hohai University, Nanjing 210098, China

Correspondence should be addressed to Lei Xu; leixu@hhu.edu.cn

Received 21 December 2016; Accepted 30 March 2017; Published 24 April 2017

Academic Editor: Francesco Caputo

Copyright © 2017 Lei Xu and Yefei Huang. This is an open access article distributed under the Creative Commons Attribution License, which permits unrestricted use, distribution, and reproduction in any medium, provided the original work is properly cited.

A two-dimensional mesoscale modeling framework, which considers concrete as a four-phase material including voids, is developed for studying the effects of voids on concrete tensile fracturing under the plane stress condition. Aggregate is assumed to behave elastically, while a continuum damaged plasticity model is employed to describe the mechanical behaviors of mortar and ITZ. The effects of voids on the fracture mechanism of concrete under uniaxial tension are first detailed, followed by an extensive investigation of the effects of void volume fraction on concrete tensile fracturing. It is found that both the prepeak and postpeak mesoscale cracking in concrete are highly affected by voids, and there is not a straightforward relation between void volume fraction and the postpeak behavior due to the randomness of void distribution. The fracture pattern of concrete specimen with voids is controlled by both the aggregate arrangement and the distribution of voids, and two types of failure modes are identified for concrete specimens under uniaxial tension. It is suggested that voids should be explicitly modeled for the accurate fracturing simulation of concrete on the mesoscale.

1. Introduction

Concrete is widely used as a construction material and is traditionally treated as a homogeneous continuum on the structural scale (macroscale). This homogenization assumption can hold well as long as the mechanical response of concrete remains in the elastic regime [1, 2]. However, when fracturing occurs, the macroscale mechanical behavior of concrete is greatly controlled by its components and their interactions taking place on a finer scale (mesoscale) [3, 4], which means accurate modeling of concrete fracturing calls for the consideration of its mesostructure.

Up to date, several mesoscale models have been developed to provide tools for a better understanding of concrete fracturing. From the simulation strategy point of view, most of the existing concrete mesoscale models can be broadly grouped into two types: the continuum model and the lattice model. In the continuum model, concrete is usually characterized by a continuum composite material with each component discretized by finite elements, while, for the lattice model, a discrete system composed of lattice elements is used

to represent concrete. Moreover, the discrete element method (DEM) has been recently used to perform the mesoscale simulation of concrete [5], and it is shown that the discrete model requires a huge numerical effort that is necessary for this approach to obtain a reasonable representation of concrete mesostructure.

Several researchers studied the concrete fracturing by employing the continuum modeling strategy, and representative contributions can be found in [6–12]. The most recent investigations following this strategy were carried out by Du et al. [13] who studied the dynamic tensile fracturing of concrete by assuming concrete to be composed of aggregate and mortar matrix, by Huang et al. [14] who performed a 3D mesoscale fracturing simulation based on the actual concrete mesostructure, and by Wang et al. [15, 16] who developed a computational technology using the interface element with a cohesive law to perform Monte Carlo simulations of concrete fracturing and to study the 3D mesostructure effects on concrete damage and failure. Overall, the principal merit of the continuum model lies in the detailed representation of concrete mesostructure, which ensures the ability to

realize reasonable simulations of cracking initiation on the mesoscale and coalescence of multiple distributed cracks into localized macroscale cracks and fracture propagation. However, it tends to be computationally intensive even for laboratory-scale specimens, especially for three-dimensional cases.

With respect to the lattice modeling strategy, representative studies were carried out in [17–20], and the most recent improvements are performed by Cusatis et al. [21, 22] who proposed a novel model named the lattice discrete particle model (LDPM) by exploiting the merits of both the lattice model and the discrete particle model. In contrast to the continuum model, the lattice model is considered computationally less demanding as concrete mesostructure is roughly represented by a discrete system with relatively less degrees of freedom and meanwhile can still possess the ability to capture the most important aspects of concrete fracturing. However, it is hard to investigate the interactions of concrete components in a real sense since the actual concrete mesostructure is not fully taken into account in the lattice model.

Voids (or pores) with different sizes always exist in concrete and typically take up 2–6% of the total volume, and the use of entrained air void system is a common approach in concrete technology to resist cyclic freezing and thawing degradation [23]. However, the effects of voids on concrete fracturing on the mesoscale are still not well understood. Wang et al. [15] built numerical concrete samples with pores using interface elements and studied the effects of porosity on concrete loading-carrying capability under uniaxial tension, but the fracturing mechanism on the mesoscale was not detailed. Huang et al. [14] reported the distribution of voids greatly influences the tensile strength and crack patterns based on the simulation results of a single 3D specimen. On the whole, it has been recognized that the existence of voids affects the concrete mechanical behavior to a large extent, but further research is needed to reveal the effects of voids on concrete fracturing.

With this in mind, a 2D finite element (FE) mesoscale modeling framework for concrete is proposed in this study in which concrete is considered as a four-phase material composed of aggregate, mortar, interfacial transitional zone (ITZ), and void, and the effects of voids on concrete tensile fracturing under the plane stress condition are detailed by performing several simulations. The rest of this paper is organized as follows: Section 2 presents the generation procedures of concrete mesostructure; the FE modeling methodology including mesh discretization, insertion of ITZ elements, and constitutive modeling of mortar and ITZ is described in Section 3; in Section 4, the effects of voids on concrete tensile fracturing are discussed in detail based on the simulation results of several concrete specimens with different mesostructures; finally, the study is summarized with conclusions in Section 5.

2. Generation of Concrete Mesostructure

In this study, concrete is treated as a four-phase composite material, that is, coarse aggregate, mortar composed of

cement matrix and fine aggregate, interfacial transitional zone (ITZ), and void randomly distributed in the mortar. Regarding aggregate generation, gravel is idealized as circle, while crushed aggregate is considered as polygon. Mortar is assumed as a homogenous continuum, and the interface with a specified thickness between coarse aggregate (hereinafter referred to as aggregate) and mortar is used to represent ITZ. Moreover, void is viewed as circle for simplicity.

2.1. Size Distribution of Aggregates and Voids. The aggregate size distribution of concrete is described by Talbot's equation as

$$F_p(d_a) = \left(\frac{d_a}{d_{\max}} \right)^n, \quad (1)$$

where d_a is the size of aggregate, d_{\max} is the maximum size of aggregate, $F_p(d_a)$ represents the ratio of aggregates by weight passing through a sieve of characteristic size equal to d_a , and n is the exponent of Talbot's equation. For $n = 0.5$, the corresponding curve is known as Fuller's curve extensively employed in concrete grading design for optimal packing properties.

For a concrete specimen with total volume V , the volume of aggregates within a grading segment $[d_i, d_{i+1}]$ can be calculated by

$$V_{\text{agg}}[d_i, d_{i+1}] = \frac{F_p(d_{i+1}) - F_p(d_i)}{F_p(d_{\max}) - F_p(d_{\min})} \times A_F \times V, \quad (2)$$

where d_{\min} is the minimum size of aggregate and A_F represents the aggregate volume fraction.

Currently, the size distribution of voids in concrete has not been detailed. In general, these voids can be broadly grouped into two types according to different formation ways and the resulting different sizes: the (smaller) entrained voids with typical sizes on the order of 0.1 mm and the (larger) entrapped voids with typical sizes commonly more than 1 mm. In this study void size is considered to be uniformly distributed, and the same assumption is also employed by other researchers [15, 16]. Thus, denoting the size range of void by $[d_{\min}^v, d_{\max}^v]$, the void size can be calculated by $d_v = d_{\min}^v + P \times (d_{\max}^v - d_{\min}^v)$ (P is a uniformly distributed random number between 0 and 1).

2.2. Generation and Placement of Aggregates and Voids. In order to build numerical concrete specimens automatically, a mesostructure generator for concrete (MGC) is developed using MATLAB based on the take-and-place method [24, 25].

In the take-process, aggregates and voids, which will be placed into the specimen volume in the place-process, are generated separately. For the aggregate generation, the aggregate volume for each grading segment is first calculated according to (2). Then, starting with the grading segment with the maximum average size, the aggregates are generated one by one for each grading segment. For a certain grading segment $[d_i, d_{i+1}]$, the generation of aggregates takes the following procedures.

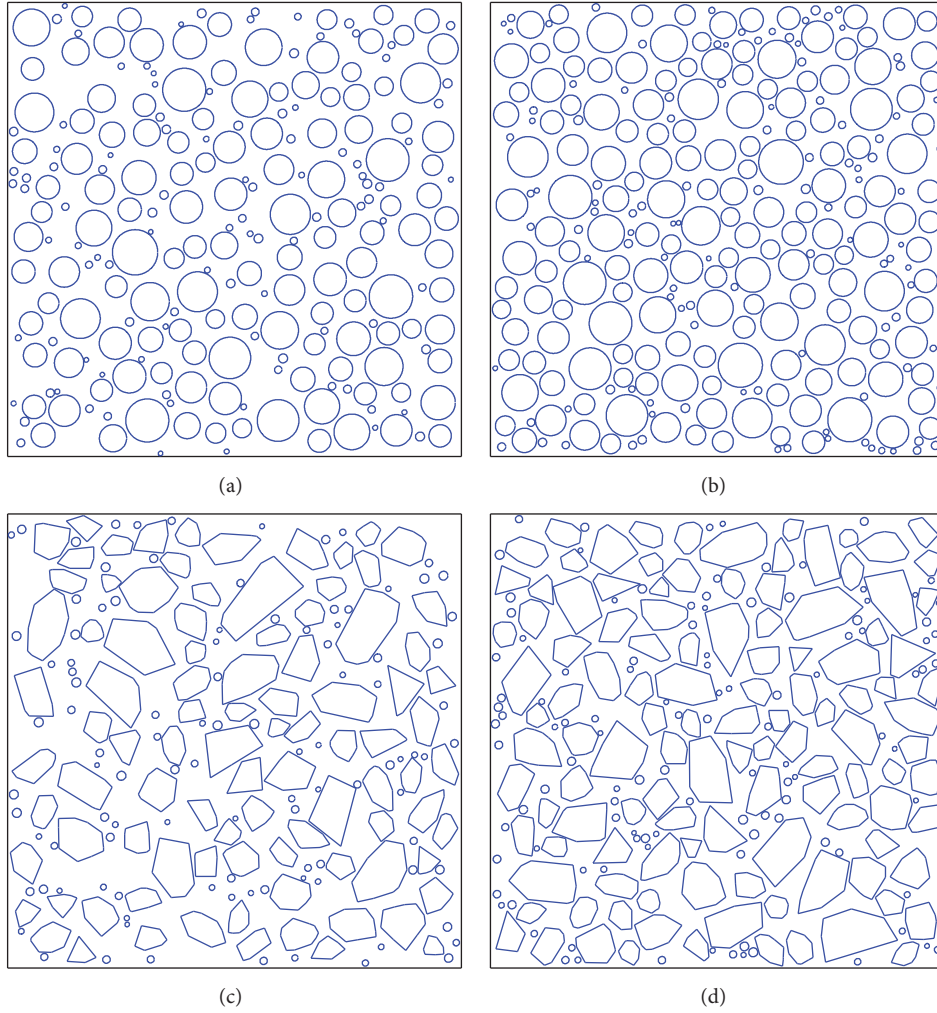


FIGURE 1: Numerical concrete specimens. (a) Circular aggregate ($A_F = 40\%$, $A_v = 2\%$). (b) Circular aggregate ($A_F = 50\%$, $A_v = 2\%$). (c) Polygonal aggregate ($A_F = 40\%$, $A_v = 2\%$). (d) Polygonal aggregate ($A_F = 50\%$, $A_v = 2\%$).

Step 1. Generate a random number representing the aggregate size d_a , which is assumed to follow a uniform distribution and therefore can be taken as $d_a = d_i + P \times (d_{i+1} - d_i)$.

Step 2. For gravel, a circle with radius of $d_a/2$ is defined to represent the aggregate, while, for crushed aggregate, a polygon with the random number of sides ranging from 4 to 10 and with the smallest width equal to d_a is generated to represent the aggregate (see [24] for more details). Then, the volume of the current generated aggregate is calculated.

Step 3. Repeat the previous two steps until the remaining volume left is less than $\pi d_a^2/4$, namely, not enough to generate a new aggregate.

Step 4. Transfer the remaining volume to the next grading segment.

Following the similar procedures for generating gravel aggregates, the generation of voids can be performed with ease provided by the given void volume fraction and size

range, which is followed by the placement of aggregates and voids (the place-process).

In the place-process, the generated aggregates and voids are first sorted according to their volume, respectively. Then, for the convenience of mesh discretization discussed in Section 3, the size of each aggregate is increased by a specified value (the thickness of ITZ, T_{ITZ}) to consider the surrounding ITZ, which means the aggregate finally placed consists of two parts (i.e., aggregate piece and the surrounding ITZ with a specified thickness). After the modification of aggregate size, all aggregates are placed into the specified specimen one by one starting with the aggregate with the largest volume, followed by the placement of voids starting from the biggest one. The procedures of the placement of aggregates and voids are detailed as follows.

Step 1. Define the shape of concrete specimen using X and Y coordinates of the boundary vertices numbered clockwise or anticlockwise, which will be used in Step 3 to check if an aggregate is inside the concrete specimen.

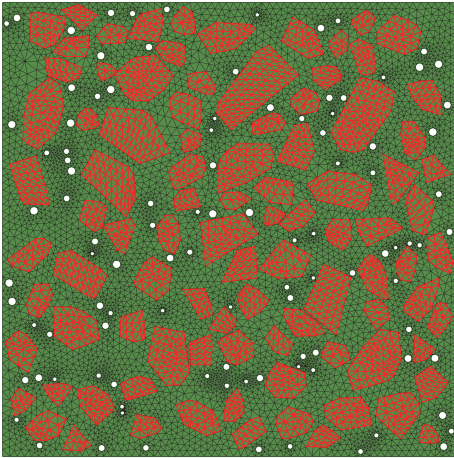


FIGURE 2: FE mesh discretization (polygonal aggregate).

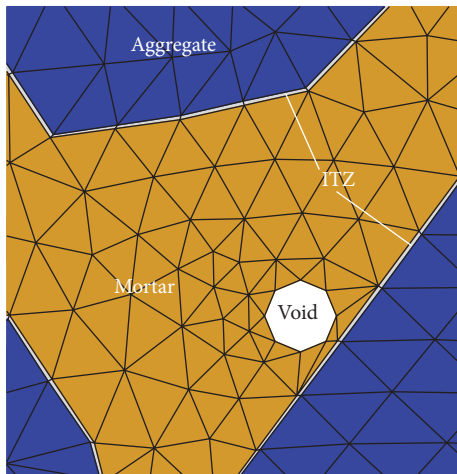


FIGURE 3: FE mesh discretization after inserting and adjusting.

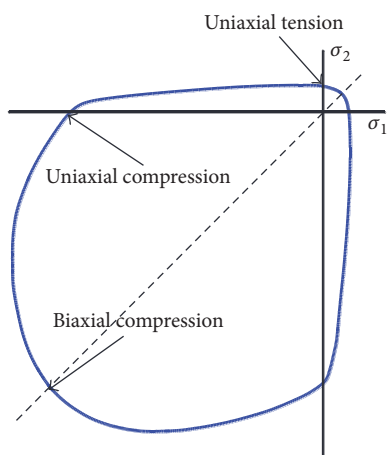


FIGURE 4: Yield surface in plane stress.

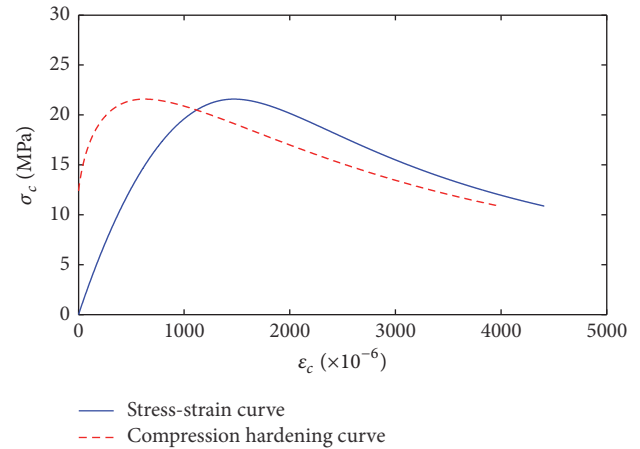


FIGURE 5: Total stress-strain relation under uniaxial compression and compression hardening curve of mortar.

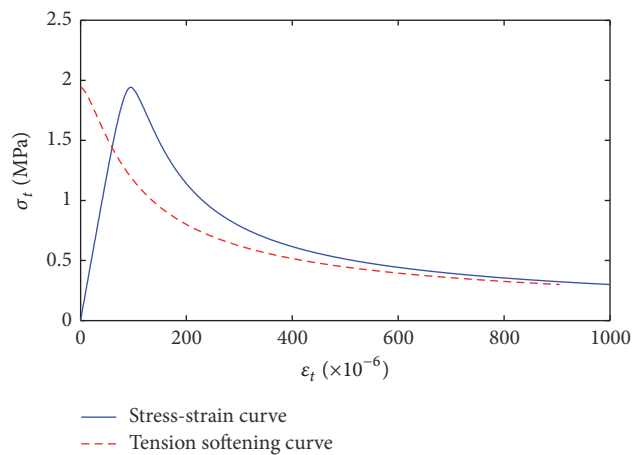


FIGURE 6: Total stress-strain relation under uniaxial tension and tension softening curve of mortar.

Step 2. Generate random numbers to define the position (and orientation if polygon is used to represent the crushed aggregate) of the aggregate using X_{\min} , X_{\max} , Y_{\min} , and Y_{\max} , which represent the minimum and maximum value of X and Y coordinates of all boundary vertices, respectively.

Step 3. Perform the aggregate placing. The placement is considered to be successful if the following four conditions are satisfied: (1) the whole aggregate should be within the concrete specimen; (2) no overlapping/intersection occurs between the aggregate to be placed and any existing aggregate; (3) a minimum distance (defined by r_1) should exist between the aggregate and the specimen boundary; and (4) a minimum gap (defined by r_2) should exist between any two aggregates. If any of the four conditions is violated, Step 2 is repeated to make a new attempt until the placement of the aggregate is completed.

Step 4. Repeat Steps 2-3 until all aggregates are placed inside the specimen.

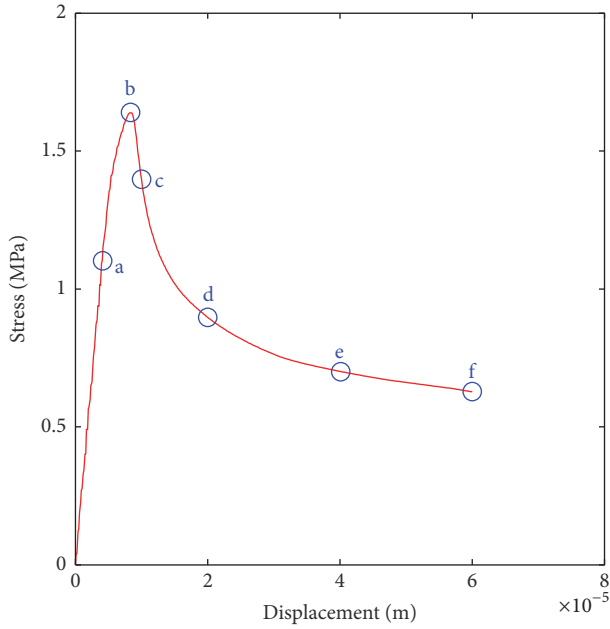


FIGURE 7: Stress-displacement curve ($A_F = 40\%$, without void).

After the placement of aggregates, voids should also be placed into the specimen, which can be carried out by following the similar steps given above. It is worth noting that voids are considered to be embedded in mortar in this study.

Using MGC, numerical concrete specimens can be built with ease. The specimens shown in this paper are 100 mm squares, and the 4-segment Fuller curve is used to describe the aggregate grading for all specimens. For aggregates, d_{\max} and d_{\min} are set to 10 mm and 4 mm, respectively, while, for voids, $d_{\max}^v = 2$ mm and $d_{\min}^v = 1$ mm are used. In addition, T_{ITZ} is approximately set to 100 μm according to the experimental observation [1], and both r_1 and r_2 are taken as 0.1 times of the size of aggregate or void to be placed.

Figures 1(a) and 1(b) sketch two numerical samples using circular aggregates with the same void volume fraction ($A_v = 2\%$) and the aggregate volume fraction $A_F = 40\%$ and 50%, respectively, whereas two numerical samples using polygonal aggregates with $A_v = 2\%$ and $A_F = 40\%$ and 50%, respectively, are plotted in Figures 1(c) and 1(d).

3. Finite Element Modeling Methodology

Once the concrete mesostructure is obtained, a corresponding FE model is required for performing numerical simulations. The details of the FE modeling methodology developed in this study are presented as follows.

3.1. Mesh Discretization. In order to automatically carry out the mesh discretization of the concrete specimen with complex mesostructure, a mesh generator is developed using MATLAB by exploiting the powerful preprocessing modules provided by the commercial finite element software ABAQUS. For a numerical concrete specimen with pre-generated mesostructure, a two-part python file, which defines

the boundary of the specimen together with the locations and shapes of aggregates and voids using the first part of the file and specifies the mesh discretization parameters using the second part of the file, is first generated using the mesh generator by taking concrete mesostructure as input data. Then, a FE mesh composed of linear triangular elements can be obtained by the mesh generator through calling ABAQUS/CAE kernel to execute the generated python file. An example of the FE mesh discretization with aggregate elements highlighted is shown in Figure 2. It must be noted that ITZ elements are not included in the original generated FE mesh as the tiny thickness of ITZ makes the mesh discretization harder and leads to a poor mesh quality, and therefore a modification of the original FE mesh is needed for obtaining the final FE mesh, which is discussed in detail in Section 3.2.

3.2. Insertion of ITZ Elements. As stated in Section 2, the size of an aggregate is increased by a specified value determined by the thickness of ITZ before placing this aggregate into the specimen volume. Hence, the aggregate elements in the FE mesh generated in Section 3.1 not only occupy the volume of aggregates but also take up the volume of ITZs. In order to explicitly represent the surrounding ITZs and the actual sizes of aggregates in the FE model, ITZ elements should be inserted between aggregate elements and the corresponding mortar elements and the coordinates of nodes on the boundaries of aggregate elements are required to be adjusted for accurately representing the actual aggregate sizes.

To this end, a four-step procedure is proposed. Firstly, the original nodes on the boundaries of amplified aggregates are identified, followed by the definition of new nodes based on the coordinates of original nodes on the boundaries and the given thickness of ITZ. Then, the connectivities of the aggregate elements associated with these nodes are redefined by replacing the number of the original nodes by the number of the corresponding new nodes. Subsequently, 4-noded ITZ elements are formulated one by one using the original nodes and the corresponding new nodes. Finally, an updated input file for ABAQUS, which contains final mesh data, is generated. An in-house MATLAB program, which follows the above procedure, is developed, and part of the final FE mesh discretization corresponding to Figure 2 is illustrated as an example in Figure 3.

3.3. Continuum Damaged Plasticity Model. Without considering voids, it is well recognized that ITZ is weaker than aggregate and mortar, and consequently mesoscale cracking in concrete under loading is commonly considered to first appear in ITZs. After that, mesoscale cracks propagate into mortar and additional cracks initiate within mortar with the further increase of loading [1]. In general, aggregates behave elastically during the process of concrete fracturing. Hence, the isotropic linear elastic model is employed to model the mechanical behavior of aggregates, while a continuum damaged plasticity (CDP) model [26, 27] implemented in ABAQUS is utilized to describe the mechanical behavior of both mortar and ITZ, which is briefly summarized as follows.

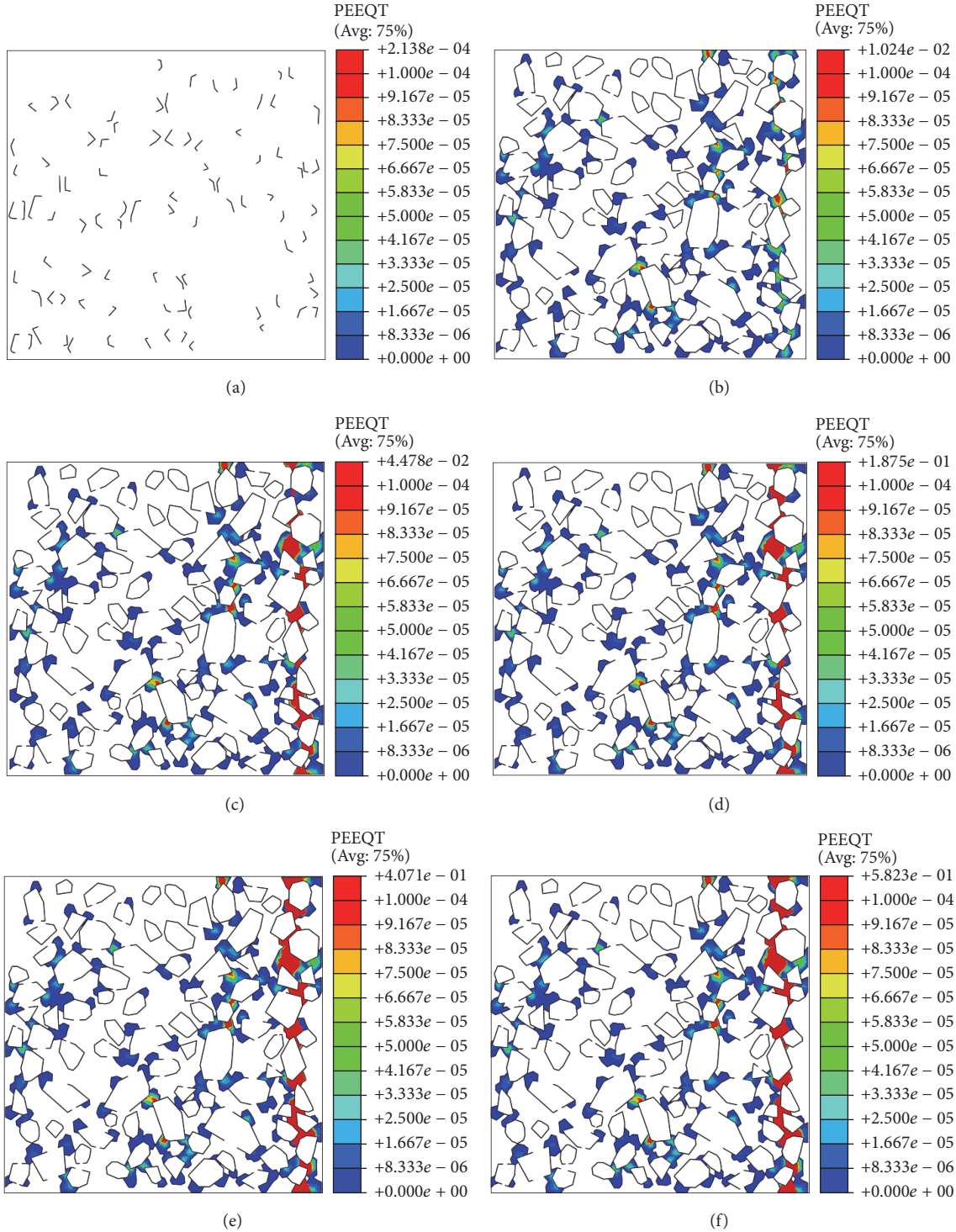


FIGURE 8: Mesoscale cracking development at different loading levels of the concrete specimen without void ($A_F = 40\%$). (a), (b), (c), (d), (e), and (f) show the equivalent tensile plastic strain distributions at points a–f, respectively.

In CDP model, two independent hardening variables, that is, equivalent compressive and tensile plastic strains $\bar{\varepsilon}_c^p$ and $\bar{\varepsilon}_t^p$, are introduced for considering compressive crushing and tensile cracking, respectively. Then, two independent damage variables, $d_c(\bar{\varepsilon}_c^p)$ and $d_t(\bar{\varepsilon}_t^p)$, are defined to represent

the compressive and tensile damage states. Furthermore, in order to describe the overall damage in an isotropic manner, a scale variable d is defined as

$$d = 1 - (1 - s_t d_c)(1 - s_c d_t), \quad (3)$$

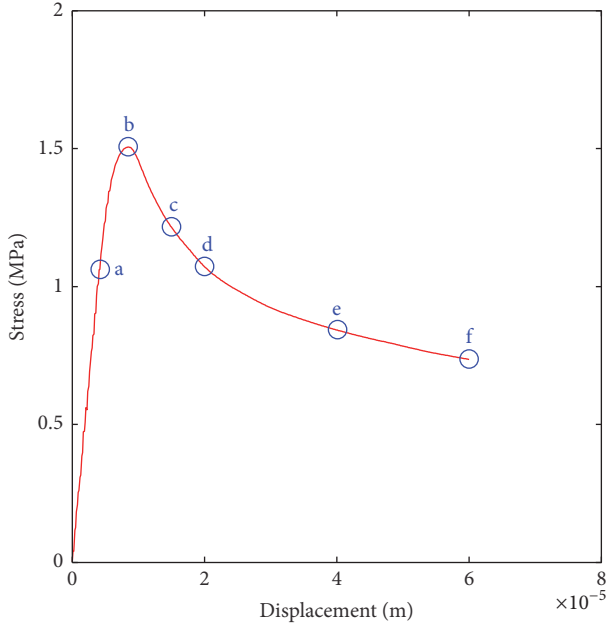


FIGURE 9: Stress-displacement curve ($A_F = 40\%$, $A_v = 2\%$).

where s_t and s_c are functions of the stress state that are introduced to represent stiffness recovery effects associated with stress reversals (see [27] for more details).

Then, the damaged elastic modulus E depending on different failure mechanisms under tension and compression can be described by

$$E = (1 - d) E_0 \quad (4)$$

in which E_0 represents the initial elastic modulus.

Based on the concept of damage mechanics, the effective stress $\bar{\sigma}$ can be calculated by

$$\bar{\sigma} = \frac{\sigma}{1 - d}, \quad (5)$$

where σ is the Cauchy stress.

The yield function of CDP model is given in the effective stress space as

$$F(\bar{\sigma}, \tilde{\epsilon}^p) = \frac{1}{1 - \alpha} (\bar{q} - 3\alpha\bar{p} + \beta(\tilde{\epsilon}^p) \langle \hat{\sigma}_{\max} \rangle - \gamma \langle -\hat{\sigma}_{\max} \rangle) - \bar{\sigma}_c(\tilde{\epsilon}_c^p), \quad (6)$$

where $\tilde{\epsilon}^p = [\tilde{\epsilon}_t^p \ \tilde{\epsilon}_c^p]^T$; \bar{p} and \bar{q} are the effective hydrostatic pressure and the effective Mises equivalent deviatoric stress, respectively; $\hat{\sigma}_{\max}$ is the algebraically maximum eigenvalue of $\bar{\sigma}$; the brackets $\langle \cdot \rangle$ are used in Macaulay sense; $\bar{\sigma}_c(\tilde{\epsilon}_c^p)$ is the uniaxial compressive effective strength; α and γ are dimensionless material constants, which can be determined by comparing the initial equibiaxial and uniaxial compressive yield stress and by comparing the yield conditions along the

tensile and compressive meridians, respectively; and $\beta(\tilde{\epsilon}^p)$ can be calculated by

$$\beta(\tilde{\epsilon}^p) = \frac{\bar{\sigma}_c(\tilde{\epsilon}_c^p)}{\bar{\sigma}_t(\tilde{\epsilon}_t^p)} (1 - \alpha) - (1 + \alpha) \quad (7)$$

in which $\bar{\sigma}_t(\tilde{\epsilon}_t^p)$ is the uniaxial tensile effective strength. Figure 4 illustrates the yield surface in the case of plane stress.

In order to describe the dilatancy reasonably, nonassociated flow rule is employed in CDP model, and the flow potential takes the form as

$$G(\bar{\sigma}) = \sqrt{(\epsilon\sigma_{t0} \tan \psi)^2 + \bar{q}^2} - \bar{p} \tan(\psi) \quad (8)$$

in which ϵ is a parameter defining the rate at which the function approaches the asymptote; σ_{t0} is the uniaxial tensile stress at failure; ψ is the dilation angle measured in \bar{p} - \bar{q} plane at high confining pressure.

As presented earlier, the material softening under tension is defined by the relationship between the uniaxial tensile effective strength and equivalent tensile plastic strain (see (7)), which means mesh sensitivity will be encountered when applying the CDP model in FE simulations. Therefore, a stress-displacement relation is used in this study to define the tensile softening behavior for alleviating the influence of mesh sensitivity on the simulation results.

3.4. Numerical Solution Algorithm. Due to the highly nonlinear and softening behavior of concrete in the process of fracturing, the ABAQUS/Explicit solver is employed in all simulations with the aim of capturing the entire fracturing process of concrete.

As is well known, the dynamic effect inevitably exists in an explicit FE analysis, and its influence on the solution of a quasi-static problem should be small enough to be neglected. In order to minimise the dynamic effect, the loading time should be large enough, while, on the other hand, the computational effort increases proportionally with the increase of loading time. Hence, a balance has to be made between the computational efficiency and simulation accuracy, which can be achieved through comparing the results under different loading time (or loading rates).

4. Results and Discussion

4.1. Numerical Specimens and Mechanical Properties. Aiming to investigate the effects of voids on the tensile fracturing of concrete with different aggregate volume fractions, three sets of numerical concrete specimens with dimensions of 100 mm \times 100 mm using polygonal aggregates are generated, and each set contains four specimens with the same aggregate arrangement and different A_v (0%, 2%, 4%, and 6%, resp.). For Set I, A_F is set to 30%, while $A_F = 40\%$ and 50% are chosen for Sets II and III, respectively. The typical element size is chosen as 0.4 times that of the minimum aggregate size; however the number of both elements and nodes of numerical specimens increases with the increase of A_v . For example, the number of elements and nodes for the specimen with $A_F = 40\%$ and $A_v = 2\%$ is 15796 and 9136, respectively,

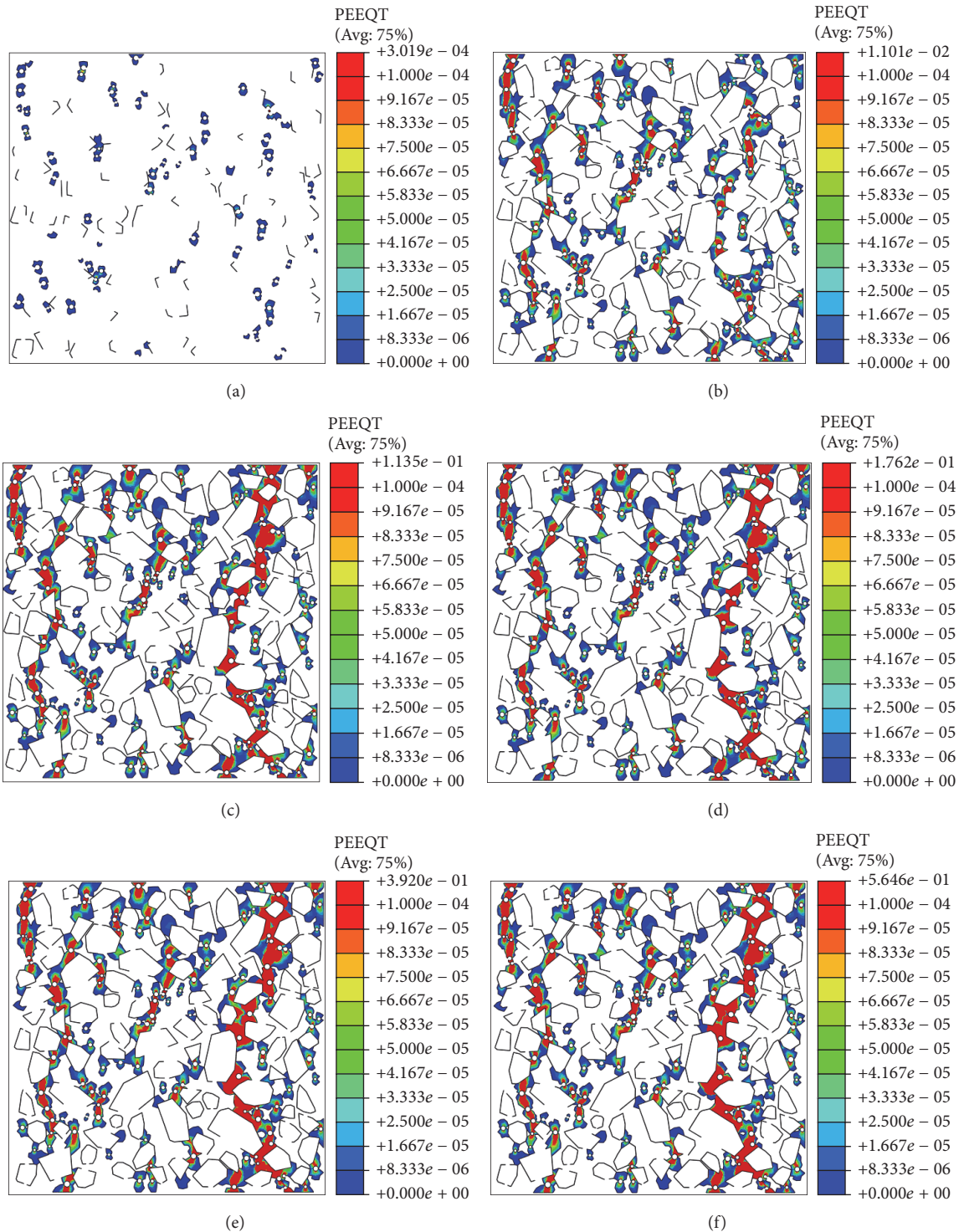


FIGURE 10: Mesoscale cracking development at different loading levels of concrete specimen with $A_F = 40\%$ and $A_v = 2\%$. (a), (b), (c), (d), (e), and (f) show the equivalent tensile plastic strain distributions at points a–f, respectively.

and the number of elements and nodes for the specimen with $A_F = 40\%$ and $A_v = 6\%$ is 20528 and 12126, respectively.

For each specimen, uniaxial tensile fracturing is simulated. In FE simulations, the left end of concrete specimen is fixed in the horizontal direction, while the opposite end

is subjected to a uniformly distributed horizontal displacement up to 0.06 mm, namely, a displacement-controlled loading scheme is used. Following the strategy discussed in Section 3.4, the loading time is set to 0.012 s, which corresponds to a loading rate 5 mm/s.

TABLE I: Mechanical properties of concrete components.

| Material | E_0 (GPa) | Poisson's ratio (—) | σ_{t0} (MPa) | ϵ (—) | ψ ($^\circ$) | α (—) | γ (—) |
|-----------|-------------|---------------------|---------------------|----------------|---------------------|--------------|--------------|
| Aggregate | 60 | 0.2 | — | — | — | — | — |
| Mortar | 20 | 0.2 | 1.94 | 0.1 | 35 | 0.12 | 2.0 |
| ITZ | 15 | 0.2 | 1.46 | 0.1 | 35 | 0.12 | 2.0 |
| Void | — | — | — | — | — | — | — |

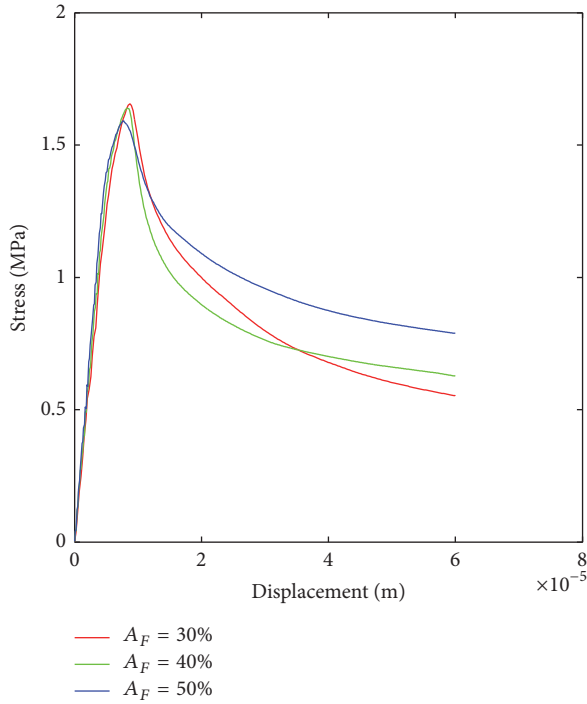


FIGURE 11: Stress-displacement curves of different aggregate volume fractions.

The same mechanical properties of aggregate, mortar, and ITZ are adopted for all specimens, as listed in Table 1. It is noted that the mechanical properties of mortar are directly obtained from Chinese code GB 50010-2002 (code for design of concrete structures), and the compression hardening curve and the tension softening curve are shown in Figures 5 and 6, respectively. Moreover, due to the lack of detailed experimental results for ITZ, the compressive and tensile strengths and elastic modulus of ITZ are assumed to be 75% of those of mortar for the sake of modeling the weaker ITZ, while the other mechanical properties of ITZ are taken as the same of mortar.

4.2. Effects of Voids on Concrete Tensile Fracturing Mechanism. In order to study the effects of voids on concrete tensile fracturing mechanism, the simulation results of two specimens in Set II, which include one without void and the other one with voids taking up 2% of the specimen volume, are discussed in detail in the following.

The macroscopic stress versus displacement curve of the concrete specimen without void ($A_F = 40\%$) under uniaxial tension is shown in Figure 7, and the elements with

nonzero equivalent tensile plastic strain at different loading levels are illustrated in Figure 8, in which the elements with equivalent tensile plastic strain bigger than 100 microstrains are highlighted in red color.

It can be observed that although concrete specimen initially exhibits elastic response on the macroscale, mesoscale cracking still occurs in ITZs (see Figure 8(a)) due to their lower fracture properties than mortar. With the increase of applied displacement, cracking develops in ITZs and subsequently propagates into mortar. The mesoscopic crack at the peak stress is shown in Figure 8(b), and it can be found that a macroscale crack close to the right end is formed as a result of the coalescence of mesoscopic cracks. In the softening stage, strain localization, which is accompanied by the decrease of macroscopic stress (see Figure 7) and finally leads to macroscopic tensile failure, can be clearly identified from Figures 8(c), 8(d), 8(e), and 8(f).

The macroscopic stress versus displacement curve of the concrete specimen ($A_F = 40\%$ and $A_v = 2\%$) under uniaxial tension is shown in Figure 9, and the elements with nonzero equivalent tensile plastic strain at different loading levels are illustrated in Figure 10. Compared to the case without void discussed above, mesoscale cracking appears in both ITZs and the mortar around voids in the macroscale elastic stage (see Figure 10(a)), and, additionally, cracked mortar generally suffers from bigger equivalent tensile plastic strain (see Figure 10(b)) at the peak stress as a result of the existence of voids. Similar to the specimen without void, a macroscale crack is formed at the peak stress point due to the coalescence of mesoscopic cracks. However, the fracture pattern is quite different from the one observed in the specimen without void even if the same aggregate arrangement is employed in both specimens, which indicates the existence of void dominates the fracturing behavior of concrete to a large extent. The phenomenon of strain localization, which is accompanied by the decrease of macroscopic stress (see Figure 9) and leads to the final tensile failure, is visualized in Figures 10(c), 10(d), 10(e), and 10(f).

Overall, different fracturing mechanisms can be observed for the two concrete specimens by comparing the development processes of mesoscale cracking shown in Figures 8 and 10. For the concrete specimen without void, mesoscale crack first appears in ITZ and then propagates into the neighboring mortar, while, for the concrete specimen with voids, mesoscale cracks are first found in both ITZ and mortar around voids and then coalesce in the fracturing process.

4.3. Effects of Void Volume Fraction. In this section, the effects of aggregate volume fraction (A_F) on concrete tensile

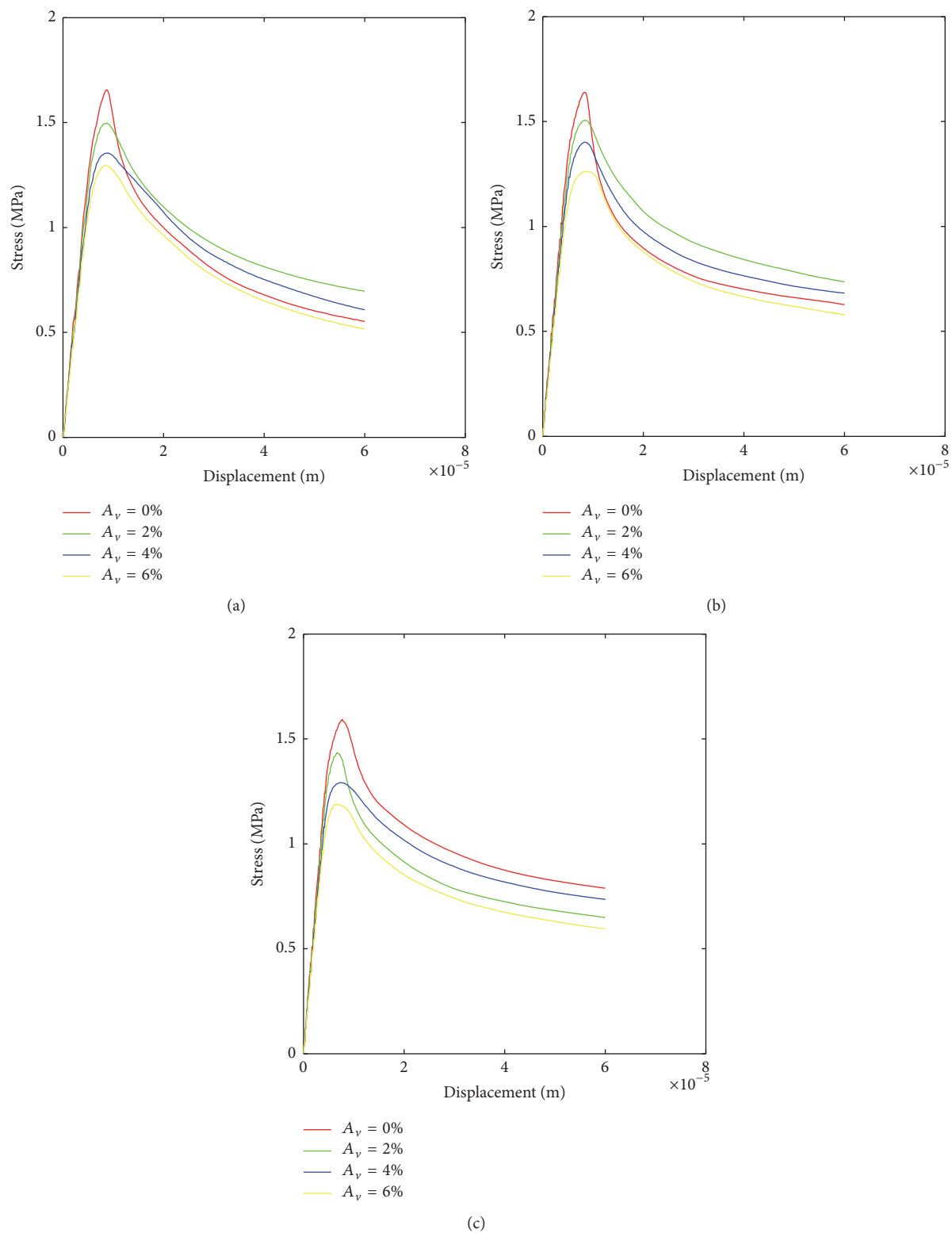


FIGURE 12: Stress-displacement curves for (a) $A_F = 30\%$; (b) $A_F = 40\%$; (c) $A_F = 50\%$.

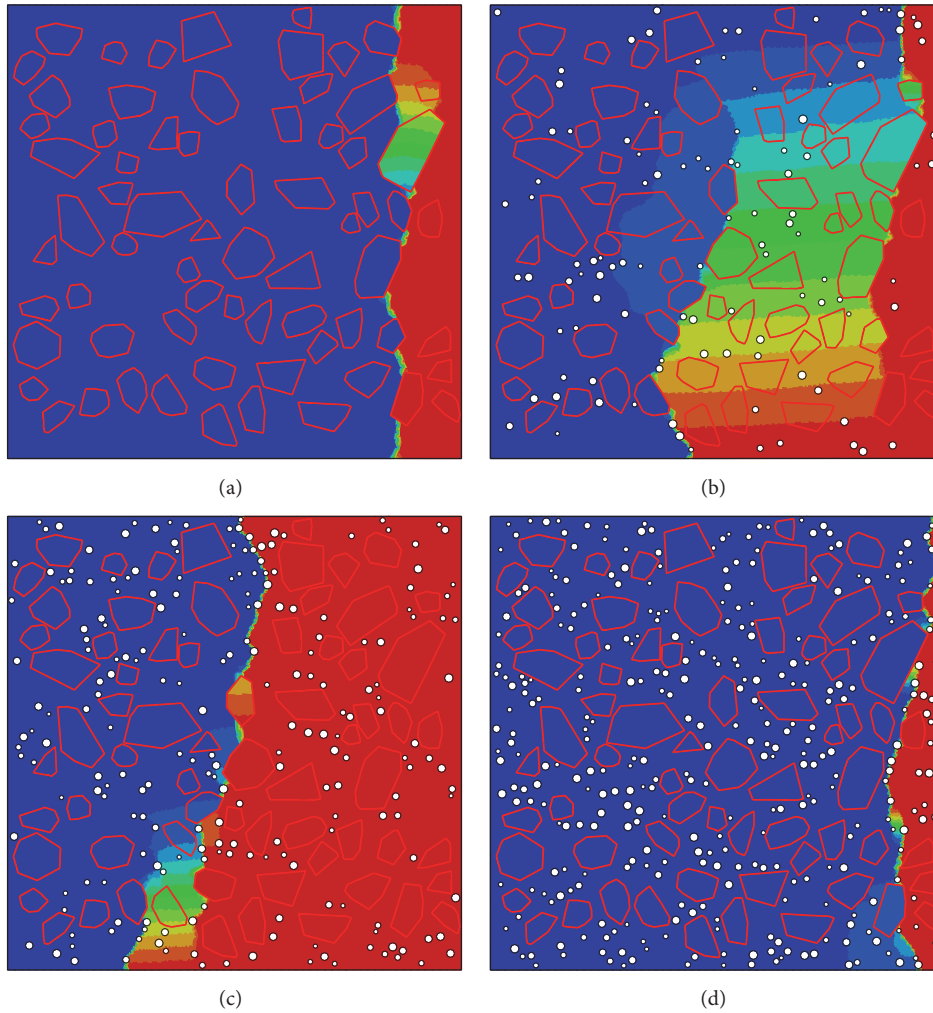


FIGURE 13: Fracture patterns of concrete specimens with $A_F = 30\%$ for (a) $A_v = 0\%$; (b) $A_v = 2\%$; (c) $A_v = 4\%$; (d) $A_v = 6\%$.

fracturing are first investigated, followed by the detailed discussion on the effects of void volume fraction on concrete with different aggregate volume fractions.

The specimens without void in Sets I, II, and III are simulated, and the macroscopic stress versus displacement curves are depicted in Figure 11. It is shown that the elastic responses of the three specimens are almost identical, which are in general linear and can be approximately characterized by the same elastic modulus. As A_F increases, the reached peak tensile stress slightly decreases (similar to the results reported in [15]), which can be attributed to the fact that more ITZs exist in the case of higher A_F . On the other hand, the postpeak stress in the case of $A_F = 40\%$ generally drops more quickly than in the case of $A_F = 30\%$, as expected. However, in the case of $A_F = 50\%$, the postpeak drops less quickly than in the other two cases, which may be due to the fact that this specimen finally fails with a different failure mode (two dominant macroscale cracks; see Figure 15(a)) from that of the other two specimens (one dominant macroscale crack; see Figures 13(a) and 14(a)), leading to higher fracture energy dissipated in tensile fracturing. From the above discussion,

it can be concluded that the postpeak behavior of concrete highly depends on the failure mode, namely, the more macroscale cracks appear, the higher fracture energy should be expected.

Provided the simulation results of Sets I, II, and III, the effects of void volume fraction (A_v) on concrete tensile fracturing are analyzed in the following. Figures 12(a), 12(b), and 12(c) present the stress-displacement relations of concrete specimens with $A_F = 30\%$, 40% , and 50% , respectively, and Figures 13, 14, and 15 illustrate the fracture patterns of concrete specimens with $A_F = 30\%$, 40% , and 50% , respectively. In Figures 12(a), 12(b), and 12(c), it is shown that the macroscale elastic modulus in prepeak stage can be considered to be independent of A_v , while the peak stress decreases as A_v increases. Moreover, the relation between A_v and the postpeak behavior is not straightforward as depicted. As shown in Figures 13, 14, and 15, the fracture patterns of concrete specimens with the same aggregate arrangement (represented by highlighted red polygons) and different A_v differ from each other. For concrete specimens without void, fracture pattern is mainly controlled by the distribution of

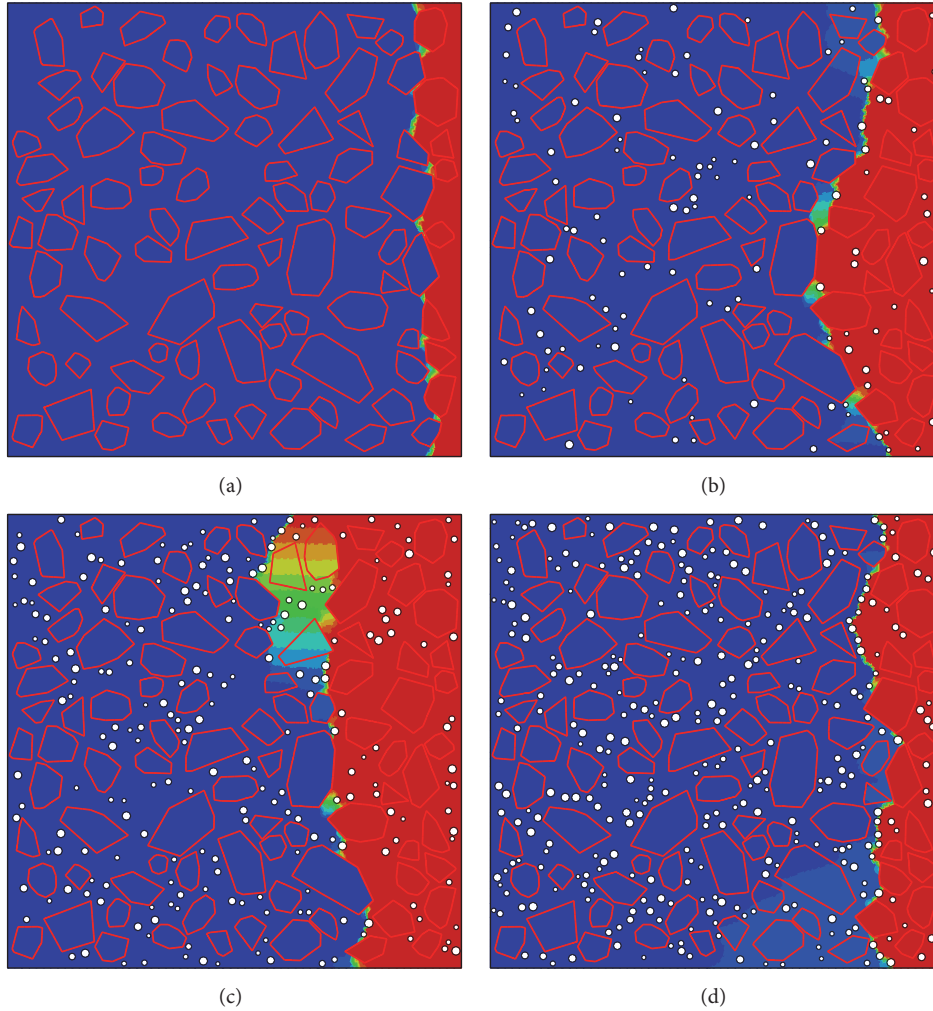


FIGURE 14: Fracture patterns of concrete specimens with $A_F = 40\%$ for (a) $A_v = 0\%$; (b) $A_v = 2\%$; (c) $A_v = 4\%$; (d) $A_v = 6\%$.

aggregates (or ITZs), whereas, for concrete specimens with voids, the fracture pattern is dominated not only by the aggregate arrangement but also by the distribution of voids in mortar, leading to the differences of fracture patterns illustrated in Figures 13, 14, and 15. Consequently, accurate fracturing analysis of concrete calls for the explicit modeling of voids. Furthermore, both the concrete specimen without void and the concrete specimens with voids present two types of failure modes: one is with a single macroscale crack (Type I, typically shown in Figure 15(b)), and the other is with two macroscale cracks (Type II; see Figure 13(b), e.g.). Owing to the longer crack length, the higher fracture energy is dissipated in Type II, and therefore the postpeak stress-displacement curve of Type II drops less quickly than that of Type I, which can be found in Figure 12.

5. Conclusions

A finite element modeling strategy of concrete with random mesostructure explicitly taking void into consideration has

been proposed in the present work. The tensile fracturing mechanism of concrete with voids is detailed on the mesoscale by comparing the simulation results of two specimens consisting of one without void and the other one with voids with the same aggregate arrangement. Then, several simulations are carried out with prime attention placed on the effects of void volume fraction on concrete tensile fracturing. The main conclusions are as follows:

- (i) Different fracturing mechanisms are observed for the two concrete specimens with the same aggregate arrangement including one without void and the other one with voids, and the fracture pattern of concrete specimen with voids is controlled by both the aggregate arrangement and the distribution of voids.
- (ii) Compared to aggregate volume fraction, void volume fraction has a larger influence on concrete tension strength. The elastic modulus of concrete in the prepeak stage can be considered to be independent

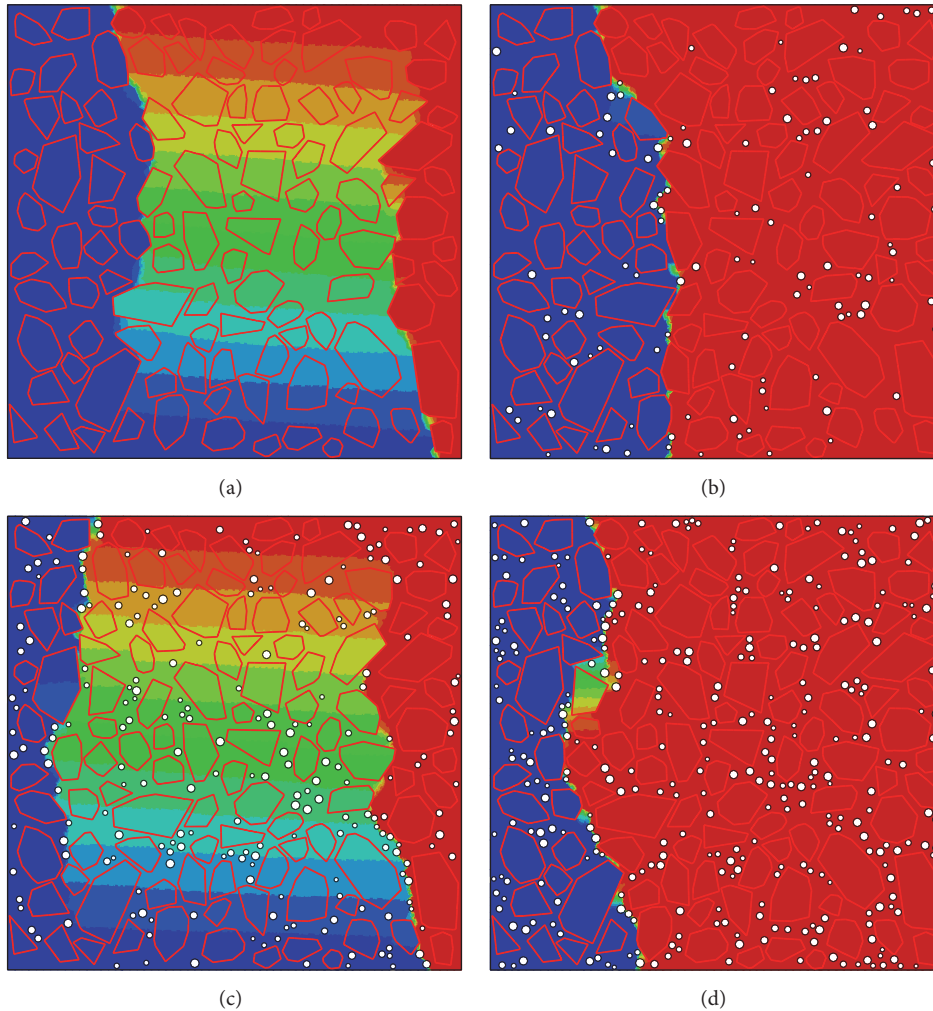


FIGURE 15: Fracture patterns of concrete specimens with $A_F = 50\%$ for (a) $A_v = 0\%$; (b) $A_v = 2\%$; (c) $A_v = 4\%$; (d) $A_v = 6\%$.

of both aggregate volume fraction and void volume fraction.

- (iii) The relation between concrete postpeak behavior and void volume fraction is not straightforward due to the randomness of void distribution and the resulting fracture pattern.
- (iv) Two types of failure modes are identified for concrete specimens under uniaxial tension, in which Type I is characterized by a single macroscale crack and Type II by two. Due to the longer crack length, the postpeak stress of Type II drops less quickly than that of Type I.
- (v) It is necessary to model void explicitly for the accurate fracturing simulation of concrete on the mesoscale.

Conflicts of Interest

The authors declare that there are no conflicts of interest regarding the publication of this paper.

Acknowledgments

This work was supported by projects of the National Natural Science Foundation of China (Grants nos. 11132003 and 51109067).

References

- [1] J. F. Unger and S. Eckardt, "Multiscale Modeling of Concrete," *Archives of Computational Methods in Engineering*, vol. 18, no. 3, pp. 341–393, 2011.
- [2] I. M. Gitman, H. Askes, and L. J. Sluys, "Coupled-volume multi-scale modelling of quasi-brittle material," *European Journal of Mechanics-A/Solids*, vol. 27, no. 3, pp. 302–327, 2008.
- [3] G. Cusatis, Z. P. Bažant, and L. Cedolin, "Confinement-shear lattice CSL model for fracture propagation in concrete," *Computer Methods in Applied Mechanics and Engineering*, vol. 195, no. 52, pp. 7154–7171, 2006.
- [4] R. Reza khani and G. Cusatis, "Asymptotic expansion homogenization of discrete fine-scale models with rotational degrees of freedom for the simulation of quasi-brittle materials," *Journal*

- of the Mechanics and Physics of Solids*, vol. 88, pp. 320–345, 2016.
- [5] M. Nitka and J. Tejchman, “Modelling of concrete behaviour in uniaxial compression and tension with DEM,” *Granular Matter*, vol. 17, no. 1, pp. 145–164, 2015.
 - [6] A. Caballero, I. Carol, and C. López, “A meso-level approach to the 3D numerical analysis of cracking and fracture of concrete materials,” *Fatigue and Fracture of Engineering Materials and Structures*, vol. 29, no. 12, pp. 979–991, 2006.
 - [7] P. Wriggers and S. O. Mofteh, “Mesoscale models for concrete: homogenisation and damage behaviour,” *Finite Elements in Analysis and Design*, vol. 42, no. 7, pp. 623–636, 2006.
 - [8] C. M. López, I. Carol, and A. Aguado, “Meso-structural study of concrete fracture using interface elements. I: numerical model and tensile behavior,” *Materials and Structures/Materiaux et Constructions*, vol. 41, no. 3, pp. 583–599, 2008.
 - [9] I. Comby-Peyrot, F. Bernard, P.-O. Bouchard, F. Bay, and E. Garcia-Diaz, “Development and validation of a 3D computational tool to describe concrete behaviour at mesoscale. Application to the alkali-silica reaction,” *Computational Materials Science*, vol. 46, no. 4, pp. 1163–1177, 2009.
 - [10] P. Grassl and M. Jirásek, “Meso-scale approach to modelling the fracture process zone of concrete subjected to uniaxial tension,” *International Journal of Solids and Structures*, vol. 47, no. 7-8, pp. 957–968, 2010.
 - [11] S. Shahbeyk, M. Hosseini, and M. Yaghoobi, “Mesoscale finite element prediction of concrete failure,” *Computational Materials Science*, vol. 50, no. 7, pp. 1973–1990, 2011.
 - [12] L. Snozzi, A. Caballero, and J. F. Molinari, “Influence of the meso-structure in dynamic fracture simulation of concrete under tensile loading,” *Cement and Concrete Research*, vol. 41, no. 11, pp. 1130–1142, 2011.
 - [13] X. Du, L. Jin, and G. Ma, “Numerical simulation of dynamic tensile-failure of concrete at meso-scale,” *International Journal of Impact Engineering*, vol. 66, pp. 5–17, 2014.
 - [14] Y. Huang, Z. Yang, W. Ren, G. Liu, and C. Zhang, “3D meso-scale fracture modelling and validation of concrete based on in-situ X-ray Computed Tomography images using damage plasticity model,” *International Journal of Solids and Structures*, vol. 67-68, pp. 340–352, 2015.
 - [15] X. F. Wang, Z. J. Yang, J. R. Yates, A. P. Jivkov, and C. Zhang, “Monte Carlo simulations of mesoscale fracture modelling of concrete with random aggregates and pores,” *Construction and Building Materials*, vol. 75, pp. 35–45, 2015.
 - [16] X. Wang, M. Zhang, and A. P. Jivkov, “Computational technology for analysis of 3D meso-structure effects on damage and failure of concrete,” *International Journal of Solids and Structures*, vol. 80, pp. 310–333, 2016.
 - [17] A. Zubelewicz and Z. P. Bažant, “Interface element modeling of fracture in aggregate composites,” *Journal of Engineering Mechanics*, vol. 113, no. 11, pp. 1619–1630, 1987.
 - [18] Z. P. Bažant, M. R. Tabbara, M. T. Kazemi, and G. Pyaudier-Cabot, “Random particle model for fracture of aggregate or fiber composites,” *Journal of Engineering Mechanics*, vol. 116, no. 8, pp. 1686–1705, 1990.
 - [19] E. Schlangen and J. G. M. van Mier, “Simple lattice model for numerical simulation of fracture of concrete materials and structures,” *Materials and Structures*, vol. 25, no. 9, pp. 534–542, 1992.
 - [20] E. Schlangen and E. J. Garboczi, “Fracture simulations of concrete using lattice models: computational aspects,” *Engineering Fracture Mechanics*, vol. 57, no. 2-3, pp. 319–332, 1997.
 - [21] G. Cusatis, D. Pelessone, and A. Mencarelli, “Lattice Discrete Particle Model (LDPM) for failure behavior of concrete. I: Theory,” *Cement and Concrete Composites*, vol. 33, no. 9, pp. 881–890, 2011.
 - [22] G. Cusatis, A. Mencarelli, D. Pelessone, and J. Baylot, “Lattice Discrete Particle Model (LDPM) for failure behavior of concrete. II: calibration and validation,” *Cement and Concrete Composites*, vol. 33, no. 9, pp. 891–905, 2011.
 - [23] F. Chen and P. Qiao, “Probabilistic damage modeling and service-life prediction of concrete under freeze–thaw action,” *Materials and Structures/Materiaux et Constructions*, vol. 48, no. 8, pp. 2697–2711, 2014.
 - [24] Z. Wang, A. Kwan, and H. Chan, “Mesoscopic study of concrete I: generation of random aggregate structure and finite element mesh,” *Computers and Structures*, vol. 70, no. 5, pp. 533–544, 1999.
 - [25] V. Palmieri and L. De Lorenzis, “Multiscale modeling of concrete and of the FRP-concrete interface,” *Engineering Fracture Mechanics*, vol. 131, pp. 150–175, 2014.
 - [26] J. Lubliner, J. Oliver, S. Oller, and E. Oñate, “A plastic-damage model for concrete,” *International Journal of Solids and Structures*, vol. 25, no. 3, pp. 299–326, 1989.
 - [27] J. Lee and G. L. Fenves, “Plastic-damage model for cyclic loading of concrete structures,” *Journal of Engineering Mechanics*, vol. 124, no. 8, pp. 892–900, 1998.

Research Article

Experimental Analysis and Discussion on the Damage Variable of Frozen Loess

Cong Cai,^{1,2} Wei Ma,¹ Shuping Zhao,³ and Yanhu Mu¹

¹State Key Laboratory of Frozen Soil Engineering, Cold and Arid Regions Environmental and Engineering Research Institute, Chinese Academy of Sciences, Lanzhou 730000, China

²University of Chinese Academy of Sciences, Beijing 100049, China

³Key Lab of Visual Geographic Environment, Ministry of Education, Nanjing Normal University, Nanjing 210023, China

Correspondence should be addressed to Wei Ma; cc20109163@163.com

Received 25 October 2016; Revised 2 January 2017; Accepted 8 February 2017; Published 13 March 2017

Academic Editor: Paulo M. S. T. De Castro

Copyright © 2017 Cong Cai et al. This is an open access article distributed under the Creative Commons Attribution License, which permits unrestricted use, distribution, and reproduction in any medium, provided the original work is properly cited.

The damage variable is very important to study damage evolution of material. Taking frozen loess as an example, a series of triaxial compression and triaxial loading-unloading tests are performed under five strain rates of 5.0×10^{-6} – 1.3×10^{-2} /s at a temperature of -6°C . A damage criterion of frozen loess is defined and a damage factor D_c is introduced to satisfy the requirements of the engineering application. The damage variable of frozen loess is investigated using the following four methods: the stiffness degradation method, the deformation increase method, the dissipated energy increase method, and the constitutive model deducing method during deformation process. In addition, the advantages and disadvantages of the four methods are discussed when they are used for frozen loess material. According to the discussion, the plastic strain may be the most appropriate variable to characterize the damage evolution of frozen loess during the deformation process based on the material properties and the nature of the material service.

1. Introduction

There are many defects in a material, such as voids and cracks, which may constantly grow and accumulate under external loads. These inner defects and their change processes under external loads are defined as the damage and the damage evolution of material [1]. The damage evolution can also be considered the degradation of material properties. Xu introduced a continuous variable and an evaluation law to describe the rupture process of metal materials under the creep process [1]. Since then, many achievements in the damage evaluation of materials were obtained [2–6], and a new discipline in solid mechanics has been developed, which is named continuum damage mechanics (CDM).

In general, the main methods of characterizing the damage and damage evolution of a material are the mesomethod based on material science (metal physics), the macromethod based on phenomenology, and the micromethod based on statistics. The study covers the following three major components: selection of the damage variable, definition of the

damage threshold value, and establishment of the damage evolution law. However, because of the randomness of the defects, it is too difficult to consider the effects of all defects on the degradation of material properties under external loads. Therefore, the most common investigation method of damage mechanics is to introduce a continuous variable, which can describe the changing process of microstructure defects during deformation process. Then, the changes in effective loading area or macromechanical properties of the material under loads are characterized; thus, this continuous variable is also called the damage factor [7]. The damage variable is introduced to describe the change of the damage factor. An appropriate damage variable should include three features. First, it must have a direct response to the mesoscopic changes of the material. Second, the damage variable of different materials should select this physical index, which can directly or indirectly characterize the main property of the material. Third, the selected variable better can be directly obtained from the experiment. Before selecting the damage

TABLE I: Grain size distribution and physical properties of frozen loess.

| Grain size distribution of loess in Lanzhou/% | | | Initial moisture | Liquid limit | Plastic limit |
|---|---------------|-----------|------------------|--------------|---------------|
| 0.05–0.075 mm | 0.005–0.05 mm | <0.005 mm | /% | /% | /% |
| 23.88 | 66.57 | 9.55 | 6.40 | 15.70 | 24.30 |

variable and establishing the damage evolution law, the initial criterion of damage (entering the damage status) and failure criterion of damage (damage thresholds of material) should be defined. The theory was first introduced to study the material uniaxial tension: $D = 0$, undamaged state; $D = 1$, failure state; and $0 < D < 1$, damaged intermediate state [8]. Voyiadjis also raised a key issue concerning damage of different materials: “What is failure?” [9]. According to Voyiadjis, the failure criteria of different materials ($D = 1$) should be clearly defined by considering the material properties and purposes of engineering applications; otherwise, the definition of the damage variable will lose its meaning. According to the ideal condition, the failure criterion of material is that the effective stress of the material reaches the residual strength value. However, for engineering applications, considering the unpredictable loads and structural instability, the situation that cannot satisfy safety requirements will appear even if the stress conditions do not reach failure conditions (the residual strength) [1]. For engineering requirements, CDM often provides a critical damage D_c to represent failure conditions. Based on the abovementioned developments, researchers have proposed many different methods, such as the stiffness degradation [10], dissipated energy increase [11], and development of plastic strain [12]. Lapovok [12] and Shi et al. [13] studied the damage evolution of metal by deformation and density variation. Cao et al. studied the damage evolution of rock using the digital speckle correlation method (DSCM) and compared with the results from computed tomography (CT) [14]. Swoboda and Yang considered that the dissipated energy could be turned as the driving force of crack growth based on the view of Griffith crack in fracture mechanics under the isothermal and insulate condition [11]. In addition, the constitutive model of some materials has been obtained, but it cannot clearly observe the damage evolution law. Then, the law can be derived by the theory of effective stress [7, 15].

However, few studies compared the advantages and disadvantages among different damage variables or discussed the selection criteria of the damage variable to the same material. In this paper, the frozen loess is a typical complex material with a four-phase medium [16], which is notably sensitive to environmental conditions. In addition, the microdefects are difficult to describe because of the complexity of the material structure. Thus, many microtest methods, including CT and scanning electron microscope (SEM), cannot be used for their damage testing [5]. At present, the common method of damage research of frozen loess depends on the macroexperimental results. This paper studies the damage evolution of frozen loess under external loads based on a series of triaxial test results on frozen loess; the evolution characteristics of different damage variables during deformation are investigated and compared.

The comparison analysis is also conducted by using different damage factors to evaluate the mechanical properties of frozen loess based on experimental results and previous studies.

2. Specimen Preparation and Test Conditions

Loess soils from Jiuzhoutai town (a seasonal frozen region) of Lanzhou City, northwest China, are used in this study. The particle size distribution and associated physical parameters of the soils are shown in Table I. To ensure the uniformity, the soil specimens are prepared according to the following steps: air drying of the undisturbed soils, crushing and 2 mm screening, measuring the initial moisture content, mixing to obtain a 16.5% moisture content, and maintaining that content for 6 h without evaporation. The specimens are compacted using variable loading rates in a cylinder. The dimensions of the specimens are 61.8 mm in diameter and 125.0 mm in height. After the compaction, the specimens are completely saturated using distilled water in vacuum conditions for 10 h. Then, they are put into rigid molds and quickly frozen at a low temperature of -25°C for over 48 h to limit water loss and migration. After the freezing, the specimens are taken from the molds and mounted with epoxy resin platens on both ends and covered with rubber sleeves. Finally, the specimens are kept in an incubator for over 12 h until the specimens reached the target testing temperature of -6°C [17].

Two types of mechanical tests are conducted using a material testing machine (MTS-810): constant strain rate triaxial compression (C) and loading-unloading compression (L-U-C). All tests are performed at a constant confining pressure ($\sigma_3 = 0.1 \text{ MPa}$) and a constant temperature ($T = -6^{\circ}\text{C}$). The strain rates of the tests are $1.3 \times 10^{-2}/\text{s}$, $5.0 \times 10^{-3}/\text{s}$, $5.0 \times 10^{-4}/\text{s}$, $5.0 \times 10^{-5}/\text{s}$, and $5.0 \times 10^{-6}/\text{s}$. The loading and unloading tests are performed at the identical strain rate to avoid the effect of the strain rate on the same trial.

3. Results and Analysis

The C test results under five different strain rates are shown in Figure 1. The deviator stress ($\sigma_1 - \sigma_3$) and axial strain (ϵ_1) relation of frozen loess strongly depends on the strain rate. At small strain, the stress-strain behavior performs as hardening. With the continuous loading, the specimen damage gradually develops and the stress-strain behavior performs as strain softening. With the increase in strain rate, the peak axial strain ϵ_1^u sharply increases and approaches the maximum at a strain rate of $5.0 \times 10^{-3}/\text{s}$. Then, the peak axial strain decreases with the strain rate increase, as shown in Figure 2. This result suggests that the damage of frozen loess is strain-dependent and strongly rate-dependent. Variations

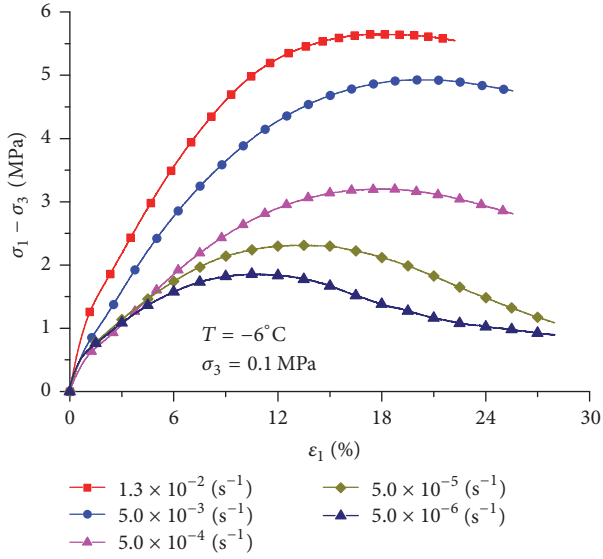


FIGURE 1: Deviator stress-axial strain curves for frozen loess under C tests.

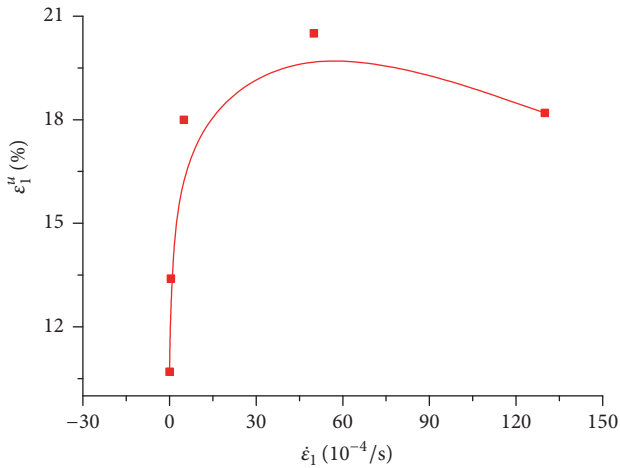


FIGURE 2: Peak strain for frozen loess under C tests.

of the stress-strain relations and the peak axial strains with the strain rates are related to the rheological characteristics of frozen loess.

The $L-U-C$ test results under the five different strain rates are shown in Figure 3, and the comparison of C and $L-U-C$ test results is shown in Figure 4. It can be seen that the loading and unloading cycles test do not affect the deformation behavior of frozen loess. To verify the accuracy of the test data, some repeated tests are carried out, as shown in Figure 5.

4. Damage Features of Frozen Loess

In this paper, the following studies are conducted on the premise of the phenomenism and isotropic continuum medium. The changes of the mesofabric are characterized by

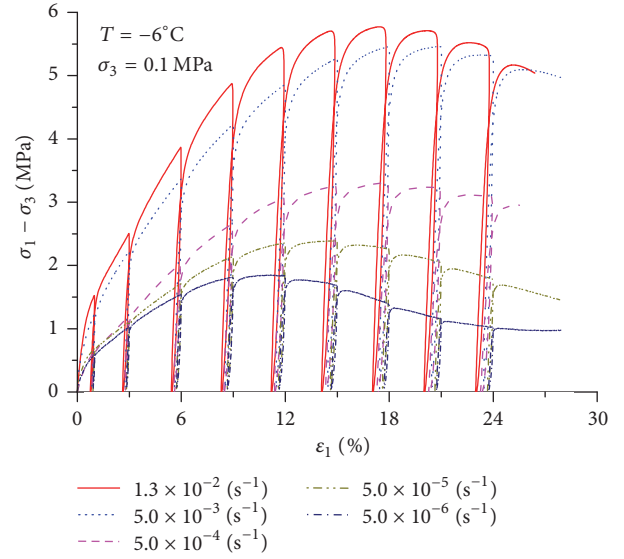


FIGURE 3: Deviator stress-axial strain curves for frozen loess under $L-U-C$ tests.

introducing a continuous variable. Then, the macro description of damage accumulation can be expressed by a scalar equation as follows [12, 18]:

$$D = D(\sigma_{ij}, \epsilon_{ij}, \dot{\epsilon}_{ij}). \quad (1)$$

There were different damage variables with different damage evolution laws even when the identical physical process is described. The concept of damage variable was first introduced from the concept of effective stress, which was proposed by Kachanov [19].

$$\sigma_{\text{eff}} = \frac{\sigma_0}{1-D}. \quad (2)$$

Then, the damage evolution law can be written as

$$\frac{dD}{dt} = f(D, \sigma_{ij}), \quad (3)$$

where D is the damage variable; σ_{eff} is the effective stress; and σ_0 is the nominal stress. If a reasonable damage evolution law can be established, then the damage state, residual strength, and longevity of material can be easily and accurately predicted.

4.1. Damage Criterion of Frozen Loess. According to the studies of Zhao et al. [5], Xu et al. [6], and Huang and Li [20] and the test results of this study, the material is softening when the deformation reaches a certain level. Then, the cracks in the material expand rapidly, the strength decreases rapidly, and the structure becomes unstable. Therefore, some researchers proposed that the failure condition of material could be defined as the status that the stress reaches the extreme value point [1]. The status can be expressed as follows:

$$\left. \frac{d\sigma}{d\epsilon} \right|_{D_c} = 0. \quad (4)$$

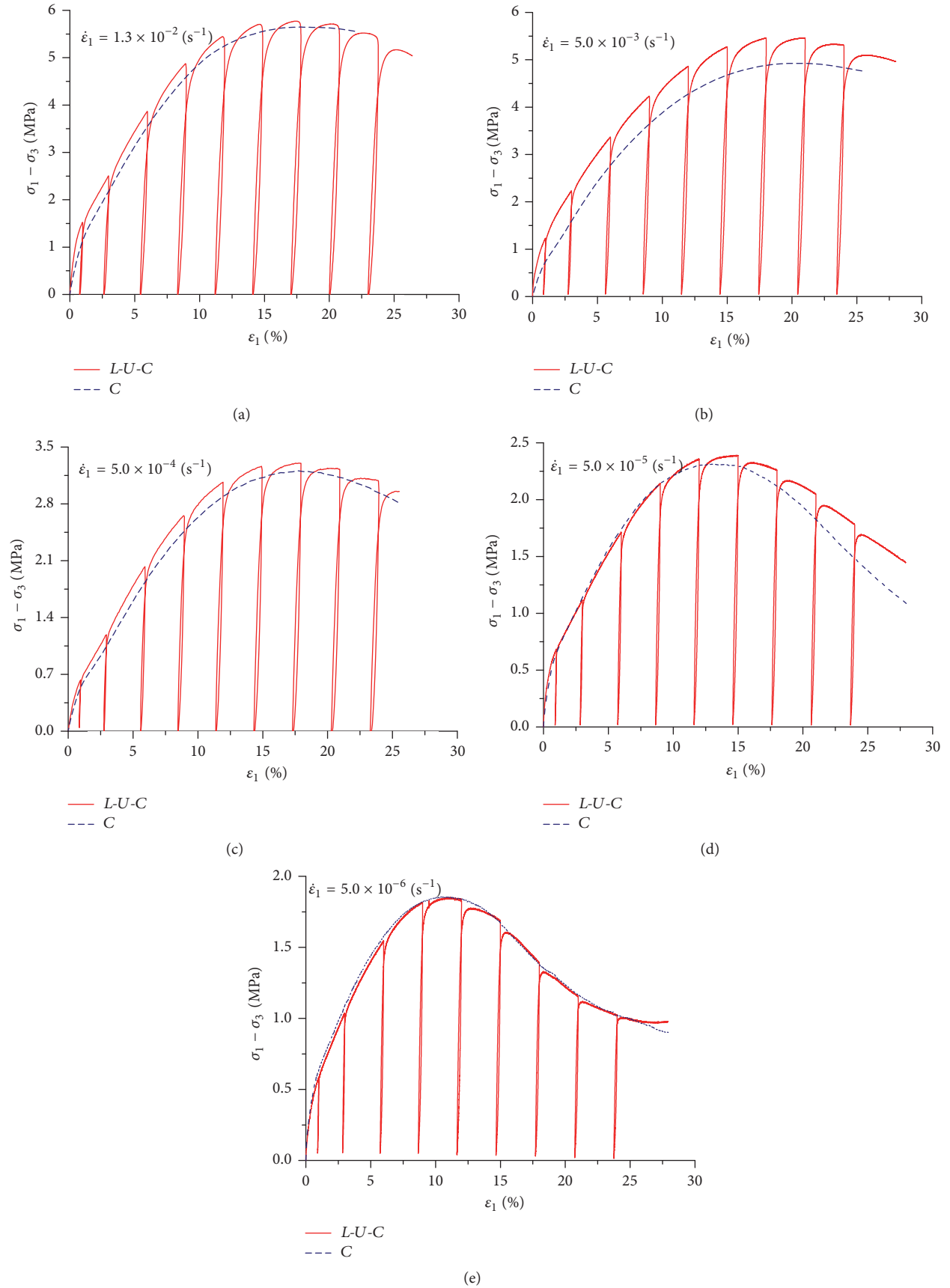


FIGURE 4: The comparison of C and L-U-C tests under different strain rates.

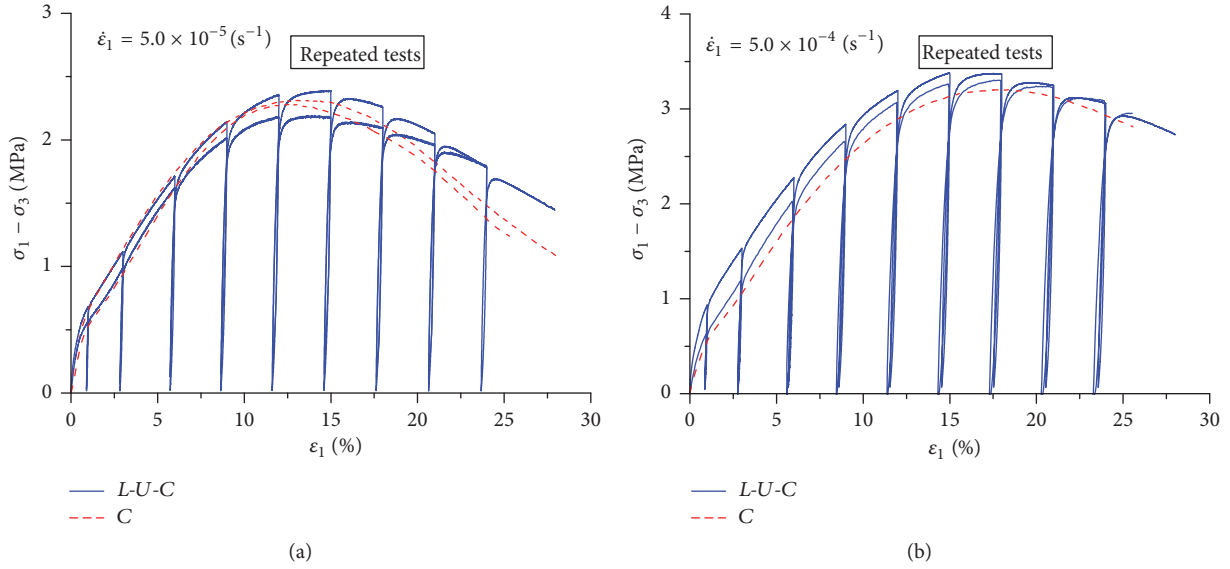


FIGURE 5: The accuracy of the test data.

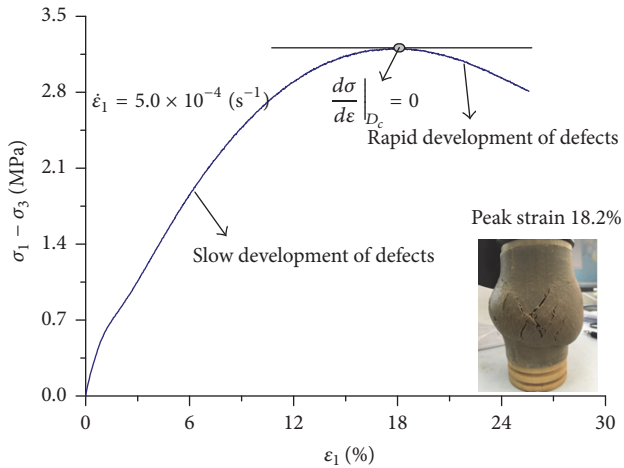


FIGURE 6: The selected criterion of critical damage for frozen loess.

Based on a series of repeated tests, the peak strain of frozen loess is obtained under different strain rates according to the statistics principle. The new test is accomplished when the strain reaches the peak strain. The typical physical status of frozen loess around the peak strain is shown in Figure 6. The cracks on the frozen loess surface are large and rapidly develop after the peak strain. Thus, this status is unsuited for continuous loading and can be referred to as the critical damage status of frozen loess material.

In addition, the selection of the damage factor and quantitative relationship between the damage factor and the damage variable should be considered. Based on previous studies and the test results of this study, this paper discusses four common damage factors and damage variables.

4.2. Damage Variables of Frozen Loess

4.2.1. Stiffness Degradation Method. The stiffness of the material continuously degenerates with the increase of deformation. The degradation of mechanical properties of the material is due to the nucleation and development of the material damage at the microscale level, such as voids and cracks. According to the above discussions and previous studies [8, 10, 21], the unloading modulus is selected to characterize the stiffness of the material under different damage states. Then, the damage variable can be written as follows:

$$D = 1 - \frac{\tilde{E}}{E_0}, \quad (5)$$

where E_0 is the initial elastic modulus of the material, which is also known as the undamaged modulus. \tilde{E} is the elastic modulus under different damage state.

To obtain the component of the elastic strain ϵ_1^e , plastic strain ϵ_1^p , and the change law of unloading modulus during the deformation, the hysteretic loop is addressed using the approximation-linearized method [22], as shown in Figure 7.

There are two selections for the unloading modulus: modulus of hysteretic loop E_h and the secant modulus E_s . The variations of E_h and E_s with the axial strain are shown in Figures 8(a) and 8(b), respectively.

In Figure 8, the unloading modulus of frozen loess decreases with the increase in axial strain when the strain rate is below $5.0 \times 10^{-4}/s$, but the change trend is not obvious when the strain rate is above $5.0 \times 10^{-4}/s$. The phenomenon is verified by repeated tests. According to Xie [23] and Yu [24], the unloading modulus was selected as a damage factor based on the equivalence hypothesis of strain and the method of elastic modulus. However, this hypothesis can only be

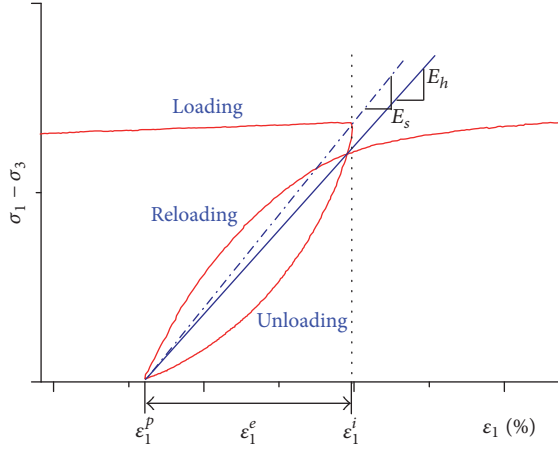


FIGURE 7: The decoupling principle on the hysteretic loop.

applied for elastic damage. The frozen loess is an elastic-plastic coupling material, which can be verified from the L - U - C tests that the plastic deformation is dominant even if the axial strain is 1%. Thus, the actual damage feature of frozen loess is significantly simplified or hidden when the unloading modulus is selected as the damage factor.

Many experimental results show that the unloading modulus can only decrease when the deformation reaches a certain status [23]. This phenomenon suggests that there is a damage threshold value for elastic-plastic materials, which is consistent with the law that the granular material is first compacted, and subsequently shear failure under external loads. The unloading modulus may be greater than or equal to the initial elastic modulus of the material before this certain status. Then, using the unloading modulus (E_h or E_s) to calculate the material damage will lead to a wrong conclusion; for example, no damage or even negative damage occurs. However, for the unloading modulus, E_s may be better than E_h because E_s is only a part of the unloading curve.

To study the stiffness degradation of the material during the deformation, some researchers proposed that the deformation modulus should be adopted, which is defined as the slope of the secant line of the stress-strain curve from the loading point to the instantaneous damage point (see Figure 9) [24–26]. The deformation modulus E_d is used to describe the damage evolution of the material.

The evolution law of E_d with axial strain under different strain rates is shown in Figure 10. The damage variable is expressed as follows:

$$D = 1 - \frac{E_d}{E_0}. \quad (6)$$

In addition, there is a quantitative relationship between the unloading modulus E_s and the deformation modulus E_d under the same strain and stress [23]:

$$E_d = \frac{\varepsilon_1 - \varepsilon_1^p}{\varepsilon_1} E_s, \quad (7)$$

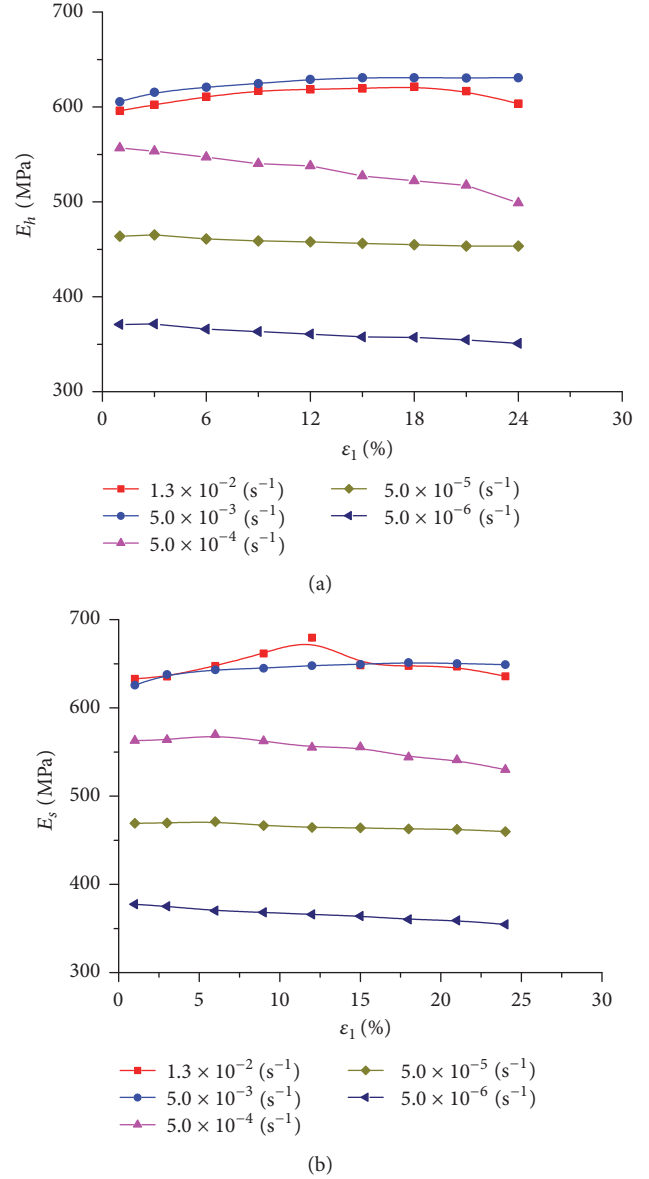


FIGURE 8: Variation of E_h and E_s with axial strain under different strain rates.

where ε_1^p is the axial plastic strain. Then, the damage variable can be described with the unloading modulus (E_s).

$$D = 1 - \frac{\varepsilon_1 - \varepsilon_1^p}{\varepsilon_1} \left(\frac{E_s}{E_0} \right). \quad (8)$$

Then, the unloading modulus (E_s) can describe the increase in damage and the stiffness degradation of material like the deformation modulus (E_d). Based on the test results of this study, the relationship between axial strain and damage variable is established as follows:

$$D = \frac{\varepsilon_1}{a\varepsilon_1^2 + b\varepsilon_1 + c}, \quad (9)$$

where a , b , and c are material parameters corresponding to the strain rate. The test results and fitting curves are shown in

TABLE 2: Material parameters a , b , and c under different strain rates (stiffness).

| $\dot{\varepsilon}_1$ | $1.3 \times 10^{-2}/s$ | $5.0 \times 10^{-3}/s$ | $5.0 \times 10^{-4}/s$ | $5.0 \times 10^{-5}/s$ | $5.0 \times 10^{-6}/s$ |
|-----------------------|------------------------|------------------------|------------------------|------------------------|------------------------|
| a | -0.381 | -0.377 | -0.544 | -0.463 | -0.532 |
| b | 1.142 | 1.150 | 1.189 | 1.134 | 1.127 |
| c | 0.014 | 0.009 | 0.003 | 0.005 | 0.004 |

TABLE 3: Material parameter θ under different strain rates (plastic strain).

| $\dot{\varepsilon}_1$ | $1.3 \times 10^{-2}/s$ | $5.0 \times 10^{-3}/s$ | $5.0 \times 10^{-4}/s$ | $5.0 \times 10^{-5}/s$ | $5.0 \times 10^{-6}/s$ |
|-----------------------|------------------------|------------------------|------------------------|------------------------|------------------------|
| θ | 5.520 | 4.710 | 5.448 | 7.241 | 9.075 |

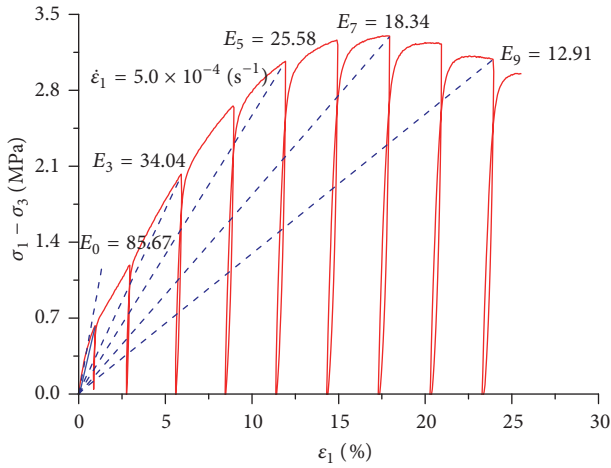
FIGURE 9: The definition of deformation modulus E_d .

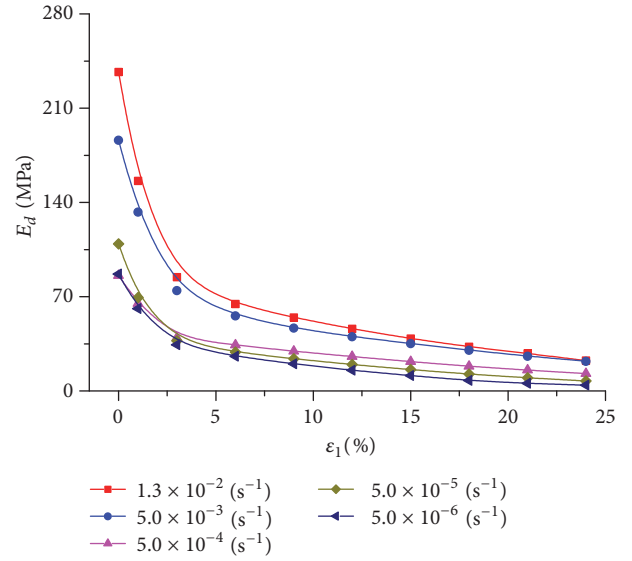
Figure 11, and the parameters a , b , and c under different strain rates are listed in Table 2.

4.2.2. Plastic Strain Method. Considering the process of fatigue damage, Lemaitre [27] and Lapovok [12] proposed that plastic strain or permanent strain was an irreversibility macroscopic behavior as a result of microcrack growth and development (damage-fatigue equivalent analogy method). Therefore, the plastic deformation can be selected as the damage factor according to the ability of the material to resist permanent deformation. Then, according to Liao et al. [28], the damage variable can be written as follows:

$$D = 1 - \exp\left(-\frac{\varepsilon_1^p}{\varepsilon_1^u}\right), \quad (10)$$

where ε_1^u is the peak strain (see Figure 2) and ε_1^p is plastic strain under different deformation statuses.

The variation of ε_1^p with axial strain under different strain rates is shown in Figure 12. Within the total deformation, the plastic strain is dominant, and the elastic deformation contributes very little. In addition, the development of plastic strain is almost independent of the strain rate. Based on the test results of this study, the relationship between the damage variable and the axial strain is shown in Figure 13.

FIGURE 10: Variation of E_d with axial strain under different strain rates.

Liao et al. introduced the following negative exponential function in order to establish the relationship of the damage variable and the axial strain [28]:

$$D = 1 - \exp(-\theta\varepsilon_1), \quad (11)$$

where θ is a material parameter corresponding to time, which controls the damage degree and degradation of material properties. Parameter θ under different strain rates is listed in Table 3 according to the test results of this study. Different strain rates that correspond to the critical damage (D_c) are shown in Figure 13. The strains considerably vary when the critical damage approaches under different strain rates, but the critical damage value (D_c) differs a little. This result suggests that the plastic strain, elastic strain, and their contributions to the total deformation are independent of the deformation degree and strain rate.

4.2.3. Energy Dissipation Method. According to thermodynamics and fracture mechanics, the work performed by external loads is not entirely stored as elastic strain energy under the isothermal and adiabatic condition, and a part of it is consumed in damage nucleation and evaluation. For

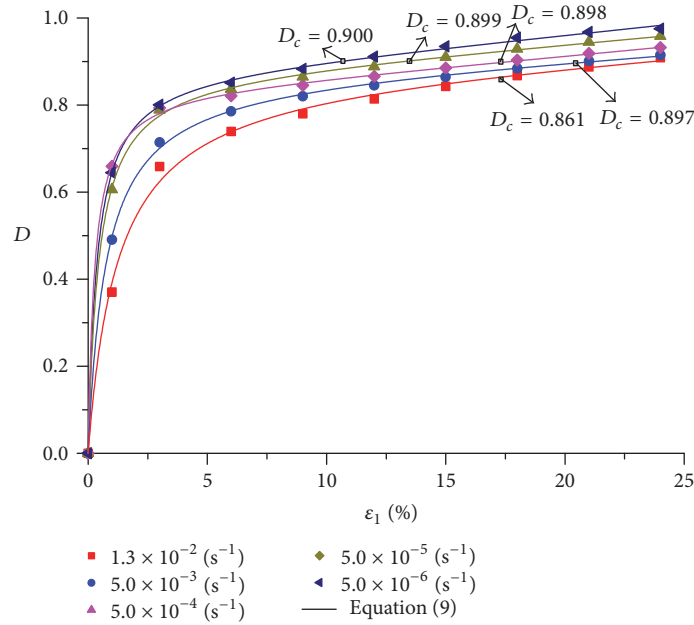


FIGURE 11: Variation of the damage variable with axial strain under different strain rates (stiffness).

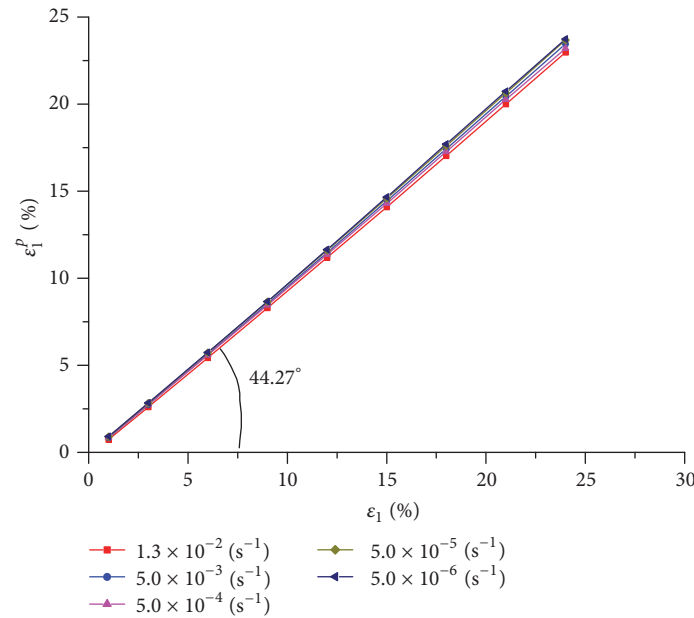


FIGURE 12: Variation of the plastic strain with axial strain under different strain rates.

convenience, it is a hypothesis that the dissipated energy can contribute to the development of material damage according to the view of J integral in fracture mechanics. Thus, the dissipated energy can also be treated as a damage factor for the damage evolution. Regarding the dissipated energy, the hysteresis loop area W_h of loading and unloading curves is commonly considered the dissipated energy of the material [6].

According to the principle of energy conservation and damage evolution, the initial damage of the specimen should

be selected as the reference point of damage evolution. However, the hysteresis loop area is only the dissipated energy of one loading-unloading cycle (the dissipated energy within the rebound strain) [29].

Based on the test results in this study, the variation of the hysteresis loop area of frozen loess with axial strain under different strain rates is shown in Figure 14. The area of the hysteresis loop decreases after the peak strain because the shear failure of the frozen loess mesostructure makes the strength reduction. Then, the hysteresis loop area cannot

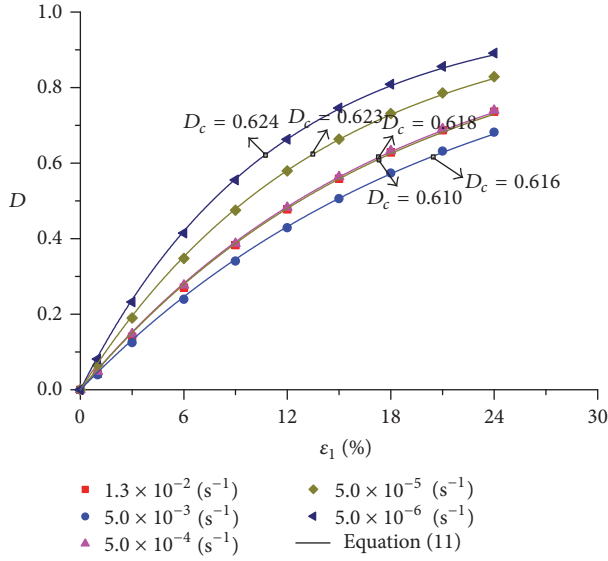


FIGURE 13: Variation of the damage variable with axial strain under different strain rates (plastic strain).

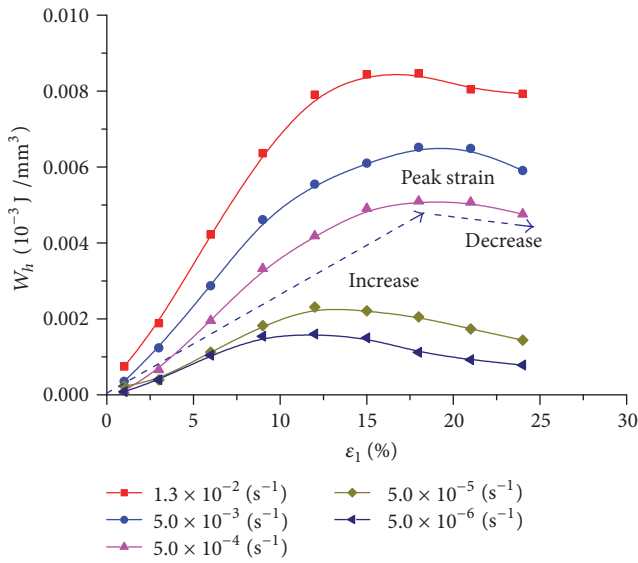


FIGURE 14: Variation of the hysteresis loop area with axial strain under different strain rates.

accurately reflect the mesofailure process of frozen loess. The test results again indicate that the hysteresis loop area could not be directly considered the damage factor.

Based on the view of fracture mechanics and energy conservation, the dissipated energy is recalculated as follows:

$$W = W_s + W_b + W_r, \quad (12)$$

where W_s is the storage elastic energy of the testing system during loading; W_b is the dissipated energy of the testing machine damping; and W_r is the absorbed energy by the specimen. W_s , W_b can be ignored because the stiffness of the testing machine is far greater than the frozen loess specimen.

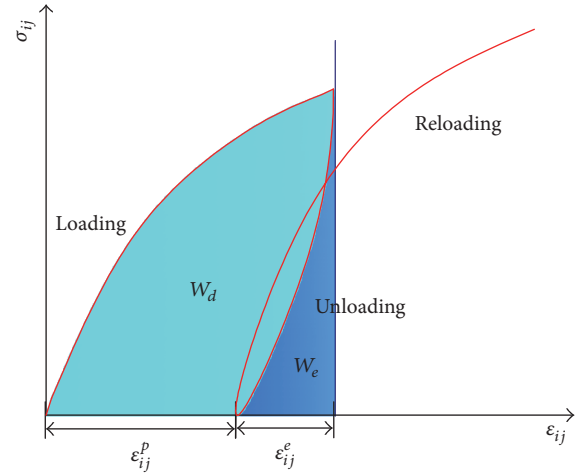


FIGURE 15: The calculation method of dissipated energy (ϵ_{ij}^p is the plastic strain).

Then, the entire work (W) can be considered absorbed by the specimen (W_r). In the isothermal and adiabatic conditions, one part of the work performed by external loads is stored in the form of elastic energy (W_e), which is released after unloading. Another part of the work is consumed by the development of plastic deformation and cracks based on Huang and Li [20]. Thus, this part can also be called the dissipated energy (W_d).

$$W \approx W_r = W_e + W_d = \int_0^\epsilon \sigma_{ij} d\epsilon_{ij} \quad (13)$$

$$W_e = \int_s \sigma_{ij} d\epsilon_{ij}^e,$$

where s is the unloading path and ϵ_{ij}^e is the elastic strain. Then, the dissipated energy can be calculated from the $L-U-C$ test results, and the calculation method is shown in Figure 15.

The variation of dissipated energy with axial strain is shown in Figure 16. The dissipated energy increases with the increase in axial strain. With the increase in dissipated energy, the cracks and holes in the specimen increase, and the specimen eventually achieves the extreme damage status. Considering the irreversibility of the damage, the damage variable can be expressed as follows:

$$D = \frac{\sum_{i=1}^n W_d^i}{W_d^u}, \quad (14)$$

where W_d^u is the dissipated energy of the specimen corresponding to the critical damage; W_d^i is the dissipated energy under different damage stages. The relationship between the damage variable and the axial strain is shown in Figure 17. Based on the test results of this study and Darabi et al. [15], the damage evolution law can be written as follows:

$$D = \alpha \left(\frac{\epsilon_1}{\epsilon_1^u} \right) \exp \left(\beta \frac{\epsilon_1}{\epsilon_1^u} \right), \quad (15)$$

TABLE 4: Material parameters α and β under different strain rates (dissipated energy).

| $\dot{\epsilon}_1$ | $1.3 \times 10^{-2}/s$ | $5.0 \times 10^{-3}/s$ | $5.0 \times 10^{-4}/s$ | $5.0 \times 10^{-5}/s$ | $5.0 \times 10^{-6}/s$ |
|--------------------|------------------------|------------------------|------------------------|------------------------|------------------------|
| α | 0.415 | 0.482 | 0.369 | 0.468 | 0.474 |
| β | 0.881 | 0.748 | 1.001 | 0.773 | 0.760 |

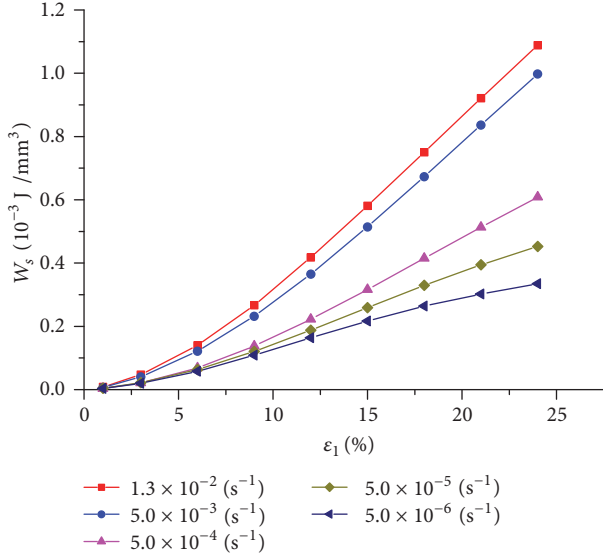


FIGURE 16: Variation of dissipated energy with axial strain under different strain rates.

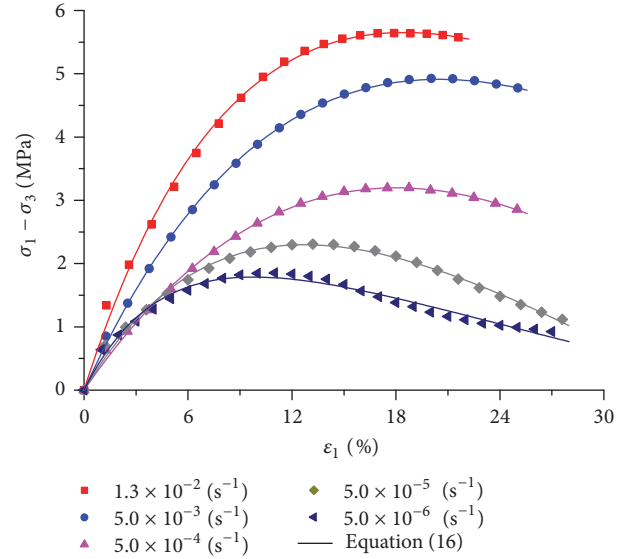


FIGURE 18: The model matches effect.

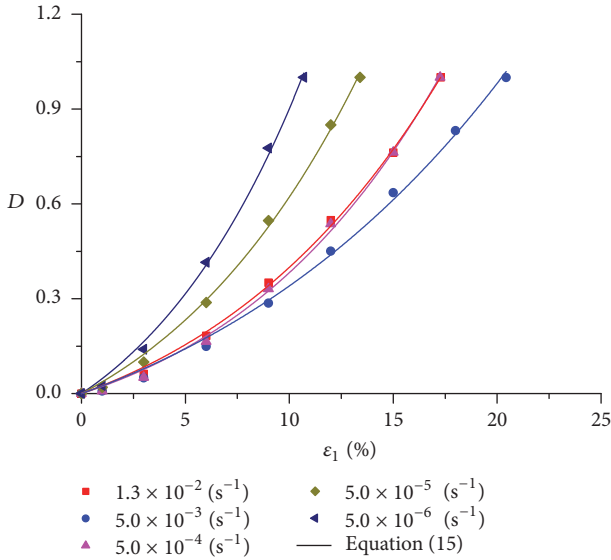


FIGURE 17: Variation of the damage variable with axial strain under different strain rates (dissipated energy).

where α and β are material parameters corresponding to the strain rate. These parameters under different strain rates are listed in Table 4.

4.2.4. *Damage Evolution Laws Deduced from the Constitutive Model.* The constitutive model of some materials has been

known, but the damage evolution law cannot be clearly observed from the model. Then, the damage evolution law can be deduced from the constitutive model. Bažant and Mazars [25] and Lemaitre [30] calculated the damage of a material by fitting stress-strain curves according to the phenomenological theory.

Considering the deformation features of frozen loess, a generalized hyperbolic model is used in this study [31]. With the model, the C test results are fitted, as shown in Figure 18.

$$\sigma_1 - \sigma_3 = \frac{l + m\epsilon_1}{(l + n\epsilon_1)^2} \epsilon_1 = (1 - D) E_0^* \epsilon_1 \quad (16)$$

$$\frac{\sigma}{(1 - D)} = \sigma_{\text{eff}}, \quad (17)$$

where E_0^* is the initial modulus that corresponds to the fitting curves; l , m , and n are material parameters that are related to the strain rate. These parameters under different strain rates are listed in Table 5. The physical significance of these parameters can be found in Prévost [31]. The methods can characterize stiffness degradation of material by modulus (16) and the strength change of material by the effective stress (17) in the deformation process. The two variables can be deduced from the same method [23]. In the paper, we used the modulus as an example.

Then, the equation of damage evolution can be obtained as follows:

$$D = 1 - \frac{l + m\epsilon_1}{E_0^* (l + n\epsilon_1)^2}. \quad (18)$$

TABLE 5: Material parameters l , m , and n under different strain rates (constitutive model).

| $\dot{\epsilon}_1$ | $1.3 \times 10^{-2}/s$ | $5.0 \times 10^{-3}/s$ | $5.0 \times 10^{-4}/s$ | $5.0 \times 10^{-5}/s$ | $5.0 \times 10^{-6}/s$ |
|--------------------|------------------------|------------------------|------------------------|------------------------|------------------------|
| l | 0.01159 | 0.01660 | 0.02520 | 0.02200 | 0.01800 |
| m | -0.01853 | -0.03000 | -0.06200 | -0.06200 | -0.04540 |
| n | 0.02570 | 0.02090 | 0.01660 | 0.04720 | 0.09450 |

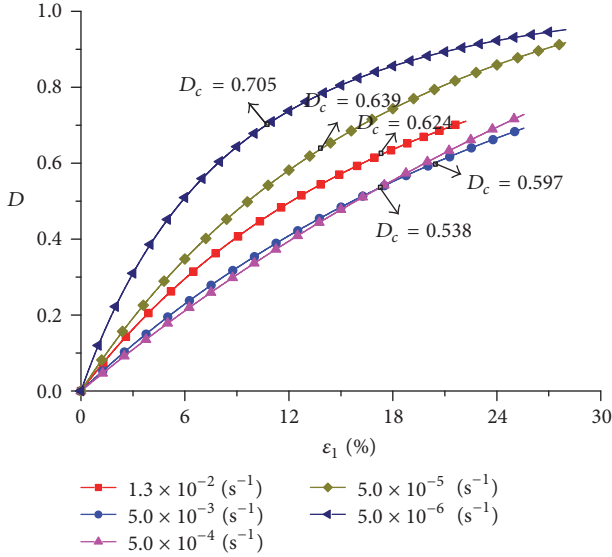


FIGURE 19: Variation of the damage variable with axial strain under different strain rates (constitutive model).

The variation of the damage variable with axial strain is shown in Figure 19. The development of damage is closely related to the loading time, which is consistent with the results of the C tests. The critical damage (D_c) is shown in Figure 19.

5. Discussion

At present, few studies compared the advantages and disadvantages among different damage factors or discussed the selection criteria of the damage variable to the same material. In this paper, four damage factors were studied and compared based on macro tests results of frozen loess. Based on the above studies, the four methods can describe the damage and damage evolution of frozen loess under ideal conditions. However, considering the special properties and engineering service purposes on frozen loess, the advantages and disadvantages of these damage factors and damage variables will be assessed as follows.

For frozen loess, it is difficult to accurately measure the dissipated energy by experiments, and it is not for presenting the damage process considering the special physical property of the granular material [32]. In the paper, the dissipated energy of the frozen loess was calculated based on many hypotheses. Thus, the dissipated energy is hardly investigated and not recommended in this area. The fourth method is that the damage evolution law is obtained from the constitutive model based on the theory of effective stress, but the premise

is that the constitutive model of the material is known. Because of the complexity of the geotechnical property, such as large regional characteristics and the complex structure, it is difficult to obtain a simple and accurate model. Therefore, this method is also difficult to apply. The theory of stiffness degradation can be used for most materials and the stiffness of material is also easy to measure. Thus, many researchers choose the stiffness as the damage factor to study the mechanical damage of material. The main limitation of the method is that damage is uniformly distributed in the volume on which strain is measured. Thus, it is also difficult regarding frozen loess. For frozen loess engineering, the key engineering problem is the deformation issue, for example, subgrade settlement and foundation deformation, which is the safety evaluation index to these engineering. Therefore, plastic deformation (permanent deformation) is the most suitable for the damage research of frozen loess based on the material properties and the nature of the material service.

In addition, the problem of establishing a quantitative relationship between the damage factor and the damage variable for different materials and different purposes should be considered. Different relationships lead to different evolution processes, such as the comparison results of the exponential function (10) and linear function ((6) and (14)). The key point to understand is how to exactly define the damage criterions.

Selecting an appropriate damage factor has been a hot topic for a long time in CDM. Based on this discussion, it can be seen that a new technology (microscopic scanning) and method must be developed to more accurately describe the damage evolution of the material under external loads. The method is a comprehensive method that contains macro- and micromethods (the combination of material science and continuous media mechanics or mechanical damage and physical damage). Both methods are essential; otherwise, the damage process of the material can only be described from one side. In other words, the method must be able to verify and inverse the macromechanical properties of the material according to the change law of mesoscopic fabric status. Selecting a cross-scale damage variable is also the key bridge to explore the essence of deformation and failure of materials. This subject is also a main issue of the study of material properties in current solid mechanics [33].

6. Conclusions

This paper presented a series of tests, including monotonic and load-unloading-loading tests, to the frozen loess under five strain rates in order to investigate the rate-dependent deformation behavior and the damage evolution law. Four damage factors were studied and compared based on tests

results. Some conclusions drawn from experimental and theoretical results are summarized below.

(1) The strength and the deformation behavior of frozen loess strongly depend on the strain rate. In addition, the loading and unloading cycles test does not affect the deformation behavior of frozen loess.

(2) E_h and E_s cannot describe the stiffness degradation of the frozen loess in the deformation process. So E_d is selected based on the test results and previous studies.

(3) The hysteresis loop area cannot accurately reflect the dissipated energy of frozen loess. The value of dissipated energy is recalculated according to the view of fracture mechanics and energy conservation in order to describe the development of the material damage.

(4) According to the discussion, the plastic deformation is the most suitable for the damage research of frozen loess based on the material properties and the nature of the material service.

Conflicts of Interest

The authors declare that there are no conflicts of interest regarding the publication of this paper.

Acknowledgments

This work was supported by the National Natural Science Foundation of China (41630636, 41401077, and 11502266) and the Science and Technology Major Project of Gansu Province (143GKDA007).

References

- [1] J. Q. Xu, *Theory on the Strength of Materials*, Shanghai Jiaotong University Press, 2009.
- [2] R. A. Schapery, "Correspondence principles and a generalized J integral for large deformation and fracture analysis of viscoelastic media," *International Journal of Fracture*, vol. 25, no. 3, pp. 195–223, 1984.
- [3] S. Dhar, P. M. Dixit, and R. Sethuraman, "A continuum damage mechanics model for ductile fracture," *International Journal of Pressure Vessels and Piping*, vol. 77, no. 6, pp. 335–344, 2000.
- [4] R. W. Sullivan, "Development of a viscoelastic continuum damage model for cyclic loading," *Mechanics of Time-Dependent Materials*, vol. 12, no. 4, pp. 329–342, 2008.
- [5] S. P. Zhao, W. Ma, J. F. Zheng, and G. D. Jiao, "Damage dissipation potential of frozen remolded Lanzhou loess based on CT uniaxial compression test results," *Chinese Journal of Geotechnical Engineering*, vol. 34, pp. 2019–2025, 2012.
- [6] X. T. Xu, Y. H. Dong, and C. X. Fan, "Laboratory investigation on energy dissipation and damage characteristics of frozen loess during deformation process," *Cold Regions Science and Technology*, vol. 109, pp. 1–8, 2015.
- [7] J. Shao, A. Chiarelli, and N. Hoteit, "Modeling of coupled elastoplastic damage in rock materials," *International Journal of Rock Mechanics and Mining Sciences*, vol. 35, no. 4–5, p. 444, 1998.
- [8] J. Lemaitre, "Continuous damage mechanics model for ductile fracture," *Journal of Engineering Materials and Technology, Transactions of the ASME*, vol. 107, no. 1, pp. 83–89, 1985.
- [9] G. Z. Voyiadjis, *Handbook of Damage Mechanics*, Springer, 2015.
- [10] M. Alves, J. Yu, and N. Jones, "On the elastic modulus degradation in continuum damage mechanics," *Computers and Structures*, vol. 76, no. 6, pp. 703–712, 2000.
- [11] G. Swoboda and Q. Yang, "An energy-based damage model of geomaterials—I. Formulation and numerical results," *International Journal of Solids and Structures*, vol. 36, no. 12, pp. 1719–1734, 1999.
- [12] R. Lapovok, "Damage evolution under severe plastic deformation," *International Journal of Fracture*, vol. 115, no. 2, pp. 159–172, 2002.
- [13] Z. M. Shi, H. L. Ma, and J. B. Li, "A novel damage variable to characterize evolution of microstructure with plastic deformation for ductile metal materials under tensile loading," *Engineering Fracture Mechanics*, vol. 78, no. 3, pp. 503–513, 2011.
- [14] Y. Y. Cao, S. P. Ma, X. Wang, and Z. Y. Hong, "A new definition of damage variable for rock material based on the spatial characteristics of deformation fields," *Advanced Materials Research*, vol. 146–147, pp. 865–868, 2011.
- [15] M. K. Darabi, R. K. Abu Al-Rub, E. A. Masad, C.-W. Huang, and D. N. Little, "A thermo-viscoelastic-viscoplastic-viscodamage constitutive model for asphaltic materials," *International Journal of Solids and Structures*, vol. 48, no. 1, pp. 191–207, 2011.
- [16] H. Du, W. Ma, S. Zhang, Z. Zhou, and E. Liu, "Strength properties of ice-rich frozen silty sands under uniaxial compression for a wide range of strain rates and moisture contents," *Cold Regions Science and Technology*, vol. 123, pp. 107–113, 2016.
- [17] Z. Zhou, W. Ma, S. Zhang, H. Du, Y. Mu, and G. Li, "Multiaxial creep of frozen loess," *Mechanics of Materials*, vol. 95, pp. 172–191, 2016.
- [18] L. M. Kachanov, *Introduction to Continuum Damage Mechanics*, M. Nijhoff, 1986.
- [19] L. M. Kachanov, "Time of the rupture process under creep conditions," *Akad. Nauk SSR Otd. Tech.*, vol. 8, p. 6, 1958.
- [20] D. Huang and Y. Li, "Conversion of strain energy in Triaxial Unloading Tests on Marble," *International Journal of Rock Mechanics and Mining Sciences*, vol. 66, pp. 160–168, 2014.
- [21] A. S. Chiarelli, J. F. Shao, and N. Hoteit, "Modeling of elastoplastic damage behavior of a claystone," *International Journal of Plasticity*, vol. 19, no. 1, pp. 23–45, 2003.
- [22] G. E. Mann, T. Sumitomo, C. H. Cáceres, and J. R. Griffiths, "Reversible plastic strain during cyclic loading-unloading of Mg and Mg-Zn alloys," *Materials Science and Engineering A*, vol. 456, no. 1–2, pp. 138–146, 2007.
- [23] H. P. Xie, *Rock and Concrete Damage Mechanics*, China University of Mining and Technology Press, 1990.
- [24] S. W. Yu, *Damage Mechanics*, Tsinghua University Press, 1997.
- [25] Z. P. Bažant and J. Mazars, "France-U.S. workshop on strain localization and size effect due to cracking and damage," *Journal of Engineering Mechanics*, vol. 116, no. 6, pp. 1412–1424, 1990.
- [26] I. Carol, E. Rizzi, and K. Willam, "A unified theory of elastic degradation and damage based on a loading surface," *International Journal of Solids and Structures*, vol. 31, no. 20, pp. 2835–2865, 1994.
- [27] J. Lemaitre, *A Course on Damage Mechanics*, Springer, 1998.
- [28] M. Liao, Y. Lai, E. Liu, and X. Wan, "A fractional order creep constitutive model of warm frozen silt," *Acta Geotechnica*, pp. 1–13, 2016.
- [29] Y. Yugui, G. Feng, C. Hongmei, and H. Peng, "Energy dissipation and failure criterion of artificial frozen soil," *Cold Regions Science and Technology*, vol. 129, pp. 137–144, 2016.

- [30] J. Lemaitre, "Formulation and identification of damage kinetic constitutive equations," in *Continuum Damage Mechanics Theory and Application*, vol. 295 of *International Centre for Mechanical Sciences*, pp. 37–89, Springer, Vienna, Austria, 1987.
- [31] J. Prévost, "Mathematical modelling of monotonic and cyclic undrained clay behaviour," *International Journal for Numerical and Analytical Methods in Geomechanics*, vol. 1, no. 2, pp. 195–216, 1977.
- [32] J. Lemaitre and J. Dufailly, "Damage measurements," *Engineering Fracture Mechanics*, vol. 28, no. 5-6, pp. 643–661, 1987.
- [33] F. Hild, A. Bouterf, and S. Roux, "Damage measurements via DIC," *International Journal of Fracture*, vol. 191, no. 1-2, pp. 77–105, 2015.

Research Article

Flexural Strengthening of Damaged T-Joists with Severe Corrosion Using CFRP Sheets

Jose Vercher,¹ Enrique Gil,² Ángeles Mas,¹ Carlos Lerma,¹ and M. Eugenia Torner²

¹Department of Architectural Constructions, Universitat Politècnica de València, Camino de Vera, s/n, 46022 Valencia, Spain

²Department of Structural Construction, Universitat Politècnica de València, Camino de Vera, s/n, 46022 Valencia, Spain

Correspondence should be addressed to Jose Vercher; jvercher@csa.upv.es

Received 27 January 2017; Accepted 19 February 2017; Published 12 March 2017

Academic Editor: Francesco Caputo

Copyright © 2017 Jose Vercher et al. This is an open access article distributed under the Creative Commons Attribution License, which permits unrestricted use, distribution, and reproduction in any medium, provided the original work is properly cited.

This paper evaluates the residual safety of isolated T-joists with severe corrosion for the two extreme cases of boundary conditions, simply supported and fixed-ended, in order to help in making decisions about the magnitude of the necessary intervention. When the T-joist is part of a complete slab, the boundary conditions will be in an intermediate situation between these two extreme cases, so that it is possible to assess the safety with respect to its degree of embedding. The research is conducted for the cases of healthy T-joist, T-joist with complete corrosion of the lower reinforcement, and repaired T-joists with a variable number of CFRP sheets. This work is based on the ACI 318 load test to maintain a structure in use and proposes a Load Factor (LF), which estimates the safety reserve. The simply supported T-joists specimens with severe corrosion do not meet the Load Factor or ACI 318 criteria, even with a large number of CFRP sheets. On the other hand, fixed-ended cases can be kept in use despite corrosion by applying light CFRP strengthening, and with four sheets the initial safety is restored.

1. Introduction

The rehabilitation sector has achieved a greater importance than the construction of new buildings in recent years, due to the crisis in the construction of buildings. According to the Instituto de Tecnología de la Construcción [1], the forecasts for the coming years in Spain indicate that rehabilitation will be the sector with more activity (Figure 1). Because of this, it is essential to pay attention to the entire set of actions carried out in cases of rehabilitation.

But in the growing sector of rehabilitation, the flexural elements are the structural elements in which the higher percentages of damage appear. In Spain, lesions appear in 25.6% of the slabs, and corrosion in one-way slabs represents 68% of these cases [2].

In some cases of large damage, the severe corrosion of the lower level of tendons of a joist causes the spalling of the lower concrete cover. This effect is enhanced by the use of aluminous cement in prefabrication, widely used for a few decades because of its shorter time of manufacture. This occurs due to the conversion of this type of cement, since

the concrete becomes more porous and attackable and less resistant [3]. In Spain, it is estimated that, of the 3,400,000 households built between 1950 and 1970, between 12 and 24% of them have used this type of cement in the slabs [4].

When the technicians analyze a case of structural pathology, they find the difficulty of assessing the remaining safety, in order to decide the magnitude of the intervention to be performed. This research quantifies the residual safety and helps to make this important decision.

Strengthening may be required when structures are damaged due to an aggressive environment. In these cases, the most common rehabilitation techniques have been accomplished by the use of conventional materials such as steel structural profiles (see Figure 2). However, recently the use of innovative materials like fiber-reinforced polymer (FRP) has emerged as an alternative to the use of the conventional techniques and it seems to be the most promising method to be used in structural engineering [5].

FRP is typically organized in a laminated structure, where each sheet contains an arrangement of unidirectional fibers or woven fiber fabrics embedded within a thin layer of

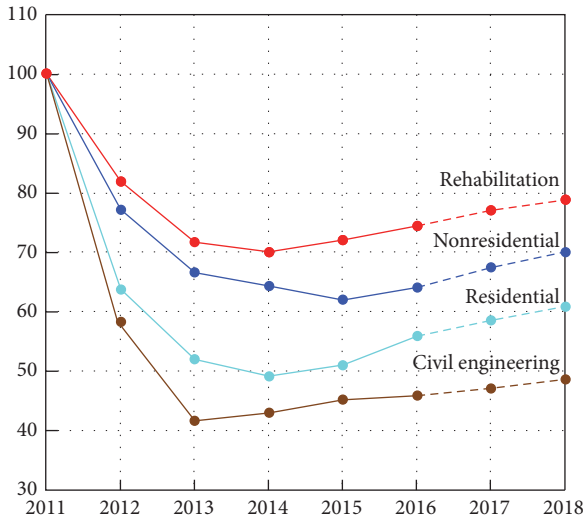


FIGURE 1: Evolution of the different subsectors in the Spanish building construction market. Production rates at constant prices, basis 2011 = 100.

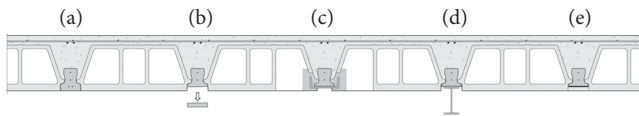


FIGURE 2: Constructive detail (a) healthy joist, (b) joist with severe corrosion and spalling, (c) joist repaired with UPN profile, (d) joist repaired with IPE profile, and (e) joist repaired with CFRP sheet.

light polymer matrix material. Fibers are typically composed of carbon, aramid, or glass. The matrix protects the fibers from damage and transfers the stresses between fibers. This matrix is commonly made of polyester, epoxy, or nylon. There are two additional types of FRP composite, bidirectional fibers, which are used commonly for strengthening two-way slabs, and the FRP rods, which became an alternative for reinforcement steel bars [6].

Externally bonded FRP reinforcement has been shown to be applicable for the strengthening of many types of reinforced concrete (RC) structures such as columns, beams, slabs, and walls and can be used to improve flexural and shear capacities [7–9] and also provide confinement and ductility to compression members [10–12].

Externally bonded strengthening system, where the FRP sheets or plates are bonded to the concrete tensile surface, is widely used to improve the flexural capacity of concrete structures. Their application has multiple benefits, including increased ultimate flexural strength capacity and increased postcracking stiffness, as well as concrete crack control [13], high tensile strength, high durability, minimum increases in structural size and weight, ease of site handling, and good corrosion resistance. There are even some studies that aim to improve the properties of FRP sheets with carbon nanotubes or graphene nanoplatelets [14, 15]. Recently, near-surface-mounted technique was introduced, where the FRP bars of

plates are inserted into a groove made in the concrete surface [16].

Although there are some authors who evaluate other types of FRP [17], the Carbon Fiber-Reinforced Polymer (CFRP) is mostly employed. There are numerous works which research about externally bonded CFRP reinforcement in order to strengthen many types of RC structures to resist higher design loads [18–22], but there is less available research on corroded, patched, and CFRP-repaired RC specimens [23, 24].

Most of the work done by other authors is centered on isolated linear elements, usually beams, although there is some study of bidirectional elements like solid slabs [25]. There is no research on safety of joists inside a one-way slab. The aim of this research is to evaluate the residual safety increase of joists with a high degree of damage when they are part of a complete unidirectional slab, by gluing CFRP sheets on the underside. For this reason, specimens of isolated T-joists are assessed, with the different boundary conditions of usual modeling in structure analysis (simply supported and fixed-ended). When the joist is in a slab, its boundary conditions will be between these two extreme cases, so that we can assess its safety with respect to the degree of embedding that they have. This work focuses on the evaluation of slabs whose failure is dominated by flexion. This happens in most cases, because corrosion usually occurs in the lower reinforcement, due to it has less concrete cover.

2. Materials and Methods

Researchers have not made great efforts to accurately assess the remaining safety in cases of corrosion, in the field of building construction. The habitual action is to repair or reinforce, leaving the existing building on the side of safety.

The structural simplification of considering the actual three-dimensional elements such as lines does not represent the minimum balance of work with which they behave in reality. The loads are transmitted in various simultaneous forms in space. Mechanisms such as struts and ties or the arch effect appear in the elements subjected to flexion and contribute considerably if these elements have the horizontal displacement restrained. Because of this, it is necessary to study the elements in three dimensions, to properly assess the safety they possess.

2.1. Methodology for Assessing the Remaining Safety. The methodology used for the evaluation of the remaining safety of prestressed joists with severe corrosion and repaired with CFRP sheets is similar to the one the authors have developed in some publications of pathology in complete buildings [26], but in this case with CFRP strengthening. The novelty of this research is that it quantifies the remaining safety. Some healthy and damaged specimens of prestressed joist with compression layer (T-section) are simulated with ANSYS finite element software. With these simulations, the load-vertical displacement curves at midspan can be drawn. The proposed method to assess the remaining safety is based on the study of two aspects in these behavioral curves. First, the ACI 318 [27] load test for existing structures indicates

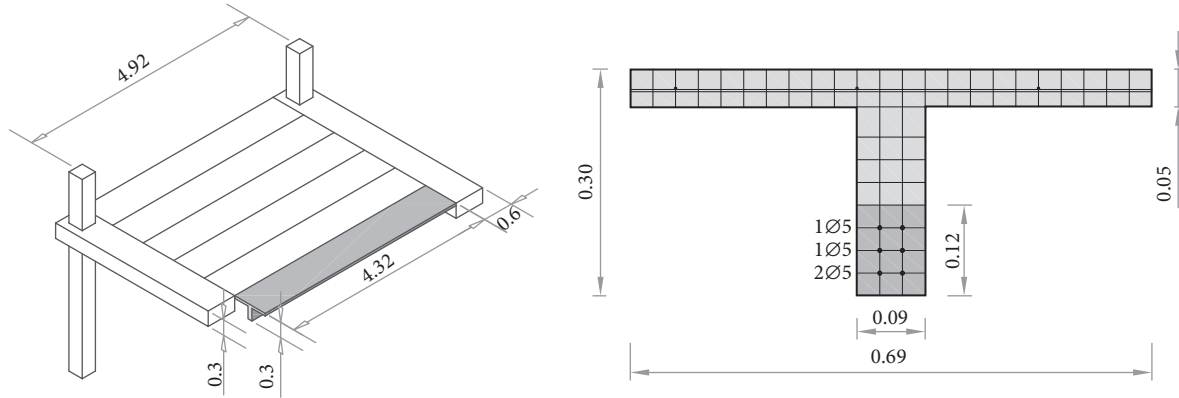


FIGURE 3: Simulated T-joint.

TABLE 1: Process of load application.

| Load (N/m ²) | |
|-------------------------------------|-------|
| Joist + compression layer dead load | 3,500 |
| Flooring + ceiling dead load | 1,000 |
| Partition walls dead load | 1,000 |
| <i>Total dead load</i> | 5,500 |
| Quasipermanent live load | 600 |
| Service load | 6,100 |
| <i>Total live load</i> | 2,000 |
| <i>Total standard load</i> | 7,500 |
| ACI 318 load test | |
| Load | 9,435 |
| Deflection increase limitation (mm) | 3.11 |

whether a structure may continue in use and then the evaluation of the proposed Load Factor (LF).

According to ACI 318, the analyzed area must be loaded to $0.85(1.4D + 1.7L)$, including dead load already present. D is the sum of the dead loads, and L is the total live load. Therefore, the total load value for the load test is equal to $9,435 \text{ N/m}^2$ (see Table 1). If the deflection increase caused by the test satisfies $\Delta_1 \leq l_t^2/20,000h$, the specimen can continue in use, where l_t is the span between supports (4.32 m in the present research) and h is the specimen thickness (0.3 m). Thus, a deflection increase equal to 3.11 mm is allowed. When exceeding this limitation, retrieved deflection must be measured after the unloading. If the retrieved deformation is greater than 75%, the specimen is also accepted to continue in use.

And when it has been found that the slab can remain in use, the Load Factor is analyzed in order to quantify the remaining safety and the magnitude of the necessary intervention. This factor is obtained making the ratio between the load at which each specimen reaches the permissible active deflection for the partition walls and the total standard load (total dead load + total live load). The LF relates the load that each model bears and the total load that they must bear, according to standards. According to the Spanish code on structural concrete [28], the limitation on the permissible

active deflection for the partition walls of $L/400$ is given, L being the span. In this research, this value is 1.08 cm. This deflection occurs from the moment that the partition walls are constructed. A vertical displacement of 1.08 cm is allowed from this moment, and the supported load in each specimen is related to the total standard load.

2.2. Specimens Geometry. Nonlinear simulations of prestressed T-joists throughout their load range were performed using the finite element method (FEM). The T-joint models are very accurate, with the real 3D geometry and the reinforcement in its exact position (Figure 3). The simulated joist is part of a one-way slab of 30 cm thickness with a span of 4.92 m between column axes, with flat beams of 60 cm width. Therefore the joist length is 4.32 m.

The compression layer is centered on the joist and has 69 cm width, because it is the spacing between joists in the one-way slab, and 5 cm thickness. The reinforcement mesh inside the compression layer is composed of a 6 mm rod every 24 cm in both directions. The filler blocks are not simulated because they are not resistant elements. The prestressed joist is the T12.3 model of the Spanish company Prevalsa S. L., with four 5 mm prestressed tendons on three levels. The middle and the upper level have one tendon, simulated as two half tendons in order to keep the section symmetry in the simulations.

This research work comprises 12 T-joint specimens, in which the influence of the boundary conditions, the damage level, and the CFRP strengthening are assessed. Simply supported models are from (A1) to (A6) specimens, and fixed-ended joists models are presented in (B1) to (B6) specimens. As previously stated, when a T-joint is part of a complete building, it does not behave in any of these two ways, because it is in an intermediate position between full restraint and freedom. In order to assess the increased safety in damaged joists with CFRP repair, there are six variants: healthy, extreme corrosion without CFRP repair, with 1, 2, 3, and 4 CFRP sheets.

2.3. Process of Loads and Constructive Elements. The strict simulation of the process of loads and order of appearance of structural and building elements is very important, in order

TABLE 2: Mechanical properties of materials.

| | Concrete | | Material | | | CFRP |
|------------------------------|----------|---------|----------|-------------------|----------|------|
| | HA-30 | HP-40 | B-500-SD | Steel Y-1860-C | | |
| Density (kN/m ³) | 25 | 25 | 78.5 | 78.5 | — | |
| Elastic modulus (GPa) | 28.6 | 30.9 | 200 | 200 | 230 | |
| Compression strength (MPa) | 38 | 48 | — | — | — | |
| Tensile strength (MPa) | 3.39 | 3.96 | — | — | 4850 | |
| Poisson's ratio | 0.2 | 0.2 | 0.3 | 0.3 | — | |
| Yielding strength (MPa) | — | — | 500 | 1581 | — | |
| Ultimate strain | — | — | — | — | 0.02 | |
| Element type | SOLID65 | SOLID65 | LINK180 | Prest. F | SHELL181 | |

to capture the behavior and get the closest results to the actual situation when the joist is part of a complete building.

The simulated steps, which correspond with real steps in the constructive process and are summarized in Table 1, are the following:

- (i) Prestressed joist: in a first step, only the prestressed joist is simulated, and therefore at this point only these elements are active. The prestress is introduced as equivalent prestressing forces at the corresponding points. The equivalent force per 5 mm diameter rebar is equal to 17,000 N, after a 29% loss over infinite time. At the end of this step, the joist has a negative deflection, as in reality.
- (ii) Structural dead load: in a second step, the concrete is poured in situ in order to complete the slab thickness and the compression layer.
- (iii) Flooring and ceiling dead load: these constructive elements appear in this moment and are simulated as a load increment of 1,000 N/m².
- (iv) Partition walls dead load: now, the partition walls appear as a dead load increment of 1,000 N/m². The active deflection with respect to the partition walls will start as soon as this load is completely added. This deflection is limited to 1.08 cm in the assessed specimens, due to their length.
- (v) Service load: when the building is finished, the T-joist is supporting the service load. The service load is the load to which the structure will be subjected most of its useful life. It consists of the dead loads and the quasipermanent part of the live load, according to the standard CTE-06 [29]. The characteristic value of the live load for housing in Spain is 2,000 N/m², and the quasipermanent value is 600 N/m².
- (vi) Corrosion: corrosion damage appears during the service life. The most severe pathological cases are assessed in this research. Therefore, the corrosion is modeled as the removal of the lower level of prestressed tendons and the concrete cover spalling, as it may occur in some extreme cases. But the other two levels of prestressed tendons are maintained, because they continue to assist in supporting the joist. The assessment of the most severe cases provides the

lowest value of failure load, so that it is on the side of safety. Due to their boundary conditions, simply supported specimens experience a large vertical displacement at midspan if the disappearance of the lower tendons and concrete cover is simulated to the load corresponding to the service load (6,100 N/m²). Because of this, corrosion was simulated to a lower load value in these cases (4,000 N/m²), and from this point, the following load steps were loaded successively as explained in this part. This consideration does not affect the results of the research, since the objective is to assess residual safety and achieve adequate safety at the end.

- (vii) CFRP sheet: the prefabricated sheets are bonded to the tension side of the specimens after sandblasting, brushing, and cleaning the concrete surface to guarantee a good bond between the adhesive and the concrete [30]. The choice and placement of the CFRP sheet must follow the ACI Committee 440 guidelines [31].
- (viii) Total standard load: at this point, the specimens are loaded with the total live load, in order to reach the total standard load. This is the total load that the slab must support according to standards.
- (ix) Load until failure: finally, the T-joist is loaded until collapse.

2.4. Materials. For the T-joist specimens, the simulation of the behavior of five materials is needed: two types of concrete and two types of steel and the CFRP sheet. Because the joists are prefabricated and the rest of the reinforced concrete T-joist is constructed in situ, different qualities of both steel and concrete appear. The assessed prestressed joist is the T12.3 model of the Spanish company Prevalesa S. L., with four 5 mm prestressed tendons on three levels. HP-40 concrete and Y-1860-C high performance prestressing steel form precast joists. Instead, the concrete in situ is the commonly used HA-30 and the steel reinforcements are made with B-500-SD steel. In addition, CFRP sheets are placed to repair damaged specimens. The chosen CFRP sheet for this research work is MAPEI MapeWrap C UNI-AX 300/10 with 0.166 mm thickness. Table 2 summarizes the mechanical properties of the employed materials.

2.5. Finite Element Model. The finite element method (FEM) is conducted to simulate the behavior of the test specimens in ANSYS software. The investigated T-joint specimens were developed in three-dimensional models in order to account for the materials nonlinear behavior.

Eight-node solid brick elements (Solid65) were used to simulate the concrete. This solid is capable of cracking in tension and crushing in compression, creep nonlinearity, and large deflection geometrical nonlinearity. The concrete requires multilinear isotropic material properties and the Willam-Warnke [32] spatial failure criteria to properly model its behavior. The uniaxial stress-strain relation was defined by the civil engineering Eurocode. Two simulation techniques have been used for steel reinforcements. The prestressed bars of the precast joist are introduced as equivalent prestressing forces at the corresponding points, and 3D spar elements (Link180) were employed to simulate the reinforcement mesh inside the compression layer. This three-dimensional element is a uniaxial tension-compression element with three degrees of freedom at each node. Plasticity, creep, swelling, stress stiffening, and large deflection capabilities are included. The steel is assumed to be an elastic-perfectly plastic material and identical in tension and compression, and its behavior can be simplified by an isotropic bilinear curve. And finally, a shell element (Shell181) was used to simulate the CFRP sheets. It is a four-node 3D element with six degrees of freedom at each node and is well-suited for linear, large rotation, and/or large strain nonlinear applications. The CFRP-material is considered as linear elastic until failure. This type of element needs a failure criterion for the complete definition of behavior. The physical failure criteria are specially formulated to account for different damage mechanisms (fiber and matrix failure) in fiber-reinforced composite materials. Hashin maximum stress failure criteria were used in this research [33] for the CFRP sheets. To complete the material damage definition, it is also necessary to specify a compatible damage initiation criteria and evolution law. Progressive damage evolution based on continuum damage mechanism was chosen. In this case, energies dissipated per unit area G_C are specified individually for all damage modes (fiber tension, fiber compression, matrix tension, and matrix compression). For a specific damage mode, G_C is given by

$$G_C = \int_0^{U_e^f} \sigma_e dU_e. \quad (1)$$

where σ_e is the equivalent stress, U_e is the equivalent displacement, and U_e^f is the ultimate equivalent displacement, where total material stiffness is lost for the specific mode [34]. For complex stress state, the equivalent stresses and strains are calculated based on Hashin failure criteria. Viscous damping coefficients η are also specified respectively for all four damage modes. For a specific damage mode, the damage evolution is regularized as follows:

$$d'_{t+\Delta t} = \frac{\eta}{\eta + \Delta t} d'_t + \frac{\Delta t}{\eta + \Delta t} d_{t+\Delta t}. \quad (2)$$

where $d'_{t+\Delta t}$ is the regularized damage variable at current time, d'_t is the regularized damage variable at the end of the

TABLE 3: Esfahani et al. test results of reinforcing bars.

| Bar diameter (mm) | 8 | 10 | 16 |
|-----------------------|-----|-----|-----|
| Yielding stress (MPa) | 350 | 365 | 406 |
| Ultimate stress (MPa) | 459 | 572 | 583 |

last substep, and $d_{t+\Delta t}$ is the unregularized current damage variable [34].

Half of the T-joint specimen has been simulated, seeking to optimize computing time. Therefore, it was necessary to simulate suitable boundary conditions to behave in the same manner as the complete T-joint. The simulated boundary conditions were of symmetry at the midspan, allowing the vertical displacement and roller support or embedding in the end, according to the assessed model. A total of 5679 elements were required for T-joint analysis (5040 3D elements, 423 link elements, and 216 shell elements). The total nodes of each specimen were 7592. Most of the concrete elements are a prism with $30 \times 30 \times 30$ mm. The choice of mesh size was based on preliminary studies in which different sizes were used [35]. This number of elements represents a good balance between the computational time and the numerical accuracy of results.

The Newton-Raphson equilibrium iterations were used in the nonlinear solutions. Convergence criteria for the specimens were based on force and displacement. The convergence tolerance limits were selected by analysis program [36].

In this study, a perfect bond between concrete and steel was assumed. The nodes of the CFRP elements are also connected to those of adjacent concrete elements [37]. The interaction between the concrete joist and the CFRP is modeled without considering debonding. The bond does not have to be explicitly modeled in the numerical analysis [38].

The ANSYS software allows the generation of load steps and the birth and death of elements in the different steps. The cases of corrosion evaluated in this work are the most severe, involving the total loss of the concrete cover and the lower level of tendons. Therefore, corrosion is simulated in the model by the death of the elements constituting the cover and the lower reinforcement in the proper load step.

2.6. Model Verification. A very careful calibration of the numeric simulations has been made in order to verify the accuracy of the used hypothesis and models regarding the behavior of CFRP sheets. The FE software is used to predict the flexural behavior of strengthened beams reported by Esfahani et al. [39] in order to validate the research methodology and its results and final conclusions.

For the Esfahani et al. specimens, the design compressive strength of 25 MPa was used for concrete and different sizes of reinforcing bars were used in specimens. The yield and ultimate strength of different bars are given in Table 3. The mechanical properties of CFRP are the following: the ultimate strain is 0.012, the tensile strength is 2845 MPa, and the modulus of elasticity is 237 GPa. Reaction force versus CFRP strain relationship in simulated sheet can be seen in Figure 4.

The specimens (B5) and (B7) were selected. The dimensions details of the beam are shown in Figure 5. The 8 mm

TABLE 4: Load at permissible active deflection, Load Factor values, and ACI 318 load test results for simulated specimens.

| Specimen | | Load at permissible active deflection (N/m ²) | Load Factor (LF) | ACI 318 load test | |
|------------------------|------|---|------------------|-------------------|----------|
| Simply supported joist | (A1) | Healthy | 9,984 | 1.33 | Right |
| | (A2) | Corroded without repair | 5,216 | 0.70 | Negative |
| | (A3) | Corroded with 1 CRRP sheet | 5,960 | 0.79 | Negative |
| | (A4) | Corroded with 2 CRRP sheets | 7,085 | 0.94 | Negative |
| | (A5) | Corroded with 3 CRRP sheets | 8,107 | 1.08 | Negative |
| | (A6) | Corroded with 4 CRRP sheets | 9,080 | 1.21 | Negative |
| Fixed-ended joist | (B1) | Healthy | 18,685 | 2.49 | Right |
| | (B2) | Corroded without repair | 14,520 | 1.93 | Right |
| | (B3) | Corroded with 1 CRRP sheet | 15,706 | 2.09 | Right |
| | (B4) | Corroded with 2 CRRP sheets | 16,874 | 2.26 | Right |
| | (B5) | Corroded with 3 CRRP sheets | 17,589 | 2.33 | Right |
| | (B6) | Corroded with 4 CRRP sheets | 18,096 | 2.42 | Right |

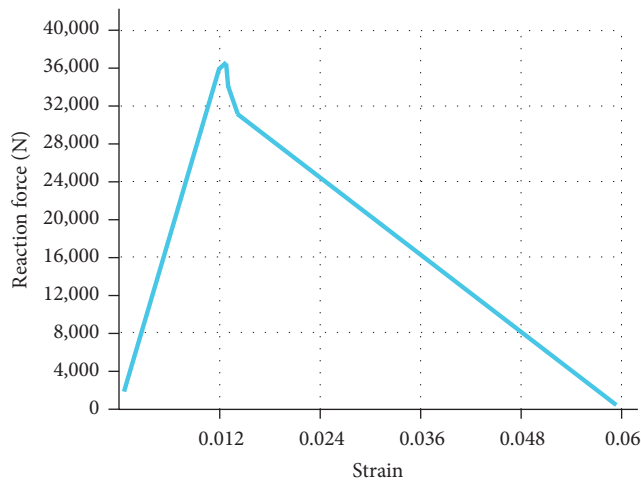


FIGURE 4: Reaction force versus strain relationship in simulated CFRP sheet.

steel rods are employed for stirrups each 80 mm. The nominal thickness and width of the CFRP were 0.176 mm and 150 mm, and the specimen (B7) was strengthened with one CFRP sheet.

All specimens have been reproduced successfully in FE software. A good correspondence in the behavior of the different models has been achieved, following their specifications when performing the simulations. A great concordance in the load-displacement curves has been obtained in all cases. In Figure 6 the B5 and B7 specimens are shown, as an illustrative example, where it can be seen that our work improves the correlation between the results of the analytical and the experimental study. The validated results are consistent in all models, so that both the software and the materials properties are accepted as valid tools for the research.

3. Results and Discussion

The prestressed T-joists simulation throughout their load range has been performed. Load-vertical displacement plots at midspan are compared in healthy, corroded, and repaired models in order to assess the residual safety. Figures 7 and 8 represent the load-vertical displacement at midspan relationships for the 12 specimens. Table 4 shows the load at permissible active deflection, the Load Factor (LF) values, and ACI 318 load test results for simulated specimens.

Several aspects can be seen in a deep analysis of the load-vertical displacement curves, which are as follows:

- (i) The initial precamber produced by the process of prestressing in prefabrication.
- (ii) The horizontal stretch due to corrosion: the end of this step is the starting point for the simulation of the load test acceptance criterion of existing structures proposed by the ACI 318. For simply supported specimens, it must be remembered that cases with severe corrosion have a large vertical displacement if corrosion appears at 6100 N/m², so that the corrosion has been simulated to a load of 4000 N/m². But load test is correctly performed from the service load, with the deflection that the T-joist would have in service life with pathology. The Load Factor has also been obtained with the permissible active deflection from the appearance of the partition walls.
- (iii) ACI 318 load test evaluation: this test determines whether a structure can remain in use, and its compliance is graphically analyzed in Figures 7 and 8. The procedure consists of limiting graphically the service load and ACI 318 load test and then also limiting the allowed deflection increase.
- (iv) Load Factor: the load supported at permissible active deflection for the partition walls and the standard

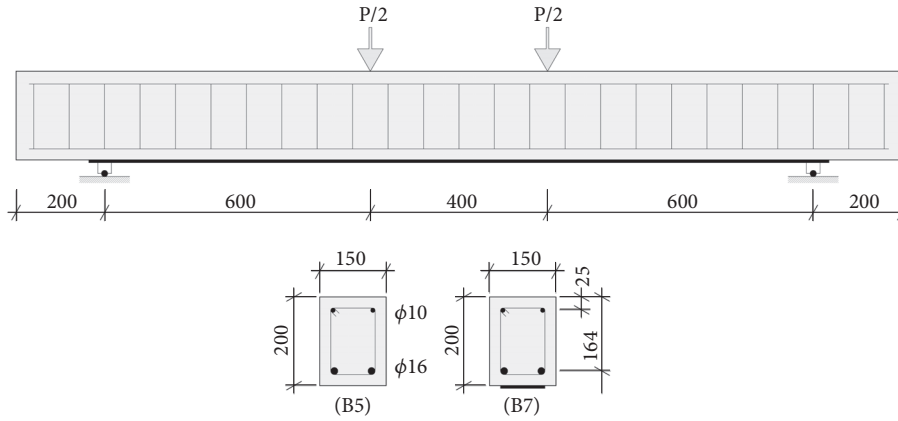


FIGURE 5: Details of Esfahani et al. beam specimens.

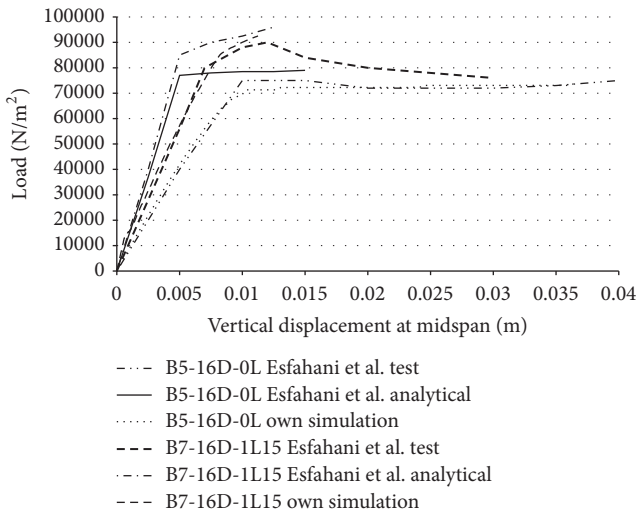


FIGURE 6: Load versus vertical displacement relationship for B5 and B7 Esfahani et al. specimens. Comparison of Esfahani et al. test results and analytical predictions with our simulations.

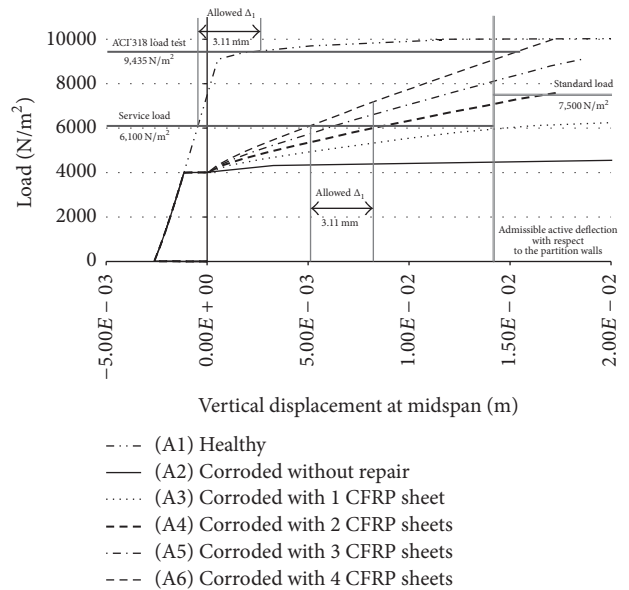


FIGURE 7: Load-vertical displacement at midspan curves for simply supported T-joist specimens.

load can be analyzed in Figures 7 and 8 and graphically understand the relationship with which the Load Factor is obtained.

Simply supported damaged specimens do not withstand the loads established by Building Technical Code CTE-06 [40] with less than 3 CFRP sheets ((A2), (A3), and (A4) specimens), so they have a Load Factor of less than 1. A safety coefficient of 1.08 and 1.21 was obtained with 3 and 4 sheets, respectively ((A5) and (A6) specimens), remaining with an unacceptable safety in structure analysis. In addition, no simply supported damaged specimen meets the criteria for continue in use of the ACI 318, even with 4 CFRP sheets. Severe corrosion in the simply supported specimen causes a 47.4% reduction in the ultimate capacity of the T-joist. The inclusion of CFRP sheets improves the bearing capacity of the specimen with respect to the damaged joist without repair as follows:

+12.9% with 1 sheet, +34.3% with 2 sheets, +54.3% with 3 sheets, and +72.9% with 4 sheets, not reaching initial safety.

Fixed-ended damaged T-joist without repair ((B2) specimen) support the loads established by the standard with a safety coefficient of 1.93, almost double of the standard load (dead loads + live loads). When gluing one CFRP sheet, the Load Factor 2 is exceeded, and with 2, 3, and 4 sheets, the safety coefficients of 2.26, 2.33, and 2.42, respectively, are reached. All studied fixed-ended specimens can continue in use according to ACI 318. The complete corrosion of the lower level of tendons and the loss of the concrete cover in the fixed-ended specimen causes a 22.5% reduction in the ultimate capacity. The capacity of the severe damaged T-joist is improved with the inclusion of CFRP sheets as follows: +8.3% with 1 sheet, +17.1% with 2 sheets, +20.7% with 3 sheets, and +25.4% with 4 sheets, getting close to recovering initial safety.

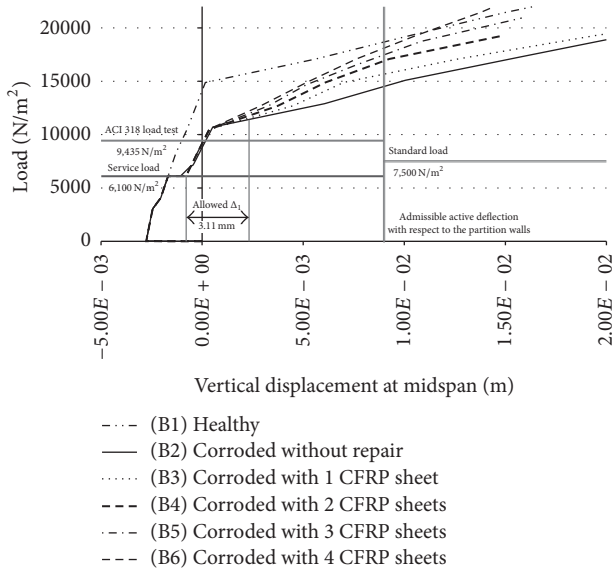


FIGURE 8: Load-vertical displacement at midspan curves for fixed-ended T-joint specimens.

Severe corrosion reduces the ultimate capacity of the simply supported T-joists in a more noticeable way. But, on the other hand, the addition of CFRP sheets improves to a greater extent the capacity of this type of joists.

The regulations establish clear safety coefficients for the calculation of structures in new construction, where they have a great control of the materials and the processes of construction. The acceptable Load Factor in cases of rehabilitation remains the responsibility of the expert performing the project and depends on local standards. Anyway, it seems sensible to assume a value near 2 as a minimum, depending on the reliability of the materials tests.

4. Conclusions

The actual boundary conditions of a T-joist when it is part of an entire one-way slab are in an intermediate case of restriction on the ends, neither totally free nor totally restrained. The evaluation of the two extreme theoretical cases presented in this paper is very important because it allows the technician to establish some actuation limits.

Cases of severely damaged simply supported T-joist do not support the service load without the help of neighboring joists. The added stiffness by strengthening with CFRP sheets with low thickness does not solve the problem, and it can not be accepted as constructive solution. Vertical displacement can not be controlled according to EHE-08 [28], even in the case with the addition of 4 CFRP sheets. Damaged simply supported specimens do not meet the ACI 318 load test to maintain the structure in use, not even with 4 CFRP sheets. Perhaps proper safety can be reached with a higher number of sheets, but it is not a common solution. The most common cases in actual practice are in which one or two sheets are used. Load Factor assessment indicates that none of the repairs reaches an acceptable safety, notwithstanding

the loads with the safety factors established by the standards. Our experience tells us that if there is a group of contiguous and hardly damaged joists in a one-way slab, the loads transmission perpendicular to joists force them to collaborate one with each other. Despite the damage in the lower tendons, damage may not appear in the rest of construction elements in some cases. But even if the damage does not appear on the other elements, an immediate shoring up and deep repair are necessary.

The boundary conditions in the cases of fixed-ended T-joists are theoretical. This degree of embedment is attainable in the central bays of slabs with a large symmetry of spans or with a very small difference in lengths. It is remarkable that in the evaluated real cases of this type of slab it can be seen that in spite of a great deterioration in the joists no cracking or damage appears in the other elements of the building. This can be understood watching the simulations of these cases with severe corrosion, where the vertical displacement at midspan with heavy loads remains small in magnitude. The ACI 318 load test for these cases of isolated T-joist with a span of 4.32 m indicates the meeting of all safety criteria. The simulation of the load test in these specimens gives vertical displacements around 30% of standard limitation, because the boundary conditions maintain a high stiffness, even with a severe degree of corrosion. The Load Factor for all these cases exceeds the safety factors proposed by standards. It is noted that the case with four CFRP sheets recovers the initial safety.

Conflicts of Interest

The authors declare that there are no conflicts of interest regarding the publication of this paper.

References

- [1] Instituto de Tecnología de la Construcción (ITEC), *Informe Euroconstruct*, Instituto de Tecnología de la Construcción, Barcelona, Spain, 2015.
- [2] J. A. Veitez Chamosa and J. L. Ramírez Ortiz, "Patología de la construcción en España: aproximación estadística," *Informes de la Construcción*, vol. 36, no. 364, pp. 5–15, 1984.
- [3] Instituto Valenciano de la Edificación (IVE), *Guía para la Inspección y Evaluación Preliminar de Estructuras de Hormigón en Edificios Existentes*, Serie Guías de la Calidad, Generalitat Valenciana—Conselleria de Medi Ambient, Aigua, Urbanisme i Habitatge, Valencia, Spain, 2008.
- [4] Instituto Valenciano de la Edificación (IVE), *Experiencia en Inspección de Estructuras en Edificios. Comunidad Valenciana 1991–2008*, Serie Guías de la Calidad, Generalitat Valenciana—Conselleria de Medi Ambient, Aigua, Urbanisme i Habitatge, Valencia, Spain, 2008.
- [5] L. Anania, A. Badalà, and G. Failla, "Increasing the flexural performance of RC beams strengthened with CFRP materials," *Construction and Building Materials*, vol. 19, no. 1, pp. 55–61, 2005.
- [6] F. A. Fathelbab, M. S. Ramadan, and A. Al-Tantawy, "Strengthening of RC bridge slabs using CFRP sheets," *Alexandria Engineering Journal*, vol. 53, no. 4, pp. 843–854, 2014.

- [7] A. Khalifa and A. Nanni, "Improving shear capacity of existing RC T-section beams using CFRP composites," *Cement and Concrete Composites*, vol. 22, no. 3, pp. 165–174, 2000.
- [8] H. M. Tanarlan, "The effects of NSM CFRP reinforcements for improving the shear capacity of RC beams," *Construction and Building Materials*, vol. 25, no. 5, pp. 2663–2673, 2011.
- [9] J. Dong, Q. Wang, and Z. Guan, "Structural behaviour of RC beams with external flexural and flexural-shear strengthening by FRP sheets," *Composites Part B: Engineering*, vol. 44, no. 1, pp. 604–612, 2013.
- [10] H. Toutanji, M. Han, J. Gilbert, and S. Matthys, "Behavior of large-scale rectangular columns confined with FRP composites," *Journal of Composites for Construction*, vol. 14, no. 1, pp. 62–71, 2010.
- [11] B. Csuka and L. P. Kollár, "Analysis of FRP confined columns under eccentric loading," *Composite Structures*, vol. 94, no. 3, pp. 1106–1116, 2012.
- [12] C. Desprez, J. Mazars, P. Kotronis, and P. Paultre, "Damage model for FRP-confined concrete columns under cyclic loading," *Engineering Structures*, vol. 48, pp. 519–531, 2013.
- [13] A. M. Ceci, J. R. Casas, and M. Ghosn, "Statistical analysis of existing models for flexural strengthening of concrete bridge beams using FRP sheets," *Construction and Building Materials*, vol. 27, no. 1, pp. 490–520, 2012.
- [14] F. Inam, D. W. Y. Wong, M. Kuwata, and T. Peijs, "Multiscale hybrid micro-nanocomposites based on carbon nanotubes and carbon fibers," *Journal of Nanomaterials*, vol. 2010, Article ID 453420, 12 pages, 2010.
- [15] M.-Y. Shen, T.-Y. Chang, T.-H. Hsieh et al., "Mechanical properties and tensile fatigue of graphene nanoplatelets reinforced polymer nanocomposites," *Journal of Nanomaterials*, vol. 2013, Article ID 565401, 9 pages, 2013.
- [16] H. T. Choi, J. S. West, and K. A. Soudki, "Partially bonded near-surface-mounted CFRP bars for strengthened concrete T-beams," *Construction and Building Materials*, vol. 25, no. 5, pp. 2441–2449, 2011.
- [17] N. Attari, S. Amziane, and M. Chemrouk, "Flexural strengthening of concrete beams using CFRP, GFRP and hybrid FRP sheets," *Construction and Building Materials*, vol. 37, pp. 746–757, 2012.
- [18] Y. Shen, S. Lu, and F. Li, "An experimental study on concrete flat slabs prestressed with carbon fibre reinforced polymer sheets," *Advances in Materials Science and Engineering*, vol. 2015, Article ID 792320, 11 pages, 2015.
- [19] M. M. Önal, "Strengthening reinforced concrete beams with CFRP and GFRP," *Advances in Materials Science and Engineering*, vol. 2014, Article ID 967964, 8 pages, 2014.
- [20] J. F. Bonacci and M. Maalej, "Behavioral trends of RC beams strengthened with externally bonded FRP," *Journal of Composites for Construction*, vol. 5, no. 2, pp. 102–103, 2001.
- [21] S. T. Smith and J. G. Teng, "FRP-strengthened RC beams. I: review of debonding strength models," *Engineering Structures*, vol. 24, no. 4, pp. 385–395, 2002.
- [22] A. F. Ashour, S. A. El-Refaie, and S. W. Garrity, "Flexural strengthening of RC continuous beams using CFRP laminates," *Cement and Concrete Composites*, vol. 26, no. 7, pp. 765–775, 2004.
- [23] H. K. Lee and L. R. Hausmann, "Structural repair and strengthening of damaged RC beams with sprayed FRP," *Composite Structures*, vol. 63, no. 2, pp. 201–209, 2004.
- [24] A. H. Al-Saidy and K. S. Al-Jabri, "Effect of damaged concrete cover on the behavior of corroded concrete beams repaired with CFRP sheets," *Composite Structures*, vol. 93, no. 7, pp. 1775–1786, 2011.
- [25] S. Pirayeh Gar, J. B. Mander, M. Head, and S. Hurlebaus, "FRP slab capacity using yield line theory," *Journal of Composites for Construction*, vol. 18, no. 6, 2014.
- [26] J. Vercher, E. Gil, A. Mas, and C. Lerma, "Diagnosis and intervention criteria in slabs damaged by severe corrosion of prestressed joists," *Journal of Performance of Constructed Facilities*, vol. 29, no. 1, 2015.
- [27] ACI Committee 318, *ACI 318-08: Building Code Requirements for Structural Concrete and Commentary. Strength Evaluation of Existing Structures*, American Concrete Institute, Detroit, Mich, USA, 2008.
- [28] Ministerio de Fomento, *EHE-08: Instrucción de Hormigón Estructural*, Boletín Oficial del Estado, Madrid, Spain, 2008.
- [29] Ministerio de Vivienda, *CTE-06: Código Técnico de la Edificación*, Boletín Oficial del Estado, Madrid, Spain, 2006.
- [30] G. Camata, E. Spacone, and R. Zarnic, "Experimental and nonlinear finite element studies of RC beams strengthened with FRP plates," *Composites Part B: Engineering*, vol. 38, no. 2, pp. 277–288, 2007.
- [31] ACI Committee 440, *ACI 440.2R-08: Guide for the Design and Construction of Externally Bonded FRP Systems for Strengthening Concrete Structures*, American Concrete Institute, Detroit, Mich, USA, 2008.
- [32] K. J. Willam and E. D. Warnke, "Constitutive model for the triaxial behavior of concrete," in *Proceedings of the International Association for Bridge and Structural Engineering (ISMES '75)*, vol. 19, p. 30, Bergamo, Italy, 1975.
- [33] Z. Haszin, "Failure criteria for unidirectional fiber composites," *Journal of Applied Mechanics, Transactions ASME*, vol. 47, no. 2, pp. 329–334, 1980.
- [34] ANSYS Academic Research, Release 15.0, ANSYS Help, ANSYS, Inc.
- [35] J. Vercher, E. Gil, and A. Mas, *Load-Bearing Capacity of Corroded Reinforced Concrete Joists*, Structures and Architecture: Concepts, Applications and Challenges, Taylor & Francis Group, London, UK, 2013.
- [36] Y. Zhou, M. Gou, F. Zhang, S. Zhang, and D. Wang, "Reinforced concrete beams strengthened with carbon fiber reinforced polymer by friction hybrid bond technique: experimental investigation," *Materials and Design*, vol. 50, pp. 130–139, 2013.
- [37] A. Agbossou, L. Michel, M. Lagache, and P. Hamelin, "Strengthening slabs using externally-bonded strip composites: analysis of concrete covers on the strengthening," *Composites Part B: Engineering*, vol. 39, no. 7-8, pp. 1125–1135, 2008.
- [38] O. Enochsson, J. Lundqvist, B. Täljsten, P. Rusinowski, and T. Olofsson, "CFRP strengthened openings in two-way concrete slabs—An Experimental And Numerical Study," *Construction and Building Materials*, vol. 21, no. 4, pp. 810–826, 2007.
- [39] M. R. Esfahani, M. R. Kianoush, and A. R. Tajari, "Flexural behaviour of reinforced concrete beams strengthened by CFRP sheets," *Engineering Structures*, vol. 29, no. 10, pp. 2428–2444, 2007.
- [40] Ministerio de Vivienda, *Código Técnico de la Edificación (CTE)*, Boletín Oficial del Estado, Madrid, Spain, 2006.

Research Article

Analytical Model for Deflections of Bonded Posttensioned Concrete Slabs

Min Sook Kim,¹ Joowon Kang,² and Young Hak Lee¹

¹Department of Architectural Engineering, Kyung Hee University, 1732 Deogyong-daero, Yongin, Republic of Korea

²School of Architecture, Yeungnam University, 280 Daehak-ro, Gyeongsan, Republic of Korea

Correspondence should be addressed to Young Hak Lee; leeyh@khu.ac.kr

Received 13 December 2016; Accepted 7 February 2017; Published 5 March 2017

Academic Editor: Francesco Caputo

Copyright © 2017 Min Sook Kim et al. This is an open access article distributed under the Creative Commons Attribution License, which permits unrestricted use, distribution, and reproduction in any medium, provided the original work is properly cited.

This paper presents a finite element analysis approach to evaluate the flexural behavior of posttensioned two-way slabs depending on the tendon layout. A finite element model was established based on layered and degenerated shell elements. Nonlinearities of the materials are considered using the stress-strain relationships for concrete, reinforcing steel, and prestressing tendons. Flexural testing of the posttensioned two-way slabs was conducted to validate the developed analytical process. Comparing the analytical results with the experimental results in terms of deflections, it showed generally good agreements. Also a parametric study was performed to investigate the effects of different types of tendon layout.

1. Introduction

Posttensioned concrete slabs have many advantages, such as rapid construction, reduction of overall member depth, and reduced materials. In addition, posttensioned concrete slabs with proper posttensioning show little deflection and few cracks under service loads. Although posttensioned concrete slabs have many advantages, their performance is still not fully understood, and the behaviors of two-way slab systems are more difficult to determine than those of one-way slabs. To evaluate posttensioned concrete slabs, several experimental studies have been performed. Burns and Hemakom [1] observed the strength and behavior of posttensioned flat plates. They applied the banded tendon layout in column strips in the x -direction and distributed single tendons in the y -direction on the slabs. Through this study they found that the banded and distributed tendon layout improved the flexural and shear capacities. Kosut et al. [2] experimentally evaluated the behavior of posttensioned flat plates with distributed and banded tendon arrangements in each direction. They found that banded tendons on the column strip can resist punching shear failure, and distributed tendons can improve flexural capacity. Roschke and Inoue [3] tested prestressed concrete flat slabs to investigate

strain distribution in regions adjacent to the transverse posttensioning bands.

To analyze complex posttensioned concrete slabs efficiently, some researchers have proposed finite element approaches. Van Greunen and Scordelis [4] researched a numerical procedure for the materials and a geometric nonlinear analysis for prestressed concrete slabs. Wu et al. [5] proposed a tendon model based on the finite element method that can represent the interaction between tendons and concrete. They verified the accuracy of their proposed equation against existing experimental data. El-Mezaini and Çitipitioğlu [6] developed quadratic and cubic finite elements with movable nodes to predict the behavior of different bond conditions for the tendons. Kang and Huang [7] proposed nonlinear finite element models to evaluate the behavior of unbonded posttensioned slab-column connections. The spring elements and contact formation were applied to the model to consider the interface between the concrete and prestressing tendon. Kang et al. [8] compared the structural performance of the bonded and unbonded posttensioned concrete members through experiment and analysis. Ghallab [9] suggested using simple equations to predict the prestressing tendons at ultimate stage of continuous concrete beams. The simple equations were verified by comparing

with existing experimental data. Although much analytical research has been performed to evaluate the behavior of bonded and unbonded posttensioned concrete members, a relatively limited number of studies have been reported for the prediction of flexural behavior considering tendon layouts.

Two-way slab systems offer several possible arrangements for the tendon layout [10]: banded, distributed, or a mixed layout. Posttensioned slabs are used for long spans and heavy live loads, so flexural strength and ductility are important. Flexural strength usually governs the behavior of the interior panel in two-way slabs. In other words, the distribution of tendons can affect the flexural behavior and ductility of the interior panel of the two-way slabs. Though many researchers have focused on the development of finite element models, little information is available on the flexural behavior of post-tensioned two-way slabs with different tendon layouts. In this study, examined was the flexural behavior of posttensioned two-way slabs depending on the tendon layout.

The objective of this paper is to present an efficient numerical analysis approach for the materials and a geometric nonlinear analysis for the posttensioned two-way slabs. In this study, developed was a nonlinear finite element model that can simulate the behavior of posttensioned two-way slabs. The reinforced concrete was modeled as combination of concrete, steel, and prestressing tendons. The test results were compared with those from the finite element model as well.

2. Finite Element Model

2.1. Layered Element Formulation. A finite element model formulated using layered and degenerate shell elements can be used in a three-dimensional global analysis of structures. Eight-node isoparametric degenerated shell elements were formulated following the procedure of Hinton and Owen [11]. It was assumed that plane cross-sections remain both plane and normal during bending. Layered elements were applied to account for the behaviors of the reinforced concrete members, which exhibited different properties in the thickness direction because of the placement of the reinforcements. Each element is divided into layers, and each layer has one integration point on its midsurface. Each layer was composed of different materials; concrete, steel reinforcement, and prestressing tendon are defined separately. The strains and stresses are calculated at midpoint of each layer. The strain-displacement matrix and the constitutive matrix are calculated at the midpoint of each layer. Stress resultants are evaluated by integrating the corresponding stress. Normal forces and bending moments can be obtained by

$$\begin{aligned} N_{x(y)} &= \int_{-h/2}^{h/2} \sigma_{x(y)} dz = \frac{h}{2} \sum_{i=1}^n \sigma_{x(y)}^i \Delta \zeta^i, \\ M_{x(y)(xy)} &= - \int_{-\frac{h}{2}}^{\frac{h}{2}} \sigma_{x(y)(xy)} z dz \\ &= - \frac{h^2}{4} \sum_{i=1}^n \sigma_{x(y)(\tau_{xy})}^i \zeta^i \Delta \zeta^i, \end{aligned} \quad (1)$$

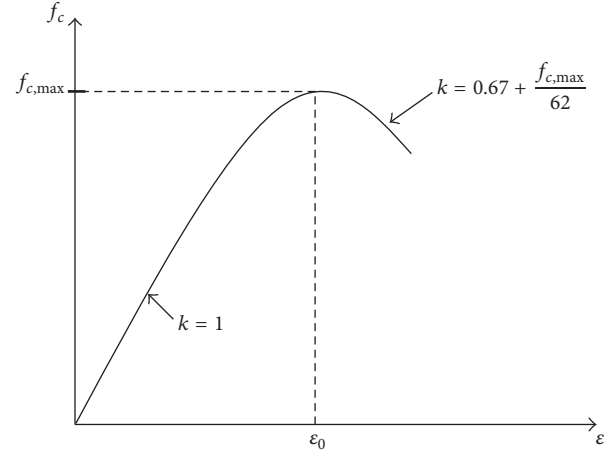


FIGURE 1: Stress-strain relationship in compression by Collins and Porasz (1989).

where N_x is normal force, M_x is bending moment, σ is normal stress, h is layer depth, and n is number of layers.

The reinforcement layers were used to model the in-plane reinforcement. Transverse reinforcement can be specified as a property of a concrete layer. The prestressing tendons at a single depth were grouped with the same prestressing force into one layer [12]. The concrete, steel reinforcement, and prestressing tendons were assumed to be perfectly bonded. The perfect bond is applicable to the analysis of reinforced concrete and posttensioned concrete with bonded tendons. The same degrees of freedom were assigned to concrete and reinforcement nodes occupying a single location.

2.2. Constitutive Models. In this paper, the failure of concrete two-way slabs is considered to be tension cracking or plastic yielding of reinforcement. Uncracked concrete was assumed to be a linear elastic material. After cracking, the concrete was treated as an orthotropic material. The total material matrix consists of concrete, steel reinforcement, and prestressing tendons.

Figure 1 shows the stress-strain relationship for concrete in compression [13]. The compressive stress of concrete can be calculated by

$$\begin{aligned} f_c &= \frac{f_{c2,max} (n\epsilon/\epsilon'_c)}{(n-1) + (\epsilon/\epsilon'_c)^{nk}}, \\ f_{c,max} &= \frac{f'_c}{0.8 - 0.34(\epsilon_c/\epsilon'_c)} \leq f'_c, \\ n &= 0.8 + \frac{f_{c2,max}}{17}, \end{aligned} \quad (2)$$

where f_c is the concrete stress; $f_{c2,max}$ is the compressive stress of cracked concrete; ϵ_c is the concrete strain; ϵ'_c is the concrete strain corresponding to peak compressive stress; and f'_c is the compressive cylinder strength of concrete.

After cracking, the stiffness of the reinforced concrete decreases, but it does not drop to zero because the intact

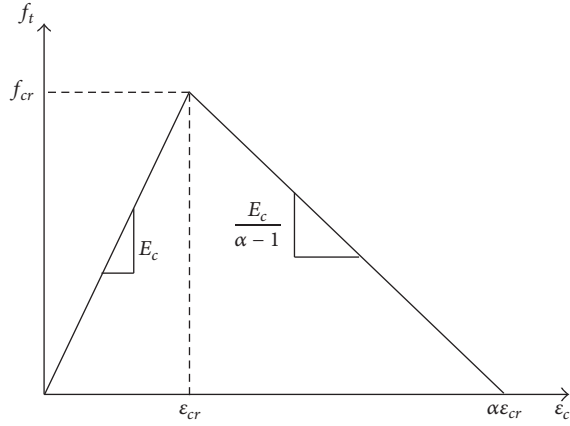


FIGURE 2: Average stress-strain relationship proposed by Lin and Scordelis (1975).

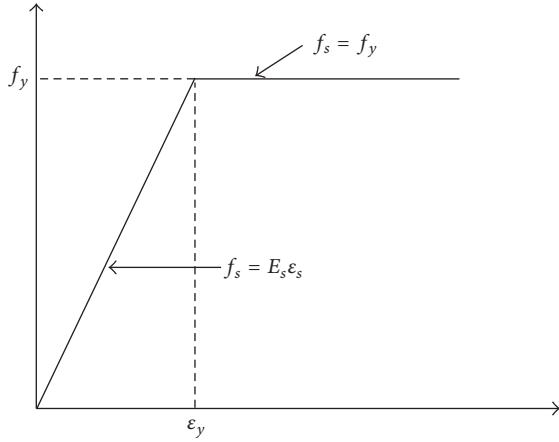


FIGURE 3: Stress-strain relationship of steel reinforcement.

concrete between adjacent cracks can still carry some tensile stress due to the bond between the reinforcement and surrounding concrete. In this paper, tension stiffening was modeled as a constitutive model [14], as shown in Figure 2.

The steel reinforcement was considered as steel layers with uniaxial behavior. A bilinear model was adopted for the elastoplastic stress-strain relationship, as shown in Figure 3. The stress-strain relationship was characterized by Young's modulus E_s and the uniaxial yield stress f_y .

For the prestressing tendon, Menegotto and Pinto's model [15] was adopted (Figure 4). The mathematical expression is given as follows:

$$\sigma_p = E_p \varepsilon_p \left[Q + \frac{1 - Q}{\left[1 + (E_p \varepsilon_p / K f_{py})^N \right]^{1/N}} \right], \quad (3)$$

$$Q = \frac{f_{pu} - K f_{py}}{E_p \varepsilon_{pu} - K f_{py}},$$

where σ_p is the stress of a prestressing tendon; E_p is Young's modulus of the prestressing tendon; ε_p is the strain of the

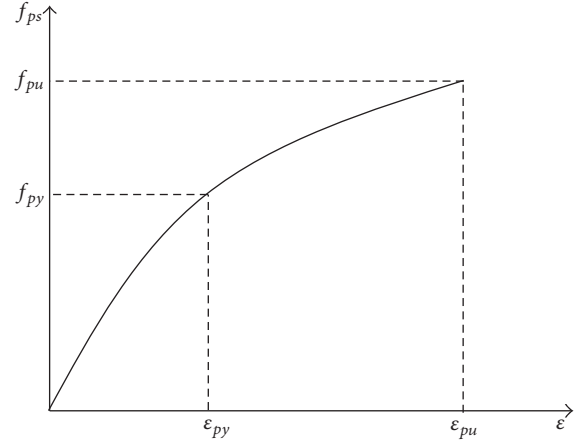


FIGURE 4: Constitutive model of prestressing tendon proposed by Menegotto and Pinto (1973).

prestressing tendon; f_{py} is the yield stress; f_{pu} is the ultimate yield stress; ε_{cu} is the ultimate strain; and N , K , and Q are empirical parameters whose values were recommended by Naaman [16] as 6.06, 1.0325, and 0.00625, respectively.

2.3. Analysis Procedures. Direct method is applied as solution algorithm [11]. In each iterative step, the full load is applied to the structures. The obtained unknowns are the full displacements. In the first iteration, the materials have linearly elastic behavior and the initial displacements are zero. After that, the model can calculate the new stiffness matrix considering the appropriate material constitutive models. Full load is reapplied to the model, then the stiffness matrix is updated, and displacement can be found. The steps of evaluation and update of stiffness matrix are repeated until the satisfied convergence condition.

The displacement criterion was selected as the convergence condition. The displacement convergence is as follows:

$$\sqrt{\frac{\sum (D_a - D_p)^2}{\sum D_a^2}} \times 100\% < T, \quad (4)$$

where D_a is current step displacement, D_p is previous step displacement, and T is tolerance.

Large tolerance value can lead to inaccurate results, and the tolerance was set to 0.8.

3. Experimental Program

To validate the suggested finite element model, flexural testing was performed. The designed compressive strength of the concrete used for the fabrication of the specimens was 35 MPa. The average compressive strength measured at 28 days was 36.7 MPa. Deformed steel bars with a diameter of 13 mm and 10 mm were used for longitudinal reinforcements and stirrups, respectively. Their tensile strength and modulus of elasticity were 400 MPa and 200 GPa, respectively. Seven wire steel-strand tendons with 12.7 mm of diameter were used. Their nominal ultimate tensile strength was 1860 MPa.

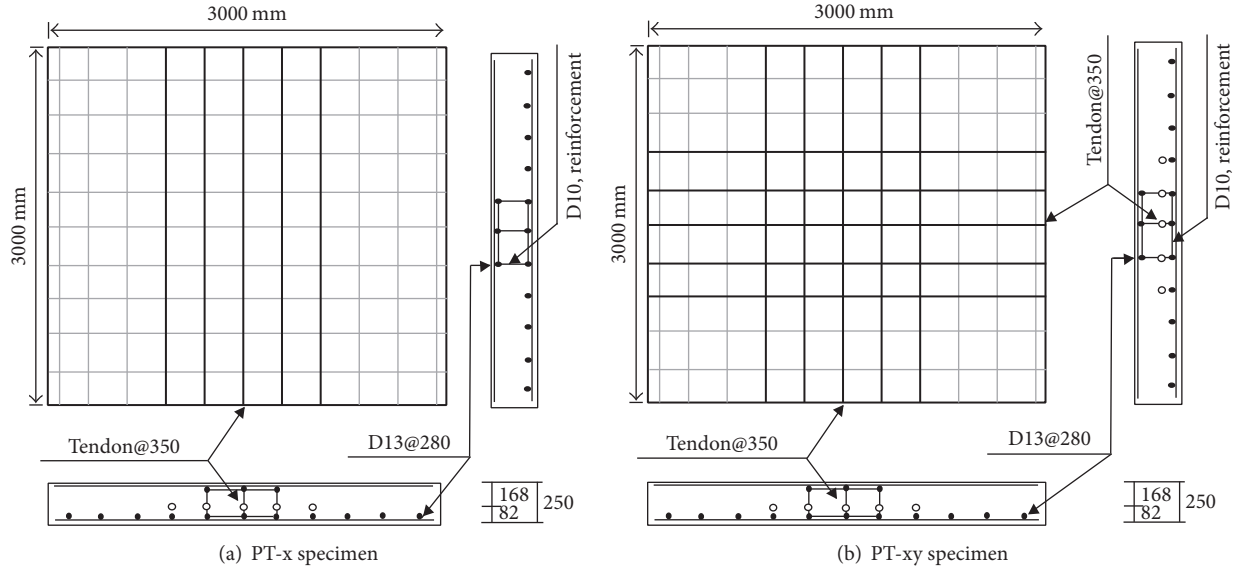


FIGURE 5: Details of the specimens.

TABLE 1: Details of specimens.

| Specimen | $A_{s,x}$ (mm ²) | $A_{s,y}$ (mm ²) | f_{pe} (MPa) | f_{pe}/f_{pu} | $\rho_{p,x}$ (%) | $\rho_{p,y}$ (%) | $\rho_{s,x}$ (%) | $\rho_{s,y}$ (%) | d_p (mm) | f'_c (MPa) |
|----------|------------------------------|------------------------------|----------------|-----------------|------------------|------------------|------------------|------------------|------------|--------------|
| PT-x | 493.5 | — | 1488 | 0.8 | 0.198 | — | 0.185 | 0.185 | 168 | 36.7 |
| PT-xy | 493.5 | 493.5 | 1488 | 0.8 | 0.198 | 0.198 | 0.185 | 0.185 | 168 | |

Two posttensioned two-way slabs were manufactured for the test. One specimen had tendons distributed in only the x-direction (PT-x), and the other had tendons distributed in both the x- and y-directions (PT-xy). Details of the specimens are presented in Figure 5 and summarized in Table 1. The size of the test specimens was 3000 mm × 3000 mm with 250 mm thickness. Both specimens were posttensioned with a constant eccentricity of 43 mm. A prestressing force of 1488 MPa was applied corresponding to approximately 80% of the tensile strength of the tendon.

Load was applied to each specimen using a hydraulic jack with maximum capacity of 5000 kN. The test specimens were simply supported along the four sides. The force generated by the hydraulic jack was transmitted to a loading plate placed at the middle of the specimen. The distance from support to loading point was 1.25 m, giving a shear span to depth ratio of 6.

4. Numerical Modeling and Discussion

In order to evaluate the accuracy of the analytical model, the theoretical value is compared with test results. Comparison is made in terms of load-deflections curves. The analytical model size was set to match the posttensioned specimens, and the model contained 100 elements. It was divided into nine layers in the direction of different thickness. The thicknesses of the first and last layers were determined by considering the concrete cover. The steel reinforcements were placed at the 2nd and 8th layers in the direction of the thickness. The prestressing tendons were placed at the 6th layer in the

direction of the thickness. In this paper, Young's modulus of concrete (E_c) was determined according to ACI 318 [17]. Poisson's coefficient (ν) is 0.15, and the equation to compute the modulus of rupture of concrete is $0.32\sqrt{f'_c}$ (Table 2). To simulate the experimental support conditions, four sides of slabs are simply supported and the load is applied to the center of the slab.

The model values were compared with load-displacement curves obtained from the posttensioned two-way slabs under flexural loads. The comparisons between the test results and the analytical results are shown in Figures 6 and 7. As shown in the Figures, both test and analytical results indicated that the load-displacement curves exhibit three stages: elastic, cracking, and plastic. Overall, the analytical model predicted the deflection of the posttensioned specimens in a relatively accurate manner. However, in all cases the models show a slightly stiffer response at the cracking stage because prestressing loss and slip were not considered in the finite element analysis. Both the testing and analytical results showed that the one-way and two-way prestressing tendon layout did not significantly affect the maximum load capacity and deflection.

The validated finite element model was used to investigate the effects of changes in span length, height, and concrete strength. In total, nine posttensioned slabs were analyzed as shown in Table 3. To perform the parametric analysis, the same geometry and material properties were used same as in the verification of the proposed model, along with the one-way tendon layout. The same load to each model was

TABLE 2: Material properties used in the finite element analysis.

| | | Concrete | | | Steel and prestressing tendon | | |
|--------------|-------------|-------------|-----------------|---------|-------------------------------|-------------|---------|
| f'_c (MPa) | f_t (MPa) | E_c (MPa) | ϵ_{cr} | ν_c | f_y (MPa) | E_s (GPa) | ν_s |
| 36.7 | 3.8 | 28472.9 | 0.002 | 0.15 | 360 | 210 | 0.25 |

TABLE 3: Analytical dimensions and results of parametric study.

| Model | Span (mm) | Height (mm) | Compressive strength of concrete (MPa) | Displacement (mm) |
|-------|-----------|-------------|--|-------------------|
| PT1 | 3000 | 250 | 35 | 41.77 |
| PT2 | 4500 | 250 | 35 | 48.54 |
| PT3 | 6000 | 250 | 35 | 56.13 |
| PT4 | 7500 | 250 | 35 | 67.20 |
| PT5 | 3000 | 180 | 35 | 43.62 |
| PT6 | 3000 | 350 | 35 | 40.14 |
| PT7 | 3000 | 450 | 35 | 37.32 |
| PT8 | 3000 | 250 | 50 | 40.33 |
| PT9 | 3000 | 250 | 65 | 38.16 |

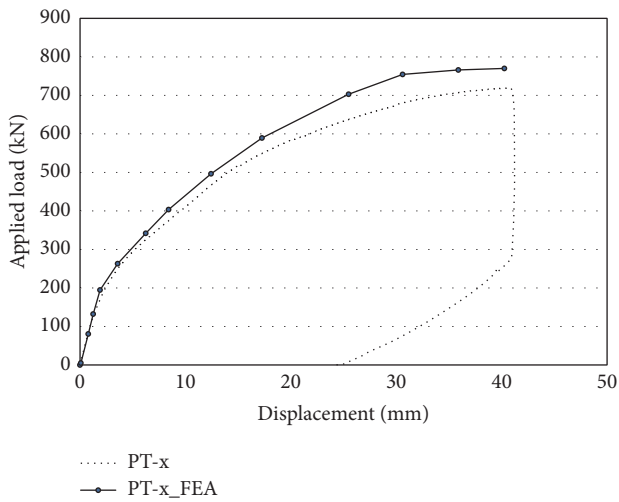


FIGURE 6: Load-displacement relations of PT-x specimen.

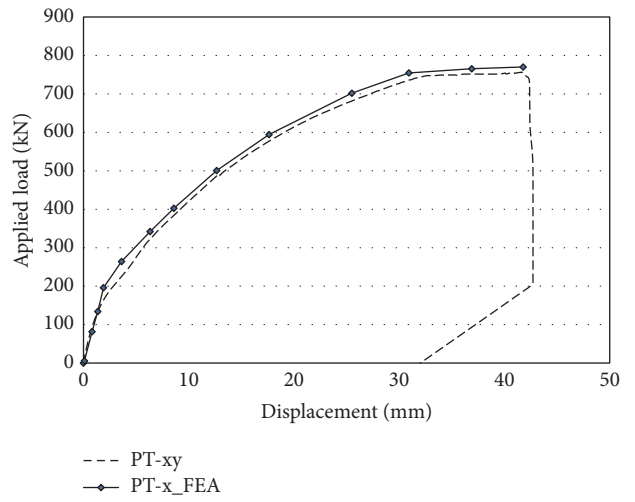


FIGURE 7: Load-displacement relations of PT-xy specimen.

applied and compared the results in terms of deflections. Figure 8–10 show the displacement according to span length, slab height, and the compressive strength of the concrete. The displacement increased with the span length and decreased as the height and concrete strength increased. The results of the parametric analysis indicate that the deflection of posttensioned two-way slab is more affected by the span length than by the other variables.

5. Conclusions

In this paper, the flexural behavior of posttensioned concrete two-way slab was analytically investigated. A finite element analysis model was proposed to predict the flexural behavior of specimens depending on the tendon layout and conducted flexural tests to evaluate the validity and applicability of the

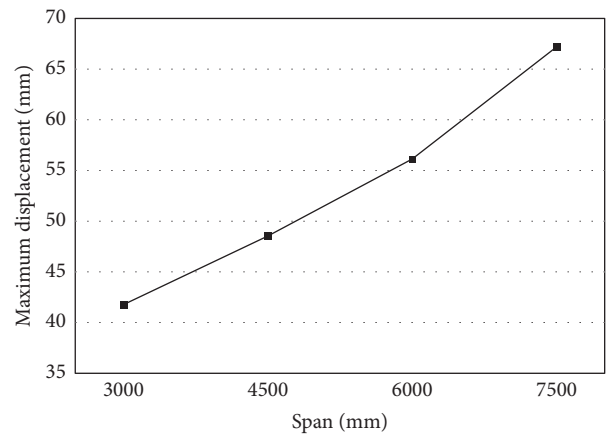


FIGURE 8: Effect of span length on displacement.

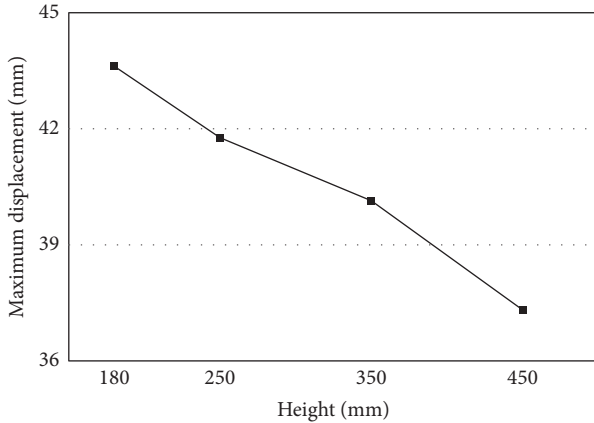


FIGURE 9: Effect of height of slabs on displacement.

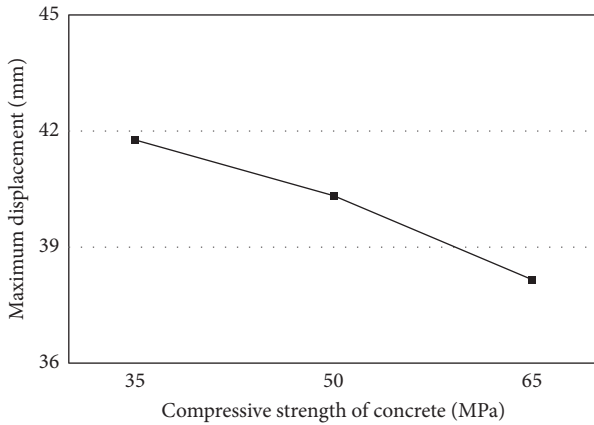


FIGURE 10: Effect of compressive strength of concrete on displacement.

proposed model. The following specific conclusions were drawn from this study:

- (1) A finite element analysis model has been developed to evaluate the flexural behavior of posttensioned two-way slabs considering tendon layout. The proposed finite element model, which considers the nonlinear behavior of concrete and reinforcement and neglects the bond slip and loss of prestressing force, gives relatively good predictions for the load-deflection curves.
- (2) The increase in the maximum load capacity was unaffected by tendon layouts. Regardless of the direction of the tendon, the load-displacement curves indicated similar responses. The analytical response is slightly stiffer than the test results at the cracking stages, possibly because of bond slip and the loss of prestressing force. Consideration of bond slip and the loss of prestressing force could improve the model accuracy. However, the difference in deflection between the analytical and test results is relatively small. The proposed finite element analysis demonstrates

the rationality of the posttensioning two-way slabs model.

- (3) To investigate the effects of span length, slab height, and concrete strength on posttensioned two-way slabs, a parametric study was conducted. The displacement increased with the span length and decreased as the concrete strength and member height increased. The span length, height, and concrete strength all contribute to the flexural strength.

Competing Interests

The authors declare that they have no competing interests.

Acknowledgments

This work was supported by a National Research Foundation of Korea (NRF) grant funded by the Korean Government (MSIP) (NRF-2013R1A2A2A01067754).

References

- [1] N. H. Burns and R. Hemakom, "Test of post-tensioned flat plate with banded tendons," *Journal of Structural Engineering*, vol. 111, no. 9, pp. 1899–1915, 1985.
- [2] G. M. Kosut, N. H. Burns, and C. V. Winter, "Test of four-panel post-tensioned flat plate," *Journal of Structural Engineering*, vol. 111, no. 9, pp. 1916–1929, 1985.
- [3] P. N. Roschke and M. Inoue, "Effects of banded post-tensioning in prestressed concrete flat slab," *Journal of Structural Engineering*, vol. 117, no. 2, pp. 563–583, 1991.
- [4] J. Van Greunen and A. C. Scordelis, "Nonlinear analysis of prestressed concrete slabs," *Journal of Structural Engineering*, vol. 109, no. 7, pp. 1742–1760, 1983.
- [5] X.-H. Wu, S. Otani, and H. Shiohara, "Tendon model for nonlinear analysis of prestressed concrete structures," *Journal of Structural Engineering*, vol. 127, no. 4, pp. 398–405, 2001.
- [6] N. El-Mezaini and E. Çitipitioglu, "Finite element analysis of prestressed and reinforced concrete structures," *Journal of Structural Engineering*, vol. 117, no. 10, pp. 2851–2864, 1991.
- [7] T. H. K. Kang and Y. Huang, "Nonlinear finite element analyses of unbonded post-tensioned slab-column connections," *PTI Journal*, vol. 8, no. 1, pp. 4–19, 2012.
- [8] T. H.-K. Kang, Y. Huang, M. Shin, J. D. Lee, and A. S. Cho, "Experimental and numerical assessment of bonded and unbonded post-tensioned concrete members," *ACI Structural Journal*, vol. 112, no. 6, pp. 735–748, 2015.
- [9] A. Ghallab, "Calculating ultimate tendon stress in externally prestressed continuous concrete beams using simplified formulas," *Engineering Structures*, vol. 46, pp. 417–430, 2013.
- [10] B. O. Alami, "Layout of post-tensioning and passive reinforcement in floor slabs," *PTI Technical Notes* 8, 1999.
- [11] E. Hinton and D. R. J. Owen, *Finite Element Software for Plates and Shells*, Pineridge Press, Swansea, UK, 1984.
- [12] J. Chern, C. You, and Z. P. Bazant, "Deformation of progressively cracking partially prestressed concrete beams," *PCI Journal*, vol. 37, no. 1, pp. 74–85, 1992.
- [13] M. P. Collins and A. Porasz, "Shear design for high strength concrete," in *Proceeding of the Workshop on Design Aspects of High Strength Concrete*, pp. 75–83, 1989.

- [14] C.-S. Lin and A. C. Scordelis, "Nonlinear analysis of rc shells of general form," *Journal of the Structural Division*, vol. 101, no. 3, pp. 523–538, 1975.
- [15] M. Menegotto and P. E. Pinto, "Method of analysis for cyclically loaded R. C. Plane frames, including changes in geometry and non-elastic behavior of elements under combined normal force and bending," in *Proceedings of the IABSE Symposium on Resistance and Ultimate Deformability of Structures Acted on by Well-Defined Repeated Loads*, pp. 15–22, Lisbon, Portugal, 1973.
- [16] A. E. Naaman, "A new methodology for the analysis of beams prestressed with external or unbonded tendons," *External Prestressing in Bridges ACI SP120-16*, American Concrete Institute, Detroit, Mich, USA, 1990.
- [17] American Concrete Institute (ACI), "Building code requirement for reinforced concrete and commentary," ACI 318-14, American Concrete Institute (ACI), Farmington Hills, Mich, USA, 2014.

Research Article

Mechanical and Failure Criteria of Air-Entrained Concrete under Triaxial Compression Load after Rapid Freeze-Thaw Cycles

Feng-kun Cui,¹ Huai-shuai Shang,² Tie-jun Zhao,² Guo-xi Fan,³ and Guo-sheng Ren²

¹School of Highway, Chang'an University, Xi'an, Shaanxi 710064, China

²School of Civil Engineering, Qingdao University of Technology, Qingdao, Shandong 266033, China

³School of Engineering, Ocean University of China, Qingdao, Shandong 266100, China

Correspondence should be addressed to Feng-kun Cui; 929599342@qq.com and Huai-shuai Shang; shanghuaishuai@aliyun.com

Received 19 November 2016; Accepted 24 January 2017; Published 13 February 2017

Academic Editor: Paulo M. S. T. De Castro

Copyright © 2017 Feng-kun Cui et al. This is an open access article distributed under the Creative Commons Attribution License, which permits unrestricted use, distribution, and reproduction in any medium, provided the original work is properly cited.

The experiment study on the air-entrained concrete of 100 mm cubes under triaxial compression with different intermediate stress ratio $\alpha_2 = \sigma_2^D : \sigma_3^D$ was carried out using a hydraulic-servo testing system. The influence of rapid freeze-thaw cycles and intermediate stress ratio on the triaxial compressive strength σ_3^D was analyzed according to the experimental results, respectively. The experimental results of air-entrained concrete obtained from the study in this paper and the triaxial compression experimental results of plain concrete got through the same triaxial-testing-system were compared and analyzed. The conclusion was that the triaxial compressive strength is greater than the biaxial and uniaxial compressive strength after the same rapid freeze-thaw cycles, and the increased percentage of triaxial compressive strength over biaxial compressive strength or uniaxial compressive strength is dependent on the middle stress. The experimental data is useful for precise analysis of concrete member or concrete structure under the action complex stress state.

1. Introduction

In cold regions, such as northern China, Russia, Canada, and northern Europe, the performance (e.g., strength, deformation and elasticity modulus) deterioration of concrete applied in practical engineering can be caused by the action of rapid freeze-thaw cycles. Özgan and Serin [1] investigated the effect of freeze-thaw cycles on asphalt concrete materials according to Marshall stability values and ultrasonic velocity and so forth. The value of fracture parameters of lightweight concrete after different freeze-thaw cycles was determined through a three-point bending test in [2]. The weight loss, pulse velocity, and resonance frequency of silica fume concrete after the action of freeze-thaw cycles were reported in [3]. The influence of freeze-thaw cycles on the behavior (compressive strength, weight loss, and relative pulse velocity) of concrete with synthetic fibre additions was studied in [4]. The experimental results show that the

freeze-thaw cycles can cause the degradation of the strength and deformation properties of asphalt concrete, lightweight aggregate concrete, silica fume concrete, and so forth.

Several kinds of mechanisms, such as “microscopic ice lens growth” [5] and “hydraulic pressure” [6] could be used to explain the frost damage in concrete. Some researches demonstrated that the inner structures and material properties of concrete have more significant effect on this damage degree than the external environment [7–9]. And the internal structure of concrete may be affected by the frost damage caused by the inner pressure and the associated micro cracks. Based on this, air-entrained agent is added to the concrete to make air-entrained concrete. One of the advantages of air-entrained concrete is its greater resistance to damage caused by freeze-thaw cycles [10–12] which make it especially suitable in the construction of dam, long span bridges, and offshore oil platforms in cold environment. So far, air-entrained concrete [13] has been widely used in the field

TABLE 1: Mix proportions of air-entrained concrete.

| w/c | Cement (kg/m ³) | Sand (kg/m ³) | Coarse Aggregate (kg/m ³) | Water (kg/m ³) | Air-entraining agents (kg/m ³) | Air content (%) |
|------|-----------------------------|---------------------------|---------------------------------------|----------------------------|--|-----------------|
| 0.40 | 412.67 | 586.83 | 1186.00 | 164.30 | 1.03 | 5.80 |

of hydraulic engineering and civil engineering. However, a lot of experimental tests are carried out to determine the freeze-thaw durability of different type concrete, while, for air-entrained concrete, the research is still comparatively rare. Pheeraphan and Leung [14] studied the freeze-thaw resistance of microwave cured air-entrained concrete. According to the test results of Pheeraphan and Leung, the freeze-thaw durability of high w/c concrete will be impaired by microwave curing. Shang et al. [15] investigated the weight loss, relative dynamic modulus of elasticity, tensile strength, compressive strength, cubic compressive strength, and cleavage strength of air-entrained concrete after different freeze-thaw cycles. And it can be seen from [14, 15], for air-entrained concrete or other types of concrete, that most of the previous researchers mainly focused their attention on the dynamic elastic modulus, weight loss, flexural strength, and uniaxial compression strength after different freeze-thaw cycles. Meanwhile, in civil engineering, it can be well-known that concrete materials in member of structure (e.g., shear walls, thin shells, and slabs) are essentially in a complex stress state: such as biaxial compression, triaxial tension-tension-compression, triaxial compression [16–19]. For refined calculation, the behavior of concrete materials under a stress state of multiaxial loads should be examined carefully. The mechanical performance of plain concrete under biaxial and triaxial compression was studied after freeze-thaw cycles [20–22]. Wang and Song [23] investigated the failure criterion of the haydite concrete under triaxial loading. The strength criterion of lightweight aggregate concrete under multiaxial loads was also studied based on the unified twin-shear strength theory [24].

According to experimental results in the literature, it has been realized that although a large number of test data are available regarding the triaxial compression behavior of plain concrete and some special concrete, very little information on the behavior of air-entrained concrete under triaxial stress state can be found, especially the behavior of air-entrained concrete under triaxial compressive loads after the action of different rapid freeze-thaw cycles. Many literatures [1–4, 9–12, 19–21] illustrated that the strength and peak strain in concrete are influenced significantly by the inner damage caused by freeze-thaw cycles. Hanjari [25] pointed out that the results obtained from the undamaged concrete can not be applied directly for the frost-damaged concrete.

In order to better understand and predict the performance of structure and member made with air-entrained concrete material, the mechanical properties of air-entrained concrete should be figured out. Shang [26] investigated the triaxial compression behavior of air-concrete with stress ratio $\sigma_2^D : \sigma_3^D = 1.00 : 1.00$. The experiment on strength behavior of air-entrained concrete under triaxial compression load with $\sigma_1^D : \sigma_3^D = 0.10 : 1.00$ after rapid freeze-thaw cycles was carried out. Results obtained from the experimental studies will be

used to develop a simple relationship between mechanical behavior and number of rapid freeze-thaw cycles for air-entrained concrete. The relationship can be used as input to computer programs to analyze the behavior of air-entrained concrete structural members subjected to different rapid freeze-thaw cycles.

2. Experimental Program

2.1. Materials and Mix Proportions. The 42.5[#] Ordinary Portland cement (the compressive strength should reach 22.0 MPa and 42.5 MPa at days 3 and 28; the flexural strength should reach 4.0 MPa and 6.5 MPa at days 3 and 28), tap water, river sand (fineness modulus was 2.6), crushed natural stone aggregate (diameter ranges from 5 mm to 20 mm), and air-entrained admixture (rosin soap air-entraining agent was used) were used in this experimental study. The proportions by weight of cement: water: sand: coarse aggregate are 1:0.4:1.42:2.87. The mixing proportions in this experiment were given in Table 1. The air content of the concrete mixture was 5.8% after mixing. The compressive strength of 28 days is 25.64 MPa.

2.2. Specimen and Testing Programs. In this experiment study, horizontal forced action mixer with 0.1 m³ was used to elaborate the mixture. The following mixing procedure was used: first, fine aggregate, coarse aggregate, and cement were put into the mixer and the components were mixed for 1 minute; then, tap water was added and continued to stir for 2~3 minute; next, the fresh concrete material was cast in cubical molds with size 100 mm × 100 mm × 100 mm and a vibrating table with size 1 m × 1 m was used to compact concrete. After the fresh concrete was mixed, the air content was measured with air-content measuring instrument. At the same time, freshly cast specimens were kept in the molds for 24 hours. Finally, they were demoulded and stored in a curing room which can keep 95 percent relative humidity and the temperature of 20 ± 3 °C. At 24 days of age, some air-entrained concrete specimens were taken out from the curing room and immersed in water for 4 days.

According to “the test method of long-term and durability on ordinary concrete” [21, 27], the rapid freeze-thaw tests were performed in a rapid freeze-thaw apparatus at 28 days of age for concrete specimen. In a single rapid freeze-thaw cycle, the center temperature of the specimens should cool from 6 °C to –15 °C and then warm to 6 °C during about 2.5–3 h. The temperature of the concrete specimens was measured and controlled by a Pt sensor embedded in the center of concrete specimen. And the test is similar to the ASTM C 666, “Standard Test Method for Resistance of Concrete to Rapid Freezing and Thawing” [28]. In a single cycle according to

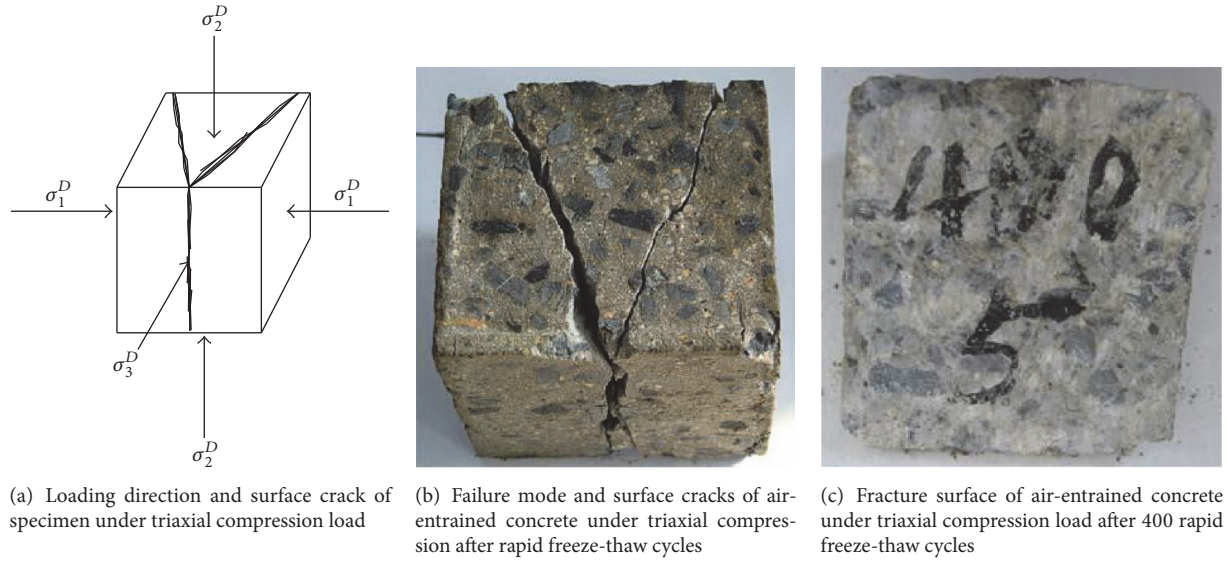


FIGURE 1: The failure mode and fracture surface of air-entrained concrete specimen after different freeze-thaw cycles.

ASTMC 666, the temperature of the specimens cools from 4.4 to -17.8°C and then warms to 4.4°C within 2 to 5 h.

And the triaxial compression experiment was carried out in a triaxial-testing-system [21, 29]. The stress ratios were $\alpha = \sigma_1^D : \sigma_2^D : \sigma_3^D = 0.10 : 0.25 : 1.00$, $0.10 : 0.50 : 1.00$, $0.10 : 0.75 : 1.00$, and $0.10 : 1.00 : 1.00$. The relationship of principal compressive stresses was expressed as $\sigma_1^D \leq \sigma_2^D \leq \sigma_3^D$ (compression stress denoted as positive). The friction between loading plate of testing machine and surface of concrete specimen will affect the experimental results; in order to eliminate the influence of friction, the friction-reducing pads [30] (consisting of three plastic membranes with three layers of butter between them) were used which were placed between the specimen and the loading plate.

3. Results and Discussions

3.1. Failure Modes. Figure 1(a) gives the triaxial compression loading direction for air-entrained concrete specimens. The triaxial compression failure mode and surface crack of air-entrained concrete specimen after different freeze-thaw cycles were given in Figure 1(b).

A gradual failure was observed in the triaxial compression experiment on air-entrained concrete specimens after different freeze-thaw cycles. The failure surfaces are “neat surfaces” and cracks pass through the “broken aggregate.” The failure surface contained fractures through both cement mortar and coarse aggregate. A typical fracture surface of an air-entrained concrete specimen is shown in Figure 1(c).

Under triaxial compression load with stress ratios $\alpha = \sigma_1^D : \sigma_2^D : \sigma_3^D = 0.10 : 0.25 : 1.00$, $0.10 : 0.50 : 1.00$, $0.10 : 0.75 : 1.00$, and $0.10 : 1.00 : 1.00$, the failure mode of the specimens was slant-shear failure, which was caused by the splitting tensile strain along σ_1^D direction. The angle between the direction of σ_3^D and the crack was about $20^{\circ} \sim 30^{\circ}$.

There were two cracks on σ_2^D surfaces; the number of cracks on the σ_3^D surfaces was one or two, respectively.

Under triaxial compression load with stress ratios $\alpha = \sigma_1 : \sigma_2 : \sigma_3 = 0.05 : 1 : 1$, $0.1 : 1 : 1$, $0.15 : 1 : 1$, and $0.2 : 1 : 1$ in [26], the failure mode of the specimens of air-entrained concrete specimen was parallel plate-type fragments mode and slant-shear failure mode; the angle between the crack and the direction of σ_3 was about $20^{\circ} \sim 30^{\circ}$ when the stress ratios were $\alpha = 0.1 : 1 : 1$, $0.15 : 1 : 1$, and $0.2 : 1 : 1$; the angle between the crack and the direction of σ_3 was about $10^{\circ} \sim 20^{\circ}$ when $\alpha = 0.05 : 1 : 1$; and parallel plate-type fragments were formed on the surface of σ_2 and σ_3 under triaxial compression load with stress ratios $\alpha = \sigma_1 : \sigma_2 : \sigma_3 = 0 : 1.00 : 1.00$. According to the experiment results of plain concrete conducted on the same triaxial-testing-system with this paper [20], the splitting cracks in slice shapes were formed on surface of σ_2 and σ_3 under triaxial compression load with stress ratios $\alpha = \sigma_1 : \sigma_2 : \sigma_3 = 0.1 : 1 : 1$, and the slant-shear cracks are in good agreement with experimental results obtained in this paper when triaxial compression stress ratios are $\alpha = \sigma_1 : \sigma_2 : \sigma_3 = 0.1 : 0.25 : 1.0$; $0.1 : 0.5 : 1.0$; $0.1 : 0.75 : 1.0$. Reference [20] studied triaxial compression strength of plain concrete through experiment, and three failure modes were observed in this experiment, which are (1) splitting cracks in slice shapes, (2) splitting cracks in column shapes, and (3) flow and deformation.

3.2. Experimental Results. Table 2 listed the test results of air-entrained concrete under triaxial compression load with different intermediate stress ratio $\alpha_2 = \sigma_2^D : \sigma_3^D$ after rapid freeze-thaw cycles. The compressive stresses σ_1^D , σ_2^D , and σ_3^D were got through dividing compressive loads with loading area (0.01 m^2). σ_{oct}^D and τ_{oct}^D are the normal stress and the shear stress in octahedral stress space after different freeze-thaw cycles [20, 31] which can be computed from

TABLE 2: Experimental results of air-entrained concrete under triaxial compression after rapid freeze-thaw cycles (MPa).

| Freeze-thaw cycles | α | σ_1^D | σ_2^D | σ_3^D | σ_{oct}^D | τ_{oct}^D | σ_{oct}^D/f_c | τ_{oct}^D/f_c |
|--------------------|------------|--------------|--------------|--------------|------------------|----------------|----------------------|--------------------|
| 0 | 0.1:0.25:1 | 10.45 | 24.38 | 95.81 | 43.55 | 37.39 | 1.70 | 1.46 |
| | 0.1:0.5:1 | 11.84 | 52.92 | 105.39 | 56.72 | 38.29 | 2.21 | 1.49 |
| | 0.1:0.75:1 | 9.96 | 69.30 | 92.35 | 57.20 | 34.71 | 2.23 | 1.35 |
| | 0.1:1:1 | 10.04 | 85.01 | 85.22 | 60.09 | 35.39 | 2.34 | 1.38 |
| 100 | 0.1:0.25:1 | 10.45 | 24.29 | 95.40 | 43.38 | 37.22 | 1.69 | 1.45 |
| | 0.1:0.5:1 | 10.98 | 49.92 | 99.60 | 53.5 | 36.27 | 2.09 | 1.41 |
| | 0.1:0.75:1 | 9.95 | 66.92 | 89.20 | 55.36 | 33.37 | 2.16 | 1.30 |
| | 0.1:1:1 | 10.13 | 84.51 | 84.75 | 59.80 | 35.12 | 2.33 | 1.37 |
| 200 | 0.1:0.25:1 | 9.49 | 21.62 | 84.95 | 38.69 | 33.09 | 1.51 | 1.29 |
| | 0.1:0.5:1 | 9.32 | 42.45 | 84.48 | 45.42 | 30.76 | 1.77 | 1.20 |
| | 0.1:0.75:1 | 8.82 | 59.55 | 79.46 | 49.28 | 29.74 | 1.92 | 1.16 |
| | 0.1:1:1 | 8.77 | 73.12 | 73.33 | 51.74 | 30.38 | 2.02 | 1.19 |
| 300 | 0.1:0.25:1 | 7.15 | 16.20 | 63.46 | 28.94 | 24.69 | 1.13 | 0.96 |
| | 0.1:0.5:1 | 8.22 | 37.14 | 73.92 | 39.76 | 26.89 | 1.553 | 1.05 |
| | 0.1:0.75:1 | 8.58 | 57.09 | 76.09 | 47.25 | 28.42 | 1.843 | 1.11 |
| | 0.1:1:1 | 7.87 | 66.10 | 66.33 | 46.77 | 27.50 | 1.823 | 1.07 |
| 400 | 0.1:0.25:1 | 6.66 | 15.41 | 60.51 | 27.53 | 23.59 | 1.07 | 0.92 |
| | 0.1:0.5:1 | 7.49 | 34.22 | 68.25 | 36.65 | 24.86 | 1.43 | 0.97 |
| | 0.1:0.75:1 | 6.92 | 45.52 | 60.70 | 37.71 | 22.64 | 1.47 | 0.88 |
| | 0.1:1:1 | 7.57 | 59.55 | 59.97 | 42.36 | 24.60 | 1.65 | 0.96 |

the following: $\tau_{oct}^D = (1/3)(\sigma_1^D + \sigma_2^D + \sigma_3^D)$ and $\sigma_{oct}^D = (1/3)\sqrt{(\sigma_1^D - \sigma_2^D)^2 + (\sigma_2^D - \sigma_3^D)^2 + (\sigma_3^D - \sigma_1^D)^2}$.

3.2.1. Effect of Rapid Freeze-Thaw Cycles on Peak Stress σ_3^D .
The effect of rapid freeze-thaw cycles on strength of air-entrained concrete under triaxial compression load with different stress ratio was depicted in Figure 2. Table 3 demonstrates the loss of ultimate strength of air-entrained concrete under triaxial compression with increasing the rapid freeze-thaw cycles. It can be got from Figure 2 and Table 3 that the principal stress σ_3^D decreases as number of rapid freeze-thaw cycles increases. The reduction of triaxial compression strength of air-entrained concrete is slower than that of uniaxial and biaxial compression strength as number of rapid freeze-thaw cycles increases. After the action of 200 rapid freeze-thaw cycles, the uniaxial compression strength and biaxial equal compression strength decreased to 81.0 and 83.1 percent of those prior to the rapid freeze-thaw cycles, respectively; meanwhile, under the action of triaxial compression with stress ratio $\alpha = 0.10 : 1.00 : 1.00$, the strength decreased to 86.05 percent of that prior to the rapid freeze-thaw cycles. After the action of 200 rapid freeze-thaw cycles, the strength under triaxial compression with stress ratios $\alpha = 0.10 : 0.25 : 1.00$, $0.10 : 0.50 : 1.00$, $0.10 : 0.75 : 1.00$, and $0.10 : 1.00 : 1.00$ varied from 80.16% to 88.67% of initial value prior to freeze-thaw cycles.

For air-entrained concrete specimen under triaxial compression with stress ratios $\alpha = 0.05 : 1.00 : 1.00$, $0.10 : 1.00 : 1.00$, $0.15 : 1.00 : 1.00$, and $0.20 : 1.00 : 1.00$ [26], the strength after the action of 200 rapid freeze-thaw cycles varied from 83.15% to 93.82% of that prior to rapid freeze-thaw cycles. The

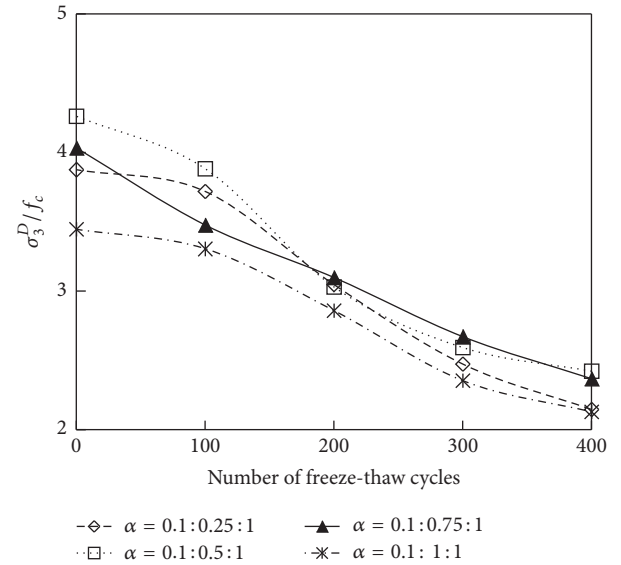


FIGURE 2: Effect of rapid freeze-thaw cycles on triaxial compressive strength under different intermediate stress ratio.

effect of rapid freeze-thaw cycles on strength of air-entrained concrete under triaxial compression load with stress ratios $0:1.0:1.0$, $0.05:1.0:1.0$, $0.15:1.0:1.0$, and $0.2:1.0:1.0$ was given in Table 3. The effect of rapid freeze-thaw cycles on strength of plain concrete under triaxial compression load with stress ratios $\alpha = 0.10 : 0.25 : 1.00$, $0.10 : 0.50 : 1.00$, $0.10 : 0.75 : 1.00$, and $0.10 : 1.00 : 1.00$ was given in Table 4 as well.

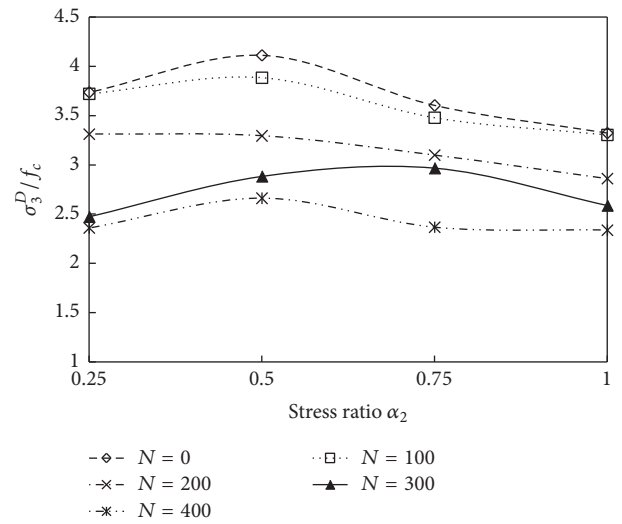
TABLE 3: Loss of ultimate strength of air-entrained concrete under triaxial compression load with rapid freeze-thaw cycles (%).

| Stress ratio | Number of rapid freeze-thaw cycles | | | |
|---------------------------|------------------------------------|-------|-------|-------|
| | 100 | 200 | 300 | 400 |
| 0.1:0.25:1.0 | 99.57 | 88.67 | 66.24 | 63.16 |
| 0.1:0.50:1.0 | 94.51 | 80.16 | 70.14 | 64.76 |
| 0.1:0.75:1.0 | 96.59 | 86.04 | 82.39 | 65.73 |
| 0.1:1.0:1.0 | 99.45 | 86.05 | 77.83 | 70.37 |
| Uniaxial compression | 90.36 | 81.05 | 65.02 | 47.31 |
| Biaxial equal compression | 92.09 | 83.15 | 68.50 | 56.67 |
| 0:1.0:1.0 in [26] | 92.09 | 83.15 | 68.50 | 56.67 |
| 0.05:1.0:1.0 in [26] | 94.32 | 89.54 | 75.67 | 68.23 |
| 0.15:1.0:1.0 in [26] | 96.63 | 93.82 | 89.12 | 81.00 |
| 0.2:1.0:1.0 in [26] | 98.29 | 91.88 | 86.08 | 86.61 |

TABLE 4: Loss of ultimate strength of plain concrete under triaxial compression with rapid freeze-thaw cycles (%).

| Stress ratio | Number of rapid freeze-thaw cycles | | |
|--------------|------------------------------------|-------|-------|
| | 25 | 50 | 75 |
| 0.1:0.25:1.0 | 95.88 | 89.13 | 80.38 |
| 0.1:0.50:1.0 | 96.68 | 93.30 | 90.65 |
| 0.1:0.75:1.0 | 98.20 | 93.18 | 87.04 |
| 0.1:1.0:1.0 | 96.50 | 92.80 | 89.38 |

For plain concrete specimens of 100 mm cube, the mechanical properties under the action of uniaxial compression load, biaxial compression load, and triaxial compression load with stress ratios $\alpha = 0.10:0.25:1.00$, $0.10:0.50:1.00$, $0.10:0.75:1.00$, and $0.10:1.00:1.00$ after 0, 25, 50, and 75 freeze-thaw cycles have been investigated by Shang et al. [20]. According to the information in [20], the same conclusion that the reduction of triaxial compressive strength is slower than that of uniaxial and biaxial compression strength with increasing the number of rapid freeze-thaw cycles was got. To illustrate, after the action of 75 rapid freeze-thaw cycles, compared with the initial strength of plain concrete under triaxial compression load with stress ratio $\alpha = 0.10:1.00:1.00$ prior to the rapid freeze-thaw cycles, the triaxial compressive strength decreased to 89.4 percent of initial value, while the biaxial equal compression strength and uniaxial compression strength decreased to 78.3 and 63.4 percent of initial value prior to the rapid freeze-thaw cycles, respectively. And, for plain specimen under triaxial compression with stress ratios $\alpha = 0.10:0.25:1.00$, $0.10:0.50:1.00$, $0.10:0.75:1.00$, and $0.10:1.00:1.00$ [20], the strength after the action of 75 rapid freeze-thaw cycles varied from 80.38% to 90.65% of initial value prior to rapid freeze-thaw cycles. It can be obtained from Table 3 that the effect of rapid freeze-thaw cycles on mechanical behavior (triaxial compression strength, biaxial compression strength, or uniaxial compression strength) of air-entrained concrete is much greater than that on mechanical behavior of plain concrete. That is, compared with plain concrete, air-entrained concrete is more applicable to be used in the cold regions.

FIGURE 3: Influence of middle stress ratio α_2 on triaxial compressive strength after rapid freeze-thaw cycles.

3.2.2. *Effect of Stress Ratio α_2 on Peak Stress σ_3^D .* According to the experiment result of air-entrained concrete after the same rapid freeze-thaw cycles listed in Table 2, compared with the uniaxial compression strength, the triaxial compression strength improved greatly due to the action of lateral compression stress. Under the action of triaxial compression load, the increasing percentage of ultimate strength after different freeze-thaw cycles compared with uniaxial compression strength prior to freeze-thaw cycles is shown in Figure 3. Just as demonstrated in Figure 3, the triaxial compressive strength with all stress ratios is greater than the uniaxial compressive strength after the same rapid freeze-thaw cycles. And the improved value will change with the change of stress ratio of triaxial compression. After the action of 0, 100, and 400 rapid freeze-thaw cycles, the triaxial compressive strength is largest when the stress ratio was equal to $0.10:0.50:1.00$. Consistent with this, for plain concrete under triaxial compression, the same conclusion was got in [20]. According to the experimental results in [20], for plain concrete subjected to 0, 25, 50, and 75 rapid freeze-thaw cycles, the improved value

TABLE 5: Increased percentage of triaxial compression strength over uniaxial compression strength (%).

| Stress ratio | Number of rapid freeze-thaw cycles | | | | | | | | |
|--------------|--|------|------|------|--|------|------|------|------|
| | Test results of air-entrained concrete | | | | Test results of plain concrete in [16] | | | | |
| | 0 | 100 | 200 | 300 | 400 | 0 | 25 | 50 | 75 |
| 0.1:0.25:1.0 | 3.74 | 4.11 | 3.60 | 3.32 | 3.74 | 3.94 | 3.78 | 3.51 | 3.16 |
| 0.1:0.50:1.0 | 3.72 | 3.88 | 3.48 | 3.31 | 3.72 | 4.15 | 4.01 | 3.87 | 3.76 |
| 0.1:0.75:1.0 | 3.31 | 3.29 | 3.10 | 2.86 | 3.31 | 3.71 | 3.64 | 3.45 | 3.23 |
| 0.1:1.0:1.0 | 2.48 | 2.88 | 2.97 | 2.59 | 2.48 | 3.28 | 3.16 | 3.04 | 2.93 |

TABLE 6: The value of a_1 , a_2 , a_3 , and r .

| | Stress ratio | | | |
|-------|--------------|------------|-----------|------------|
| | 0.05:1.0:1 | 0.1:0.25:1 | 0.1:0.5:1 | 0.1:0.75:1 |
| a_1 | 0.1902 | -0.0051 | -0.0739 | 0.0490 |
| a_2 | 0.5250 | 0.8608 | 0.7091 | 0.5842 |
| a_3 | -0.0161 | -0.0004 | 0.0077 | -0.0061 |
| r | 0.998 | 1.00 | 1.00 | 1.00 |

of triaxial compressive strength over uniaxial compression strength is largest when triaxial compression stress ratio $\alpha = 0.10:0.50:1.00$.

For air-entrained concrete under triaxial compression with different stress ratios prior to rapid freeze-thaw cycles, the ratio between triaxial compression strength and uniaxial compression strength varied from 2.48 to 3.74. And, after the action of 300 rapid freeze-thaw cycles, the ratio between triaxial compression strength and uniaxial compression strength varied from 2.59 to 3.32.

Meanwhile, for plain concrete under triaxial compression load with different stress ratios prior to rapid freeze-thaw cycles [20], the ratio between triaxial compression strength and uniaxial compression strength varied from 3.28 to 4.15, and, after the action of 50 rapid freeze-thaw cycles, the ratio varied to be from 3.04 to 3.87 times the uniaxial compression strength. The increased percentage of triaxial compression strength over uniaxial compression strength for air-entrained-concrete and plain concrete is shown in Table 5.

3.3. Failure Criteria. The failure criteria expressed in shear stress τ_{oct} and normal stress σ_{oct} in octahedral stress space [20, 31] can be proposed as follows:

$$\frac{\tau_{\text{oct}}}{f_c} = a_1 + a_2 \frac{\sigma_{\text{oct}}}{f_c} + a_3 N, \quad (1)$$

where a_1 , a_2 , and a_3 are the regress parameters, respectively, N is the number of rapid freeze-thaw cycles, the correlative coefficient r can be got through regression of the test results of air-entrained concrete under triaxial compression load after the action of different rapid freeze-thaw cycles, and the values of a_1 , a_2 , a_3 , and r were given in Table 6.

Figure 4 gives the testing results of air-entrained concrete under triaxial compression load and the computed results obtained according to (1). Through comparing the test results

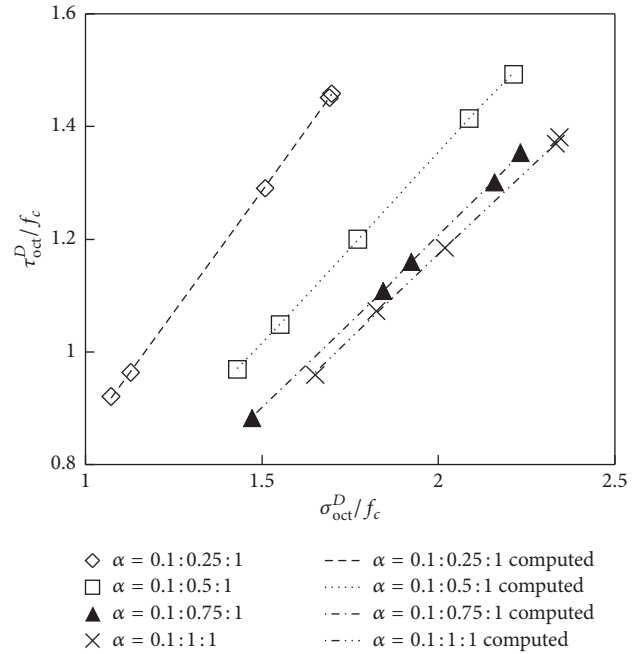


FIGURE 4: Test results of triaxial compressive strength after rapid freeze-thaw cycles in octahedral stress space.

with the computed results, it can be seen from Figure 2 that they are in good agreement.

3.4. Discussion. The deterioration of concrete material will be caused by the action of rapid freeze-thaw cycles. Compared with plain concrete, the form of the bubble in air-entrained concrete is more uniform due to the introduction of air-entraining agent. Under the effect of rapid freeze-thaw cycles, the existence of the bubble could relieve the internal expansion pressure caused when the water freezes. Then, after the action of same rapid freeze-thaw cycles, the strength loss of air-entrained concrete under triaxial compression load is lower than that of plain concrete.

The damage of concrete under triaxial compression load, biaxial compression load, and uniaxial compression load is caused by the transverse cracking. Compared with concrete specimen under uniaxial compression load, the existence of lateral compression stress σ_2^D under biaxial compression will have inhibitory effect on lateral expansion or lateral

cracking in the direction of σ_2^D , and the existence of lateral compression stresses σ_1^D and σ_2^D under triaxial compression will have inhibitory effect on lateral expansion or lateral cracking in the direction of σ_1^D and σ_2^D . So the triaxial compression strength and biaxial compression strength of air-entrained concrete are higher than uniaxial compression strength, and the triaxial compression strength is higher than biaxial compression strength due to the fact that there are inhibitory effect in the direction of σ_1^D and σ_2^D .

4. Conclusions

Based upon the test results in the study and the discussion on the experiment results, the following conclusions and recommendations can be got:

- (1) For air-entrained concrete under triaxial compression load, the effect of the action of rapid freeze-thaw cycles did not change the failure mode; slant-shear failure caused by the splitting tensile strain along σ_1^D direction was observed, and the angle between the crack and the direction of σ_3^D was about $20^\circ \sim 30^\circ$. There were two cracks on σ_2^D surface; the number of cracks on σ_3^D surface was one or two, respectively.
- (2) The triaxial compressive strength with all stress ratios is greater than the biaxial and uniaxial compressive strength after the same rapid freeze-thaw cycles; the increased percentage of triaxial compressive strength over biaxial compressive strength or uniaxial compressive strength is dependent on the middle stress.
- (3) The triaxial compression strength of air-entrained concrete decreases as number of rapid freeze-thaw cycles increases. The reduction of triaxial compression strength of air-entrained concrete is slower than that of uniaxial and biaxial compression strength as number of rapid freeze-thaw cycles increases.
- (4) The failure criteria taking account of the action of stress ratio and rapid freeze-thaw cycles in octahedral stress space were suggested.

Competing Interests

The authors declare that they have no conflict of interests.

Acknowledgments

This work was supported by the "Projects of International Cooperation and Exchanges" (Grant no. 51420105015), "Project Funded by China Postdoctoral Science Foundation" (Grant no. 2015M580576), "The Special Funds for Shandong Province Postdoctoral Innovative Projects" (Grant no. 201501008), and "Primary Research & Development Plan of Shandong Province" (Grant no. 2016GSF122003). And the authors gratefully acknowledge the financial support.

References

- [1] E. Özgan and S. Serin, "Investigation of certain engineering characteristics of asphalt concrete exposed to freeze-thaw cycles," *Cold Regions Science and Technology*, vol. 85, pp. 131–136, 2013.
- [2] B. Kucharczyková, Z. Keršner, and O. Pospíchal, "Influence of freeze-thaw cycles on fracture parameters values of lightweight concrete," *Procedia Engineering*, vol. 2, no. 1, pp. 959–966, 2010.
- [3] B. B. Sabir, "Mechanical properties and frost resistance of silica fume concrete," *Cement and Concrete Composites*, vol. 19, no. 4, pp. 285–294, 1997.
- [4] A. E. Richardson, K. A. Coventry, and S. Wilkinson, "Freeze/thaw durability of concrete with synthetic fibre additions," *Cold Regions Science and Technology*, vol. 83–84, pp. 49–56, 2012.
- [5] M. J. Setzer, "Micro-ice-lens formation in porous solid," *Journal of Colloid and Interface Science*, vol. 243, no. 1, pp. 193–201, 2001.
- [6] G. Fagerlund, "The significance of critical degrees of saturation at freezing of porous and brittle materials," in *Proceedings of the Conference on Durability of Concrete: ACI Symposium Sessions*, pp. 13–65, American Concrete Institute, 1975.
- [7] L. Petersen, L. Lohaus, and M. A. Polak, "Influence of freezing-and-thawing damage on behavior of reinforced concrete elements," *ACI Materials Journal*, vol. 104, no. 4, pp. 369–378, 2007.
- [8] W. Sun, Y. M. Zhang, H. D. Yan, and R. Mu, "Damage and damage resistance of high strength concrete under the action of load and freeze-thaw cycles," *Cement and Concrete Research*, vol. 29, no. 9, pp. 1519–1523, 1999.
- [9] K. Z. Hanjari, P. Utgenannt, and K. Lundgren, "Experimental study of the material and bond properties of frost-damaged concrete," *Cement and Concrete Research*, vol. 41, no. 3, pp. 244–254, 2011.
- [10] B. B. Sabir and K. Kouyiali, "Freeze-thaw durability of air-entrained CSF concrete," *Cement and Concrete Composites*, vol. 13, no. 3, pp. 203–208, 1991.
- [11] A. Gokce, S. Nagataki, T. Saeki, and M. Hisada, "Freezing and thawing resistance of air-entrained concrete incorporating recycled coarse aggregate: the role of air content in demolished concrete," *Cement and Concrete Research*, vol. 34, no. 5, pp. 799–806, 2004.
- [12] H.-S. Shang and Y.-P. Song, "Behavior of air-entrained concrete under the compression with constant confined stress after freeze-thaw cycles," *Cement and Concrete Composites*, vol. 30, no. 9, pp. 854–860, 2008.
- [13] S. Chatterji, "Freezing of air-entrained cement-based materials and specific actions of air-entraining agents," *Cement and Concrete Composites*, vol. 25, no. 7, pp. 759–765, 2003.
- [14] T. Pheeraphan and C. K. Y. Leung, "Freeze-thaw durability of microwave cured air-entrained concrete," *Cement and Concrete Research*, vol. 27, no. 3, pp. 427–435, 1997.
- [15] H. Shang, Y. Song, and J. Ou, "Behavior of air-entrained concrete after freeze-thaw cycles," *Acta Mechanica Solida Sinica*, vol. 22, no. 3, pp. 261–266, 2009.
- [16] A. Mahboubi and A. Ajorloo, "Experimental study of the mechanical behavior of plastic concrete in triaxial compression," *Cement and Concrete Research*, vol. 35, no. 2, pp. 412–419, 2005.
- [17] C.-Z. Wang, Z.-H. Guo, and X.-Q. Zhang, "Experimental investigation of biaxial and triaxial compressive concrete strength," *ACI Materials Journal*, vol. 84, no. 2, pp. 92–100, 1987.

- [18] Y. P. Song, G. F. Zhao, F. Peng et al., "Strength behavior and failure criterion of steel fiber concrete under triaxial compressive stress," *China Civil Engineering Journal*, vol. 27, no. 3, pp. 14–23, 1994.
- [19] L. K. Qin, *Study on the strength and deformation of concrete under multi-axial stress after high-temperature of freeze-thaw cycling [Ph.D. thesis]*, Dalian University of Technology, Dalian, China, 2003 (Chinese).
- [20] H.-S. Shang, Y.-P. Song, and L.-K. Qin, "Experimental study on strength and deformation of plain concrete under triaxial compression after freeze-thaw cycles," *Building and Environment*, vol. 43, no. 7, pp. 1197–1204, 2008.
- [21] H. S. Shang and Y. P. Song, "Experimental study of strength and deformation of plain concrete under biaxial compression after freezing and thawing cycles," *Cement and Concrete Research*, vol. 36, no. 10, pp. 1857–1864, 2006.
- [22] Y. Sun, B. Huang, J. Chen et al., "Characterization of triaxial stress state linear viscoelastic behavior of asphalt concrete," *Journal of Materials in Civil Engineering*, Article ID 04016259, 10 pages, 2016.
- [23] L.-C. Wang and Y.-P. Song, "Mechanical behavior and failure criterion of the gangue-based haydite concrete under triaxial loading," *Materials and Structures*, vol. 48, no. 5, pp. 1419–1433, 2015.
- [24] L.-C. Wang, "Multi-axial strength criterion of lightweight aggregate (LWA) concrete under the Unified Twin-shear strength theory," *Structural Engineering and Mechanics*, vol. 41, no. 4, pp. 495–508, 2012.
- [25] K. Z. Hanjari, *Load-carrying capacity of damaged concrete structures [Ph.D. thesis]*, Chalmers University of Technology, Gothenburg, Sweden, 2008.
- [26] H. S. Shang, "Triaxial compressive strength of air-entrained concrete after freeze-thaw cycles," *Cold Regions Science and Technology*, vol. 91, no. 1, pp. 33–37, 2013.
- [27] GB/T50082-2009, *The Test Method of Long-Term and Durability on Ordinary Concrete*, China Architecture & Building Press, Beijing, China, 2009.
- [28] ASTM International Committee C09 on Concrete and Concrete Aggregates, *Standard Test Method for Resistance of Concrete to Rapid Freezing and Thawing*, ASTM International, 2008.
- [29] M. G. Li, Q. Zhang, J. Wang et al., "Large scale static and dynamic concrete hydraulic servo triaxial testing equipment," *Journal of Dalian University of Technology*, vol. 43, no. 6, pp. 812–817, 2003 (Chinese).
- [30] P.-Y. Lu, Y.-P. Song, and Z.-M. Wu, "Strength and deformation characteristics of concrete subjected to different loading rates combined with confined stress," *Journal of Dalian University of Technology*, vol. 41, no. 6, pp. 716–720, 2001.
- [31] Y. P. Song, *Failure Criteria and Constitutive Relations of Concrete*, WaterPower Press, Beijing, China, 2002 (Chinese).

Research Article

Mechanical and Durability Evaluation of Concrete with Sulfate Solution Corrosion

Feng Ming,^{1,2} You-sheng Deng,¹ and Dong-qing Li¹

¹State Key Laboratory of Frozen Soil Engineering, Northwest Institute of Eco-Environment and Resources, Chinese Academy of Sciences, Lanzhou 730000, China

²Qinghai Research and Observation Base, Key Laboratory of Highway Construction & Maintenance Technology in Permafrost Region, Xining 810000, China

Correspondence should be addressed to Feng Ming; mf0329@163.com

Received 10 October 2016; Accepted 21 November 2016

Academic Editor: Francesco Caputo

Copyright © 2016 Feng Ming et al. This is an open access article distributed under the Creative Commons Attribution License, which permits unrestricted use, distribution, and reproduction in any medium, provided the original work is properly cited.

Concrete material has been a choice for the construction structures, even in the cold regions and saline zone. However, these environmental factors have critical damaging effect on the concrete characters. Consequently, this damage will decrease the servicing time of the concrete construction within this environment. In order to evaluate the durability of concrete, the behavior of concrete specimens under the sulfate solution corrosion attacks was studied in this presented work. Two groups of the specimens were immersed into the sulfate solutions with a concentration of 10% and 20%, respectively. The strength development of the specimens under different immersing time was studied. Based on Fick's law, a steady diffusion equation for sulfate ions in concrete was presented, and the depth of penetration of the attacking sulfate ions was also determined. Based on the depth of penetration and the definition of damage, a damage model for concrete material is developed and a new equation (strength-time) describing the chemical corrosion concrete material is proposed. Results show that the suggested analytical methods can quantify the damage process of concrete under sulfate attack, and the power laws damage developing formula can be used to describe the damage development of the concrete construction subjected to chemical corrosion.

1. Introduction

With a global production over 10000 million tons per year [1], the concrete material has been one of the most famous man-made materials in civil engineering. With the developing of concrete technology, the concrete material has been a choice for the construction structures, which is exposed to the extreme conditions (cold regions, saline zone) [2, 3]. However, because the durability is not strong enough to withstand the applied loads in this environment after the concrete structures constructed in the saline zone about 5~10 years, the concrete structures need to be repaired or replaced [4, 5]. According to the statistics, spending on repair and replacement of deteriorated concrete structures is astronomical. Therefore, the durability problem has been a social focal problem due to the poor performance of concrete caused by various factors [6, 7]. Recently, with the project (China Western Development) implementation, many constructions of infrastructure

including energy, transport, and telecommunications facilities and other key projects will be built up in the saline zone. Consequently, there is an urgent need for a better understanding of the durability of concrete structure, especially when the concrete structures were placed in the saline zone.

The domestic and overseas scholars have studied the durability of concrete under different environmental conditions [8–13]. The previous results pointed out that the key affecting factors for the durability of concrete structure are material factor, environmental factor, and construction factor [8, 9, 14]. The environmental factors such as physical and chemical factors [8], freezing-thawing action [10], and sulfate attack [9, 11] have a critical effect on the durability of concrete. Compared to the freezing-thawing action and the continuous immersing, the wet-dry cycling is the most primary factor, which decreases the durability of concrete [15]. Thus, more attention has been focused on the wet-dry cycling action on the durability of concrete [16, 17]. However, single attacks

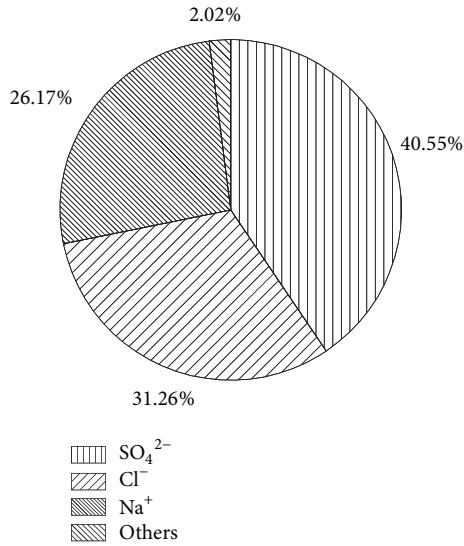


FIGURE 1: Ion contents in soil from Qinghai-Tibet Plateau.

tested in laboratory conditions yield different results than what may actually be experienced in field applications, where multiple deterioration types are occurring simultaneously [8]. According to the field investigation, the contents of SO₄²⁻, Cl⁻, and Na⁺ ions were obtained, as shown in Figure 1. Consequently, most of the studies about the concrete deterioration were focused on anticorrosion of concrete against the sulfate solution [5, 16]. For the abovementioned, the durability of concrete immersed into the sulfate solution is seldom considered. Because the long-term immersion in the salt condition has an influence on the concrete deterioration, thus, a study of concrete members (such as piles) immersed into the sulfate solution is an important aspect of engineering durability problems.

In order to investigate the durability of concrete subjected to external salt attack, the durability tests of concrete were conducted in laboratory and field [9, 12, 18]. Based on these test results, the damage mechanism of concrete was analyzed. However, the tests were carried out in a limited time. As a result, the results can not reflect the long-term performance of the concrete [6, 9]. Thus, the deterioration mechanism model, which is used to predict the concrete durability, was presented. Based on these deterioration mechanism models, the long-term performances, such as load-bearing capacity and durability, can be evaluated [12, 19]. Generally, these models mainly focus on the following aspects: the process of the sulfate ion diffusion, the increment of the expansion strain and stress, and the cracking of a concrete plate [20–22]. However, due to the ideal assumptions of these deterioration mechanism models, the predicted result has a large difference with the testing result [23]. Furthermore, in many practical applications, not only do chemical attacks occur in the concrete structures, but also simultaneously the actions of chemical attacks, freezing-thaw, and mechanical stresses take place [8, 10, 14]. Thus, the deterioration mechanism of concrete is very complex, especially when there are interactions between the concrete constructions and the environment

[24]. As a result, these models mentioned above, which try to build a deterioration model from the aspect of microstructure physical and chemical characteristics, are not suitable for predicting the service life of the concrete constructions [23, 24]. The engineering practice indicates that concrete deterioration is a progressive reduction in properties and ultimately makes concrete no longer serviceable for its intended application [16]. Motivated by this phenomenon, based on the results of systematic experiments, the damage development of concrete subjected to freezing-thawing cycles and/or wet-dry cycles and/or chemical attack was studied by the damage mechanics principles [21, 25, 26]. Of all, the long-term performance is a critical factor for service life prediction. Thus, it is important to find a reasonable method to predict the long-term performance of the concrete constructions.

After reviewing the history and the present situation of the investigation on the concrete durability, it can be found that there are many works that have been done about the durability of concrete. This paper presents aspect of the research performed in the laboratory using natural testing procedures and looking at the deterioration of sulphane ingress. The depth of penetration of the attacking sulphane ions was determined after a certain time. Based on the concept of the damage degree, a new equation (strength-time) describing the chemical corrosion concrete material is proposed. On the basis of the experimental results, the prediction model was obtained and this model can be used to predict the durability of the concrete construction.

2. Experimental Designs

2.1. Characteristics of Concrete Mixtures

2.1.1. Cement. The cement is ordinary Portland cement (PO 42.5) produced by Qilianshan Corporation in Gansu Province, China. The performance index of the used cement is shown in Table 1.

2.2. Sample Preparing. The ratio mass (water):mass (cement) is 0.45, the ratio mass (sand):mass (cement) is 1.23, and the ratio mass (stones):mass (cement) is 2.63. The details of the concrete mixture are listed in Table 2.

All specimens were prepared as cube of 100 mm × 100 mm × 100 mm in the laboratory. Raw materials included Portland cement, silica sand, stone, and water. All specimens were cured for one day in nature condition before being demoulded and for another 27 days cured at 20 ± 1°C with a relative humidity at 95 ± 5%.

2.3. Continuous Immersing Tests. In order to measure the sulfate erosion damage of the concrete specimens, Na₂SO₄ solution was chosen as the sulfate liquor, and two concentrations of 10% and 20% were considered. After all the specimens were cured for 28 days, the specimens were immersed into the sulfate solution. During the continuous immersing tests, the sulfate solution was changed once a month to ensure the mass fraction unchanged. After immersing 0 d, 30 d, 60 d, 90 d, 120 d, 180 d, 270 d, 360 d, and 450 d, the specimens are picked out, and then the compressive strength test was conducted,

TABLE 1: PO 42.5 performance index of Portland cement.

| Specific surface area [m ² ·kg ⁻¹] | Chloride ion [%] | Alkali content [%] | Sulphur trioxide [%] | Ignition loss [%] | Setting time [min] | | Compressive strength [MPa] | |
|---|------------------|--------------------|----------------------|-------------------|--------------------|-------|----------------------------|---------|
| | | | | | Initial | Final | 3 days | 28 days |
| 347 | 0.012 | 0.43 | 2.44 | 1.52 | 185 | 325 | 21.7 | 48.6 |

Sand: well-graded medium river sand, the fineness modulus being 2.7; stones: continuous grading gravel, 5~20 mm; Na₂SO₄: analytical reagent with a quality fraction of 99.28% and the relative molecular mass being 142.04; the running water was used to mix these raw materials.

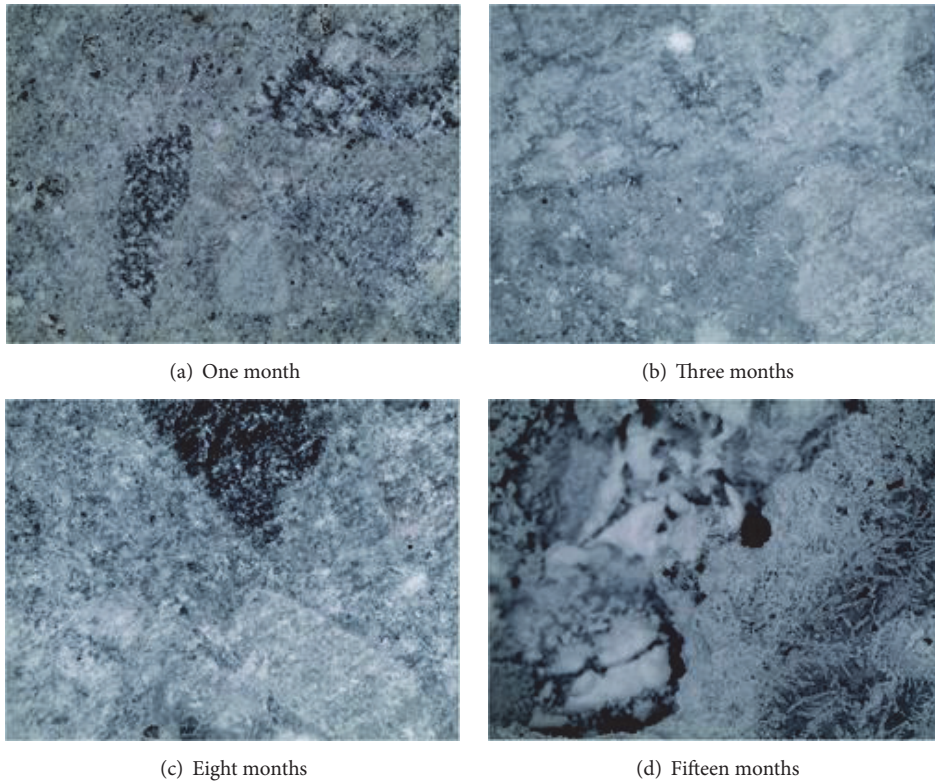


FIGURE 2: Microstructures of concrete specimens subjected to different immersing time.

TABLE 2: Concrete mixture.

| Water [kg] | Cement [kg] | Sand [kg] | Stone [kg] | W/C | Sand percentage [%] |
|------------|-------------|-----------|------------|------|---------------------|
| 205 | 455 | 562 | 1195 | 0.45 | 32 |

with a loading rate of 0.5 MPa/s. During the test events, when the two duplicate samples' tolerance bias is over 5 MPa, this result is rejected.

3. Test Result

Figure 2 shows the microstructure of concrete specimens subjected to different immersing times in sulfate solution with a concentration of 10%. As shown in Figure 2(a), there is no ettringite crystal that can be seen in the pores after one month of immersion. With the increasing of immersing time, a little amount of ettringite crystals can be seen in the

pores after immersion for three months (Figure 2(b)). With the amount of ettringite crystals continuously increasing with immersion time, the sulfate solution has little destroying effect on the concrete and is accompanied by small fracture and convex protrusion (Figure 2(c)). After immersion for eight months, massive ettringite crystals and gypsum crystals could be noted in the pores (Figure 2(c)). It is well known that when the corrosion products are formed enough, the concrete has to bear the expansion stress [3]. If the expansion stress generated by the expansive products exceeds the tensile strength of concrete, the fracture may occur from the surface to the internal region [18], as shown in Figure 2(d). From the abovementioned, it can be concluded that with the increasing of immersing time the sulfate attack has an obviously destroying effect on the concrete structure.

From Figure 2, the results indicate that the sulfate solution is decreasing the durability of the concrete. However, the damage level can be not determined. In order to analyze the

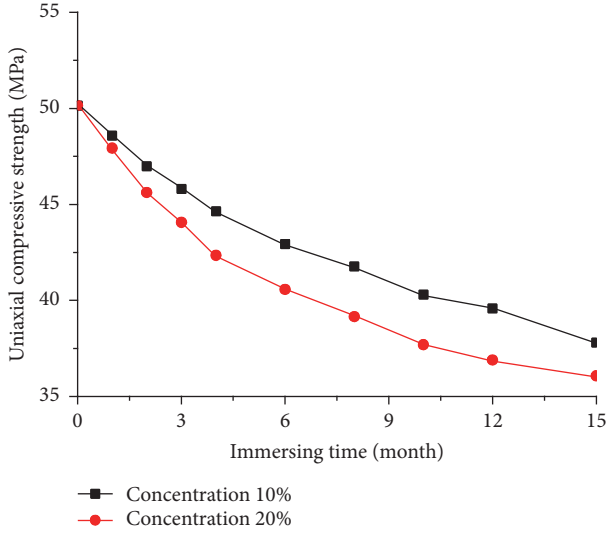


FIGURE 3: Uniaxial compressive strength results.

damage mechanism of concrete under sulfate solution environment, the uniaxial compressive tests were conducted and the uniaxial compressive strength results are presented in Figure 3. As shown in Figure 3, the uniaxial compressive strength decreases with the increasing of immersing time whatever in the low or high concentration environment. Moreover, concentration of 20% has more serious damage than the concentration of 10%. As the sulfate attack occurs continuously in the concrete, the damage caused by chemical corrosion, especially the ettringite crystals, results in more porous structure in concrete [18]. Due to the increasing of permeability, the sulfate solution can more easily penetrate into the interior; as a result, the porosity is increasing and the effective area is decreasing. Consequently, it is accelerating the process of deterioration, and the deterioration manifests as the uniaxial compressive strength decreasing with immersing time.

According to the definition of the damage degree, the following formula can be obtained [27]:

$$D_i = 1 - \frac{\sigma_i}{\sigma_0}, \quad (1)$$

where D_i is the damage degree of concrete after certain immersing time; σ_i is the uniaxial compressive strength of concrete after certain immersing time; σ_0 is the initial uniaxial compressive strength of concrete.

Figure 4 shows the damage development of concrete subjected to different sulfate solution concentrations. It can be seen clearly from Figure 4 that the damage degree of concrete in both sulfate solutions increased with the immersing time. Furthermore, the experimental results showed that the damage degree of concrete immersing to the concentration of 20% is higher than the concentration of 10%. With the damage developing, the bearing of the concrete construction is decreasing. When the damage reaches a certain degree, the concrete constructions will fail completely.

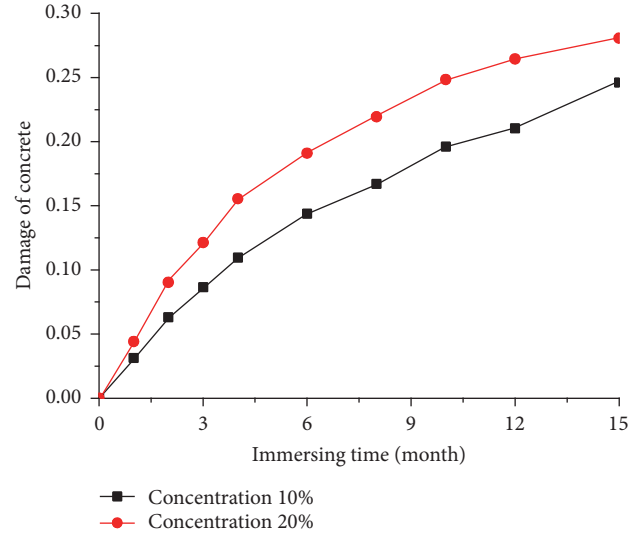


FIGURE 4: Damage developing with the immersing time.

4. Damage Developing Model for Chemical Corrosion of Concrete

It is well known that the concrete constructions, such as piles, were designed with a long service time. As a result, much attention has been paid to the durability of concrete, especially including the sulfate erosion [6, 8, 14]. Of course, the uniaxial compressive strength is an important parameter for determining the concrete durability. In this section, based on Fick's law, a steady diffusion equation of sulfate ions is presented. With the damage developing equation of concrete subjected to sulfate environment, a systematic theory for the prediction of service life of concrete constructions was presented.

The process of concrete degradation is simplified with three important assumptions as follows:

- (1) Microdefects and hydration product of SO_2^{-4} are distributed evenly in the concrete.
- (2) The expansion of the solid product is treated as a uniform expansion.
- (3) Ignoring the SO_2^{-4} concentration varies with time in the corrosion areas.

4.1. Process of Ion Diffusion. The concrete material is considered as two-phase material, which consists of a matrix and pores. Thus, the ion can migrate in the concrete constructions and the penetration depth increased with the increasing of immersing time, as shown in Figure 5.

According to Fick's law, the following equation can be obtained:

$$J(x) = \frac{dm}{dt} = -L^2 k \frac{\partial c}{\partial x}, \quad (2)$$

where $J(x)$ is the erosion ion flux; m is the mass of the ion which diffuses into the concrete; t is time in months; L is the length of the research area; k is the diffusion coefficient;

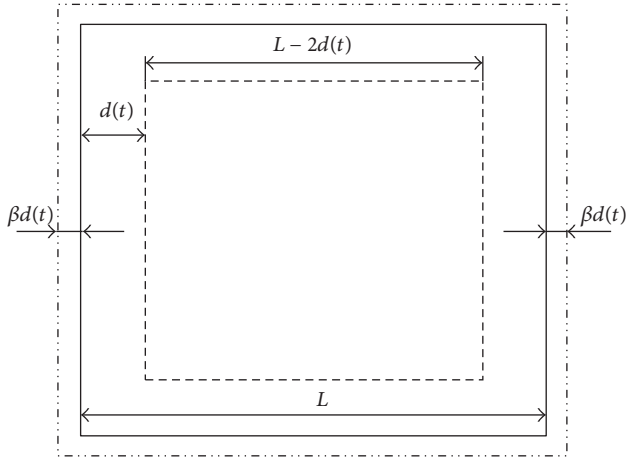


FIGURE 5: Cross section of the chemical attacked concrete specimen.

c is the solution concentration in the corrosion layer; x is coordinate.

Equation (2) can be written in another form:

$$\frac{\partial c}{\partial x} = -\frac{J(x)}{L^2 k} \frac{\partial x}{\partial x}. \quad (3)$$

Integrating (3), we obtain

$$\int_{c_0}^0 \partial c = -\int_0^{d(t)} \frac{J(x)}{L^2 k} \partial x, \quad (4)$$

where c_0 is the solution concentration at the surface of the corrosion layer; $d(t)$ is the diffusible depth.

Rewriting (4) gives

$$J(x) = \frac{L^2 k c_0}{d(t)}. \quad (5)$$

Substituting (2) into (5),

$$\frac{\partial c}{\partial x} = -\frac{c_0}{d(t)}. \quad (6)$$

Supposing that the mass of the hydration product of SO_2^{-4} in unit area is n , then the mass of the hydration product of SO_2^{-4} in $L^2 dx$ can be calculated:

$$nL^2 dx = -L^2 k \frac{\partial c}{\partial x} dt. \quad (7)$$

Substituting (6) into (7) and integrating, then the diffusible depth can be described as follows:

$$d(t) = \sqrt{\frac{2kc_0 t}{n}}. \quad (8)$$

4.2. Process of Damage Developing. During the sulfates corrosion, the penetration of aggressive media leads to an increase of the porosity of the material. It is assumed that, due to the increasing of the porosity, there is an expansion coefficient of

the attacked area as shown in Figure 5 and (9). At any time t , the length of the area can be drawn by the following formula:

$$L(t) = L + 2\beta d(t). \quad (9)$$

The length of noncorrosive areas is

$$l(t) = L - 2d(t). \quad (10)$$

On the basis of certain definitions of macrophenomenological damage mechanics, then, the damage degree D of the whole area A can be obtained by [27]

$$D = \frac{(A_1 D_1 + A_0 D_0)}{A}, \quad (11)$$

where A is the area of the sample and $A = L^2$; A_0 is the area of the noncorrosive parts and $A_0 = (L - 2d(t))^2$; D_0 is the damage degree of the noncorrosive parts; A_1 is the area of the corrosive parts and $A_1 = (L + 2\beta d(t))^2 - A_0$; D_1 is the damage degree of the corrosive areas.

Changing (11) in another form,

$$D = D_0 + \frac{4d(t) [(1 + \beta) D_1 - D_0]}{L} + \frac{4d(t)^2 [(\beta^2 - 1) D_1 + D_0]}{L^2}. \quad (12)$$

Substituting (8) into (12),

$$D = D_0 + \frac{4\sqrt{2kc_0 t/n} [(1 + \beta) D_1 - D_0]}{L} + \frac{4(\sqrt{2kc_0 t/n})^2 [(\beta^2 - 1) D_1 + D_0]}{L^2}. \quad (13)$$

Due to the parameters $D_0, D_1, L, k, c_0, n, \beta$ in (12) that can be determined by the laboratory test, thus, the damage developing of concrete is only depending on the immersing time. Consequently, the damage equation can be rewritten as

$$D = D_0 + \frac{4\sqrt{2kc_0/n} [(1 + \beta) D_1 - D_0]}{L} t^{1/2} + \frac{8kc_0 [(\beta^2 - 1) D_1 + D_0]}{nL^2} t. \quad (14)$$

After the parameters $D_0, D_1, L, k, c_0, n, \beta$ were determined, the coefficients of $t^{1/2}$ and t in (14) can be determined. Thus, (14) can be simplified as

$$D = D_0 + b_1 t^{1/2} + b_2 t, \quad (15)$$

where b_1, b_2 are the experimental constants, corresponding to the concrete characteristic.

For the porous materials, such as soil, rocks, and concrete, because they consist of a matrix and pores, these materials always have initial damage. For the engineering purpose, it is

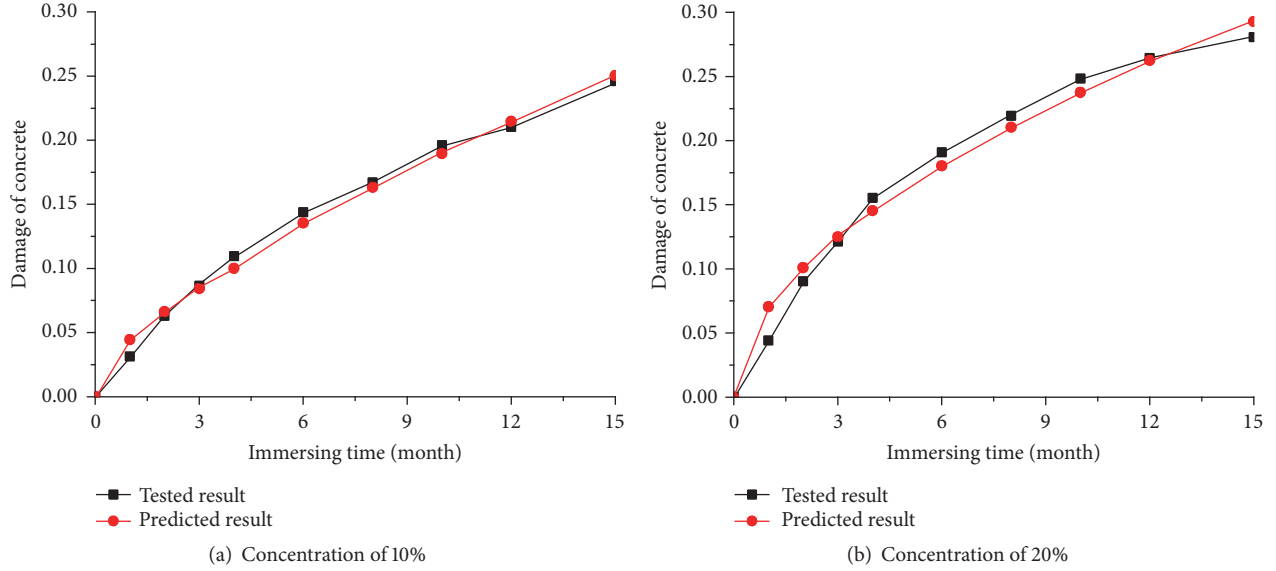


FIGURE 6: Comparison result between the tested result and the predicted result.

TABLE 3: Regression results for the corrosion of the concrete immersed into 10% and 20% sulfate solutions.

| Concentration [%] | Regression equation | Standard deviation |
|-------------------|------------------------------------|--------------------|
| 10 | $D_{rd} = 0.0391t^{1/2} + 0.0055t$ | 0.028 |
| 20 | $D_{rd} = 0.0685t^{1/2} + 0.0021t$ | 0.067 |

more convenient to use the damage degree D_{rd} , which can be described as follows:

$$D_{rd} = D - D_0 = b_1 t^{1/2} + b_2 t. \quad (16)$$

According to the previous studies [6, 14, 21], chemical corrosion can lead to an increase of the porosity and a decrease of the matrix volume of the concrete materials. Equation (14) was derived from the damage theory, which is the effective working parts decreasing with time. Thus, formula (14) including formulas (15) and (16) can be used to evaluate these corrosion effects on concrete materials. On the basis of the experimental damage developing results (Figure 4), the formulas describing the effects of chemical corrosion attacks with concrete construction immersed into sulfate solutions have been obtained by means of regression. The regression result is shown in Table 3 and Figure 6.

On the basis of the experimental result and the presented model, the comparison result between the tested result and the predicted result is shown in Figure 6. As shown in Figure 6, the theoretically derived power law (statistical regression) is complied with the tested results. The standard deviations between the tested results and predicted results are less than 10% in these two cases. This indicates that the predicted value is well in agreement with the measurement results. Consequently, the presented model is suitable for describing the effect of chemical corrosion attacks with concrete.

5. Conclusions

In order to investigate the deterioration mechanism of the concrete materials used in salt regions, two groups of concrete specimens were immersed into sodium sulfate solution with two concentrations of 10% and 20%. On the basis of the experimental result, a damage developing model of concrete was derived. As a result, the following conclusions can be drawn:

- (1) The damage degree of the concrete is increasing with the immersion time, and the macro damage features are more clear. As a result, the concrete has obvious deterioration due to the severe environmental conditions.
- (2) The depth of penetration of the corrosive salt solutions increasing with the immersing time increased. Furthermore, the velocity of penetration depends on the initial concentration, the properties, and the structure of the materials.
- (3) Based on the relationship between the depth of penetration and the damage degree, the damage developing formula was derived and the power laws can be used to describe the damage development of the concrete construction subjected to chemical corrosion.

Competing Interests

The authors declare that they have no competing interests.

Acknowledgments

This work is supported by the National Natural Science Foundation of China (no. 41271080), the Key Research Program of Frontier Sciences of Chinese Academy of Sciences (QYZDY-SSW-DQC015), and the Funding of the State Key Laboratory of Frozen Soil Engineering (no. SKLFSE-ZT-17).

References

- [1] A. Hasanbeigi, L. Price, and E. Lin, "Emerging energy-efficiency and CO₂ emission-reduction technologies for cement and concrete production: a technical review," *Renewable and Sustainable Energy Reviews*, vol. 16, no. 8, pp. 6220–6238, 2012.
- [2] S. Chatterji, "Aspects of the freezing process in a porous material-water system: part 1. freezing and the properties of water and ice," *Cement and Concrete Research*, vol. 29, no. 4, pp. 627–630, 1999.
- [3] Y. Gao, J. Zhang, and Y. D. Han, "Decay of fracture parameters of concrete under sulfate environments," *Journal of Building Materials*, vol. 14, no. 4, pp. 465–477, 2011.
- [4] J. A. Hartell, A. J. Boyd, and C. C. Ferraro, "Sulfate attack on concrete: effect of partial immersion," *Journal of Materials in Civil Engineering*, vol. 23, no. 5, pp. 572–579, 2011.
- [5] D. Niu, L. Jiang, and Q. Fei, "Deterioration mechanism of sulfate attack on concrete under freeze-thaw cycles," *Journal Wuhan University of Technology, Materials Science Edition*, vol. 28, no. 6, pp. 1172–1176, 2013.
- [6] A. Neville, "The confused world of sulfate attack on concrete," *Cement and Concrete Research*, vol. 34, no. 8, pp. 1275–1296, 2004.
- [7] E. Peris Mora, "Life cycle, sustainability and the transcendent quality of building materials," *Building and Environment*, vol. 42, no. 3, pp. 1329–1334, 2007.
- [8] E. Holt, M. Ferreira, H. Kuosa, and M. Leivo, "Performance and durability of concrete under effect of multi-deterioration mechanisms," *Journal of the Chinese Ceramic Society*, vol. 43, no. 10, pp. 1420–1429, 2015.
- [9] H. L. Zhang, Y. F. Zhu, and J. C. Han, "Study of the durability of partially-exposed concrete in chloride saline soil areas of Qinghai Province," *Journal of Hefei University of Technology*, vol. 38, no. 4, pp. 804–809, 2015.
- [10] W. J. Yan, F. J. Niu, X. J. Zhang et al., "Advances in studies on concrete durability and countermeasures against freezing-thawing effects," *Sciences in Cold and Arid Regions*, vol. 6, no. 4, pp. 398–408, 2014.
- [11] C. Faella, C. Lima, E. Martinelli, M. Pepe, and R. Realfonzo, "Mechanical and durability performance of sustainable structural concretes: An Experimental Study," *Cement and Concrete Composites*, vol. 71, pp. 85–96, 2016.
- [12] L. Tang, P. Utgenannt, and D. Boubitsas, "Durability and service life prediction of reinforced concrete structures," *Journal of the Chinese Ceramic Society*, vol. 43, no. 10, pp. 1408–1419, 2015.
- [13] J. M. Aldred and A. Castel, "Chloride penetration after field exposure compared with estimates from service life prediction models," in *Proceedings of the RILEM International Workshop on Performance-Based Specification and Control of Concrete Durability*, RILEM PRO 089, pp. 143–150, Zagreb, Croatia, June 2014.
- [14] R. Gao, Q. Li, and S. Zhao, "Concrete deterioration mechanisms under combined sulfate attack and flexural loading," *Journal of Materials in Civil Engineering*, vol. 25, no. 1, pp. 39–44, 2013.
- [15] R. D. Cody, A. M. Cody, P. G. Spry et al., *Reduction of Concrete Deterioration by Ettringite Using Crystal Growth Inhibition Techniques*, Iowa State University, Iowa, IA, USA, 2001.
- [16] H. L. Wang, Y. S. Dong, X. Y. Sun, and W. L. Jin, "Damage mechanism of concrete deteriorated by sulfate attack in wet-dry cycle environment," *Journal of Zhejiang University (Engineering Science)*, vol. 46, no. 7, pp. 1255–1261, 2012.
- [17] Z. Zhang, M. Thiery, and V. Baroghel-Bouny, "Numerical modelling of moisture transfers with hysteresis within cementitious materials: verification and investigation of the effects of repeated wetting-drying boundary conditions," *Cement and Concrete Research*, vol. 68, pp. 10–23, 2015.
- [18] M. T. Bassuoni and M. L. Nehdi, "Durability of self-consolidating concrete to different exposure regimes of sodium sulfate attack," *Materials and Structures*, vol. 42, no. 8, pp. 1039–1057, 2009.
- [19] J. Marchand, E. Samson, Y. Maltais, and J. J. Beaudoin, "Theoretical analysis of the effect of weak sodium sulfate solutions on the durability of concrete," *Cement and Concrete Composites*, vol. 24, no. 3–4, pp. 317–329, 2002.
- [20] S. Ahmad, "Reinforcement corrosion in concrete structures, its monitoring and service life prediction—a review," *Cement and Concrete Composites*, vol. 25, no. 4–5, pp. 459–471, 2003.
- [21] U. Schneider and S.-W. Chen, "Modeling and empirical formulas for chemical corrosion and stress corrosion of cementitious materials," *Materials and Structures*, vol. 31, no. 10, pp. 662–668, 1998.
- [22] T. Cho, "Prediction of cyclic freeze-thaw damage in concrete structures based on response surface method," *Construction and Building Materials*, vol. 21, no. 12, pp. 2031–2040, 2007.
- [23] Y. P. Du, Y. Yao, and L. Wang, "Research progress on the prediction of concrete's service life based on freeze-thaw damage," *Journal of Yangtze River Scientific Research Institute*, vol. 31, no. 4, pp. 77–84, 2014.
- [24] W. Sun and C. W. Miao, *The Theory and Technology of Modern Concrete*, Science Press, Beijing, China, 2012.
- [25] Q. H. Xiao, D. T. Niu, and W. P. Zhu Wen, "Strength degradation model and durability service life prediction of concrete in freezing-thawing circumstance," *Building Structure*, vol. 41, no. 2, pp. 203–207, 2011.
- [26] M. Leivo, E. Sistonen, F. Al-neahawy et al., "Effect of interacted deterioration parameters on service life of concrete structures in cold environments," VTT Research Report VTT-R-09119-11, 2011.
- [27] D. T. Niu, *Durability and Life Forecast of Reinforced Concrete Structure*, Science Press, Beijing, China, 2003.